THE UNIVERSITY OF
WARWICK

Solid State NMR Studies of Ferroelectric Relaxor Materials

by

Prodipta Bhattacharya

Thesis

submitted to the University of Warwick

for the degree of

Doctor of Philosophy

Department of Physics

October 2005

This thesis is dedicated to my Father

Contents

List of Tables

List of Figures

Acknowledgements

First of all, I would like to thank EPSRC and the Department of Physics at Warwick for providing the facilities that made this work possible. I would also like to thank Dr. A. Howes, Dr. K.J. Pike and Prof. R. Dupree for their valuable advice in NMR, and Prof. P.A. Thomas for explaining the crystallographic aspects of the work. I would also like to thank Dr Q. Jiang, Dr S.K. Singh and Dr D. Zekria for providing me with some of the samples used in this study.

Thanks to all my fellow PhD students in the NMR group: Dr. P. Gunawidjaja, K. Drake, L. Barrett, L. O'Dell and D. Carroll and other group members without whose company my time here would have been far less enjoyable.

Special thanks are also due to my parents for all their care and support over the years. I would like to thank Lucette Yvernault for her encouragement and patience throughout my PhD period.

Finally, I would especially like to thank my supervisor Prof. Mark E Smith for his friendly guidance, interest and enthusiasm during the course of this work.

Declaration

The work for this thesis was carried out in the Department of Physics of the University of Warwick from January 2002 to January 2005. It is the result of my own independent research except where specifically referenced in the text and has not been previously submitted for any other degree.

It is anticipated that parts of this thesis will be submitted for publication in the future.

Abstract

Multi-nuclear solid state nuclear magnetic resonance has been used to investigate the local atomic structure of the relaxor ferroelectric materials, lead magnesium niobate titanate (PMN-PT) and sodium potassium bismuth titanate (NKBT). In addition to these two series of materials, numerous precursor and model niobate compounds have also been analysed in order to gain a insight into the structures and phases present in these materials.

The PMN-PT series was investigated using ^{93}Nb, ^{207}Pb and ^{17}O NMR techniques. A total of 14 PMN-PT samples, from pure PMN to PMN-90PT, were investigated in order to fully understand the transitions taking place over the entire compositional range. ^{93}Nb proved to be the most informative nucleus, owing to its high sensitivity to the changes occurring at the B-site of the perovskite structure. We discovered three distinct niobium environments. We then proposed a new random-site random-layer model explaining the distribution of the cations among two different layers β' and β''. The high level of correlation between the theoretical predictions and the experimental results suggests that there are actually two different ways that PMN-PT behaves, one for titanium concentrations less than 25% and the other for concentrations over 25%. This was also clearly visible in our PMN-PT spectra, as a sharp line present in titanium concentrations below 25%, that disappears in the concentrations above 25%. We have also tied in our results with the existing literature on PMN-PT to identify possible links to the dielectric response and phase transitions in the material.

NKBT was investigated using both ^{23}Na and ^{39}K MAS NMR techniques. The ^{23}Na data proved most informative and results were obtained at different fields and different spinning speeds. We were then able to extract calculated isotropic chemical shift values and quadrupolar parameters to understand the subtle changes taking place. The preliminary results hint that there are some interesting changes taking place around the morphotropic phase boundary in the material.

List of Abbreviations

ADC	Analogue to Digital Converter
CSA	Chemical Shift Anisotropy
CYCLOPS	CYCLically Ordered Phase Sequence
DOR	Double Angle Spinning
EFG	Electric Field Gradient
EXAFS	Extended X-Ray Absorption Fine Structure
FID	Free Induction Decay
FT	Fourier Transform
IPA	Iso-Propyl Alcohol
MAS	Magic Angle Spinning
MQ	Multiple Quantum
NKBT	Sodium Potassium Bismuth Titanate
NMR	Nuclear Magnetic Resonance
PAS	Principal Axis System
PIN	Lead Indium Niobate
PLT	Lead Lanthanum Titanate
PMN-PT	Lead Magnesium Niobate Titanate
PSN	Lead Scandium Niobate
RAPT	Rotor Assisted Population Transfer
S/N	Signal to Noise Ratio
XRD	X-Ray Diffraction

Chapter One

1.1 Introduction

Nuclear Magnetic Resonance (NMR) spectroscopy is an important technique that is widely used in many different branches of science ranging from biology and chemistry through to physics and advanced materials sciences. It is now common place to use liquid state ^{1}H and ^{13}C spectra to identify organic compounds along with infra-red spectroscopy and mass spectroscopy methods. NMR is also widely used to examine biologically active peptides, proteins and nucleic acids, where it has greatly enhanced the speed and accuracy of determining these structures. The use of magnetic resonance for medical imaging purposes has provided the medical community with a ideal non invasive diagnostic tool. Magnetic Resonance Imaging (MRI) machines are now common place in hospitals around the world providing a safe way to examine patients. All the methods described above are primarily used for molecules in solution.

The application of magnetic resonance to solid state samples has been largely limited to physical chemistry laboratories in large research institutes. Over the last twenty years there has been a sudden increase in the use of such solid state NMR techniques. This has come about due to the advances in technologies such as availability of higher magnetic fields, faster spinning speeds as well as developments in multiple-pulse techniques. Probably the single most important solid state technique to be developed is magic-angle-spinning (MAS). This technique greatly reduces the broadening usually present in solid state samples. This technique is described in greater detail in the following chapter. This thesis describes the programme of work

on structural studies of the new relaxor perovskite ferroelectrics $(PbMg_{0.33}Nb_{0.67}O_3)_{1-x}$ – $(PbTiO_3)_x$ (PMN-PT) and $(Na_xK_{1-x})_{0.5}$ $Bi_{0.5}TiO_3$ (NKBT).

PMN-PT is a new and interesting material that is attracting significant interest as a 'giant piezoelectric' single crystal material with piezoelectric and electromechanical coupling over five times the industry standard ceramic material Lead Zirconate Titanate (PZT)[1]. Even now not much is known about the structures, phase transitions and properties of PMN-PT. NKBT has a potential for biological applications in the lead-free piezoelectric market. Thus the major scientific aim of the current thesis is to determine the role of crystal structure and bonding, at the atomic level in promoting ferroelectric relaxor and enhanced piezoelectric behaviour.

PMN-PT and NKBT are united by displaying ferroelectric relaxor behaviour. Relaxor ferroelectrics are defined as those ferroelectrics that show a diffuse anomaly in their dielectric constant at the ferroelectric – paraelectric phase transition and which show a frequency shift in the dielectric loss peak as a function of temperature. Structurally relaxor ferroelectrics exhibit site-sharing and compositional disorder. In order to display relaxor behaviour it is necessary to have more than one chemical element sharing the same site in the structure.

What sets PMN-PT apart from commonly used piezoelectrics is the ability to grow single crystals, as well as ceramics in the full composition range from $x = 0$ to $x = 1$. Thus PMN-PT has outstanding potential for use in electromechanical transduction devices owing to its ultrahigh piezoelectric effects.

The electromechanical properties of PMN-PT are significantly enhanced at the vertical phase boundary between the rhombohedral and the tetragonal phases, commonly known as the Morphotropic Phase Boundary (MPB). The MPB is usually characterised by a change of phase with composition, it is almost entirely independent

of temperature. In the PMN-PT system, the MPB has been suggested to occur at around x= 0.3 to x = 0.35 compositions though this has not yet been accurately determined. It is also thought that the phase transition is from rhombohedral to tetragonal, although the structures and space groups on either side of the MPB, or even whether the transition occurs via an intermediate phase has not yet been established. However it is assumed that the giant piezoactivity of PMN-PT is directly associated with this MPB.

PMN-PT crystallises in the typical perovskite type ABO_3 cell structure (Figure 1.1). The ideal cubic perovskite structure consists of corner linked oxygen octahedra, with B cations at their centres, and A cations at the interstices between them.

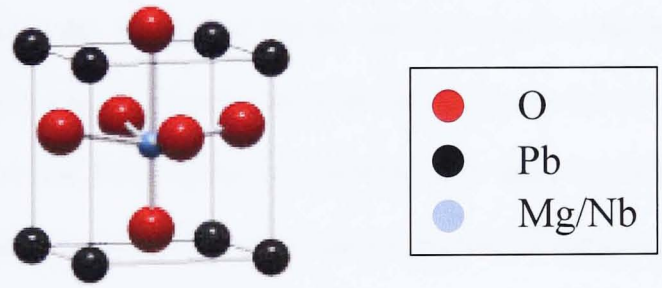

FIGURE 1.1 – ABO_3 Perovskite Structure[4]

The actual positions of the oxygen atoms of the perovskite framework play an important role in determining the crystal symmetry and physical properties. Furthermore the ferroelectric phases are produced by small, subtle distortions of this prototypic perovskite structure.

PMN-PT, in which Mg and Nb site-share, and for nearly all known examples of relaxors, the cations are substituted on the B-site of the ABO_3 perovskite. However

in the NKBT series, relaxor behaviour derives from substitution of electronically diverse ions (Na^{+} & Bi^{3+}) on the A-site. Hence it is interesting and important to compare the behaviours arising from such A and B site substitutions.

According to Park and Shrout[1] a single crystal of PMN-PT, with composition around 33% PT, exhibits a giant piezoelectric response of order 2500 pC/N, which should be compared to the industry standard PZT which is around 600 pC/N. This development of single crystal PMN-PT also opens up interesting opportunities in the field of piezo-optics.

One of the primary objectives of the research is to try and understand the atomic ordering that is the key to the interesting physical properties of both PMN-PT and NKBT. A range of techniques are now available to probe structures (Figure 1.2). Multinuclear solid state Nuclear Magnetic Resonance (NMR) is one of the best techniques that can probe at this scale. It is hoped that by employing such techniques direct and interesting information may be revealed about the atomic ordering and site distortions. Furthermore when this information is combined with high resolution Neutron Powder Diffraction data from a parallel study, the comparison of the average crystal structure of the phases with the local structure will become possible. This will help to solve some of the questions about the local order on the B site of PMN-PT and the environment of the A site of NKBT.

Effectively all of the nuclei in these systems can be examined using NMR, but the ^{93}Nb, ^{207}Pb, ^{23}Na, ^{39}K and ^{17}O are examined more closely.

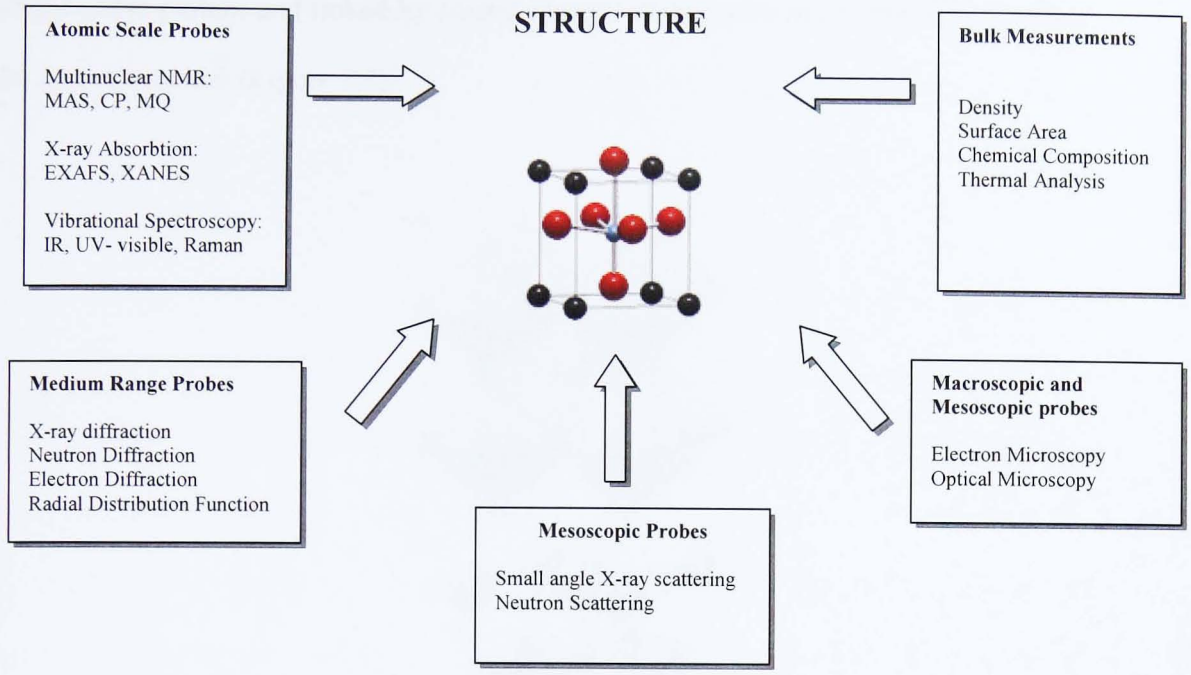

FIGURE 1.2 – Relationship between the various methods for investigating the structures of materials [2]

1.2 Ferroelectric Materials

In order to understand more about the properties of PMN-PT and NKBT it is necessary to compare them with other perovskite relaxor ferroelectric materials and discuss both the potential similarities and differences that may account for the differing properties between them. The rest of this section gives a brief overview of these materials and describes what is known about their structures and properties.

1.2.1 Perovskites

Perovskite is the name of the mineral $CaTiO_3$. However the general formula for this group of ferroelectrics with oxygen octahedra is ABO_3, where A is a monovalent or divalent metal and B is a tetra or pentavalent one. It is cubic, with the A atoms at the cube corners, B atoms at the body centers and oxygen at the face centers. The structure can also be regarded as a set of BO_6 octahedra arranged in a

simple cubic pattern and linked by shared oxygen atoms, with the A atoms occupying the spaces between (Figure 1.3).

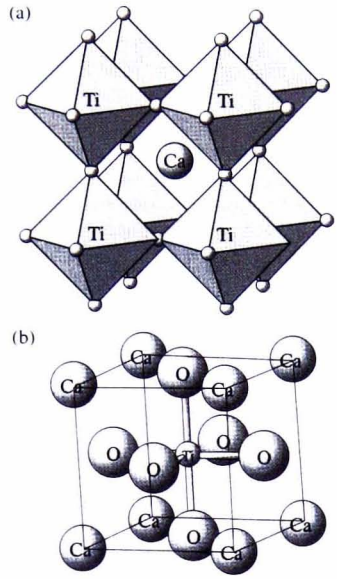

FIGURE 1.3 – $CaTiO_3$ crystal structure (a) closest packing of O + Ca atoms with Ti occupying the interstitial *O* sites (b) in the later figure only Ti at the center of the cell is shown

Perovskites have been an area of scientific importance since the 1940s. It was von Hippel *et al.*[3] who first reported on the presence of ferroelectric properties of Barium Titanate ($BaTiO_3$). Since this time almost all possible combinations of larger A cations and smaller B ions have been studied extensively. However it soon became apparent that it was also possible to make new perovskites by substituting more than one element into the A or B positions of the perovskite structure. These compounds were commonly referred to as complex perovskites.

PMN is an example of a complex double perovskite where the total number of B-sites are shared by a third of the magnesium (Mg^{2+}) ions and the other two thirds by niobium (Nb^{5+}) ions. Furthermore the charge neutrality of the entire system is thus maintained through the B-site average charge of 4+. It is however quite possible that

there are small microregions in the material where the concentration of a particular ion species is greater than another. Of course by adding titanium (Ti^{4+}) ions in PMN this charge neutrality is also maintained allowing an entire range of compositions of PMN-PT 'solid solutions' to be formed.

However the onset of ferroelectric ordering in such materials is accompanied by a variety of structural changes leading to new polar phases. One such mechanism is the movement of B-ions inside the oxygen octahedra along a specific crystallographic direction, which then becomes the polar axis. Usually this is accompanied by a change in oxygen positions, and may involve a disorder-order transition regarding site occupancy. Alternatively the oxygen octahedra may rotate or distort to reduce the A-O distance. Thus most distortions are realised through the displacements of the cations of their usual sites, tilting or distortions of the oxygen octahedra, or simply from a combination of the above. A more complete categorisation of the 23 types of tilted octahedra in perovskites including the description of the commonly used notation to describe the various space groups and orientations can be found in the original article by Glazer[4].

1.2.2 Relaxor Ferroelectrics

A material is said to be ferroelectric when it has two or more orientational states in the absence of an electric field and can be shifted from one to another of these states by an electric field. These materials also show polarisation, and the direction of this polarisation may also be reversed on application of an electric field. These materials are characterised by a transition temperature τ_m (Curie point) above which their symmetry is non-polar and below which its symmetry is polar. A material can also be considered ferroelectric when the ionic displacements are along the same direction in alternate unit cells (Figure 1.4). If the displacements are of alternating

directions in successive unit cells this type of material is commonly called antiferroelectric. Lead titanate ($PbTiO_3$) is a typical example of a normal ferroelectric material while Lead zirconate ($PbZrO_3$) is a typical antiferroelectric material.

All ferroelectric materials are piezoelectric but not all piezoelectric materials are ferroelectric. Piezoelectric materials are simply those materials that can change shape when subject to an electric field. The polarisation is changed when stress is applied or simply by a change in electric field. It is these changes that create an internal stress within such materials.

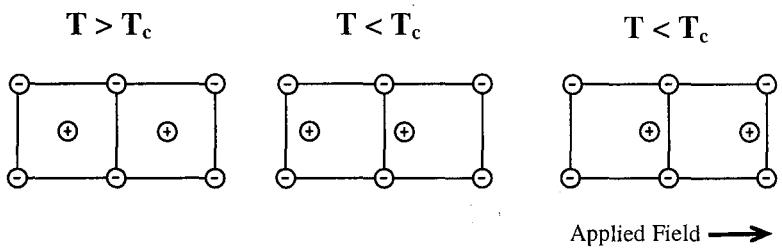

FIGURE 1.4 – Schematic representation of structural phase transition from a centrosymmetric ferroelectric prototype

Generally the piezoelectric effect is linear. However for ferroelectrics, particularly ferroelectric relaxors, the effects often show saturation and have field dependent values. It has been found experimentally by Newnham *et al.*[5] for 0.9PMN-0.1PT the polarisation value P, it is P^2 that is proportional to the applied strain.

Relaxor ferroelectrics differ from conventional ferroelectrics in four main characteristics (Cross *et al.*[6])

1. The phase transition involved is diffuse, and the dielectric susceptibility is markedly dispersive below the temperature τ_m' at which it peaks.

1. The phase transition involved is diffuse, and the dielectric susceptibility is markedly dispersive below the temperature τ_m' at which it peaks.
2. τ_m' itself is frequency dependent, increasing with increasing frequencies.
3. The dielectric response above τ_m' is not the Curie-Weiss type.
4. The mean spontaneous polarisation decays to zero at the freezing temperature which is well below τ_m', however the mean square polarisation is non-zero even at temperatures 200-300K above τ_m'.

Smolenskii and Agranovskaya[7] were the first to report on the broad peak of dielectric permeability with temperature in PMN (Figure 1.5). Thus in fact PMN can be considered quite an archetypal ferroelectric relaxor material.

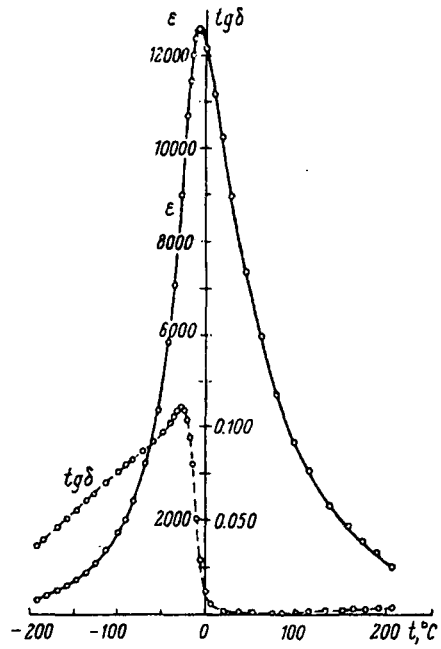

FIGURE 1.5 – Temperature dependence of the dielectric permeability and the loss tangent of PMN (Smolenskii and Agranovskaya[7])

Another issue of considerable interest in PMN and similar relaxor ferroelectrics relates to the actual distribution of the magnesium and niobium ions amongst the B-sites of the structure. Many perovskites are of the type $AB'_{1/2}B''_{1/2}O_3$ such as Lead Scandium Niobate, where it is possible for long range 1:1 ordering of the two B-site ion species to occur, hence effectively the B' and B'' ions alternately sit on the B-site throughout the material. In PMN the ions exist in a 1:2 ratio in order to preserve the charge neutrality of the material. However there is evidence to suggest that 1:1 ordering does occur in small microregions in the material.

Hilton *et al.*[8] and Zhang *et al.*[9] discovered such evidence from superlattice peaks in their X-ray diffraction studies. Thus it is possible that larger electric fields maybe generated in the material between the numerous positively charged ordered and the negatively charged ordered microregions. Thus equilibrium is achieved only when the forces responsible for B-site ordering such as the electrostatic and mechanical forces are balanced by the local space charges that tend to disorder the B-site cations. It is often suggested that these composition fluctuations and internal forces lead to variations in the Curie temperature thereby causing a mixture of ferroelectric and paraelectric phases to coexist. Thus it is this distribution of temperatures that results in the broad 'diffuse' phase transition in the profile of the dielectric constant versus temperature.

Ferroelectrics have seen a huge increase in potential applications within commercial devices. The large dielectric and piezoelectric constants of certain ferroelectrics such as PMN-PT and NKBT have made them attractive candidates for a diverse variety of applications. Ferroelectrics have widespread use in infrared detection and imaging, and also in a host of applications for optical memories and displays. They also have many uses in actuators and transducer devices. There is

also growing potential for application in computer memory devices and Ferroelectric Random Access Memory (FeRAM) and other similar capacitor based computing devices are already being fabricated. Furthermore the piezo-optic properties of PMN-PT and NKBT single crystals are yet to be fully explored.

1.3 PMN-PT

PMN is a non-polar ferroelectric relaxor material at room temperatures, however it has been found that with addition of $PbTiO_3$ (PT) it eventually evolves to form a normal ferroelectric material. PMN-PT can be synthesised at any composition from pure PMN to pure PT, as the titanium content of the composition increases in the titanium content the relaxor ferroelectric properties gradually evolve into normal ferroelectric properties. It has been proposed by Hilton *et al.*[8] that the addition of these titanium ions results in the weakening of the electrostatic and strain interactions between the magnesium and niobium ions, reducing their tendency to order.

The resulting single crystal form of PMN-PT, at a composition of around 33% PT, exhibits a giant piezoelectric response of the order 2500-3000 pC/N (Park and Shrout[1]). Figure 1.6 below shows the change of piezoelectric response versus composition

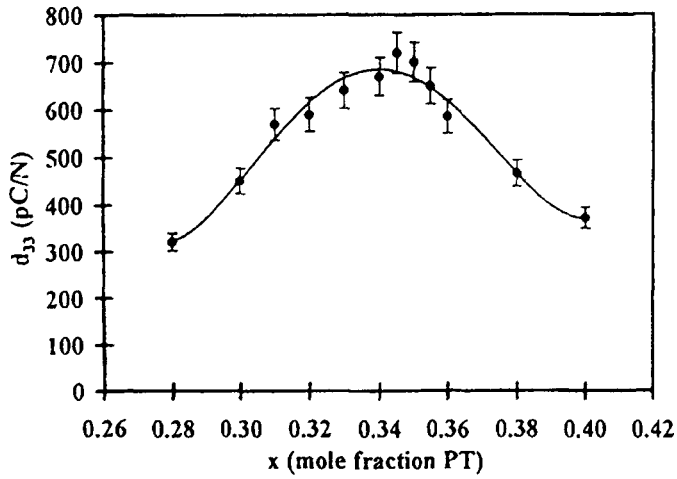

FIGURE 1.6 – Piezoelectric Charge Coeffiecient measured at room temperature and 1 kHz of PMN-PT (Kelly *et al.*[10])

It is believed that this giant piezoelectric response is due to extrinsic contributions, such as the motion of ferroelectric domains and the coexistence of different phases around the morphotropic phase boundary (MPB). As is typical with relaxor ferroelectrics there is no sharp transition, but within the composition range of x = 0.2 to x = 0.3 it is quite diffuse. Zhang *et al.*[9] however claim that the MPB is also the boundary for the PMN-PT system to transform from relaxor to normal ferroelectric. In fact several authors including Choi *et al.*[11] show that there is a sharp transition in PMN-PT concentrations around and over x = 0.4 indicating normal ferroelectric behaviour (Figure 1.7).

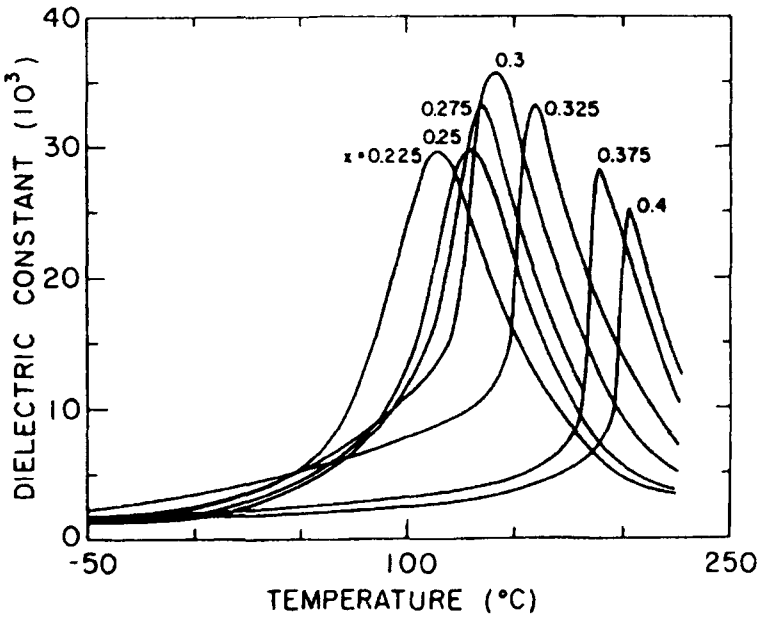

FIGURE 1.7 – Dielectric behaviour of PMN-xPT ceramics at 1 kHz measuring frequency as a function of temperature. Note the sharp peak for PMN-40PT (Choi *et al.*[11])

However there is currently a lot of debate regarding the exact composition of the MPB and whether this really does relate to the appearance of enhanced ferroelectric properties. Several authors notably Ye *et al.*[12] claim that the recent

discovery of a intermediate monoclinic phase around the MPB in Lead Zirconate Titanate (PZT) may also help in understanding the properties of PMN-PT. Furthermore the recent theoretical work by Vanderbilt and Cohen[13], has discovered a region of stability for the enhanced ferroelectric phase by extending the Devonshire-Landau expansion of free energy to the 8^{th} and 12^{th} orders. Several other groups complemented their work using several experimental techniques.

- Neutron Diffraction:- Kiat, Uesu and Dkhil[14]
- X-Ray Powder Diffraction:- Singh and Pandey[15]
- High Resolution Synchrotron Diffraction:- Noheda, Cox and Shirane[16]
- Optical Birefringence Imaging Studies:- Zekria[17]
- NMR studies:- Fitzgerald *et al.*[18]

Of course there are numerous other groups undertaking similar experiments including a variety of dielectric and characterisation experiments on PMN-PT 'solid solutions'. The following phase diagram (Figure 1.8) from Zekria[17] shows the complete temperature-composition phase diagram for the PMN-PT system.

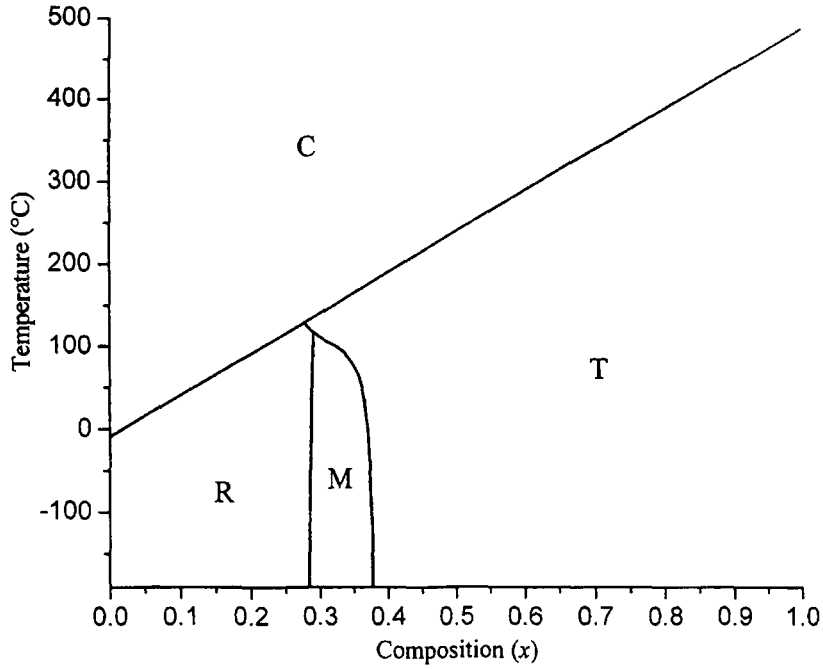

FIGURE 1.8 – Composition-temperature phase diagram of PMN-xPT (Zekria[17])

Though there is considerable debate about the exact phase diagram especially around the MPB the following diagram (Figure 1.9) from Noheda *et al.*[16] appears to summarise the current knowledge regarding the phases and phase transitions around the MPB in PMN-PT compositions.

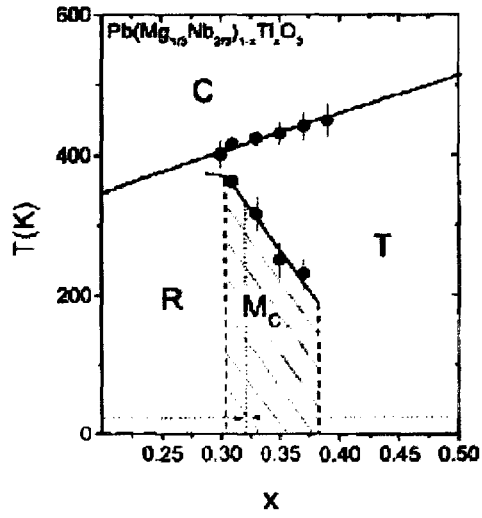

FIGURE 1.9 –Composition-temperature phase diagram of PMN-xPT around the MPB (Noheda *et al.*[16])

Noheda *et al.*[16] also proposed the existence of a secondary phase, either tetragonal or rhombohedral between (31% -37% PT) and hints at the possibility of a third minority orthorhombic phase in other monoclinic compositions. In a recent study Singh and Pandey[19] believed there may in fact be two monoclinic phases present around the MPB. Some current research by Fu and Cohen[20] tends to suggest that the giant piezoactivity may also in fact be connected with a polarisation rotation since the highest piezoelectric co-efficients are found for electric fields along the <001> direction in the rhombohedral phase, whereas the cation displacements should be found along the <111> direction. The possible presence of a monoclinic phase allows for the polarisation to rotate within the mirror plane under the application of an electric field, producing very high deformations.

However what is quite clear is that the structure of the MPB region is much more complicated than initially imagined. Unfortunately the detail with which the MPB can be examined is limited by the accuracy of the composition of the samples. From the results discussed above, we can assume that phases do indeed coexist over vary narrow ranges in compositions. Thus this current research aims to look at the relationship between the local structure and the average structure to try and understand more about the interesting ferroelectric properties of this material.

Owing to PMN-PT having a highly nonlinear electrical and electromechanical response to electric fields it can be used in various device applications. Furthermore PMN-PT materials are used in such devices in numerous different forms and can also be used in a host of useful technological applications.

- Ceramics:- existing ferroelectric applications, underwater transducers, smart material capacitors, tunable transducers, remote

control actuators, micro electromechanical systems (MEMS), ultrasonic micro motors, cantilever microphones

- Single Crystals:- existing piezo-optic applications, electro-optic modulators, laser frequency converters, acousto-optic modulators, holography and other photoferroelectric applications
- Thin Films:- thin film capacitor structures, ferroelectric random access memories (FeRAM), dynamic RAM (DRAMS), non-volatile ferroelectric RAM (NV-FRAM)

It is these properties and applications that are currently generating significant academic and industrial interest in these materials.

1.4 NKBT

Sodium bismuth titanate $Na_{0.5}Bi_{0.5}TiO_3$ (NBT), is a prototype perovskite relaxor ferroelectric[21]. It shows the typical characteristics of a relaxor, displaying a broad dielectric anomaly, the temperature of which is dependent on frequency. Doping NBT with potassium through formation of the NBT- $K_{0.5}Bi_{0.5}TiO_3$ (NKBT) solid solution introduces a morphotropic phase boundary at around the 20% potassium doping, resulting in change of symmetry from Rhombohedral to Tetragonal. As discussed above most ferroelectric perovskites such as PMN-PT show a change in phase and property by changing the composition of the B-Site. NBT, NKBT and KBT are a rare type of ferroelectric as changes in their phases and properties result from substitutions at the A-sites. It is therefore of interest to follow the local structure from the Rhombohedral to the Tetragonal phase to understand at the atomic structural level, how this change in average crystallographic symmetry is

effected. Thus is also considerable potential for an informative comparison of the local structural mechanisms between the NKBT and PMN-PT systems arising from the differing substitutions of the A and B sites respectively.

Single crystals of NKBT are easily obtained and it is also a lot easier to control the stoichiometry compared to its lead-based counterparts, furthermore according to Park *et al.*[22] its sintering temperature is about 1150°C, which is quite compatible with modern multilayer technologies. The previous work by Jones *et al.*[23] has established the complete phase diagram for NKBT solid solutions and is reproduced in Figure 1.10.

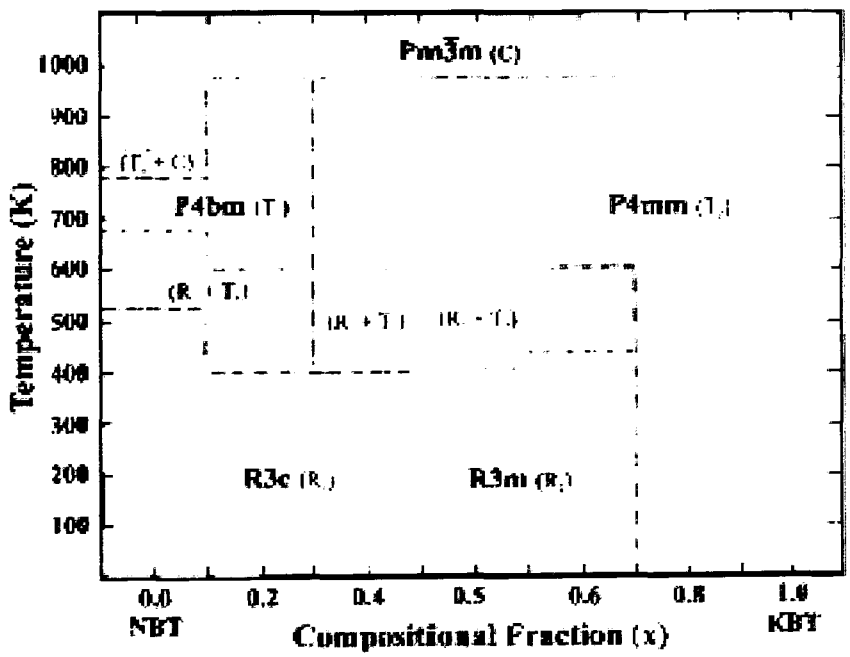

FIGURE 1.10 –Composition-temperature phase diagram of NKBT solid solutions (Jones *et al.*[23])

NKBT has potential uses in biological applications as part of the lead-free piezoelectric market. It can also be used in ultrasonic generators, actuators, transducers, and other typical ferroelectric device applications. Solid state NMR is an

ideal tool to probe the scale of the chemical bonds and to infer changes in A-O bond lengths from the materials. Thus the motivation for this research is to investigate the compositional region around the phase boundaries and to establish the local structural changes that are taking place using solid state NMR techniques.

References

[1] S.E. Park, T.R. Shrout, *J. Appl. Phys.*, 82 [4], 1804-1811 (1997)

[2] K.J.D. Mackenzie, M.E. Smith, *Multinuclear Solid-State NMR of Inorganic Materials*, Pergamon, 2002

[3] A. von Hippel *and coworkers, NDRC Rep,* 14-300 (1944), 14-540 (1945); A. von Hippel, R.G. Breckenridge, F.G. Chesley, L. Tisza, *J. Ind. Eng. Chem.*, 38, 1097 (1946)

[4] A.M. Glazer, *Acta Cryst.*, *B* 28, 3384-3392 (1972)

[5] R.E. Newnham, S. Trolier-McKinstry, H.Ikawa, *Mat. Res. Soc. Symp. Proc.*,175, 161 (1990)

[6] L.E. Cross, S.J. Jang, R.E. Newnham, S. Nomura, K.Uchino, *Ferroelectrics*,23, 187 (1980)

[7] G. A. Smolenskii, A.I. Agranovskaya, *Soviet Phys.-Solid State* (English translation), 1 [10], 1429-1437 (1960)

[8] A.D. Hilton, D.J. Barber, C.A. Randall, T.R. Shrout, *J. Mater. Sci.*, 25, 3461-3466 (1990)

[9] Q.M. Zhang, H. You, M.L. Mulvihill, S.J. Jang, *Solid State Communications*, 97 (8), 693-698 (1996)

[10] J. Kelly, M. Leonard, C. Tantigate, A. Safari, *J. Am. Ceram. Soc.*, 80 [4], 957-964 (1997)

[11] S.W. Choi, T.R. Shrout, S.J. Jang, A.S. Bhalla, *Ferroelectrics*, 100, 29-38 (1989)

[12] Z.G. Ye, B. Noheda, M.Dong, D.Cox, G. Shirane, *Physical Review B*, 64, 184114 (2001)

[13] D. Vanderbilt, M.H. Cohen, *Physical Review B*, 63, 094108 (2001)

[14] J.M. Kiat, Y.Uesu, B. Dkhil, M. Matsuda, C. Malibert, G. Calvarin, *Physical Review B*, 65, 064106 (2002)

[15] A.K. Singh, D. Pandey, *J. Phys. Condens. Matter*, 13, L931 (2001)

[16] B. Noheda, D.E. Cox, G. Shirane, Z.G. Ye, J. Gao, *Physical Review B*, 66, 054104 (2002)

[17] D. Zekria, D.Phil Thesis, Somerville College, University of Oxford, (2004)

[18] J. J. Fitzgerald, S. Prasad, J. Huang, J. S. Shore, *J. Am. Ceram. Soc.*, 122, 2556 (2000)

[19] A.K. Singh, D. Pandey, *Physical Review B*, 67, 064102 (2003)

[20] H. Fu, R.E. Cohen, *Nature 403*, 281 (2000)

[21] G. A. Smolenskii, A.I. Agranovskaya, *Soviet Phys.-Solid State* (English translation), 2 [2], 2982-5 (1960)

[22] S.E. Park, S.J. Chung, I.T. Kim, K.S. Hong, *J. Am. Ceram. Soc.*, 77, 2641 (1994)

[23] G.O. Jones, J. Kriesel, V. Jennings, M.A. Geday, P.A. Thomas, A.M. Glazer, *Ferroelectrics*, 270, 191 (2002)

Chapter Two

2.1 Introduction

Solid state Nuclear Magnetic Resonance (NMR) is a technique used to look at the local atomic structure of materials and to gain an understanding of the ordering and transitions taking place within them. It is based on the measurement of the energy separation of the ground state nuclear spin energy levels in an applied magnetic field.

Thus NMR uses magnetic nuclei as structural probes that can provide an understanding of the surrounding chemical environment within a material. NMR is also non-destructive and can detect changes in the bond length, bond angle, connectivity and co-ordination up to the third co-ordination sphere. It is these properties of NMR that make it particularly useful in this study.

NMR spectra obtained from liquids are generally much narrower than those of solids as the random molecular motion that occurs in solutions tends to average the orientation dependent interactions resulting in high-resolution spectral lines. However as there is no such motion in the solid state, the orientational dependence of the resonance frequency remains. This leads to a significant broadening of the resonance lines in polycrystalline materials (most common form of the samples studied in this work), making it considerably more difficult to identify the individual resonances in samples with multiple sites for a particular NMR nucleus. There are however several techniques that have been developed over the years to try and reduce this effect of this broadening. Of these, the most important and probably the most commonly used technique is Magic Angle Spinning[1,2] (MAS). This technique involves actually physically spinning the

sample at an angle of 54.74° to the applied magnetic field. A more detailed description of MAS is given later on the chapter where its effects on the various NMR interactions have also been discussed. Unfortunately another commonly encountered broadening mechanism (especially for the quadrupolar nuclei studied in this thesis) is the second order quadrupolar interaction $\hat{H}_Q^{(2)}$ is only partially averaged using MAS. There are two general ways however that all anisotropic broadening can be removed. Firstly there are techniques such as double rotation (DOR)[3] and dynamic angle spinning (DAS)[4] that are quite technically difficult as they involve spinning the sample around two axes simultaneously or changing the direction of the spinning axis. Secondly there are advanced MAS pulse techniques such as multiple quantum magic angle spinning (MQMAS)[5] and satellite transition magic angle spinning (STMAS)[6] that involve generating two dimensional spectra, where a spectrum with no second order quadrupolar component can be generated by projecting the second dimension of the spectra onto the *y*-axis. A more detailed explanation of MQMAS and related techniques can be found in the book by Mackenzie and Smith[7].

2.2 Principles of NMR

If a nucleus has an odd mass number it has a half integral nuclear spin $\boldsymbol{I}$ and will therefore have a magnetic moment $\mu = \gamma \boldsymbol{I}$, where γ is known as the gyromagnetic ratio and is a constant for a specific nucleus or isotope. Half-integer spin nuclei make up the great majority of NMR active nuclei. As mentioned in the previous section nuclei possess an intrinsic quantised property – nuclear spin. It is this nuclear spin that is of key importance for an NMR experiment. Nuclei that have an even mass number and even

charge have zero spin and are not considered particularly useful for NMR experiments. However almost every element will have at least one isotope that will have an integer or half integer spin quantum number. If there are an odd number of nucleons (protons and neutrons) then the nucleus will possess a net spin. As the nucleus is a charged magnetic object it is this net spin that interacts with magnetic fields, giving rise to a nuclear moment and it is this interaction that forms the basis of NMR techniques.

In a classical system when a magnetic field B_o is applied to this nucleus, the energy of the magnetic moment can be defined as

$E = -\boldsymbol{\mu}.\ \mathbf{B_o}$. However the magnetic moment can be in any one of $2I+1$ possible degenerate energy states, which correspond to the possible magnitude and orientation of the moment. Thus the moment can be redefined in quantum mechanical terms as

$$\mu = \gamma \boldsymbol{I} = \gamma \hbar m \tag{2.1}$$

where m is the magnetic quantum number which can only take half-integer values in the range $-I \leq m \leq I$. Furthermore the energy is also orientationally dependent and is given by equation 2.2.

$$E = -\boldsymbol{\mu}.\ \mathbf{B_o} = -\gamma \hbar m B_o \tag{2.2}$$

Thus when placed in a static magnetic field the moments align either with or against the field B_o depending on whether they are at the lower or higher energy levels. The moments therefore occupy 'Zeeman Split' energy levels separated by ΔE, which is constant between adjacent levels.

$$\Delta E = -\gamma \hbar B_o \tag{2.3}$$

However there are also forces that are acting upon the nuclear moments, the torque exerted by the magnetic field B_o can be represented by the vector product $\boldsymbol{\mu} \times \mathbf{B_o}$.

This according to Newton's laws of motion will cause the moment to precess around B_o. The Figure 2.1 below illustrates this precession. The angular frequency of this precession is given by

$$\omega_o = \gamma B_o \tag{2.4}$$

which corresponds to the frequency υ_o, termed the *Larmor frequency*.

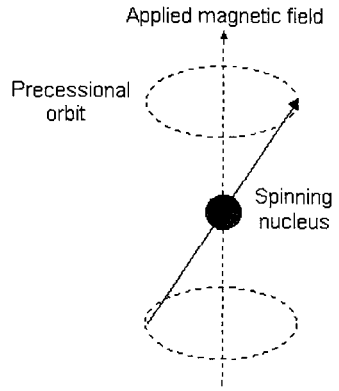

FIGURE 2.1 – Nuclear Precession in a Magnetic Field

In any sample material there are a very large number of nuclear magnetic moments occupying one of the possible $2I+1$ energy states. The energy difference between these states $\Delta E = -\gamma\hbar B_o$ is determined largely by B_o, the larger B_o the larger the energy difference hence the importance of the magnetic field in an NMR experiment. NMR is thus based on the transition between the different Zeeman levels for a given nucleus. The most fundamental aspect of the Zeeman Interaction is that it is almost always the largest nuclear spin interaction present in a system. A clearer understanding of the Zeeman Energy States and the corresponding population levels can be obtained from the figure 2.2 below.

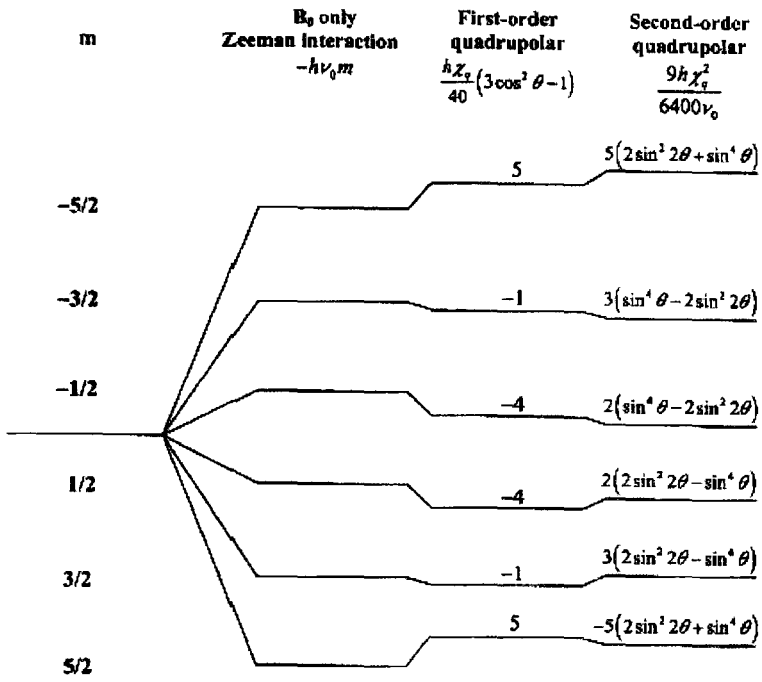

FIGURE 2.2 – The effects of the quadrupolar interaction for an $I = 5/2$ nucleus showing the energy level diagram[17]

For a system in thermal equilibrium the population levels of the various energy states follow a Boltzmann distribution. As this distribution prefers a lower energy state a net magnetisation parallel to B_0 will form. The characteristic time taken for this net magnetisation to form is referred to as the spin lattice relaxation time T_1, and is an important NMR parameter that can determine the duration of an NMR experiment. The reason this parameter is known as the spin lattice relaxation time is because the spin system is thermally coupled to the 'lattice' of the material. It is this coupling that causes the transition between the various Zeeman energy states. The coupling arises from the thermal motion of the surrounding matter that causes fluctuations in the internal electric and magnetic fields. The time taken to return to is given in equation 2.5 below

$$M_z(t) = M_0\left(1-\exp\left(\frac{-t}{T_1}\right)\right) \tag{2.5}$$

Hence approximately after a time $4T_1$ since the 90° pulse was applied, the magnetisation will fully relax back along the field. However for the transverse components of the magnetic field the decay of magnetisation is given by

$$\frac{dM_x}{dt} = \frac{-M_x}{T_2}, \qquad \frac{dM_y}{dt} = \frac{-M_y}{T_2} \tag{2.6}$$

This transverse relaxation time occurs as a result of the dephasing of the magnetisation in the xy-plane of the magnetic moments precessing about B_0. The time T_2 is called the spin-spin relaxation time and it may often have various contributions. These arise owing to the inhomogeneities in the static magnetic field B_0. Furthermore the internal fields that have components in the direction of the static field can be viewed as local field inhomogeneities too. These inhomogeneities lead to dephasing of the magnetisation that can be better understood through equation 2.7 below

$$\frac{1}{T_2^*} = \frac{1}{T_2} + \frac{1}{T_2'} \tag{2.7}$$

where T_2 is the decay of the magnetisation due to the interactions and T_2' arises from the effects of inhomogeneities in the field. Of course the real interest lies only in T_2 as this contains useful information regarding the nature of the interaction in the samples. A NMR technique known as spin echo pulse NMR can be used to measure T_2 rather than T_2^*, this has been described more thoroughly in the experimental details section of the following chapter.

2.3 Introduction to NMR Interactions

Apart from the Zeeman interaction it is important that we also consider the effect of the matter surrounding the nuclei in the sample. This is because this surrounding matter has a very significant influence on the total energy of each spin state thereby shifting the Zeeman Energy States described in section 2.2. This results in a shift in the position of the observed NMR peak. Thus the total energy in such a system is the sum of the various interactions of its nuclear moments and this is in turn is dependant on its local environment. It is for this reason that NMR is such a sensitive probe of the local chemical environment as described in Section 2.1. There are many such interactions that occur in a variety of differing materials. The most important of these are

- Chemical Shift Interactions
- Dipole-Dipole Coupling
- First and Second Order Quadrupolar Interactions
- J-Coupling
- Paramagnetic Interactions
- Hyperfine Interactions
- Knight Shift Interactions

However for the samples studied for this thesis it is important that the Chemical Shift Interaction and both the First and Second order quadrupolar interactions be clearly understood. The total hamiltonian for these interactions can be defined as

$$\hat{H}_T = \hat{H}_{Zeeman} + \hat{H}_{CS} + \hat{H}_Q^{(1)} + \hat{H}_Q^{(2)} \qquad (2.8)$$

As most of the nuclei being studied have nuclear spin I >1/2 it is actually the quadrupolar terms that are most important for determining the relaxation rate. These interactions have been discussed in much greater detail in the following sections.

2.4 Chemical Shift Anisotropy

The chemical shift interaction is a good starting point from which the major features of internal NMR hamiltonians can be understood. Chemical shifts arise from the magnetic dipole moment of the nucleus and the local magnetic fields generated by the motion of electrons in the large magnetic field (diamagnetic effects) and paramagnetic effects due to excited state of the electrons. Thus the diamagnetic effects are caused by the electrons opposing the magnetic field thereby reducing the field around the nucleus. While the paramagnetic effects are caused by the applied magnetic field mixing excited electrons with the ground state, thereby causing the ground state to acquire a paramagnetic component, which increases the field experienced. The interaction Hamiltonian used to summarise this interaction is orientation dependent and is usually described by the second rank tensor σ. The interaction Hamiltonian is thus

$$H_{CS} = -\gamma \mathbf{I} \cdot \boldsymbol{\sigma} \cdot \mathbf{B} \qquad (2.9)$$

while σ is most simply described in the frame where only the diagonal elements of the tensor are present. This is the principal axis system (PAS). It is possible to use Wigner rotation matrices to rotate an object with tensor properties between frames of reference thus in the case of equation 2.9 above the tensor has been changed from the Laboratory frame to the principal axis system. Thus by the judicious choice of reference frame the

entire problem of deriving the parameters for the chemical shift tensor is greatly simplified. The use of such Wigner rotation matrices to simplify the mathematics of rotations between frames has been described in detail in the book by MacKenzie and Smith[7]. Thus the labelling convention for the chemical shift tensor is best described in the principal axis system as below

$$\delta^{PAS} = \begin{pmatrix} \delta_{XX} & 0 & 0 \\ 0 & \delta_{YY} & 0 \\ 0 & 0 & \delta_{ZZ} \end{pmatrix} \tag{2.10}$$

Most chemical shift interactions are reported using three quantities derived from the components in equation 2.10 above. These are the isotropic chemical shift (δ^{iso}), the shielding anisotropy (Δ_{CS}), and the shielding asymmetry (η_{CS}). These are defined in equation 2.11 below

$$\delta_{iso} = \frac{1}{2}(\delta_{XX} + \delta_{YY} + \delta_{ZZ}), \qquad \Delta_{CS} = \delta_{ZZ} - \delta_{iso}, \qquad \eta_{CS} = \frac{\delta_{XX} - \delta_{YY}}{\Delta_{CS}} \tag{2.11}$$

Of these terms the isotropic chemical shift is the most important quantity and is frequently quoted in literature. The shielding anisotropy is used to measure the deviation from spherical symmetry and can be either positive or negative values. While the shielding asymmetry lies within the limits $0 \leq \eta_{CS} \leq 1$ and is a measure of the deviation in axial symmetry. The values of these terms are usually quite small and are usually reported in units of parts per million (ppm). For example in ^{13}C, the range of possible chemical shifts is from about –20 to 250 ppm which is around 27 kHz at a Larmor frequency of 100 MHz. The isotropic chemical shift is also usually measured against a known reference for the particular species of nuclei being investigated. Thus δ^{iso} can now be expressed as shown in equation 2.12 below

$$\delta^{iso}(ppm) = \frac{\delta^{iso}(Hz) - \delta^{ref}(Hz)}{\delta^{iso}} \text{x} 10^6 \qquad (2.12)$$

As long as there are no field dependent effects such as first or second order quadrupolar effects, contributing to δ^{iso}, the same ppm value will be measured regardless of the magnetic field being used in the NMR experiment.

For a crystallite at angles of θ and ϕ to B_0, the orientational dependence contribution to the lineshape is given by,

$$\delta_{ZZ} = \delta^{iso} + \frac{\Delta_{CS}}{2}\left(3\cos^2\theta - 1\right) + \eta_{CS}\left(\sin^2\theta\cos 2\phi\right) \qquad (2.13)$$

Thus for a powder the static lineshape will be made from weighted contributions from crystallites ranging over all values of both θ and ϕ. The following Figure 2.3 shows the effect of varying the principal chemical shift tensors. However there are often certain cases where the nuclear site possesses axial symmetry ($\delta_{yy} = \delta_{xx}$ or $\delta_{yy} = \delta_{zz}$) or the as in the case of PMN cubic symmetry where ($\delta_{yy} = \delta_{xx} = \delta_{zz}$).

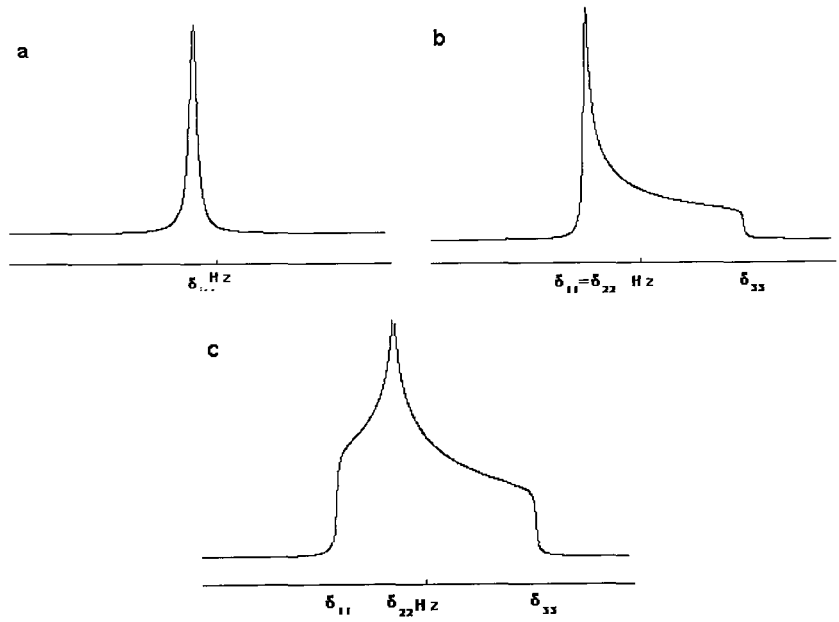

FIGURE 2.3 – Typical chemical shift-dominated NMR powder patterns: (a) spherically symmetric, (b) axially symmetric, and (c) asymmetric chemical shift tensor

2.5 Dipole-Dipole Interaction

The homonuclear and heteronuclear dipolar coupling hamiltonians are some of the most well known interactions in NMR. The magnetic dipole interaction arises from the coupling between the nuclear spin with the local fields of its neighbouring spins. This stimulates relaxation and also contains structural information of the environment around the excited nuclei. The interaction is in the same form as for the classical magnetic dipoles separated by a distance r,

$$H_D = -\sum_{j \neq 1} \hbar \omega_{D_{ij}} \sum_{m=-2}^{2} (-1)^m A_{2,m}^{D_{ij}} T_{2,m}^{D_{ij}} \tag{2.14}$$

$$\omega_{D_{ij}} = \frac{\gamma_i \gamma_j}{r_{ij}^3}$$

$$T_{2,0}^{D_{ij}} = \frac{1}{\sqrt{6}} \left(3I_{i,0} I_{j,0} - I_i . I_j \right)$$

$$T_{2,\pm 1}^{D_{ij}} = \frac{1}{\sqrt{2}} \left(I_{i,0} I_{j,\pm 1} + I_{i,\pm 1} . I_{j,0} \right)$$

$$T_{2,\pm 2}^{D_{ij}} = I_{i,\pm 1} I_{j,\pm 1}$$

Where $A_{2,m}^{D_{ij}}$ is defined as

$$A_{2,m}^{D_{ij}} = \sum_{m'=-2}^{2} D_{m',m}^{(2)} \left(\alpha_{ij}^D, \beta_{ij}^D, \gamma_{ij}^D \right) \rho_{2,m}^{D_{ij}} \tag{2.15}$$

and $$\rho_{2,0}^{D_{ij}} = \sqrt{\frac{3}{2}}$$

and $$\rho_{2,\pm 1}^{D_{ij}} = \rho_{2,\pm 2}^{D_{ij}} = 0$$

As in sec 2.4 above the Euler angles refer to the orientation of the principal axis of the dipolar coupling relative to the laboratory frame. However upon substitution of the principal axis components into the equation 2.15 above it can be observed that only B_{ij}^{D}, which corresponds to the angle between the inter-nuclear vector and the static magnetic field affects the overall hamiltonian. Thus the simplified Dipolar hamiltonian can be expressed as

$$H_D = \frac{\hbar}{2}\sum_{i<j}\frac{\gamma_i\gamma_j}{r_{ij}^3}(3\cos^2\phi - 1)(I_i.I_j - 3I_{iz}I_{jz}) \qquad (2.16)$$

The effect of this interaction is thus proportional to $\gamma_i\,\gamma_j$, thus it is especially important for nuclei with a high γ. Thus dipolar coupling may be thought of as an irreversible relaxation mechanism which leads to Gaussian decay thereby broadening the line in an NMR spectrum. However for the samples investigated in this thesis the dipolar coupling has no effect upon the spectral interpretation of the nuclear environments but is important in determining the rate at which the spin system reaches thermal equilibrium with the lattice.

2.6 Quadrupolar Interaction

The quadrupolar interaction is usually the dominant broadening mechanism for spin I > ½ nuclei, it arises from the interaction of the electric quadrupole moment (a non-spherical nuclear charge distribution) with the electric field gradients in a non-cubic environment.

The first analysis of the quadrupolar interaction in solid state NMR was by Pound[8] in an paper on the nuclear-quadrupolar interaction in 1950. Though a more comprehensive background to the quadrupole interaction is given in the classic article by Cohen and Reif (1957)[9]. More theoretical background information on the subject can be found in the book by Abragam[10] while a more recent update can be found in the article by Man[11].

The basic Hamiltonian has the same form as the chemical shift anisotropy Hamiltonian. The Hamiltonian of the quadrupole interaction can be expressed in terms of the principal axes $V_{XX} \leq V_{YY} \leq V_{ZZ}$ of the electric potential according to the following equation.

$$H_Q = \hbar\omega_Q \sum_{m=-2}^{2} (-1)^m A^Q_{2,-m} T^Q_{2,m} \tag{2.17}$$

$$\omega_Q = \frac{e^2 qQ}{2I(2I-1)\hbar}$$

$$T^Q_{2,0} = \frac{1}{\sqrt{6}}\left(3I_0^2 - I^2\right)$$

$$T^Q_{2,\pm 1} = \frac{1}{\sqrt{2}}\left(I_0 I_{\pm 1} + I_{\pm 1} I_0\right)$$

$$T^Q_{2,\pm 2} = I^2_{\pm 1}$$

Where $A^Q_{2,m}$ is defined below.

$$A^Q_{2,m} = \sum_{m'=-2}^{2} D^{(2)}_{m',m}\left(\alpha^Q, \beta^Q, \gamma^D\right)\rho^Q_{2,m'} \tag{2.18}$$

$$eq = V_{ZZ}$$

$$\rho^{Q}_{2,0} = \sqrt{\frac{3}{2}}$$

$$\rho^{Q}_{2,\pm1} = 0$$

$$\rho^{Q}_{2,\pm2} = \frac{1}{2}\eta_{Q} = \frac{V_{XX} - V_{YY}}{2V_{ZZ}}$$

Again, as in the previous section, the Euler angles refer to the orientation of the EFG axis system relative to the laboratory frame. Here η_Q is known as the *quadrupolar asymmetry parameter* and *e* is the magnitude of the electron charge. Furthermore as the quadrupolar tensor is traceless, there is no net isotropic shift due to this interaction. Thus **eq** is the anisotropy of the electric field gradient tensor. The constant $\frac{e^2qQ}{h}$ is commonly known as the *quadrupolar coupling constant* and is often given the symbol χ_Q (units rad s^{-1}). Quite often in the literature it is the quadrupolar frequency (ν_Q) and not χ_Q that is commonly quoted, this is defined as

$$\nu_q = \frac{3C_Q}{2I(2I-1)} \tag{2.19}$$

Also as demonstrated in the case of the dipole-dipole interaction it is possible to truncate the above Hamiltonian by eliminating the non-commuting ($\tilde{T}^{Q}_{2,\pm1}, \tilde{T}^{Q}_{2,\pm2}$) the remaining Hamiltonian is shown in equation 2.20 below.

$$\tilde{H}_Q = \frac{\hbar\omega_Q}{\sqrt{6}} A^{Q}_{2,0}\left(3I_0^2 - I(I+1)\right) \tag{2.20}$$

This first order pertubation result illustrates an example where higher order corrections are needed. In order to illustrate this we may look at the eigenvalues for the $2I + 1$ energy levels of the Zeeman basis states.

$$\langle I, m|\tilde{H}_Q|I, m\rangle = E_m^{(1Q)} = \frac{\hbar\omega_Q}{\sqrt{6}} A_{2,0}^Q \langle I, m|\left(3I_0^2 - I(I+1)\right)|I, m\rangle \qquad (2.21)$$

$$E_m^{(1Q)} = \frac{\hbar\omega_Q}{\sqrt{6}} A_{2,0}^Q \left(3m^2 - I(I+1)\right)$$

This is better illustrated using the following examples where m= 0 and m = ± ½

$$E_0^{(1Q)} = -\frac{\hbar\omega_Q}{\sqrt{6}} A_{2,0}^Q \left(I(I+1)\right)$$

$$E_{\pm\frac{1}{2}}^{(1Q)} = \frac{\hbar\omega_Q}{\sqrt{6}} A_{2,0}^Q \left(\frac{3}{4} - I(I+1)\right)$$

The last two energies are for the distinct cases where the spin is either an integer (I = 1,2,3,.....) or half odd integer spin (I = ½ , 3/2, 5/2,.....). Furthermore it is interesting to note that in the spin ½ case only the final $E^Q_{1/2}$ energy levels exist and are also analytically zero as there is no quadrupolar moment of the nucleus for spin ½ nuclei.

Thus it is possible to calculate the energy splitting between a variety of single quantum ($\Delta m = \pm 1$) transitions.

$$E_{m\to m-1}^{(1Q)} = E_m^{(1Q)} - E_{m-1}^{(1Q)} = \frac{\hbar\omega_Q}{\sqrt{6}} A_{2,0}^Q \left(2m - 1\right) \qquad (2.22)$$

The first feature which is immediately visible is that for m = ½, the splitting is theoretically zero. In fact for any other value of m, the splitting depends on both the size of the quadrupolar coupling and the orientation of a given crystallite. Only half integer

spins have a central transition (½ ↔ -½), which is unaffected by the quadrupolar interaction to first order.

In addition if we calculate the energy splittings for multiple quantum (*m*↔-*m*) transitions we discover that these also have no first-order quadrupolar energy splitting correction. For both the central and the multiple quantum transition, it is crucial to calculate the second-order contribution to the energy splitting as this becomes the dominant energy splitting correction. When the quadrupolar coupling is large, the second order will make significant changes to the satellite transition energy splittings. For the experiments, theory and simulations presented in the remainder of the thesis, these will pertain primarily to the central transition of half integer spins. For further information on multiple quantum spectroscopy the following references[5,12] are particularly informative.

As mentioned in the above paragraph if the quadrupolar coupling is large essentially the second order quadrupolar effects need to be considered. The second order interaction affects the spectrum and shifts the central transition with respect to the Larmor Frequency as shown in equation 2.23 below

$$\nu_q^{(2)} = -\frac{9}{64}\frac{C_q^2}{\nu_0 I^2 (2I-1)^2}(a-\frac{3}{4})(1-\cos^2\theta)(9\cos^2\theta-1) \qquad (2.23)$$

where a = $I(I+1)$. As can be seen from equation 2.23 frequency shift is dependent on $1/\nu_0$ thus at higher applied fields both the quadrupolar induced lineshift and the second order quadrupolar line broadening will be reduced. In fact the observed line position is due to contributions from both the second order quadrupolar and chemical shift interactions. The isotropic shift that arises due to the second order quadrupolar interaction is shown in equation 2.24 below

$$\delta_{iso}^{(2)} = -\frac{3}{10}\frac{((I(I+1)-\frac{3}{4}))}{(2I(2I+1))^2}\frac{C_q^2}{\nu_0^2}(1+\frac{\eta^2}{3})x10^6 \qquad (2.24)$$

The effects of first-order and second-order quadrupolar broadening on the spectrum are shown in Figure 2.4 below

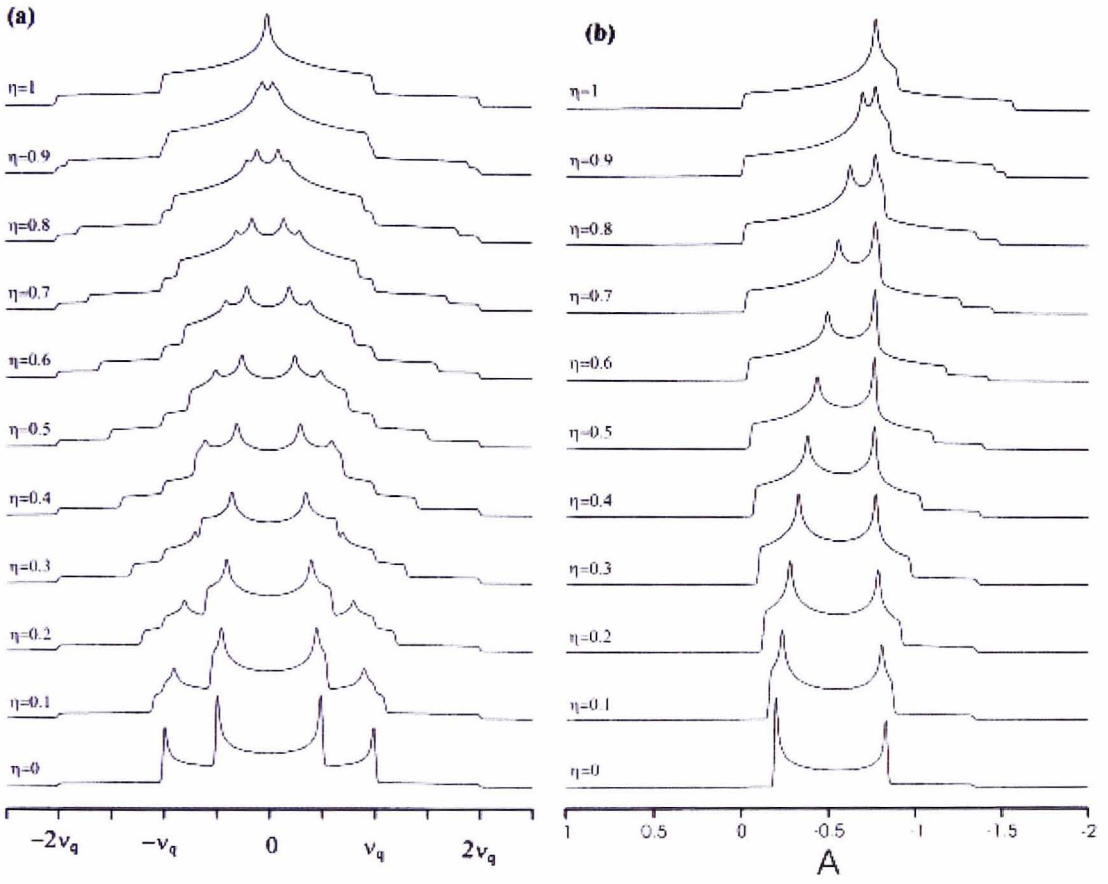

FIGURE 2.4 – Simulations showing the effects of the quadrupolar asymmetry parameter (η_q) on (a) the first-order satellite and (b) the second order central transition lineshapes. $\left(A=\left(I(I+1)-\frac{3}{4}\right)\frac{\nu_q^2}{\nu_0}\right)$. [17]

It can be seen that the lineshapes are certainly highly dependent on the values of η (Figure 2.4) and that MAS also reduces the linewidth but does not completely. Figure 2.5 below shows second order quadrupolar central transition lineshapes, both static and MAS at infinite speeds.

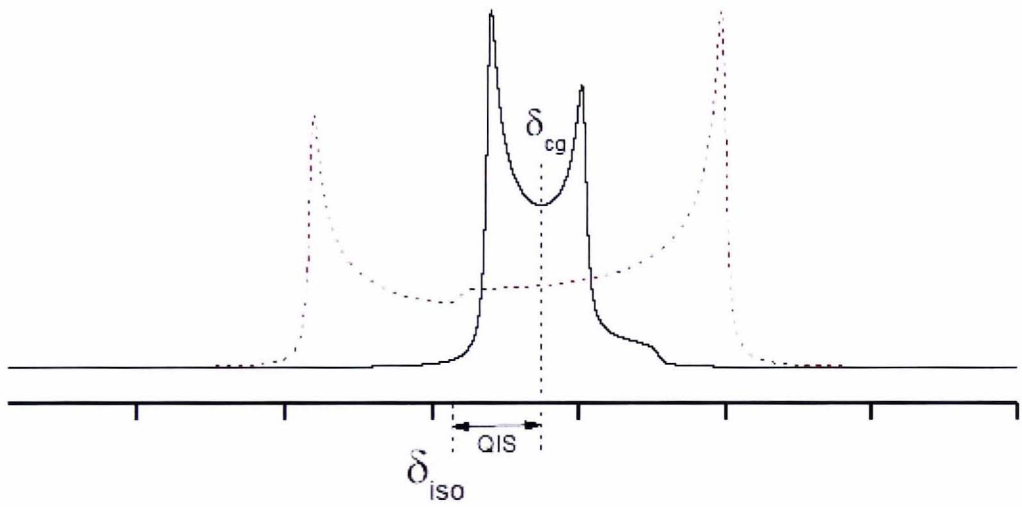

FIGURE 2.5 – MAS line narrowing of the 2nd order quadrupolar interaction. The MAS line (solid) is narrowed by a factor of $P_4(\cos(54.74°))$ from the static case (dash), QIS (Quadrupolar Induced Shift) is the centre of gravity from the isotropic chemical shift.

2.7 High Resolution Spectroscopy

All the interactions discussed above can often shift the spectral line shapes away from the positions expected from the Zeeman Hamiltonian, this of course leads to significant line broadening in poly-crystalline samples. Thus as the spectral lines from various sites in the sample overlap it becomes an increasingly more complicated task to interpret these lineshapes. There are however, many methods that can be implemented to

remove the anisotropic parts of the chemical shift and the quadrupolar interactions by manipulating both the spin and the spatial parts of the Hamiltonian as briefly described in section 2.1. Though there are currently numerous methods, for example MAS[1,2], DAS[3], DOR[4], MQ-MAS[5], ST-MAS[6] and other two-dimensional experiments[13,14] currently in use for reducing broadening in solid state NMR, for the samples studied in this thesis it is important to focus on primarily MAS and the two-dimensional nutation experiment. These are described in greater details in the following sections.

2.7.1 Magic Angle Spinning

Magic Angle Spinning (MAS) involves rotating the sample rapidly (>4 kHz) about an axis orientated at the angle $\theta_m = \cos^{-1}(1/\sqrt{3}) \approx 54.74°$ with respect to the magnetic field. This has the effect of removing the spatial tensors with time dependent spatial trajectories which approximate isotropic motion. The geometry of this experiment can be observed in Figure 2.6 below

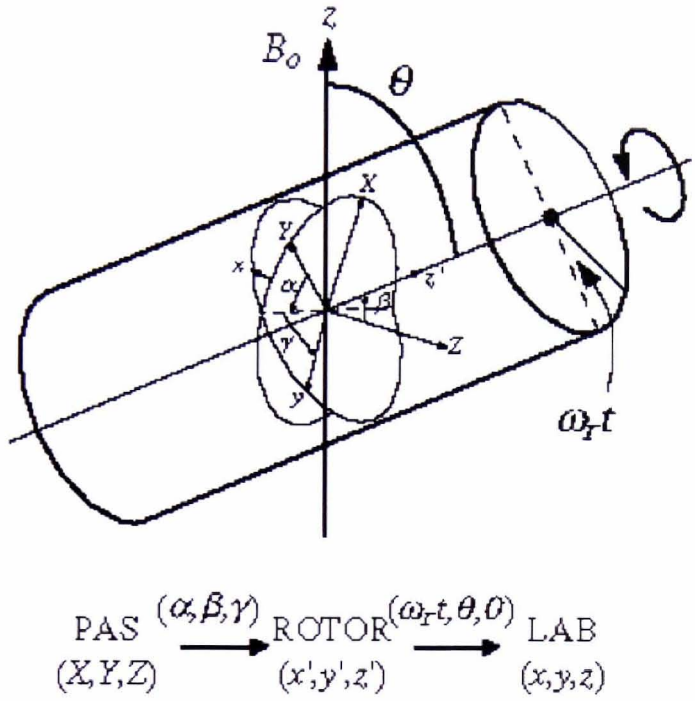

FIGURE 2.6 – PAS to ROTOR to LAB rotations. The Euler angles used in moving from a fixed PAS coordinate system to the laboratory system are shown. It involves multiple rotations.

MAS thus has the effect of introducing a time dependence for a general spinning angle to the existing spatial tensors. This is given by A^{λ}_{lm} in equation 2.25 below

$$A^{\lambda}_{lm} = \sum_{n=-l}^{l}\sum_{m'=-l}^{l} D^{(l)}_{nm}(\omega_r t,\theta,0)D^{(l)}_{m',n}(\alpha^{\lambda},\beta^{\lambda},\gamma^{\lambda})\rho^{\lambda}_{lm'} \qquad (2.25)$$

Thus the λ in the expression refers to either the chemical shift, dipolar or quadrupolar interactions. The Euler angles that define the first rotations are θ, the spinning axis angle and $\omega_r t$, the time dependent rotation angle. Therefore if the rotation is sufficiently rapid

(i.e. $\omega_r > \omega_1\delta^{csa}$ or $\omega_r > \frac{\omega_Q^2}{\omega_l}$) the time dependent terms can be ignored as they now average to zero, and only the time independent terms will remain as shown in equation 2.26 .

$$A_{lm}^{\lambda} = d_{0m}^{(1)}(\theta)\sum_{m'=-1}^{1} D_{m',0}^{(1)}(\alpha^{\lambda},\beta^{\lambda},\gamma^{\lambda})\rho_{lm'}^{\lambda} \tag{2.26}$$

Taking a more specific example we can now substitute the effect of the Chemical Shift Interaction in equation 2.26.

$$A_{20}^{cs} = \sqrt{\frac{3}{2}}\left(\frac{3\cos^2\theta - 1}{2}\right)\left[\frac{3\cos^2\beta^{cs} - 1}{2} + \frac{\eta_{cs}}{2}\cos 2\alpha^{cs}\sin^2\beta^{cs}\right] \tag{2.26}$$

Thus the only difference between this equation and the equation 2.13 shown in section 2.4 above is that a scaling factor known as the second order Legendre polynomial (P_2 [cos θ]) has now been introduced.

$$\left(P_2[\cos\theta]\right) = \frac{3\cos^2\theta - 1}{2} \tag{2.27}$$

It is also now apparent that the magic angle is simply the angle which makes this second order Legendre polynomial zero and thereby eliminates the anisotropic portion of the chemical shift interaction. Similarly it can also be shown that MAS can also remove the effects of both homonuclear and heteronuclear dipolar coupling as both have a spatial dependence which is represented as single second order tensor.

For the quadrupolar interaction the same analysis is also applicable to the first oder effect if the spinning speed is greater than the quadrupolar coupling constant.

$$\Delta E_{m\to m-1}^{1Q} = \frac{3e^2qQ}{4I(2I-1)}(2m-1)\left(\frac{3\cos^2\theta - 1}{2}\right)\left[\frac{3\cos^2\beta^{Q} - 1}{2} + \frac{\eta_{Q}}{2}\cos 2\alpha^{Q}\sin^2\beta^{Q}\right] \tag{2.28}$$

Unfortunately this is only limited to nuclei in a highly symmetric environment (for example ^{23}Na in NaCl) or nuclei with a very small nuclear quadrupolar moment (such as ^{7}Li). For quadrupolar nuclei with a larger quadrupolar coupling only the central transition is observable, this has no first-order quadrupolar contribution to the orientation dependence of the energy splitting. Thus the second order quadrupolar correction does, in fact, show strong orientational dependence. This has been shown by Mueller[15] to represent equation 2.29 below

$$\Delta E^{2Q}_{\frac{1}{2}\rightarrow-\frac{1}{2}} = \frac{\hbar C_Q^2\left(I(I+1)-\frac{3}{4}\right)}{32I^2(2I-1)^2\omega_l}\sum_{i=0}^{2}\sum_{j=0}^{2} a_{ij}^{'}\cos 2i\alpha^{Q}\cos 2j\beta^{Q} \qquad (2.29)$$

However the coefficients $a_{ij}^{'}$ are now defined as

$$a_{ij}^{'} = a_{ij}^{(0)} + a_{ij}^{(2)}P_2[\cos\theta] + a_{ij}^{(4)}P_4[\cos\theta]$$

where the fourth order Legendre polynomial is given in equation 2.30 below

$$P_4[\cos\theta] = \frac{1}{8}\left(35\cos^4\theta - 30\cos^2\theta + 3\right) \qquad (2.30)$$

Thus as can be seen from Figure 2.7 below the effects of the fourth order Legendre polynomial in the second order quadrupolar interaction cannot be fully removed by MAS.

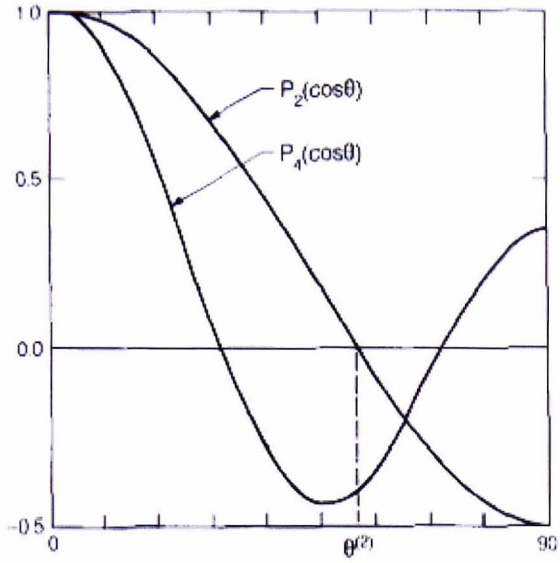

FIGURE 2.7 – The Legendre functions $P_2(\cos\theta)$ and $P_4(\cos\theta)$.[7]

2.5 from that of the static line. Thus if a line shape is dominated by the second order quadrupolar interaction, it is necessary to spin at a rate of at least the order of the static linewidth, ie $\delta_r \approx \Delta\omega$. The difference between these two cases lies in the concept of homogenous and inhomogeneous interactions, and is explained in an article by Maricq and Waugh[16]. However for many instances MAS spectra can provide sufficient resolution in order to obtain valuable information about the quadrupolar parameters.

2.7.2 Nutation studies

In many cases the distinct features of a quadrupolar lineshape are often hard to observe (even with MAS) owing to a spread in the chemical shifts and/or the quadrupolar interaction. Nutation NMR allows the study of the quadrupolar interaction by following the evolution of the spin system in the rotating frame, in the presence of the rf field B_1 provided by the rf pulse in t_1. This reduces the influence of the chemical shifts as they scale linearly with this applied field.

The pulse t_1 is thus referred to as the nutation pulse. The Hamiltonian during t_1 in the rotating frame is given by

$$H_1 = \nu_{rf} I_x + \nu_q(\theta,\phi)(3I_z^2 - I^2) \qquad (2.31)$$

where

$$\nu_q(\theta,\phi) = \nu_q(3\cos^2\theta - 1 + \eta_q \sin^2\theta \cos 2\phi) \qquad (2.32)$$

The nutation frequency for a quadrupolar nucleus is $(I+1/2)\ \nu_1$ when $\nu_1 << \nu_q$. If $\nu_1 > \nu_q$ the nutation frequency is simply ν_1 where in both cases $\nu_1 = \frac{\gamma B_1}{2\pi}$.

Unfortunately useful quadrupolar parameters can only be obtained when ν_1 is of the order of ν_q. Smith and van Eck[17] have shown that the useful range of rf-field strengths lies within the ratio $\nu_q/\nu_1 = 0.05 - 1.0$. However for most of these ratios the nutation spectrum is quite complex, heavily dependent on ν_q/ν_1 and usually consists of several frequencies. By simulating the experimental nutation spectra an accurate estimation of both the quadrupolar coupling constant and the asymmetry parameter can be obtained.

If there is more than one resonance, as in the case of many of the samples studied in this thesis, the resolution in the F2 dimension should be enhanced through MAS. Unfortunately this may often lead to a severe distortion of the nutation spectra due to the appearance of rotationally induced spin-locked magnetisation in an rf-field while spinning. Spinning speed should be very low (2 – 4 kHz) allowing the decay of the nutation spectra within a quarter rotor period. Nielsen *et al.*[18] have shown that it is however possible to simulate this behaviour of quadrupolar nuclei under the influence of MAS.

References

[1] E.R. Andrew, *Progr. Nucl. Mag. Reson.*, 34, 159 (1971)

[2] E.R. Andrew, *Int. Rev. Phys. Chem.*, 1, 195 (1981)

[3] A. Samoson, E. Lippmaa, A. Pines, *Molec. Phys.*, 65, 1013 (1988)

[4] B.Q. Sun, J.H. Baltisberger, Y. Wu, A. Samoson, A. Pines, *Solid State NMR*, 1, 267 (1992)

[5] L. Frydman, J.S. Harwood, *J. Am. Chem. Soc.*, 117, 5367 (1995)

[6] Z. Gan, *J. Am. Chem. Soc.*, 122, 3242 (2000)

[7] K.J.D. Mackenzie, M.E. Smith, '*Multinuclear Solid-State NMR of Inorganic Materials*', Pergamon, 2002

[8] R.V. Pound, *Physical Review B,* 79, 685 (1950)

[9] M.H Cohen, F. Reif, *Solid State Physics*, 5, 321 (1958)

[10] A. Abragam, '*Principles of Nuclear Magnetism*', Clarendon Press, chap 6-7 (1961)

[11] P.P. Man, *Encyclopaedia of Analytical Chemistry,* John Wiley and Sons, Chichester, p. 12224 (2000)

[12] A. Medek, J.S. Harwood, L. Frydman, *J. Am. Chem. Soc.*, 117, 12779 (1995)

[13] S. Caldarelli, F. Ziarelli, *J. Am. Chem. Soc.,* 122, 12015 (2000)

[14] G. Wu, D. Rovnyak, R. G. Griffin, *J. Am. Chem. Soc.* 118, 9326 (1996)

[15] K. T. Mueller, B. Q. Sun, G. C. Chingas, J. W. Zwanziger, T. Terao, A. Pines, *J. Magn. Reson.*, 86,470-487 (1990)

[16] M.M. Maricq, J.S. Waugh, N.C. Nielsen, *J. Chem. Phys.*, 70, 3300 (1979)

[17] M.E. Smith, E.R.H van Eck, *Progr. Nucl. Mag. Reson.*, 34, 159 (1999)

[18] N.C. Nielsen, H. Bildsøe, H.J. Jakobsen, *J. Magn. Reson.*, 97, 149 (1992)

Chapter Three

3.1 Introduction

The schematic diagram of the main equipment required in order to perform a NMR experiment is shown in Figure 3.1 below. In simplest terms the sample is contained within a rotor that is often mechanically rotated within a probe, the probe is then placed inside a superconducting solenoid magnet. A host of electronics nowadays primarily controlled by a computer is used to generate RF pulses of the appropriate length, phase and frequency which then effect the magnetisation of the sample. After a 90° pulse the magnetisation which was along the B_0 (or Z) axis gets tipped into the transverse plane. The resulting voltage induced in the signal coil by this changing magnetisation, is recorded as a function of time and is commonly known as a Free Induction Decay (FID). This characteristic FID is then stored and processed by Fourier transformation on a computer to form the spectrum.

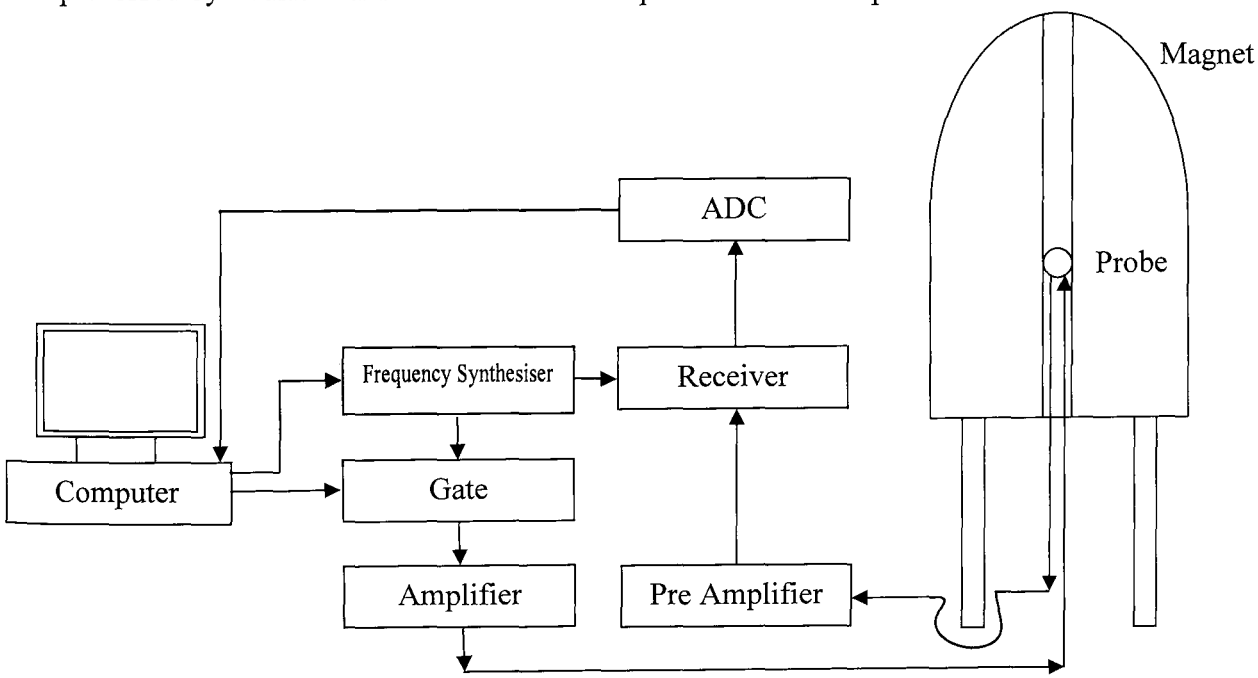

FIGURE 3.1 – Basic components of a FT NMR spectrometer

NMR is now a widely used tool and there are a multitude of variations and combinations of experimental set-ups that are used for the wide range of materials and systems studied. The following sections look at in more detail the experimental set-ups and optimised criteria for the NMR study of PMN-PT and NKBT samples.

3.2 Magnets

In order to study the properties of quadrupolar nuclei such as ^{93}Nb it is usually essential to use a high magnetic field in order to get clearer picture of the different sites within the sample. Most of the NMR experiments conducted on various quadrupolar nuclei in the PMN-PT and NKBT samples have been at the high field of 14.1 T corresponding to a proton frequency of 600 MHz. However several experiments have also been conducted at fields of 8.45 and 4.79 T corresponding to proton frequencies of 360 and 204 MHz and have also been included in this thesis.

The magnets themselves all consist of a cryostat, main coil, superconducting shim set and a high current power supply. The cryostat has two chambers, an outer one filled with liquid nitrogen and an inner chamber filled with liquid helium. There are also numerous vacuum jackets and radiation shields designed to preserve the helium by preventing any heat leakage. The main coil is usually made out of several kilometres of Nb_3Sn multifilament wire kept at the boiling point of liquid helium. As a high current typically 100A is circulated in the coil, the magnet is able store significant amounts of energy (around 10MJ) in its field[1]. It is essential that in addition to this magnetic field being strong there is also a high degree of both homogeneity and stability of the field. As the main coil is often unable to maintain these levels of homogeneity in the magnetic field, there is a set of superconducting

shim coils known as cryoshims, as well as an even finer set of room temperature shims present on most modern NMR spectrometers. Finally all the magnets used in the NMR experiments in this thesis have a standard wide bore of 89mm, allowing for larger and more specialised probes to be used, that are often necessary for MAS NMR.

3.3 Probes

The probe is used to hold the sample containing a cylindrical rotor in the main magnetic field. The rotor size is usually a compromise between the total volume of sample and maximum spinning speed that can be achieved. These rotors are made out of high strength ceramics and are capable of spinning up to 22kHz (3.2mm rotor diameter), though owing to the high density of lead based ferroelectrics most experiments have been performed at around 18kHz. The sample is contained within a signal coil, which is part of the resonant LC circuit. The circuit is "tuned" by varying the inductance and capacitance to produce resonance at the Larmor frequency, the circuit is then also "matched" to the standard impedance of 50Ω to minimise the reflections of the transmitter pulses. When the circuit is properly tuned it converts the incoming electrical pulse (frequency ω_0) to an oscillating magnetic field within the signal coil, this then couples with the nuclei absorbing a quanta of energy $\hbar\omega_0$. This causes transitions between the energy levels and is the quantum picture of the rotation of the magnetisation by the applied rf field creating the transverse magnetisation.

Another important criteria to be considered in a probe is its quality factor Q, this is a measure of the sharpness of the resonance of the probe circuit. Unfortunately probes must satisfy several competing requirements, thus most probes are usually

designed specifically for a particular application. It is also necessary to accurately set the magic angle on a probe. This is often done using YAG (Yttrium Aluminium Garnet) or KBr as the sample and adjusting the magic angle until rotational echos are clearly maximised in the acquired data.

3.4 Electronics

The pulse is usually generated by gating a monochromatic frequency source, thus the carrier frequency from the frequency synthesiser is combined with a square wave pulse of the appropriate length. This pulse is then phase shifted and amplified in the pulse amplifier before being passed into the probe as a high power RF pulse. Hence it is the same probe coil that is used for the both delivering and detecting the response of the pulses. So one of the major issues faced is that both a high power amplifier and a very sensitive receiver have to be connected to the same resonant LC circuit. This is usually overcome by the combined use of a duplexer along with shielding the receiver using quarter wavelength cable connected to a grounded diode. The rate at which the voltage decays after the applied pulse is determined by the quality factor of the probe Q, thus when the voltage remaining from the pulse has decayed to a value of approximately 0.5V, the duplexer switches the circuit from the transmission side to the receiver side. The actual signal (of order μV) generated by the sample is then amplified by the preamplifier before being passed on to two identical phase sensitive detectors (PSDs) as can be seen in Figure 3.1.

The difference between the signal and the reference is generated by the PSDs, however in one of the PSDs a phase shift of $\pi/2$ is also applied to the reference frequency to create an imaginary channel. Thus the outputs from these two PSDs are

digitised separately by two Analogue to Digital Converters (ADCs) and stored as the real and imaginary channels in the computer memory. Combining the output signals from two PSDs is commonly known as quadrature detection (QD) a detailed description of which can be found in the article by Traficante[2]. QD allows us to distinguish signals oscillating above or below the reference frequency, which would not be possible with a single PSD. Furthermore also this allows us to have the ability to set the transmitter frequency near the centre of the signal of interest improving both the pulse power efficiency and signal to noise ratio.

3.5 Pulse Sequences

In the actual NMR experiment, signal is obtained by summing the responses to a sequence of pulses. This entire procedure of summing the responses is known as signal averaging. The response from the spin system is phase coherent between the pulses and is thus dependent on the total number of acquisitions, however as the noise produced in each pulse is not correlated between the pulses it does not depend directly on the number of acquisitions but varies by the square root of the number of acquisitions. Under signal averaging conditions the signal to noise (S/N) is given by the square root of the number of acquisitions. Hence S/N increases by simply increasing the duration of an NMR experiment. However there is a wide variety of pulse sequences that exist, these all have the potential of affecting the sample's magnetisation in differing ways. The key pulse sequences used to investigate the PMN-PT and NKBT samples are described below.

3.5.1 Single Pulse

The standard single pulse experiment is depicted in Figure 3.2 below. In this experiment the magnetisation is tipped by a $\pi/2$ pulse and the FID is acquired using a four step phase cycle sequence such as CYCLOPS[3] (CYClically Ordered Phase Sequence). This phase sequence is used to minimise any imbalances between the two PSDs described in section 3.4 above.

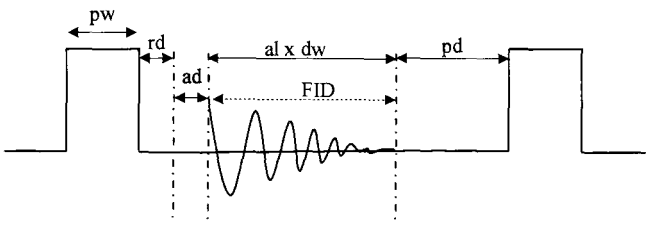

pw – pulse width (rf pulse)
rd – receiver delay
ad – acquisition delay
al – acquisition length
dw – dwell time
pd – pulse delay
FID – Free Induction Decay

FIGURE 3.2 – One Pulse Experiment

The 90° pulselength used for quadrupolar nuclei is usually found by dividing the 90° pulselength of the solution reference by a factor of I +1/2. This is because the angle a quadrupolar nucleus may be tipped to is dependent upon both the pulse length and the C_Q of the nucleus. For quantitative excitation of quadrupolar nuclei a much shorter pulse must be used, typically $< \pi/12$ so that the excitation lies within the linear regime[4].

3.5.2 Two Pulse Sequences – Oldfield Echo

One of the problems with the one pulse experiment is the fact that the NMR spectrometer cannot acquire signal immediately after the pulse has been applied, there is a finite amount of time required for the duplexing circuit to switch over from the transmission circuit to the receiver side and this delay is commonly known as receiver delay. Furthermore there is another delay known as the acquisition delay that occurs, being the time between the receiver being turned on and the FID being acquired. Thus the sum of the delays is known as "dead time" often imposes a limiting effect upon the spectra of the nuclei observed in a one pulse experiment. For broad resonance lines the FID can have largely decayed by the time the receiver begins measuring the output signal. Hence one of the most common NMR techniques for such nuclei is the use of a two pulse 'echo' sequence[5] as illustrated in Figure 3.3 below.

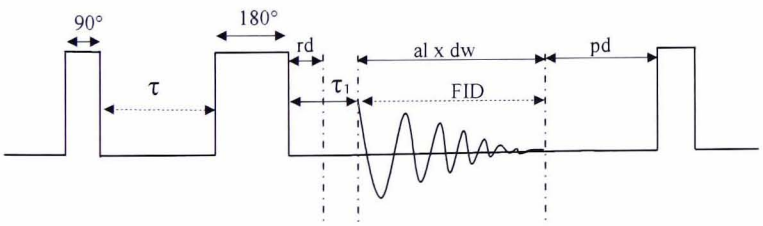

pw – pulse width (rf pulse)
rd – receiver delay
ad – acquisition delay
al – acquisition length
dw – dwell time
pd – pulse delay
FID – Free Induction Decay

FIGURE 3.3 – Two Pulse "Echo" Sequence[5]

In this experiment two pulses are used thereby refocusing the signal outside this deadtime. The signal in fact decays according to the spin-spin relaxation time T_2. Thus the amplitude of this echo follows that of the T_2 decay envelope. For a more detailed description of the echo pulse sequence and its associated phase cycling one

may refer to the article by Kunwar[6]. In essence the phase cycling of this echo sequence combines CYCLOPS phase cycling imposed on a scheme to subtract the directly excited magnetisation after the second pulse.

In an MAS experiment it is also important that the time delay between the two pulses is set to integer number of the rotor periods. This is to allow the individual crystallites contributing to the signal to be in the same orientation during the θ_1 and θ_2 pulses preventing any lineshape distortions. It is also necessary to acquire the spectra with a larger sweep-width than that of a one pulse experiment in order to ensure that the digitisation rate is high enough to allow the definition of the echo maximum.

3.5.3 Multi Pulse Sequences – RAPT sequence

The Rotor Assisted Population Transfer (RAPT) pulse sequence has been developed in order to amplify low S/N ratios for low abundance quadrupolar nuclei such as ^{17}O. It has been demonstrated[7] that using a modified RAPT scheme leads to a signal enhancement by a factor of 2.5, and is especially useful in materials with multiple sites with a range of C_q values. Figure 3.4 shows the pulse sequence and the signal enhancement.

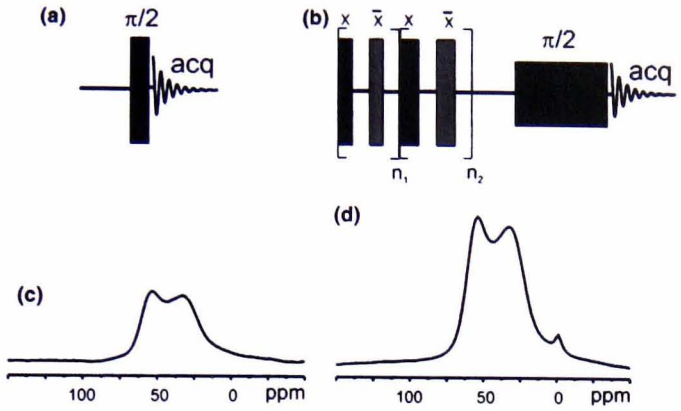

FIGURE 3.4 – MAS – RAPT scheme

This sequence has been used only in the ^{17}O NMR experiments when the S/N ratio as observed through the Oldfield echo pulse sequences were unsatisfactory. For further details of this pulse sequence and how it actually amplifies signal to noise refer to the article by Prasad *et al.*[8]

3.6 Data Processing

Usually once an FID is acquired using the pulse sequences described above the data needs to be processed in order to produce a spectrum (i.e. intensity as a function of frequency) so that the form of the spectrum can be observed. The procedures used to process the FID to form a spectrum are now discussed.

A DC offset correction is always used to average the end of the FID where there is no signal about the y=0 axis. This procedure ensures that the FID oscillates about the correct baseline, this is especially important for 2D nutation spectra as a large number of rows need similar corrections. Any DC offset will show itself up as an apparent peak at the centre of the spectral range.

As a spectrometer will always have some receiver dead time there is usually some form of degradation of the first few data points in the FID, these are thus always removed. In some cases notably one-pulse experiments a linear back prediction algorithm was occasionally used to reconstruct these points that were removed, however for complex quadrupolar lineshapes this function was never used as the time domain signal is far too complex for such an algorithm to be really relied upon. The next step is to try and maximise the S/N ratio. This can be done by multiplying the FID using several 'window functions' in a process termed apodisation, resulting in a new weighted FID A(t). Though there are many different window functions the two functions used for all spectra shown in this thesis are;

(i) Exponential multiplication – this function preferentially enhances the beginning of the FID (where the signal is usually greatest) by multiplying the entire FID with an exponential decay function

$$A(t) = S(t) \times \exp(-\pi L_B t)$$

Where S denotes the unweighted signal and L_B is the line broadening (in Hz) produced using this function. The line width however increases in a Lorentzian manner.

(ii) Trapezoidal multiplication – involves the entire FID being multiplied by a trapezoidal shape. In many of the spectra displayed in this thesis, the signal ends well before the end of the acquisition time. In these cases it is possible to truncate the high frequency noise in this part of the FID using this function.

In a lot of cases a combination of both the functions described above has been utilised.

Once the apodisation functions have been completed it is possible to gain some insight of the material from the FID, however interpretation of the time domain data is quite complicated. The most common way of viewing this data is by implementing a full discrete complex Fourier transform. This is usually done by utilising a variation of the Fast Fourier Transform algorithm developed by Cooley-Tukey[9] in 1965.

In all modern spectrometers there are two detector channels that have a phase shift between them of nominally 90°, and are termed the real and the imaginary, and on FT will produce the spectra in respectively the absorption and dispersive modes, with the absorption mode required. However in the initial set-up it is not usual to have the entire signal split between the two detector channels in this way. Initially a zero-order phase correction is carried out that simply mixes the two channels by adding a constant amount of the channels across the spectral range until the target peak is in absorption mode. If there is any dead-time (which there usually is) then there will need to be an additional correction, which mixes the channels using a factor that is proportional to the offset from a point in the spectrum and is termed first-order phase correction. After this procedure a spectrum with all the peaks in the absorption mode and preferably a flat baseline is generated. If there is any "roll" in the baseline this can be later corrected in the spectral simulation procedure.

3.7 Spectral Simulations

In order to extract some useful parameters from the processed spectra obtained, it is necessary to 'fit' or simulate the experimental data using calculated lineshapes. In many cases especially for samples where there is disorder this is

relatively simple as the line tends to be Gaussian shaped. Though there are several well known commercial packages that can fit for the chemical shift interactions and quadrupolar interactions there are very few that can cope with both of these interactions together. This is especially true if there are spreads (rather than just single values) of the parameters. Hence specialised and also custom built simulation software has been utilised in order to fit the spectra collected for this thesis. These are described in more detail below.

3.7.1 DMFIT

The program DMFIT[10] has been used for many of simulations of spectra shown in this thesis. It however could not be used for the simulations of the ^{93}Nb spectra or the ^{23}Na spectra as these not only show broadening due to the anisotropic interaction, but also seem to have a distribution associated with the quadrupolar interaction.

3.7.2 QuadFit

QuadFit[11] allows fitting of spectra which have distributions of quadrupolar interactions. Fitting distributions of interactions is still quite rarely carried out and recently a new programme has been written in the group at Warwick to carry this out. The programme has been written in Visual Basic 6.0 as a portable stand alone version capable of reading standard experimental Ascii data files (Figure 3.5). The fitting procedure is quite iterative in nature and is done manually using a trial and error method. The output is generated in standard XY data columns and can be easily imported into various spreadsheets or plotting software. An typical PMN-PT

spectrum using a modern day Intel Pentium 4 (2.8GHz) processor and 256Mb RAM takes approximately 10 minutes to generate a single distribution and around two hours for an experienced user to generate a complete fit.

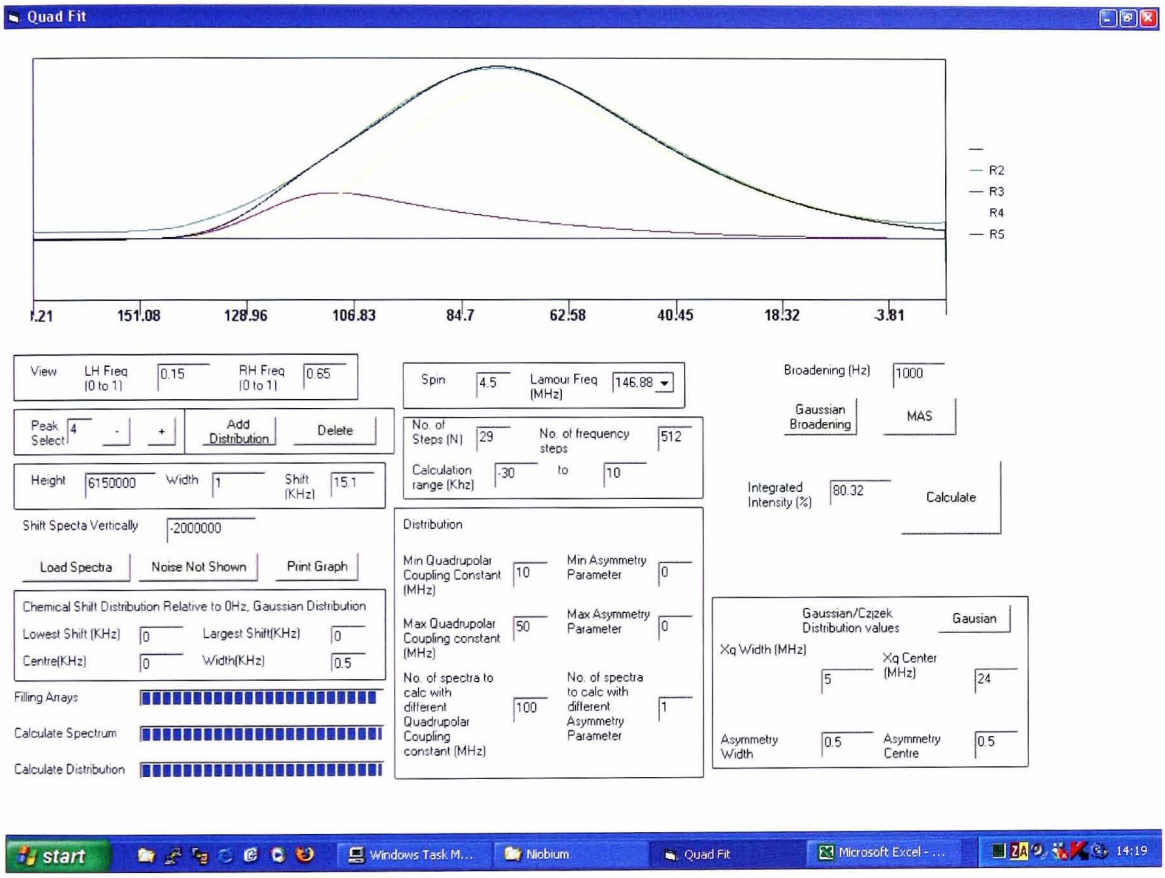

FIGURE 3.5 – QuadFit Screen shot showing fit for PMN-40PT

It is ideal for fitting the complex ^{93}Nb quadrupolar environments in PMN-PT samples which show distributions in both the chemical shift and quadrupolar interactions affecting the centre band. The contribution of the second order quadrupolar interaction can be seen from the distinctive tail towards more negative frequencies. The results and actual fits using the QuadFit software have been included in the following chapters of this thesis. A limitation of the current version of the software is

the inability to vary the asymmetry parameter η described in Chapter 2. However the effect of η on the lineshape of PMN-PT and NKBT is quite modest.

3.7.3 SIMPSON[12]

SIMPSON can be most easily described as a theoretical spectrometer. It is possible using SIMPSON and associated plotting software SIMPLOT to generate an entire Fourier transformed spectrum of a particular nucleus once a rough idea of the various spectrometer and spectral parameters are known. This allows the user to visually compare the experimental spectra with the simulated one to ensure that they are similar. Unfortunately it requires quite precise and detailed information about the sample to be known before the simulation can be carried out. Furthermore it also requires quite a long processing time and large memory requirements even for a modern day desktop PC. However once a satisfactory simulation has been generated it is of course possible then to use SIMPSON to optimise numerous parameters such as the asymmetry parameter, various pulse lengths and also decide upon optimal spinning speeds. Thus the sequence can be used to check for imperfections introduced into the spectrum due to for example finite pulse lengths and finite spinning speeds only causing partial averaging. For the SIMPSON spectra shown later on in the thesis unless otherwise mentioned the simulation spectra were created using the direct method of powder averaging using 20γ angles and the zcw4180 crystal file. The start and detect operators were selected to be I_{1Z} and I_{1C} respectively, thus concentrating solely on the central transitions. All other parameters including the inter-pulse acquisition delay, central transition selective pulse widths, inter-pulse delays were set to be equal to that of those used experimentally and have been clearly specified. The simulated binary FID was converted into an ASCII format processed

and phased spectrum using the SIMPLOT software provided with the SIMPSON package.

An example of a ^{93}Nb MAS SIMPSON simulation of Lithium Niobate is shown in Figure 3.6 (b) below

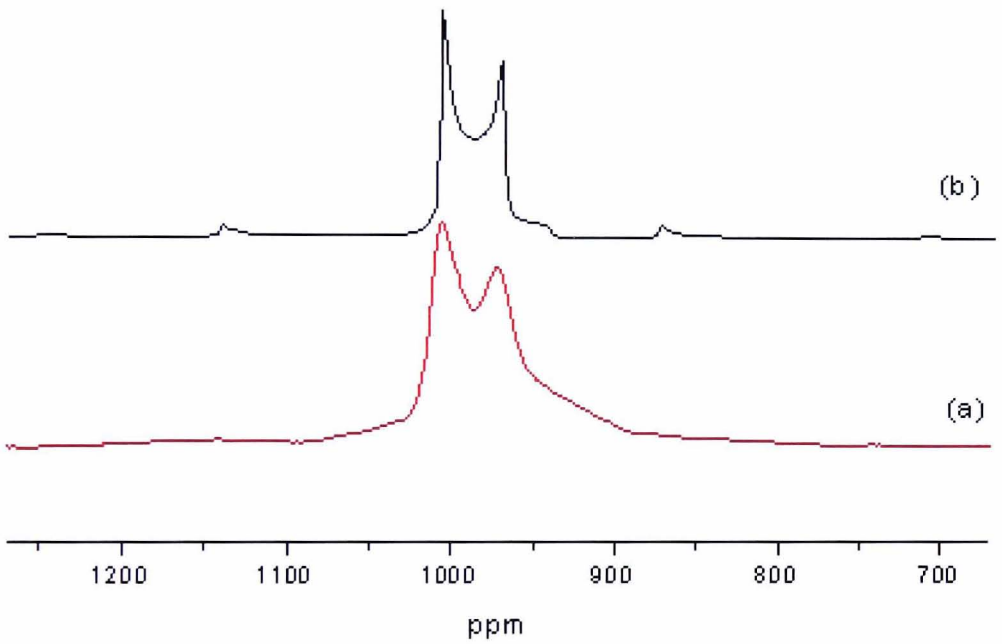

Figure 3.6 – ^{93}Nb NMR spectra of (a) Lithium Niobate MAS and (b) SIMPSON simulation of Lithium Niobate.

3.8 Sample Preparation

It is often very hard to ensure good chemical homogeneity in ceramic samples, as they often contain a spread of compositions around the nominal value. It is difficult to determine whether any coexistence of phases within a sample arises from an intrinsic property of the sample or from simply the straddling of a phase boundary by a fraction of the sample with an outlying composition. A further degree of complexity associated specifically with the synthesis of PMN-PT ceramics is trying to

achieve a homogeneous distribution between the magnesium, niobium and titanium atoms via solid state reactions. While the magnesium and the niobium ratio is constrained by the charge balance requirements of the ions, the Ti^{4+} ions tend to distribute themselves inhomogeneously throughout the material. This may also lead to titanium rich areas in the material where there are a higher concentration of TiO_2 particles and similarly areas richer in magnesium and niobium where the TiO_2 particles are absent. Of course these problems can be minimised by paying due attention to the mixing of the samples and care of preparation as well as by trying to achieve the smallest practical particle sizes. The details of the characterisation techniques used to verify that the samples are indeed the correct materials have been presented later on this thesis.

There are two main techniques that have been used to prepare the PMN-PT ceramics powders

1. PMN-PT ceramics made using a modified columbite method
2. ^{17}O-enrichment of PMN-PT and precursors using sol-gel methods

All the NKBT samples studied were kindly provided by Dr Q. Jiang from the University of Warwick, and were made in a Bridgeman Furnace using a standard Flux growth technique[12].

3.8.1 PMN-PT ceramics

One of the major problems faced in the preparation of PMN-PT is the formation of a pyrochlore phase in addition to the desired pure perovskite phase ceramic. This phase has a very low dielectric constant, which dilutes the dielectric properties of the pure perovskite phase material and hence is a problem. The usual methods of mixing oxides together to form ceramics cannot be used as it results in the formation of pyrochlore phases at low temperatures.

The most influential work regarding the formation of pure perovskite PMN ceramics was carried out by Swartz and Shrout[13]. They sought to simplify the synthesis of perovskite PMN by the introduction of a two step process. Initially the reaction of MgO and Nb_2O_5 at 1000°C led to the formation of columbite ($MgNb_2O_6$). This was then reacted with PbO at 800°C to form the stoichiometric PMN composition, this lower reaction temperature reduces the amount of lead volatilisation. This approach yields perovskite phase as the dominant phase with pyrochlore impurities less than 5%. However it was found that there was always a small excess of MgO detected even when the reaction appeared to have been completed. This confirmed that it is indeed very difficult to obtain only pure perovskite phase PMN even using a wide range of conditions.

Using their 'novel' fabrication they claimed had two distinct advantages over simply mixing oxides. Firstly in order for the PbO to react with columbite to form pyrochlore, it would have to liberate Nb_2O_5 from the columbite. As the kinetics of this particular reaction is quite slow it would prevent formation of the pyrochlore. Secondly they suggested as the desired phase was a perovskite one, the oxygen octahedral structure of the columbite itself would aid in its formation.

They also showed that using a 5% excess of MgO, no pyrochlore phase could be detected within the limits of X-ray diffraction, proving that MgO indeed acts as a suppressant on the formation of pyrochlore.

Butcher and Daglish[14] subsequently developed a technique on the work by Swartz and Shrout[13] using hydrated magnesium carbonate – magnesium hydroxide ($MgCO_3.3H_2O$) as a precursor. Using this precursor it could be shown that concentrations of pyrochlore phases could be reduced to zero in the presence of excess MgO and PbO (Singh and Bard[15]).

Another interesting study of the microstructure and properties of PMN-PT was conducted by Wang and Schulze[16]. They looked at the role of this excess MgO on the structure of PMN. These microstructural studies showed that the excess MgO exists as micrometer–sized spherical particles in either the grain boundary as a discrete particle or in the perovskite grain as an inclusion, whilst the pyrochlore phase exists in large isolated grains in the microstructure. They also showed that excess PbO did not improve the yield of the pure perovskite phase and simply decreased the dielectric constant. Hence it seems that only addition of excess MgO is necessary to eliminate the pyrochlore phase.

Ceramic samples of varying composition of PMN-PT were prepared using the two-stage technique detailed above. The precursors $PbCO_3$, Nb_2O_5, $(MgCO_3)_4.Mg(OH)_2.5H_2O$ and $PbTiO_3$ were obtained from Aldrich 99.9% purity. The columbite precursor was prepared using $(MgCO_3)_4.Mg(OH)_2.5H_2O$ and Nb_2O_5 in the appropriate stoichiometric amounts. This mixture was then dissolved in iso propyl alcohol (IPA) and ground by hand for an hour. The mixture was then dried at 120°C for two hours and ground to a fine powder using a ball mill. The powder was then analysed using a particle size analyser showing a particle size of around 5μm.

This powder was then calcined twice at 930°C for 10 hours each time with some intermediate grinding. Finally this powder was reground and sintered at 1145°C for 4 hours to obtain columbite. Perovskite phase PMN-PT was then made using the columbite with stoichiometric amounts of $PbCO_3$. To suppress the pyrochlore phase a 5% excess $(MgCO_3)_4.Mg(OH)_2.5H_2O$ was also added into the IPA solution. This mixture was then ground by hand for an hour. The mixture was then dried at 120°C for two hours and ground to a fine powder using a ball mill. The mixture was then calcined at 800°C for 10 hours and sintered at 900°C for 4 hours with some intermediate grinding. The final powder obtained was treated with 1 N acetic acid to remove any unreacted MgO. This final powder showed pure perovskite phase PMN-PT with only excess MgO as a small impurity, suggesting that indeed this small quantity of MgO may be embedded in the particles of PMN-PT as suggested by Wang and Schulze[16] and is therefore shielded from the acetic acid.

3.8.2 ^{17}O enrichment of PMN-PT and Precursors

For NMR purposes it is necessary to enrich some samples with ^{17}O as this nucleus has a very low natural abundance of approximately 0.037%. One of the main problems faced is that upon heating the sample usually most of the ^{17}O is lost through atmospheric exchange, hence only if the sample is heated in near vacuum conditions will the ^{17}O nuclei be reabsorbed upon cooling. Another potentially interesting argument for using sol-gel created PMN-PT ceramics is that as described in the previous section, solid state reactions often lead to inhomogeneous distributions in the material. Using sol-gel techniques however introduces the magnesium, niobium, lead and the titanium in solution, possibly leading to far more homogeneous distributions within the material. Unfortunately on heating such PMN compounds, corrosive PbO

vapour is released, this vapour reacts with most metals and glasses at high temperatures. Thus to create the amorphous PMN the following sol-gel methods were used.

Initially a stoichiometric amount of Niobium(V)Ethoxide, Magnesium Ethoxide, and anhydrous Lead Acetate (Aldrich 99%+ purity) were dissolved in methanol as magnesium ethoxide does not dissolve in either IPA or 2-methoxyethanol. All these ethoxides are highly reactive towards moisture and must always be handled in a "dry nitrogen" atmosphere. ^{17}O enriched water at 20% enrichment was then injected into this solution, and immediately a white cloudy precipitate begins to form. This white mixture is stirred overnight using a magnetic stirrer. A gel-like solid has now formed; this is then pumped overnight with a diffusion vacuum pump to remove any excess vapour. The dry white powder is now ground using a ball mill to create a fine white powder of amorphous PMN.

NMR tests on this amorphous powder revealed that there is a strong ^{17}O signal indicating appropriate levels of ^{17}O enrichment in the sample. The problem now faced was the high crystallisation temperature required for PMN. The initial attempts led to a complete loss of ^{17}O nuclei from the sample. After vacuum pumping a quartz tube, the excessive PbO vapour pressure caused the tube to explode. Another attempt involving sealing the sample in an evacuated platinum tube also proved unsuccessful as the corrosive PbO vapour reacts with platinum at high temperatures. Finally extra thick quartz tubing was obtained and the sample was pumped continuously for 4 nights until it stopped out-gassing. This was then pumped to around 10^{-5}bar and the sample heated to 930°C for 10 hours then left to cool. After cooling it was then reheated to 1145°C for 4 hours and left to cool. The crystalline PMN obtained was then ground into a fine powder using a ball mill. The XRD analysis of this powder

shown in chapters 4 and 5 indicate it to be pure perovskite phase with no other impurities.

3.8.3 NKBT Single Crystals

One of the major advantages of NKBT solid solution ferroelectrics is its relatively low sintering temperature around 1150°C which is currently compatible with existing multilayer[17] technologies. Furthermore it is also simpler to create NKBT as there is no corrosive PbO vapour to contend with. However it is often equally difficult to produce pure perovskite phase NKBT as it is for PMN-PT perovskite phase crystals.

There are numerous options for creating single crystals. The most commonly used methods are:

1. Bridgeman Method[18]
2. Kyropoulos Method[19]
3. Flux growth Method[12]
4. Self-Nucleation Method[20]

All the NKBT samples studied in this thesis were all made by Dr Q. Jiang at Warwick University, using the self-nucleation method. The reason this method was chosen as the preferred method was primarily because of the simpler heating programme, and the relative simplicity of the equipment required. Furthermore this is one of the favoured methods of crystal growth by researchers compared to the Bridgeman technique more commonly used in industry, as the self-nucleation method usually has a higher yield of NKBT crystals, whereas the Bridgeman technique generally produces fewer crystals, but of a larger size.

For the crystals grown for the study in this thesis 3N grade chemicals K_2CO_3, Na_2CO_3, Bi_2O_3 and TiO_2 were weighed according to their stoichiometric ratios in the formulae $(Na_{(1-x)}K_x)$-0.5Bi0.5TiO_2. 8 samples were prepared for x = 0, 0.18, 0.22, 0.35, 0.5, 0.65, 0.8 and 1. The mixtures were initially ground and mixed using an agate mortar and pestle to break up the caked lumps of starting materials and then ball milled in methanol for 24 hours to increase the homogeneity of the mixture. The mixture was then dried and pressed into pellets. These pellets were then heated in a platinum crucible in a furnace, which was programmed to heat to 1300°C at a rate of 80°C h^{-1} and then held at this temperature for 8 hours. After this the temperature was reduced very slowly at the rate of 5°C h^{-1} to 1000°C, after which it was finally reduced to room temperature at the rate of 50°C h^{-1}.

The purpose of holding at the high temperature of 1300°C was to ensure full dissolution and homogenisation of the component oxides. However as both K_2CO_3 and Na_2CO_3 melt at around 1050°C it is quite reasonable to cool very slowly to 1000°C by which temperature everything would have solidified. Once cooled the solidified crystals were removed carefully using a non–reactive polythene rod. Up to 10mm sized pale yellow NKBT crystals were obtained for the compositions x = 0, 0.18, 0.22, 0.35 and 0.5. Unfortunately as the concentration of potassium increases the yield of the perovskite phase NKBT decreases significantly, this is assumed to be due to the high concentration of K_2O being formed in the melt. Hence unfortunately for the x = 0.65, 0.8 and 1 samples, pure perovskite phase crystals could not be obtained. These samples were made in a ceramic form using a modified mixing of oxide method detailed by Jones *et al.*[21] However one of the interesting conclusions observed from these sample preparations which also correspond closely with the work of Jones *et al.*[21] is that single crystals of NKBT samples around the hypothesised

MPB (around x = 0.78 – 0.82) will need to be grown at much lower temperatures in order to facilitate crystal growth.

References

[1] K.J.D. MacKenzie, M.E. Smith., *Multinuclear Solid-State NMR of Inorganic Materials*, Pergamon, 2002

[2] D.D. Traficante, *Concepts in Mag. Reson.*, 2, 181 (1990)

[3] D.I. Hoult, R.E. Richards, *Proc. Roy. Soc. A,* 344, 311 (1975)

[4] M.E. Smith, E.R.H van Eck, *Progr. Nucl. Mag. Reson.*, 34, 159 (1999)

[5] E.L. Hahn, *Physical Review B*, 80, 580 (1950)

[6] A.C. Kunwar, G.L. Turner, E. Oldfield, *J. Mag. Reson.*, 69, 124 (1986)

[7] Z. Yao, H.T. Kwak, D. Sakellariou, L. Emsley, P.J. Grandinetti, *Chem. Phys. Lett.*, 327 [1], 85 (2000)

[8] S. Prasad, H.T. Kwak, T. Clark, P.J. Grandinetti , *J. Am. Chem. Soc.*, 124, 18, 4964 (2002)

[9] J.W. Cooley, J.W. Tukey, *Math. Comput.*, 19, 297 (1965)

[10] D. Massiot, F. Fayon, M. Capron, I. King, S. Le Calvé, B. Alonso, J.O. Durand, B. Bujoli, Z. Gan, G. Hoatson, *Magn. Reson. Chem.*, 40 70 (2002)

[11] M. Bak, J.T. Rasmussen, N.C. Nielsen, *J. Magn. Reson.*, 147, 296 (2000)

[12] H. Fan, L. Zhao, B. Tang, C. Tian, H.E. Kim, *Mat. Sci. Eng.*, B99, 183 (2003)

[13] S.L. Swartz, T.R. Shrout, *Mat. Res. Bull.*, 17, 1245 (1982)

[14] S.J. Butcher, M. Daglish, *Third Euro-Ceramics Conference Proceedings*, 2, (1993)

[15] K. Singh, S.A. Band, *Ferroelectrics*, 175, (1996)

[16] H.C. Wang, W.A. Schulze, *J. Am. Ceram. Soc.*, 73, 825 (1990)

[17] S.E. Park, S.J. Chung, I.T. Kim, K.S. Hong., *J. Am. Ceram. Soc.,* 77, 2641 (1994)

[18] P.W. Bridgeman, *Proc. Am. Acad. Arts. Sci.* 60 [6], 303 (1925)

[19] S. Kyropoulos, *Z. anorg. u. allg. Chem.,* 154, 308 (1926)

[20] E.G. Fesenko, B.G. Gavrilyachenko, R.L. Spinko, M.A. Martynenko, E.A. Grigoreva, A.D. Feronov, *Kristallografiya,* 17, 153 (1972)

[21] G.O. Jones, J. Kriesel, V. Jennings, M.A. Geday, P.A. Thomas, A.M. Glazer, *Ferroelectrics* 270, 191 (2002)

Chapter Four

4.1 Introduction

There are two key objectives of this chapter. Firstly a detailed NMR study into the actual precursor materials, used in the preparation of lead-based ferroelectric perovskites, together with an examination of the effects of various heat treatments on these precursors is presented. Secondly, by collecting here the spectra of some well known model compounds a better understanding of the local structural units and coordinations present in the actual PMN-PT samples being studied in Chapter 5 should be possible. Furthermore as all these precursor materials have been synthesised using the sol-gel method as detailed in section 3.8.2, the structural evolution in such a gel can often occur via a series of distinct amorphous states that differ in atomic arrangement and NMR can effectively look at these states and how they evolve with heat treatment. Thus, the short-range sensitivity of NMR makes it possible to study both the amorphous and crystalline components of these precursor materials.

In addition SIMPSON simulations and fits of some of these model compounds have been included so as to compare our results with those in the existing literature and build an appropriate foundation for the simulation of the more complex PMN-PT compounds in the following chapter. In some of the model compounds the NMR interaction parameters are known so that the effects of spinning speed and finite pulses on sites with large interactions can be understood.

The chapter has been divided into 3 main sections:

1. ^{17}O NMR of the various precursor materials of several lead-based ferroelectrics,

2. ^{93}Nb NMR of several well known model crystalline compounds, and
3. ^{45}Sc NMR of the successive heat treatments used in the preparation of ^{17}O-enriched lead scandium niobate (PSN).

4.2 ^{17}O NMR Studies

Oxygen is effectively uniformly distributed throughout the structure of all the materials mentioned above. Over the last decade there has been a large increase in the number of reports of ^{17}O NMR from inorganic solids as it has been realised that oxygen can be an extremely informative nucleus. It is a spin-5/2 quadrupole nucleus, with a relatively small quadrupole moment and large chemical shift range ~ 1000 ppm[1]. Its major handicap is its natural abundance of only 0.037% which necessitates isotopic enrichment, but for many oxides this is relatively straightforward to achieve by using ^{17}O-labelled water in a sol-gel process. There are now detailed ^{17}O MAS NMR studies reported of a range of sol-gel produced oxides such as ZrO_2 where three peaks in the spectra indicated the presence in the amorphous material of predominantly monoclinic-like ZrO_2 regions, along with some tetragonal-like regions[2]. On crystallization the spectrum significantly narrowed and indicated the presence of predominantly the tetragonal phase. The nature of the oxygen sites is unequivocally indicated by the ^{17}O shifts, providing in this case a precise identification of tetragonal zirconia. Other examples of the use of ^{17}O NMR to monitor the evolution of structure in sol-gel samples include TiO_2[3,4], V_2O_5[5], Y_2O_3[6], HfO_2[7], MgO[8] and Ta_2O_5[9]. In the structural development of an amorphous gel into a crystalline material it is clear that there are subtle variations between the different

oxides. The sensitivity of the ^{17}O parameters to structure has been demonstrated in ternary crystalline titanates[10], zirconates[10] and hafnates[7], both by the number of distinct oxygen sites and the NMR interaction parameters, such as chemical shift and quadrupole interaction. In amorphous materials the large shift range of oxygen means ^{17}O NMR is very sensitive to the atomic ordering, being used to detect nanoscale phase separation in binary mixtures of MO-SiO_2 (e.g. with TiO_2[11] and ZrO_2[12]) and the site preferences in aluminosilicate[13-15] and borosilicate glasses[16].

Hence ^{17}O would in principle be an ideal probe nucleus for ferroelectric relaxor perovskite phases. Thus the following sections present ^{17}O NMR data showing the local structural development in the sol-gel formation of some of the precursor oxides (Nb_2O_5, Sc_2O_3, In_2O_3) where ^{17}O NMR data has not yet been reported, and also show preliminary data from PSN and the PMN related phase columbite. Further details about ^{17}O in the PMN-PT series of materials are given in Chapter 5.

The experiments on ^{17}O NMR were largely carried out at 8.45T applied magnetic field. The Warwick Group has considerable experience of studying gel-formed oxide materials and the 8.45T magnet is usually the preferred instrument for such ^{17}O MAS NMR studies. The reason for this is that oxygen can experience both chemical shift and quadrupolar interactions. For the more ionic oxides (e.g. TiO_2, MgO, Nb_2O_5) the quadrupolar interaction tends to be small so that applying a high field to narrow this is unnecessary. The dominant broadening interaction for amorphous samples of such oxides tends to be chemical shift dispersion. Since the chemical shift dispersion scales linearly with the applied magnetic field it often pays to carry out these investigations at a moderate magnetic field such as 8.45T. Carrying out experiments at very high applied magnetic field (> 14.1T) can

occasionally result in some of the resonances from such sites that are dominantly broadened by chemical shift dispersion being very wide[17]. Hence most of the data here was collected at 8.45T although for certain samples data was collected at 14.1T. In all samples where ^{17}O was used the enrichment was checked in the initial dried amorphous gel since the signal can only become weaker on heating. The binary oxides are compared to the data available in the literature where this exists.

For each of the following, ^{17}O-enriched samples were manufactured using the sol-gel methods detailed in section 3.8.2, all the PMN and PMN-PT samples will be discussed in Chapter 5.

1. As-formed amorphous MgO
2. As-formed amorphous TiO_2
3. As-formed Nb_2O_5 and then after different heat treatments
4. As-formed In_2O_3 and then after different heat treatments
5. As-formed Sc_2O_3 and then after different heat treatments
6. As-formed amorphous $MgNb_2O_6$ (columbite)
7. Crystalline columbite
8. As-formed amorphous $PbTiO_3$
9. As-formed amorphous $(PbSc_{0.5}Nb_{0.5}O_3)_{1-x}$ (PSN)
10. Crystalline PSN
11. As-formed amorphous $(PbMg_{0.33}Nb_{0.67}O_3)$ (PMN)
12. Crystalline PMN
13. As-formed amorphous $(PbMg_{0.33}Nb_{0.67}O_3)_{0.65} - (PbTiO_3)_{0.35}$ (PMN-35PT)
14. Enriched crystalline PMN-35PT

These samples were made by hydrolysis of the relevant alkoxide, with magnesium ethoxide for MgO, titanium (IV) isopropoxide for the TiO_2, lead titanate isopropoxide for the $PbTiO_3$, niobium (V) ethoxide for the Nb_2O_5, scandium isopropoxide for Sc_2O_3, and indium (III) isopropoxide for the In_2O_3. All these chemicals were obtained from Aldrich at >99% purity. They are extremely moisture sensitive so were always handled under a "dry nitrogen" atmosphere. The alkoxides were dissolved in 2-methoxyethanol to act as a mutual solvent with the water. 20% atomic ^{17}O-enriched water was injected into the alkoxide solution, and immediately a white cloudy precipitate begins to form. This white mixture was stirred overnight using a magnetic stirrer by which time the whole system had gelled. This was then vacuum pumped overnight to remove any excess liquid and the resulting dry white solid was ground in a pestle and mortar to a fine powder, which was designated the 'as-formed' sample. Some of the samples were then successively heated at a series of temperatures under a dry nitrogen atmosphere to preserve the ^{17}O label. The temperature was raised until the sample had crystallised. For the more complex samples, mixtures of the alkoxide precursors were initially mixed in methanol, with magnesium ethoxide and niobium (V) ethoxide for columbite, with the addition of lead acetate as well for the PMN and lead titanium isopropoxide for the PMN-35PT. Scandium isopropoxide, niobium(V) ethoxide and lead acetate were used for the PSN. Methanol was used as the solvent in these cases as magnesium ethoxide does not dissolve readily in either isopropanol nor 2-methoxyethanol. Samples of PMN and columbite were then heated to 930°C for 4 hours in an evacuated quartz tube in order to produce the crystalline phases. PMN poses a challenge since its high crystallisation temperature can lead to complete loss of the ^{17}O nuclei from the sample. Care has to be taken because high PbO vapour pressure can cause the tubing

to explode, and the PbO vapour is also highly corrosive to platinum tubing at high temperatures. The best approach was to use thick quartz tubing (wall thickness 1.6mm) and pump the sample continuously for ~100 hours until it stopped out-gassing. This was then pumped to around 10^{-5} bar and the sample heated to 930°C for 10 hours then left to cool. After cooling it was then reheated to 1145°C for 4 hours in the evacuated quartz tubing and then again left to cool.

4.2.1 ^{17}O NMR Results on Binary Oxide Materials

This section deals with the ^{17}O NMR of the component binary oxides used in the preparation of more complex ferroelectric phases detailed in Chapter 5. The sol-gel formation of crystalline TiO_2[4] and MgO[8] have been previously reported in detail. Hence for these two oxides only the spectra from the initial dried gels are shown to indicate that the enrichment has been successful here. However no previous detailed ^{17}O NMR has been reported from sol-gel formed Nb_2O_5, In_2O_3, and Sc_2O_3 so these are reported in detail here.

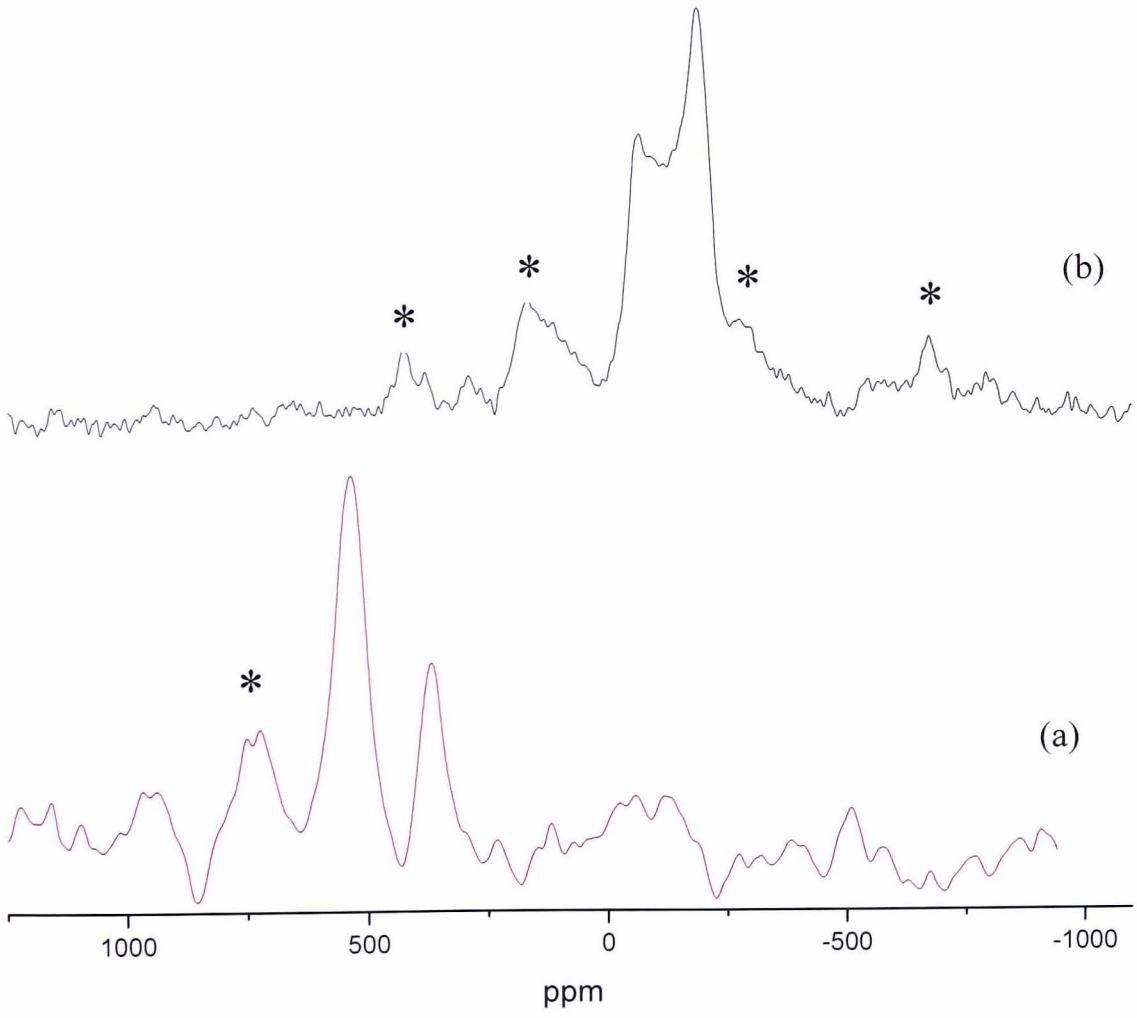

Figure 4.1 - ^{17}O MAS NMR spectra of enriched amorphous (a) TiO_2 and (b) MgO (Asterisks denote spinning sideband).

The ^{17}O spectrum for amorphous TiO_2 (Fig. 4(a)) has two distinct peaks at 532 ppm and 365 ppm which correspond to OTi_3 and OTi_4 sites respectively[4]. There are several well known polymorphs of crystalline TiO_2, differing mainly through the relative disposition of the TiO_6 units. Rutile and anatase have a shift difference of around ~ 35ppm[4].

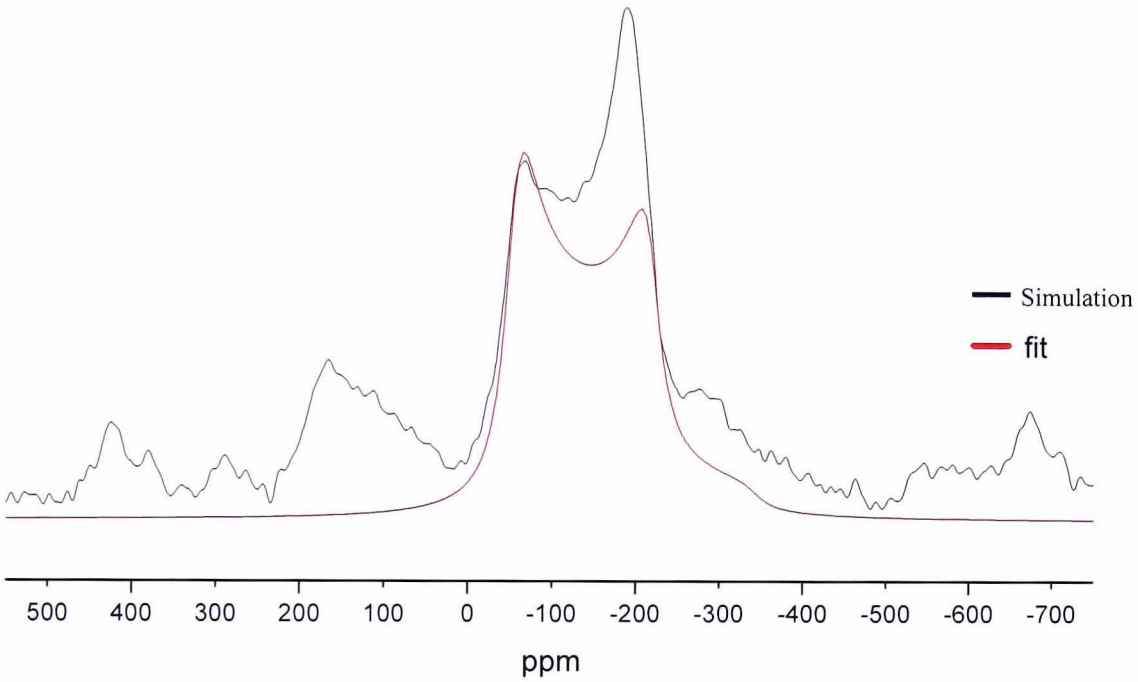

Figure 4.2 - ^{17}O NMR of amorphous, as-formed magnesium oxide showing the experimental data and a trial simulation.

Sample	^{17}O NMR at 8.45T	
	Position (ppm)	Width (ppm)
TiO_2	532	80
	365	not determined
MgO	-190	280
	-64	

* Errors: Peak Position ± 2ppm, Widths ± 2 ppm

Table 4.1 – ^{17}O NMR data of sol-gel prepared (a) amorphous TiO_2 and (b) amorphous MgO

The spectrum from the initial as-formed MgO gel is shown in Figure 4.1 (b). The spectrum has two distinct peaks at –64 ppm and –190 ppm which are much more intense than all the other features in the spectrum which are probably spinning sidebands. The strength of the signal indicates that the ^{17}O-enrichment process was successful. The peaks do not necessarily correspond to two separate phases as the overall lineshape bears similarities to a second-order quadrupolar lineshape pattern which has a Full Width at Half Maximum (FWHM) linewidth of ~ 280 ppm. From the simulation shown in Figure 4.2 a calculated χ_Q of 7.35 MHz is obtained, which corresponds well with the literature[8]. This comes from oxygen in materials such as $Mg(OH)_x(OCH_2CH_3)_{2-x}$ as partial hydrolysis has probably occurred[18]. However it can also be seen that the simulated pattern does not match exactly that expected for a second order quadrupole lineshape, with significant excess intensity at ~ –190 ppm. A previous study of MgO by Bastow and Stuart[2] has shown that the shift of the OMg_6 in MgO is 47ppm. The ^{17}O shift is more shielded in MgO than TiO_2 owing to the higher coordination number and the differing electronegativity of the magnesium and titanium. The increased linewidth of the oxygen in this MgO precursor observed here is related to the much more covalent bonds associated with the residual OH and OCH_3 compared to just MgOMg environments. Hence the excess intensity is probably as a consequence of the proximity of the spinning sideband to this edge (being symmetrically disposed about the isotropic shift and not the centre of the lineshape) and the presence of other more covalent fragments.

Figure 4.3 shows the effect of heating on the ^{17}O MAS NMR spectra of niobium (V) oxide. From the XRD of the crystalline niobium (V) oxide sample shown in figure 4.6 (a) the final sample is clearly a mixed phase sample of two of the numerous polymorphs of niobium (V) oxide – corresponding to both orthorhombic

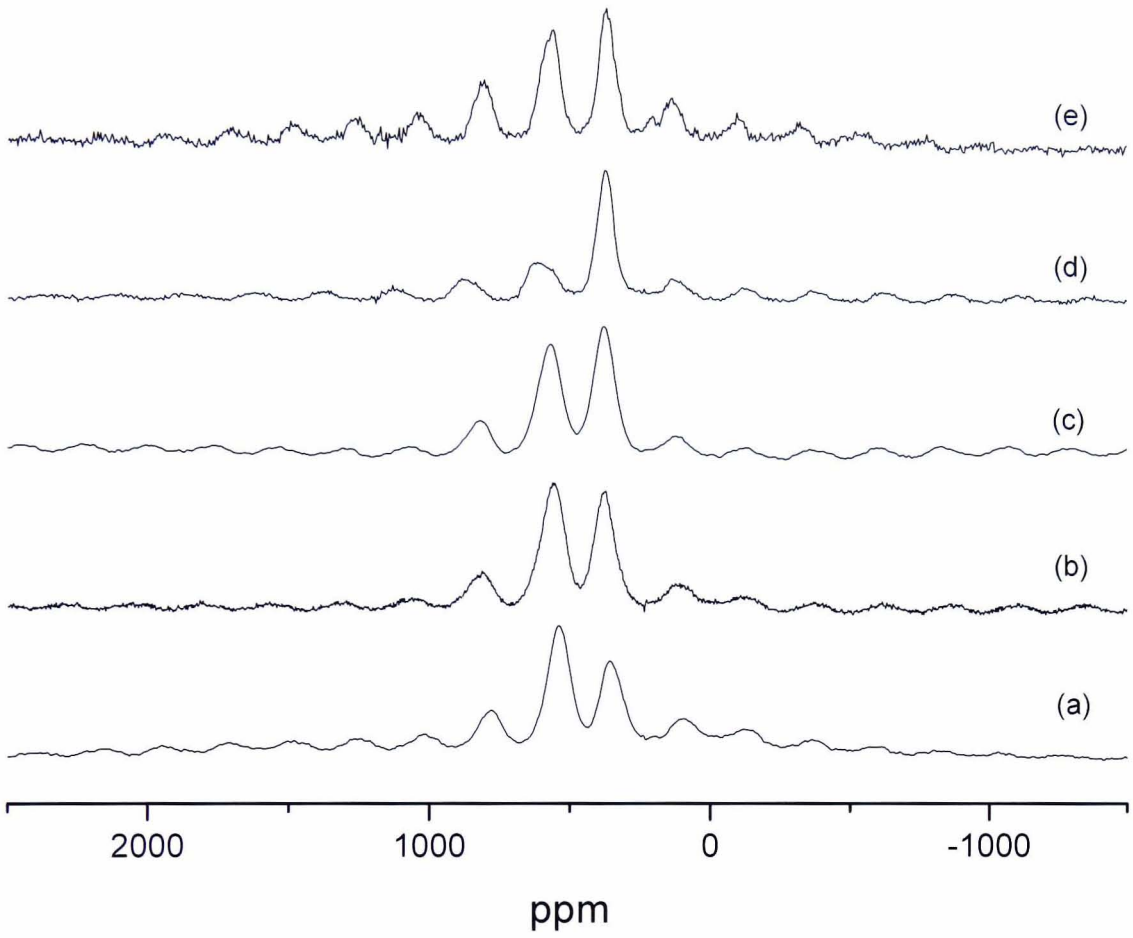

Figure 4.3 - ^{17}O MAS NMR of ^{17}O-enriched sol-gel Nb_2O_5 (a) as-formed and then heated to (b) 250°C, (b) 500°C, (d) 750°C and (e) 1000°C.

and monoclinic phases. This is unsurprising as niobium (V) oxide has a structure that is quite complicated and displays extensive polymorphism and displays significant faulting behaviour[19], though almost all the polymorphs are comprised of NbO_6 octahedra connected by differing combinations of edges and corners. The resonances observed in the Nb_2O_5 can be compared to a previous study of hydrolysed niobium ethoxide[20], where at 9.4T peaks were observed at 360 and 545ppm. These peaks were assigned on the basis of solution state NMR of niobium containing cluster compounds[20] as ONb_2 at 545ppm and ONb_3 at 360ppm. In figure 4.3 (a) two

peaks at 355ppm and 539ppm with comparable linewidths (Table 4.2) can be clearly identified. However it is also clear that the peak at 539ppm has more intensity than the other peak. Upon heating first to 250°C for 4 hours we immediately notice in figure 4.3 (b) that now the intensities of the two peaks are more comparable, after heating to 500°C for 4 hours the peak now at 375ppm is more intense than the peak at 565ppm and there is also a slight narrowing of the line at 375ppm (Table 4.2). Figure 4.3 (d) clearly shows almost a complete disappearance of the sharp peak at 565ppm being replaced by a much broader less intense peak centred at 615ppm. This clearly indicates that the material has already undergone a significant structural change. Finally in Figure 4.3 (e) the material has now crystallised and the two peaks at 370ppm and 571ppm are both present, and are approximately 30% narrower than they were in the amorphous state.

Sample	^{17}O NMR at 8.45T	
	Position (ppm)	Width (ppm)
As Formed	358	115
	540	110
250°C	374	95
	556	110
500°C	375	96
	565	105
750°C	372	70
	617	145
1000°C	371	81
	565	90

* Errors: Peak Position ± 2ppm, Widths ± 2 ppm

Table 4.2 - ^{17}O MAS NMR data for enriched Nb_2O_5 samples undergoing successive heat treatments at 250°C, 500°C, 750°C and 1000°C.

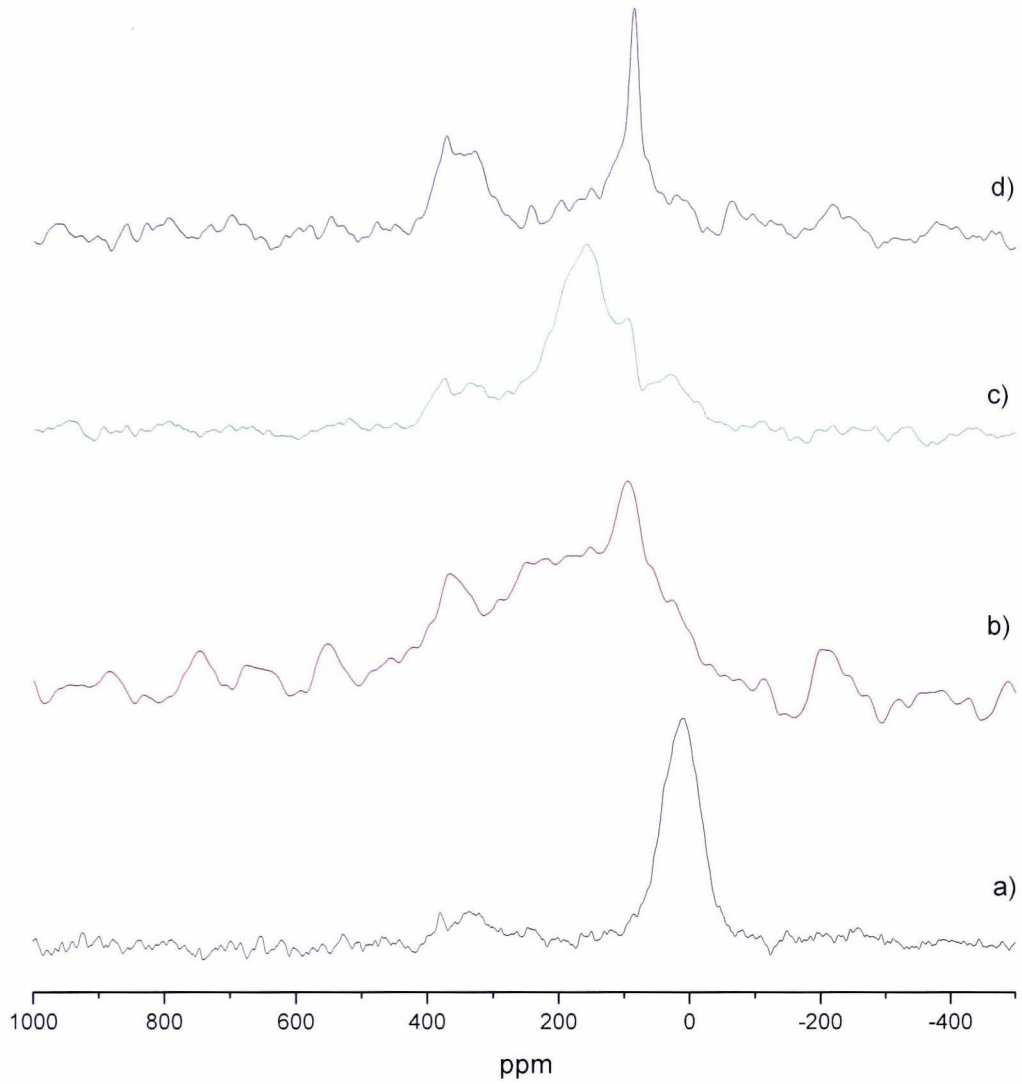

Figure 4.4 - ^{17}O MAS NMR spectra of ^{17}O-enriched In_2O_3 samples undergoing the successive heat treatments at 14.1 T (a) as made and after treatment at (b) 250°C, (c) 500°C and (d) 750°C.

Figure 4.4 shows the effect of heating on the ^{17}O NMR spectrum from sol-gel formed indium oxide. From the XRD of the crystalline indium oxide sample shown in Figure 4.6 (c) we know that the sample is indeed a single phase sample of indium oxide. Figure 4.4 (a) shows the presence of one clear peak at 10ppm. However it also shows the presence of a less intense broader structure centred at ~336ppm. It is quite common in many gel-based oxide materials that peaks often appear in the vicinity of 0ppm. This is usually attributed to hydroxyls formed during the

hydrolysis process. These are usually removed by even modest heating. Figure 4.4 (b) clearly shows there is a considerable change in the material even by only heating to 250°C for 4 hours there is a large shift in the original peak position and an even greater change in the relative intensities of the two peaks. The original peak has now moved to 97ppm while the less intense second peak is now much more distinctly visible at 368ppm. This can be interpreted as a highly disordered structure with a wide range of OIn_X environments. Figure 4.4 (c) again shows considerable differences with the previous spectra, though there is almost no significant change in shift for the second less intense peak now centred at 375ppm there is a considerable shift in the first more intense peak now at 158ppm. Figure 4.4 (d) clearly shows that the material has now crystallised with two distinct peaks at 87ppm and 375ppm. Furthermore there is an ~85% reduction in the line width of the more intense line compared to the original amorphous state. In a previous study by Oldfield *et al.*[21] it was shown that there was a single resonance at 97ppm, and assigned this to a coordination in indium oxide of a single environment of OIn_4. Thus we can attribute the single resonance at 87ppm to this OIn_4 site. To date the cause of the second peak at 375ppm remains undetermined.

Sample	^{17}O NMR at 14.1T	
	Position (ppm)	Width (ppm)
Unheated	10	61
250°C	97	not determined
500°C	158	118
750°C	87	31
	375	78

* Errors: Peak Position ± 2ppm, Widths ± 2 ppm

Table 4.3 - ^{17}O MAS NMR data of enriched In_2O_3 samples undergoing the successive heat treatments at 14.1T unheated after treatment at 250°C, 500°C and 750°C.

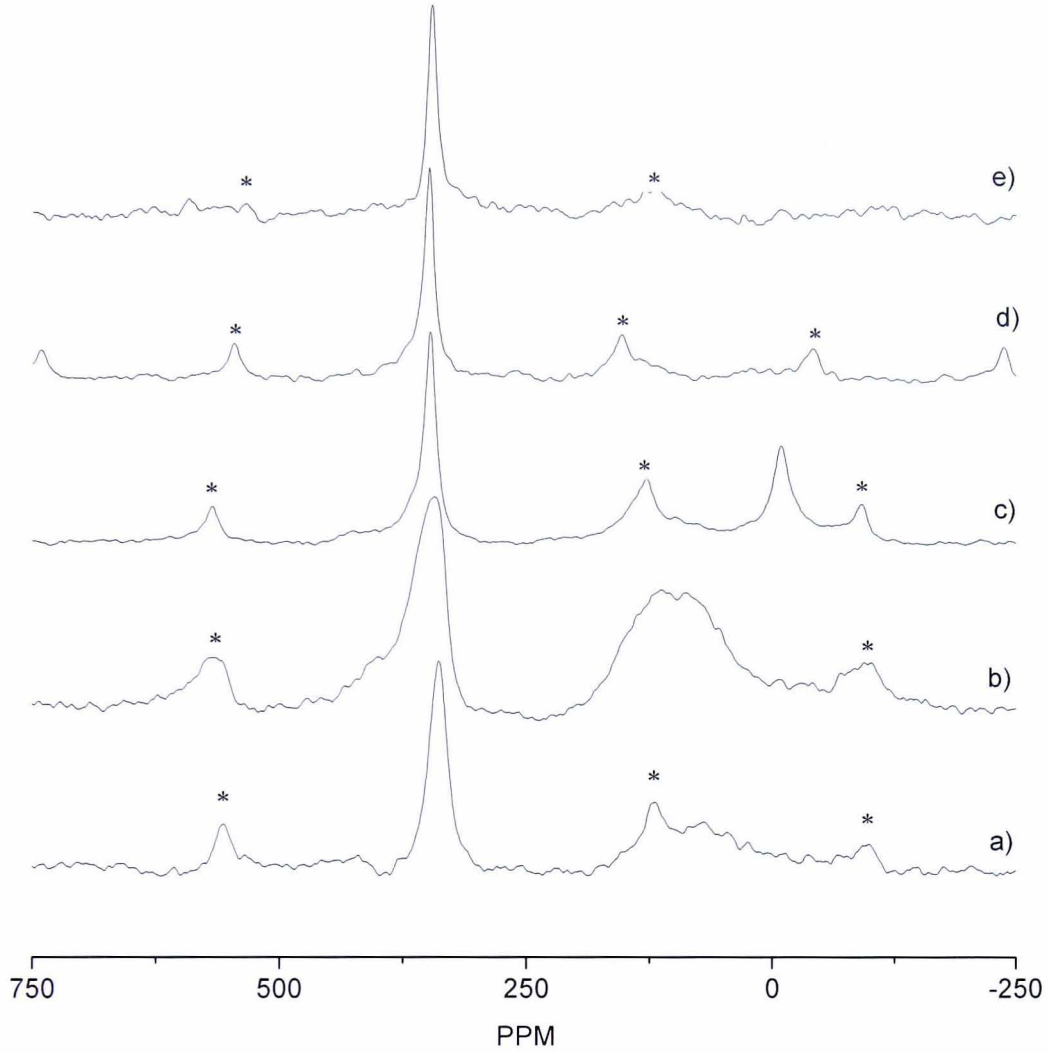

Figure 4.5 - ^{17}O MAS NMR spectra of enriched Sc_2O_3 samples undergoing the successive heat treatments detailed in table 4.4 below at 14.1 T (a) as made and after treatment at (b) 250°C, (c) 500°C, (d) 750°C and (e) 1000°C. The asterisks denote spinning sidebands.

Figure 4.5 shows the effect of heating sol-gel formed scandium oxide on its ^{17}O NMR. From the XRD, single phase crystalline scandium oxide is formed after heat treatment at 1000°C (Figure 4.6(b)) and a single associated ^{17}O NMR peak at 347ppm is observed. The development of the ^{17}O MAS NMR spectra of the gel-produced Sc_2O_3 shows very different behaviour from both Nb_2O_5 and In_2O_3. Figure 4.5 (a) clearly shows a single peak at a similar shift of 340ppm indicating that the OSc_4 coordination of the final product (as identified by Oldfield *et al.*[21] for Sc_2O_3) is formed in the early gel. There is also a small amount of broad intensity at ~100ppm. This is probably from oxygens that are enriched as OH or related organic fragments

in the early stages of gel formation. After heat treatment to 250°C the main resonance has shifted slightly (Figure 4.5 (b), Table 4.4) and is broadened by ~ 10ppm to 33ppm. This indicates that while the dominant scandium coordination remains unchanged the structure is much more disordered. The presence of a much broader ill defined peak at ~95ppm indicates that the sample has a significant number of hydroxyl/organic fragments at this temperature. On heating to 500°C the main resonance now shifts at 346 ppm, very close the final OSc_4 position and the linewidth significantly decreases. This indicates that significant ordering has now already taken place. Perhaps somewhat surprisingly there is a much weaker but nevertheless relatively sharp resonance at ~ 20ppm. The nature of this peak is uncertain but from the shift the suggestion may be that some minor component of the sample forms a hydroxide/oxyhydroxide phase where the hydroxyls are relatively isolated. After heating to 750°C and beyond the ^{17}O resonance has the characteristics of crystalline Sc_2O_3 with the single sharp line at 347ppm with a FWHM linewidth of ~10ppm, in satisfactory agreement with the reported value of 355ppm[21].

Sample	^{17}O NMR at 14.1T	
	Position (ppm)	Width (ppm)
Unheated	340	23
250°C	334	33
500°C	346	15
750°C	347	11
1000°C	347	10

* Errors: Peak Position ± 2ppm, Widths ± 2 ppm

Table 4.4 - ^{17}O MAS NMR data of enriched Sc_2O_3 samples undergoing the successive heat treatments at 14.1 T as made and after treatment at 250°C, 500°C, 750°C and 1000°C.

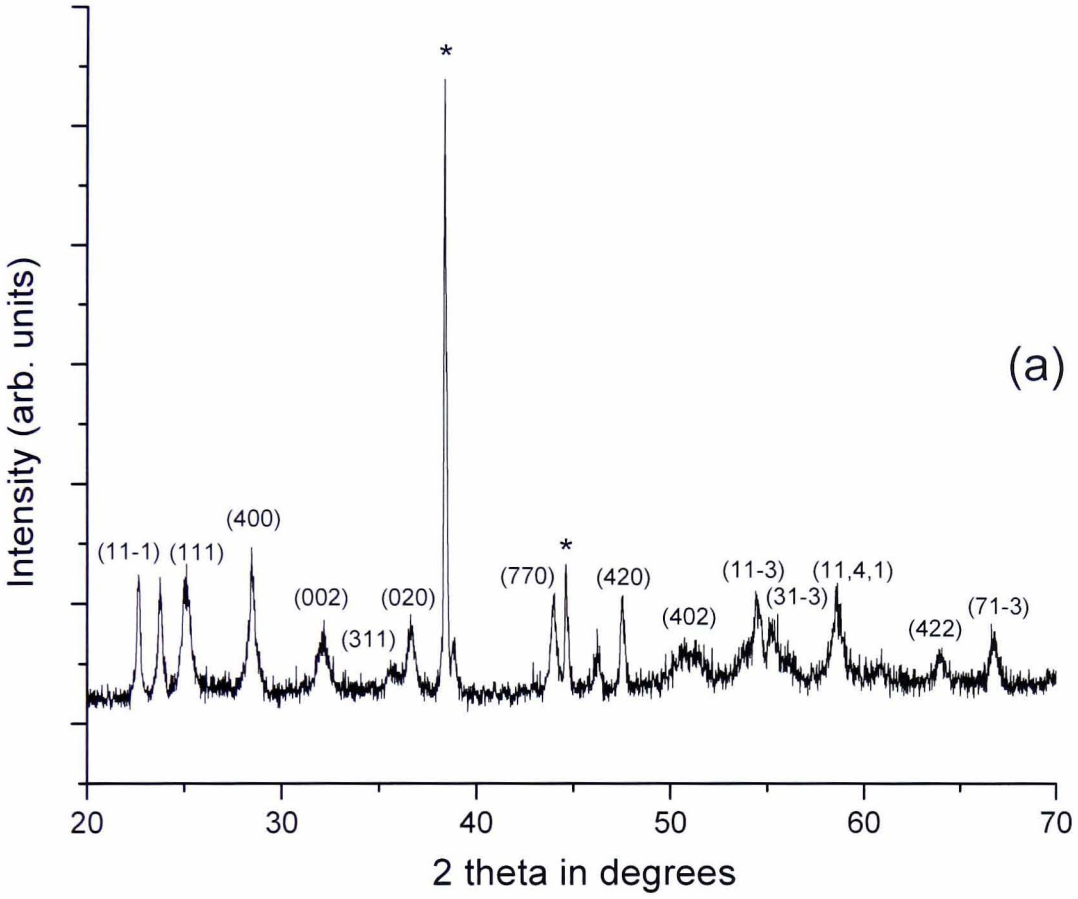
Intensity (arb. units)
(a)
(11-1)
(111)
(400)
(002)
(311)
(020)
*
(770)
*
(420)
(402)
(11-3)
(31-3)
(11,4,1)
(422)
(71-3)
20
30
40
50
60
70
2 theta in degrees

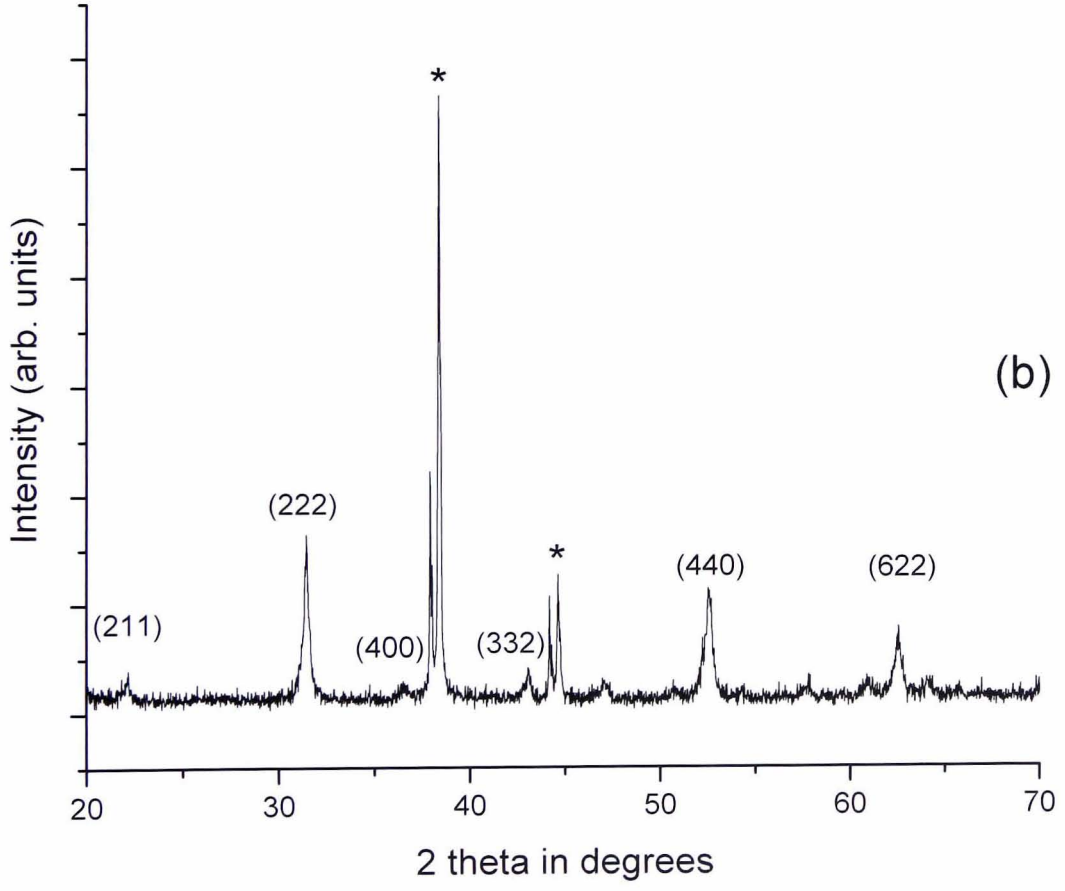
Intensity (arb. units)
(b)
(211)
(222)
(400)
*
(332)
*
(440)
(622)
20
30
40
50
60
70
2 theta in degrees

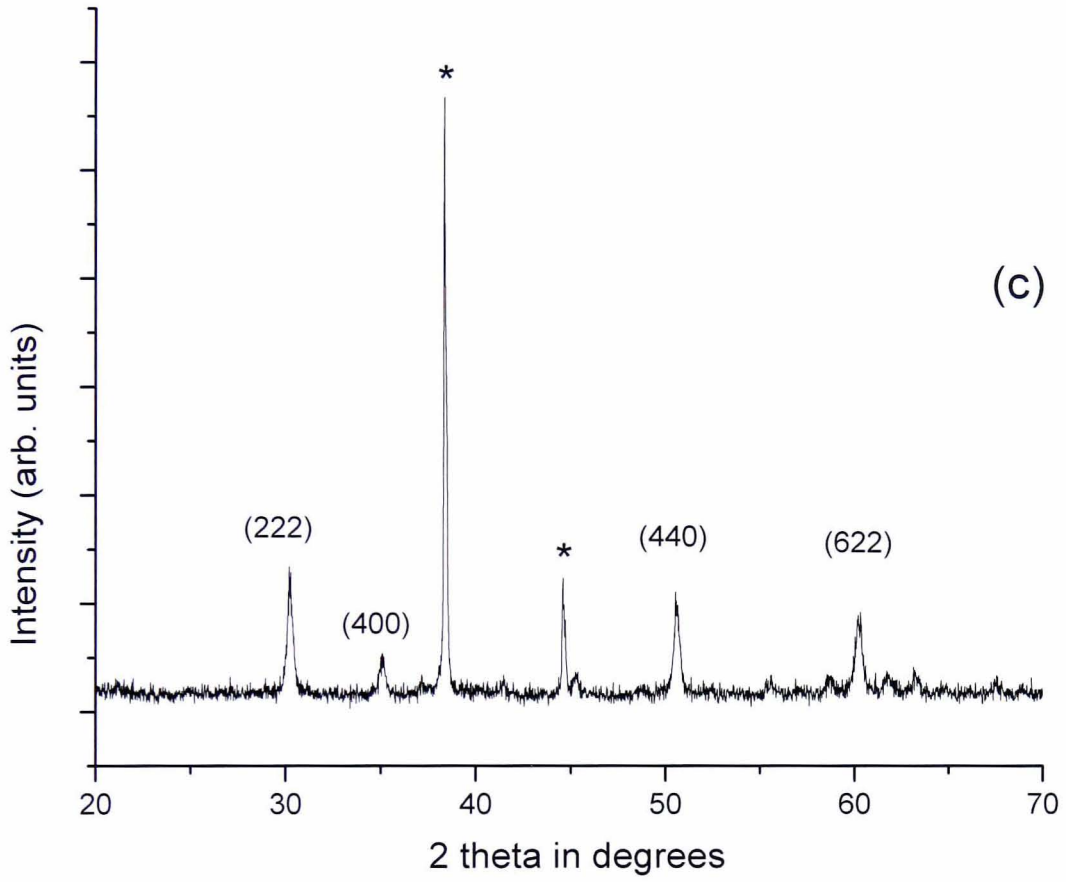

Figure 4.6 - XRD patterns of crystalline (a) Nb_2O_5, (b) Sc_2O_3 and (c) In_2O_3. Asterisks indicate presence of the sample holder.

4.2.2 Discussion of ^{17}O NMR of sol-gel Produced Binary Oxides

The sol-gel process has become very important technologically and has the added bonus that hydrolysis is a key step, so is natural for allowing ^{17}O enrichment. The evolution of the local structure of the initial as-formed gel in such binary oxides can be followed in detail by ^{17}O MAS NMR. The different local coordinations give rise to well separated chemical shifts and the amount of order can be deduced from the linewidth (at least in ionic systems such as those studied here) as chemical shift

dispersion is the dominant linebroadening mechanism. Chemical shift dispersion is a measure of the variation in the local environments giving rise to different chemical shifts. Two cases (ZrO_2 and TiO_2) have been studied in detail, well illustrating the utility of ^{17}O NMR in such studies. The three peaks in the spectrum of the as-formed ZrO_2 gel indicated the presence of disordered material that was mostly monoclinic-like, but with some tetragonal-like regions[22]. On crystallization, the ^{17}O spectrum was much narrower indicating the increased order and that the sample had become predominantly tetragonal. The chemical behaviour of hafnium is very similar to zirconium (they are in same group), but in the initial gel of HfO_2 only two resonances close to the monoclinic positions were observed[7]. Then on crystallization, although the peaks become much narrower they remain at the monoclinic position, i.e. there is no tendency to form the tetragonal form[7].

TiO_2 is another sol-gel formed system that has been studied in detail[3,4]. All crystalline titanias only exhibit OTi_3 environments. However in the as-formed gels two ^{17}O NMR resonances are observed at 514 and 368ppm assigned to OTi_3 and OTi_4 respectively. On heating all studies have shown a gradual decrease in the OTi_4 content until only OTi_3 remains at crystallisation[4,23]. One pattern emerges comparing these ^{17}O NMR studies of sol-gel formed oxides that while there are some points in common between the mechanisms, there are also some very distinct differences. Hence there is no clear common evolution route. In all there is some formation of an ill-defined hydroxylated precursor that can have remaining organic fragments. However the extent of this formation can be very variable, for example being very extensive i.e. the dominant phase for MgO, but almost non-existent for Ta_2O_5. Then as heating causes dehydroxylation sometimes a mixture of coordinations form and in other cases the final coordination is rapidly observed. For example, in TiO_2 an

extensive mixture of OTi_3 and OTi_4 occurs in the amorphous state whereas in MgO the target OMg_6 coordination occurs early in the formation. La_2O_3 formation via the sol-gel process shows a very distinct intermediate state in that a well defined, crystalline oxyhydroxide LaO(OH) forms, which can be observed through its OLa_4 peak at 546 ppm[24].

This work for the first time adds data for three other important oxides Nb_2O_5, In_2O_3 and Sc_2O_3. This adds significantly to the number of oxides for which such data has been reported and adds to the rich diversity of behaviour that is observed in such processing. Nb_2O_5 shows similar coordinations (ONb_2 and ONb_3) to those observed in the final product. However the intensity is somewhat reversed to that observed in the final product. This remains relatively stable up until just before structural rearrangement ready for crystallisation starts and then there a short period of dominance of ONb_3 until ONb_2 comes back to form a mixture in the final crystalline product. It is also worth noting that there is virtually no evidence of an enriched hydroxylated phase in the formation of Nb_2O_5. In_2O_3 exhibits very distinct behaviour in that from the shift it appears that the final coordination is dominant in the early gel and then a high degree of disorder (possibly due to dehydroxylation) occurs as the structure evolves and this is quite long-lived. There is still evidence of significant broadness even after heating to 500°C. This is not commonly observed in other binary oxides. Sc_2O_3 also demonstrates some behaviour that has not really been observed before. The final coordination is accurately reproduced in the initial as-formed gel – perhaps closer than any other sol-gel produced oxide to date. This coordination remains very stable throughout the heat treatment range with only minor amounts of disordered hydroxylated phase formed in the initial gel stages. Other oxides that have a single oxygen environment in the final product usually form

a mixture of oxygen coordinations in the evolution process, is attributed to the disorder in the structure requiring multiple oxygen sites. Hence some interesting and clear differences are observed in these oxides that adds to the data set of this sol-gel formation process and gives the structural chemist some interesting challenges to rationalise them.

4.2.3 Results and Discussion of ^{17}O NMR on Ternary and Higher Compounds

This section deals with the ^{17}O NMR of the ternary and higher compound precursor materials formed either by a combination of the binary oxides detailed above with other precursor materials, or by the sol-gel formation of more complex double ethoxide precursors.

4.2.3.1 As-formed $PbTiO_3$

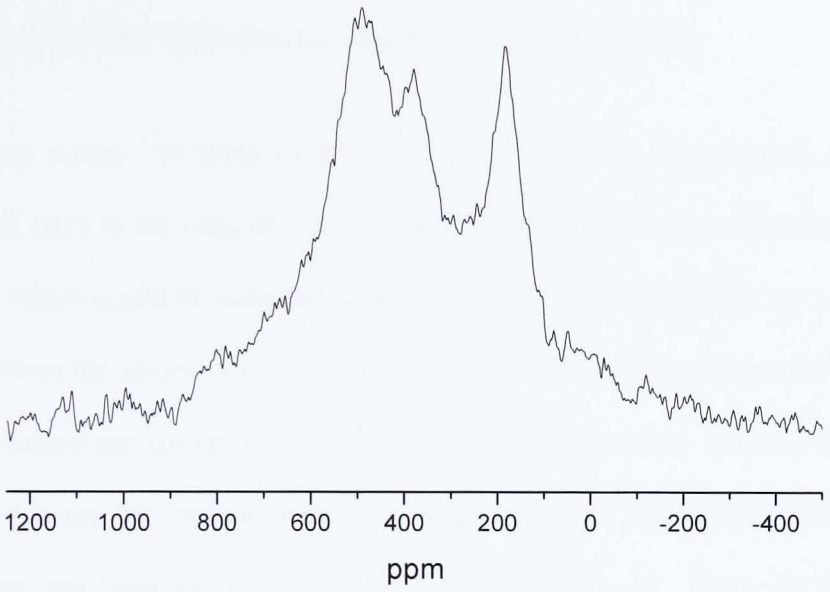

Figure 4.7 - ^{17}O MAS NMR spectra of enriched amorphous as-formed $PbTiO_3$.

Figure 4.7 shows the spectrum of an amorphous lead titanate precursor. Most NMR work on $PbTiO_3$ has been related to the solid solution with $PbZrO_3$, to probe the para- to ferroelectric transition[25]. However in the original ^{17}O NMR study of $PbTiO_3$ only one of the two inequivalent oxygens could be observed. ^{207}Pb NMR has been observed in $PbTiO_3$, characterising the chemical shift anisotropy tensor[26]. A comparison of PZT (lead zirconate titanate) solid solution produced by ceramic and sol-gel routes was made, with the ^{207}Pb NMR peaks relatively featureless and unaffected by MAS[27].

Sample	^{17}O NMR at 8.45T	
	Position (ppm)	Width (ppm)
Amorphous $PbTiO_3$	493	476
	381	Not determined
	186	Not determined

* Errors: Peak Position ± 5ppm, Widths ± 5 ppm

Table 4.5 - ^{17}O MAS NMR data for enriched amorphous $PbTiO_3$

A more recent ^{17}O study of $PbTiO_3$ has revealed two inequivalent oxygen sites O(1) and O(2) in the ratio of 1:2. At 14.1T two oxygen sites were seen at 443 and 647ppm which could be assigned to equatorial (O(2)) and axial (O(1)) oxygens respectively from the intensity ratio. Then from variable field data estimates of the composite quadrupolar interaction parameter (P_q) could be made at 0.35MHz and 0.9MHz respectively for the two sites[28]. In Figure 4.7 the ^{17}O spectrum shows that the enrichment has been successful and 3 peaks are observed. There are 3 quite distinct, but fairly broad peaks observed at 493ppm, 381ppm and 186ppm. The linewidth for the peak at 493ppm was found to be ~480ppm, however for the other two peaks linewidths could not accurately be measured owing to the overlapping lineshapes. This shows some agreement with the shift of 443ppm for the O(2) site in crystalline lead titanate detailed in [28]. The range of resonances seen here has intensity in the regions for TiO_2[3,4] at ~530 and ~330ppm and also for PbO[21] at ~290ppm. The sample was not crystallised as the ^{17}O spectrum has been reported previously in detail[28] and this amorphous precursor was mixed with PMN to form the PMN-PT solid solution discussed in Chapter 5.

4.2.3.2 Lead Scandium Niobate (PSN)

Figure 4.8 (a) shows the ^{17}O MAS NMR spectrum of amorphous PSN ($PbSc_{0.5}Nb_{0.5}O_3$). Like the spectrum of lead titanate shown in Figure 4.7 there is a single broad structure indicating several quadrupolar sites that overlap to form the overall lineshape. The range of environments deduced from the shifts tends to indicate that these are similar to those of the oxides making up PSN, i.e. PbO, Sc_2O_3 and Nb_2O_5. There is also the presence of three peaks in this structure at 446ppm, 363ppm and 249ppm. The overall width of the structure is 360ppm at the FWHM, but owing to the broad lineshapes accurate linewidths could not be derived for the other peaks. Figure 4.8 (b) shows considerable narrowing of the spectrum upon crystallisation to 86ppm at FWHM, while the spectrum has a strong peak at 378ppm with perhaps some other structure, although this is difficult to determine as the signal is now much weaker as ^{17}O is lost from the sample during heat treatment. These resonances observed are probably experiencing several interactions and it would be useful to investigate these samples further using other high resolution NMR techniques such as multiple quantum (MQ) and double angle rotation (DOR), but a much higher isotopic enrichment would be an advantage here.

In such perovskite ferroelectric (ABO_3) structures, how much structural insight ^{17}O NMR provides into the metal ordering of the B sites needs to be understood. Such B-site ordering is believed to important for the relaxor properties of these materials. In the initial amorphous PSN precursor the ^{17}O MAS NMR peaks of the component pure oxides would be at 290ppm (PbO), 347ppm (Sc_2O_3) and 565ppm (for ONb_2 in Nb_2O_5). So a peak at 468ppm extending over a range of ~±180ppm shows the expected disorder in the initial composition, with contributions from all

the different fragments such as Nb-O-Pb, Sc-O-Nb, etc. that are present. The broad line does give some hint of other features, such as at 250ppm, which indicates that there maybe some better defined local environments, but generally the width is probably an indication of the variation in each of the local environments due to variations in bond length in the amorphous state.

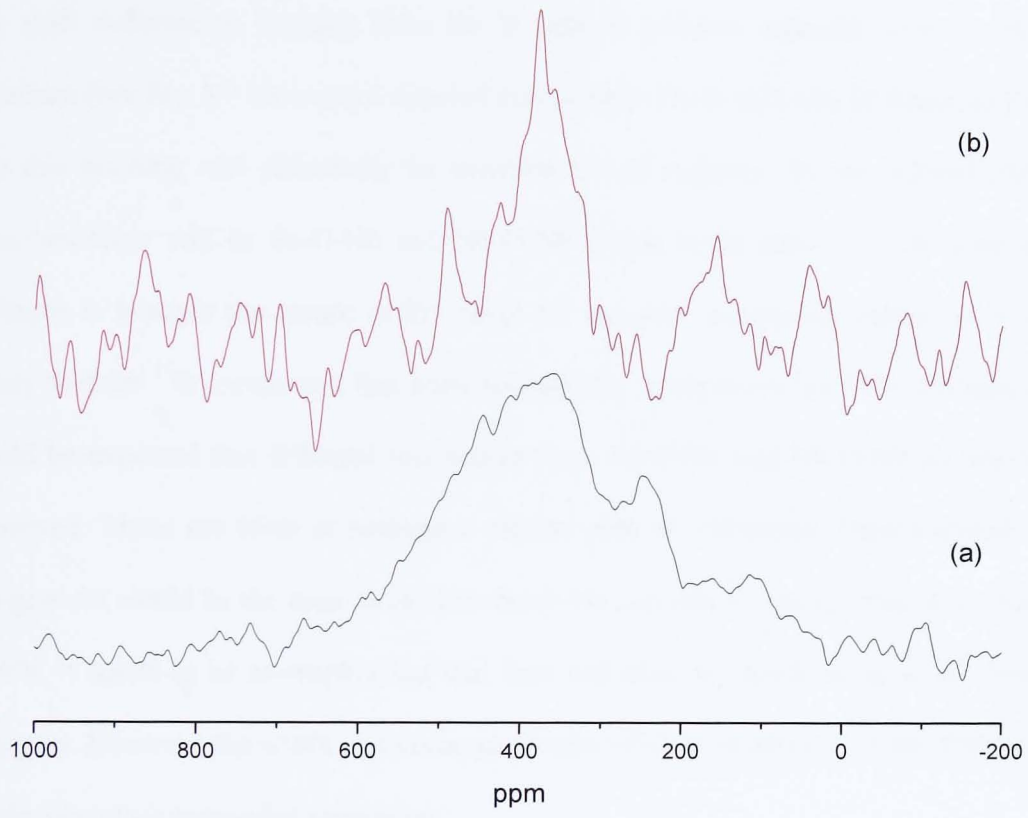

Figure 4.8 - ^{17}O MAS NMR spectra of enriched a) amorphous PSN and b) crystalline PSN

Sample	^{17}O NMR at 8.45T	
	Position (ppm)	Width (ppm)
Amorphous PSN	446	not determined
	363	360
	249	not determined
Crystalline PSN	378	86

* Errors: Peak Position ± 5ppm, Widths ± 5 ppm

Table 4.6 - ^{17}O MAS NMR data for enriched amorphous PSN and crystalline PSN

Then on crystallisation there is the definite peak at 378ppm and a large reduction in the broad component. PSN is a cubic perovskite above the transition temperature of ~360K changing to a rhombohedral symmetry at lower temperatures with lattice parameters a=4.08Å and α=89.89° [29]. There should thus be slightly inequivalent structural oxygens, but the different metal neighbours should dominate the shift differences. Oxygen links the B cations between adjacent layers in the structure (see Sec 5.7 for a more detailed discussion). There will also be bonds to Pb, but this bonding will effectively be constant for all oxygens. In the ordered PSN structure there will be Sc-O-Nb and Nb-O-Nb bonds in the ratio 2:1. The peak at 378ppm is towards the centre of the range for the pure component oxides, so it is likely that the ^{17}O enrichment has been successfully achieved in the PSN. Perhaps it could be expected that different resonances from Sc-O-Nb and Nb-O-Nb should be observed. There are hints at perhaps a second peak at ~500ppm. Then a tentative assignment would be the main peak from Sc-O-Nb and this secondary peak from Nb-O-Nb. It needs to be re-emphasised that lead will also be coordinating to all these oxygens. However the width and consequent lack of clear resolution of the different environments is somewhat surprising.

4.2.3.3 Columbite $MgNb_2O_6$

Figure 4.9 (a) shows the ^{17}O MAS NMR spectrum of as-prepared, amorphous columbite, with a single peak present at 517ppm. This observation is somewhat unexpected as the constituent oxides have well known shifts in the sol-gel as-formed state. For Nb_2O_5 as reported in section 4.2.1 there are two distinct resonances with ONb_2 at 545ppm and ONb_3 at 360ppm. MgO initially forms a mixed hydroxide/partially substituted phase which peaks around 0ppm. In the cases where initial mixed oxides have been formed through the sol-gel reaction, as opposed to subsequent high temperature reaction of enriched oxides, either a range of broad peaks is observed or a single peak is present at an intermediate shift of the constituent oxides. The columbite sample is quite different having a shift much closer to the peaks in niobia gels. This might suggest that the niobia is preferentially enriched, but the final product does show the expected spread of lines, so it is difficult to explain the observed shift in the initial gel.

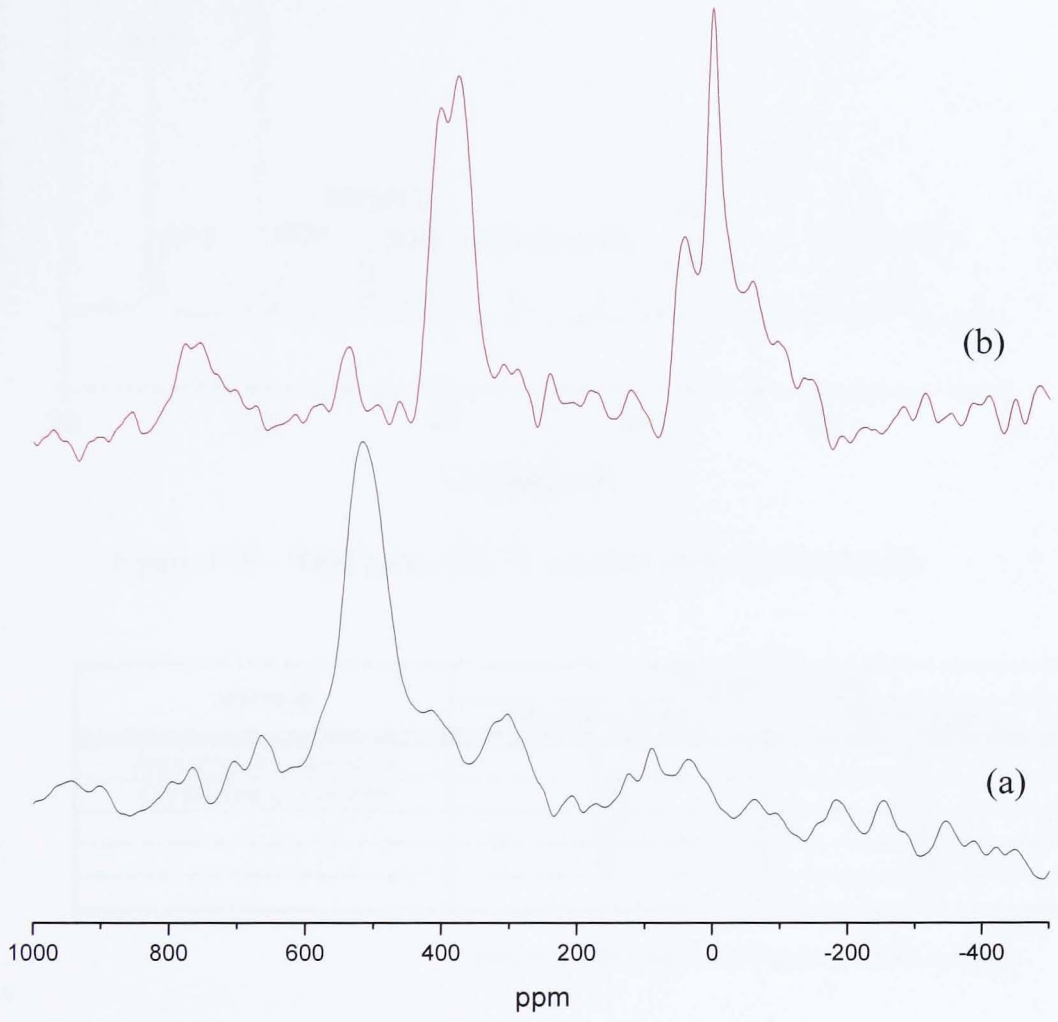

Figure 4.9 - ^{17}O MAS NMR spectra of enriched sol-gel samples (a) amorphous columbite and (b) crystalline columbite

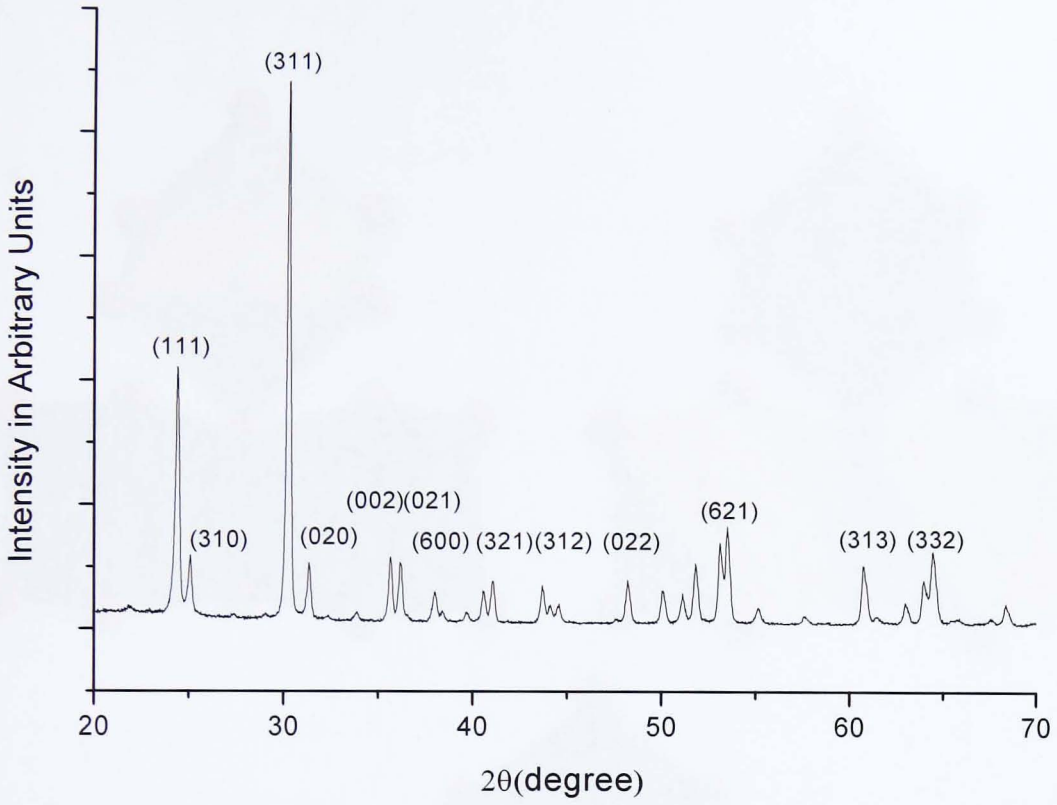

Figure 4.10 – XRD pattern of ^{17}O enriched crystalline $MgNb_2O_6$

Sample	^{17}O NMR at 8.45T	
	Position (ppm)	Width (ppm)
Amorphous Columbite	517	87
Crystalline Columbite	404	65
	375	65
	43	138
	1	28

* Errors: Peak Position ± 5 ppm, Widths ± 5 ppm

Table 4.7: ^{17}O MAS NMR data of enriched sol-gel samples amorphous columbite and crystalline columbite.

On heating to 1150°C the XRD pattern (figure 4.10) clearly shows crystallisation has occurred of columbite and ^{17}O MAS NMR spectrum shows significant narrowing (Figure 4.9 (b)), with three clear narrow peaks forming at 404ppm, 375ppm and 1ppm, with approximately equal intensity as deduced from simply fitting these lines

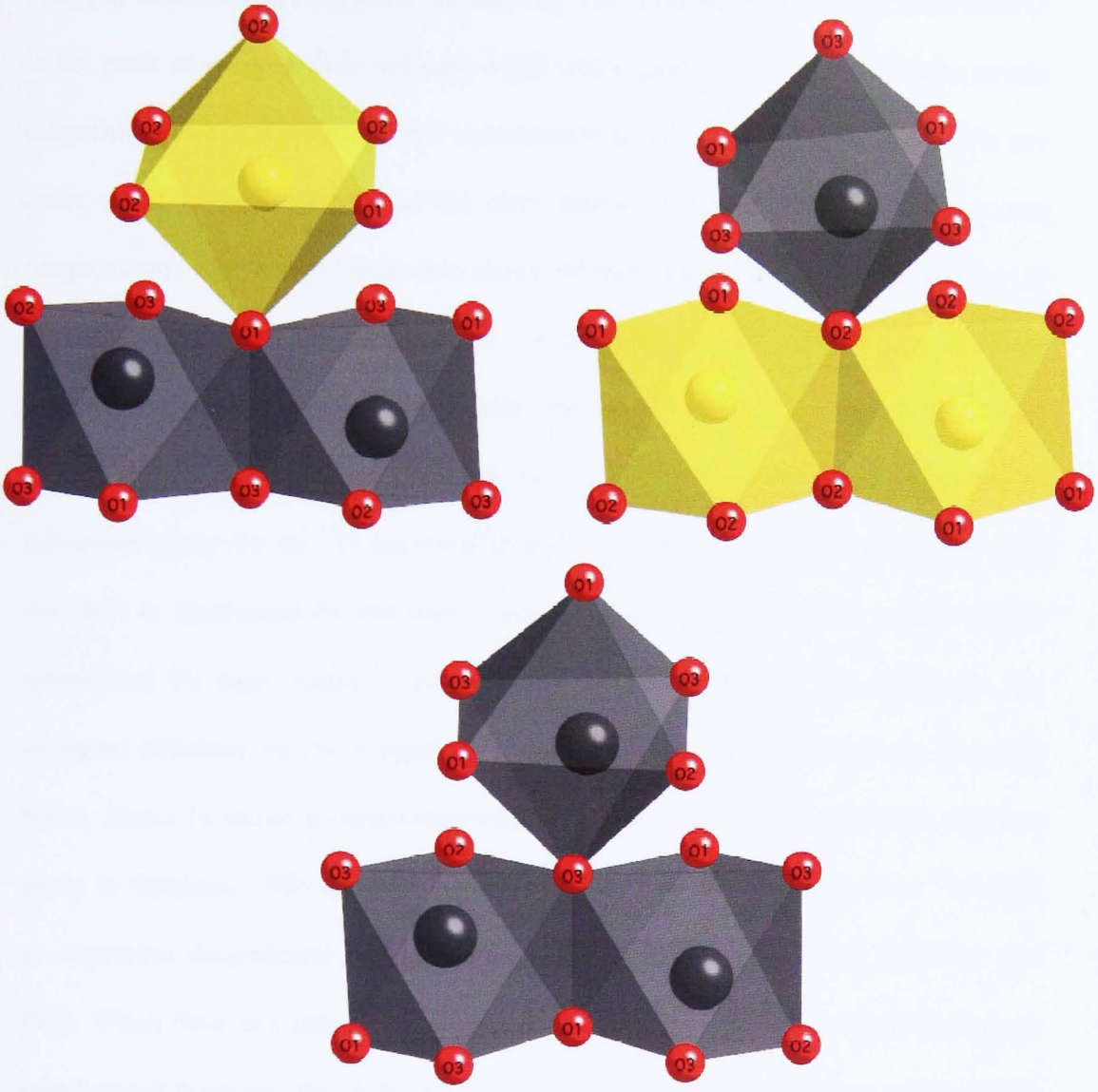

Figure 4.11 - The local oxygen coordinations in columbite of the three inequivalent oxygens O1, O2 and O3 present in $MgNb_2O_6$ with yellow being magnesium and grey niobium.

with Gaussians, together with a broad underlying feature at ~0ppm which may contain a secondary peak at ~40ppm. Within the columbite structure there are three inequivalent oxygen sites, all of which are trigonally coordinated by metals[30]. The three local oxygen environments O1, O2 and O3 are shown in Figure 4.11 with local metal nearest neighbours of Nb_2Mg, Mg_2Nb and Nb_3 respectively. One might expect perhaps the three peaks to have progressive shifts from pure Nb position around

360ppm to somewhere between Nb and Mg. The most straightforward identification is the peak at ~0 ppm. It is not pure MgO which peaks at 47 ppm, but must be the magnesium-rich environment and corresponds to O2. The other environments are quite close in shift despite having very distinct numbers of the niobiums and magnesiums. The shifts of these two peaks (404ppm and 375ppm) are much closer to niobium region, and this is expected for the ONb_3 environment (O3), which is probably the peak at 404ppm. This means that the 375 ppm peak is the O1 site. That evenly spaced lines are not observed can probably be rationalised in terms the influences observed on ^{17}O chemical shifts. When bonds of different ionicity exist the shift is dominated by the most covalent and the shifts fall in ranges largely determined by these metals[10]. For example in metal titanates and zirconates the strongest influence on the oxygen shift is titanium and zirconium and not the other metal. Hence in mixed niobium/magnesium environments it is the niobium which is likely to dominate. This has important implications for the observation of ^{17}O NMR to determine the different environments in the phases such as PMN, PMN-PT and PSN. When there is a range of local environments they may not be separated as one metal could dominate the shift and force the peaks to be confined to a small shift range.

4.3 ^{93}Nb NMR studies

4.3.1 Introduction

One of the key objectives of this thesis is to understand more about the role of crystal structure and bonding in promoting ferroelectric relaxor and enhanced piezoelectric behaviour. Given that niobium is a key element, developing ^{93}Nb NMR as a probe of ceramic and ferroelectric relaxor phases was investigated here. However ^{93}Nb has been regarded as a difficult nucleus in NMR terms because of the large quadrupole interaction arising from the interaction of the nuclear electric quadrupole moment with the electric field gradients often gives rise to considerable spectral broadening. ^{93}Nb is a nucleus with spin I= 9/2, a relatively large quadrupole moment and 100% natural abundance. However use of high speed MAS with a high applied magnetic field is a good way to help at least partially overcome the quadrupole broadening, and this has been important for the acquisition of all the spectra shown below. All the chemical shifts in the spectra shown below have been referenced to a saturated solution of dry $NbCl_5$ in acetonitrile, which is the most common reference quoted in the literature, by using the secondary reference of $LiNbO_3$ taking the most intense singularity as –1016.3ppm at 14.1T.

A detailed NMR study of ^{93}Nb in $LiNbO_3$ and $NaNbO_3$ as well as a range of lead niobates including $Pb_{1.83}Mg_{0.21}Nb_{1.71}O_{6.39}$ showed a relatively narrow shift range. Typically the quadrupole interaction parameters in the lead niobates were 13.7 – 20.6 MHz and δ_{iso} were –980 to –1010ppm, except for $PbNb_2O_6$ which had a shift of –1113ppm[31]. The much larger shift from this phase was attributed to the fact that the constituent NbO_6 units are both edge- and corner-sharing compared to the normal corner-sharing. In the PMN pyrochlore phase the shift of ^{93}Nb was still in

the same range ~-1014ppm, but the quadrupole interaction was much higher at 26.8MHz[31]. In some phases it was suggested from nutation NMR studies[31] that sites were present with quadrupole interaction >30 MHz. However as discussed further in Chapter 5 there is some doubt about this conclusion.

The number of studies reporting niobium is increasing rapidly within some cadmium oxyfluorides the local niobium octahedra displaying mixed oxygen/fluorine coordinations and the quadrupole interaction being 33-36MHz[32]. ^{93}Nb MAS NMR data has also been reported from $KNbO_3$, Nb_2O_5 and $KTeNbO_6$, although no attempt was made to extract any spectral parameters[33]. One the key objectives of this part of the thesis was to establish the sensitivity of ^{93}Nb NMR parameters to changes in the local coordination. However after the first version of this thesis had been written a very extensive paper reporting the ^{93}Nb NMR parameters from 14 crystalline inorganic niobates appeared[34]. This greatly extended the range of local niobium coordinations studied and the understanding of the structural influences on the ^{93}Nb parameters. Given that it was hoped here to understand the structural sensitivity of ^{93}Nb NMR data from PMN and PMN-PT in terms of model compounds our data will be compared to that in ref. [34], especially the shift ranges of the different coordinations. There are several model compounds studied here that were not reported in ref. [34] so that the robustness of their shift ranges and structural conclusions can be tested. Hence ^{93}Nb NMR spectra was acquired from a range of model niobates including zinc niobate and barium zinc niobate.

4.3.2 NMR of Model Niobates

Figure 4.12 shows a comparison between the static, MAS NMR and a SIMPSON simulation for $LiNbO_3$. Figure 4.12 (a) shows a static $LiNbO_3$ NMR spectrum with a

single distinct peak at around -1025ppm and a linewidth of 124ppm. In Figure 4.12 (b) the MAS NMR spectrum clearly resolves two distinct peaks at −1016ppm and -1050ppm with the overall linewidth of the spectrum showing a considerable narrowing by more than half its static linewidth to ~54ppm while spinning at approximately 18kHz. The SIMPSON simulation was also acquired using a virtual spinning speed of 18kHz and was also configured for a simulated magnetic field of 14.1 T, all the other experimental conditions were the same as the actual MAS experiment of Figure 4.12 (b). In fact SIMPSON was used to help determine, for effectively infinite spinning speed, appropriate pulse excitations for the experiment. The actual parameters determined for the quadrupolar interaction was χ_q =22.2 MHz. in good agreement with the existing literature[34,35]. Lithium niobate has a trigonal structure with the niobium coordinated as NbO_6. The NbO_6 are shared with other octahedra at each corner and the octahedra are quite symmetric with 3 × 1.876Å and 3 x 2.125Å. This is then reflected in the relatively small quadrupole interaction for niobium of 22 MHz.

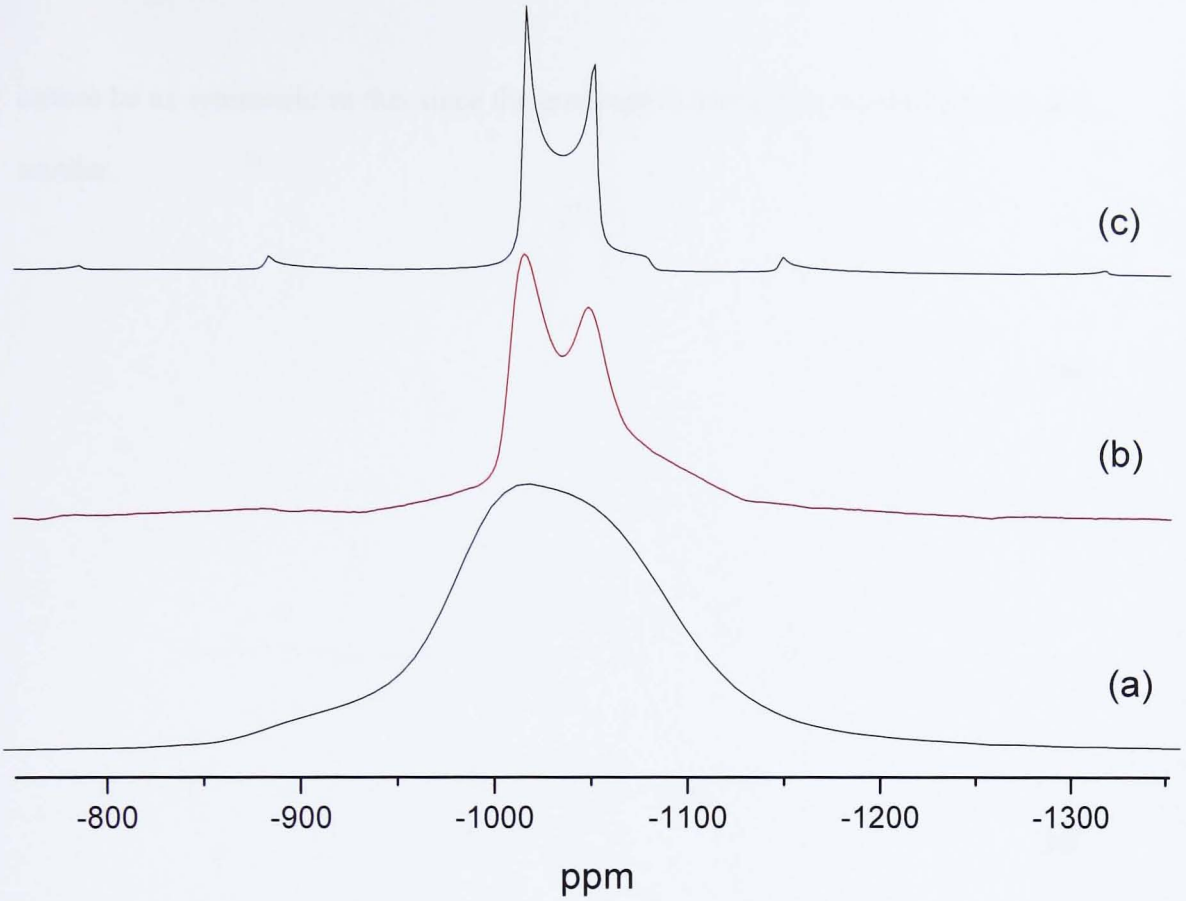

Figure 4.12 - ^{93}Nb NMR spectra of lithium niobate (a) static, (b) MAS and (c) SIMPSON simulation.

Figure 4.13 shows the comparison between static and MAS ^{93}Nb NMR spectra of $NaNbO_3$ at 14.1 T. Although the spectra do not show any definite quadrupolar features they suggest that quadrupole effects dominate the lineshape. For example the static line (Figure 4.13 (a)) is quite asymmetric, with the line spreading down to negative shift more than positive values. The MAS line is narrower by a factor of ~2.5 (Figure 4.13 (b)). This is also an indication of the quadrupolar interaction being the dominant interaction, though it is probably not the sole interaction which would result in a narrowing by a factor ~3.6 for $\eta = 0$. The crystal structure of $NaNbO_3$ is orthorhombic with again NbO_6 units sharing all their corners with other octahedra and the quoted bondlengths are 6 x 1.971Å[36]. However the unit

cannot be as symmetric as this since the quadrupole interaction would then be much smaller.

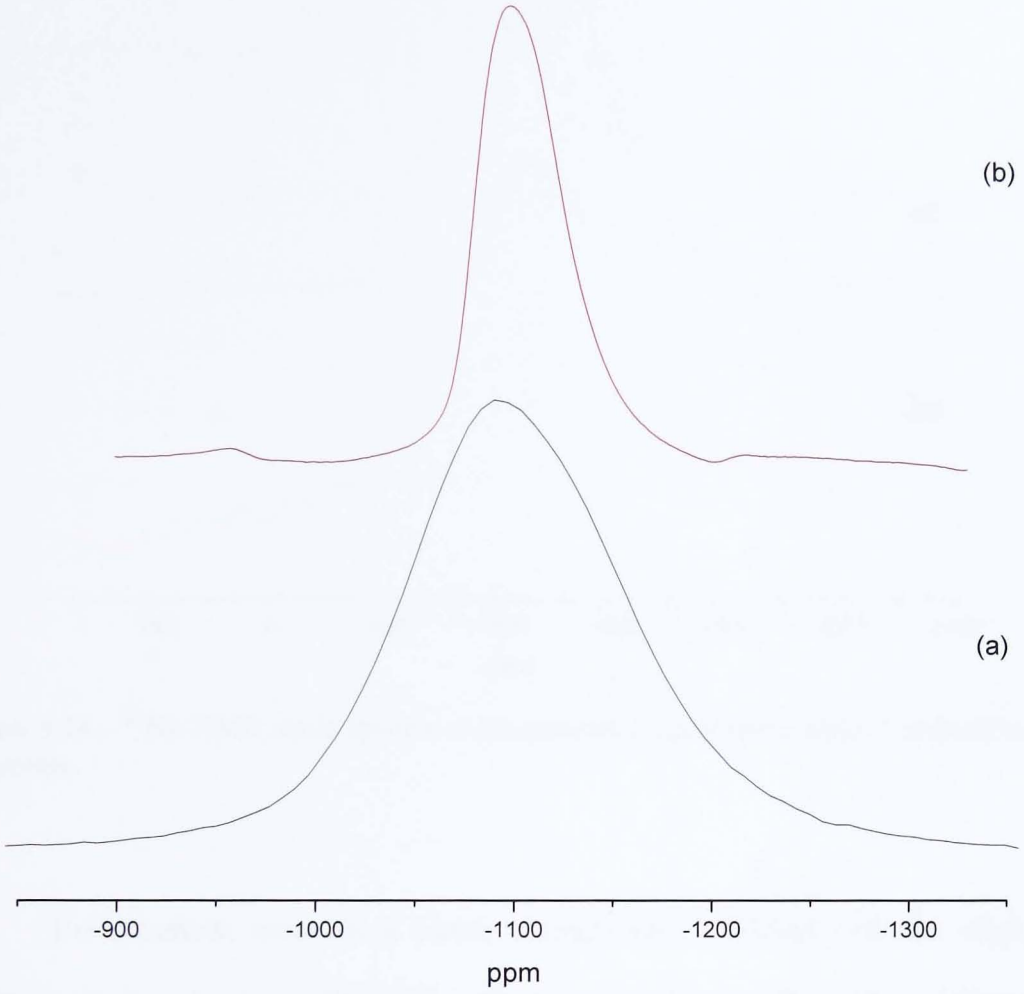

Figure 4.13 – ^{93}Nb NMR spectra of (a) sodium niobate static and (b) sodium niobate MAS

The static ^{93}Nb NMR spectrum from amorphous columbite (Figure 4.14 (a)) shows a relatively featureless lineshape with some asymmetry, typical of spectra of quadrupolar nuclei in an amorphous solid. Crystallising the sample as shown in Figure 4.14(b) into a single phase, highly crystalline sample shows a very different lineshape. The actual crystallisation is readily observed in the change of the lineshape from an effectively featureless line to the lineshape with distinct singularities.

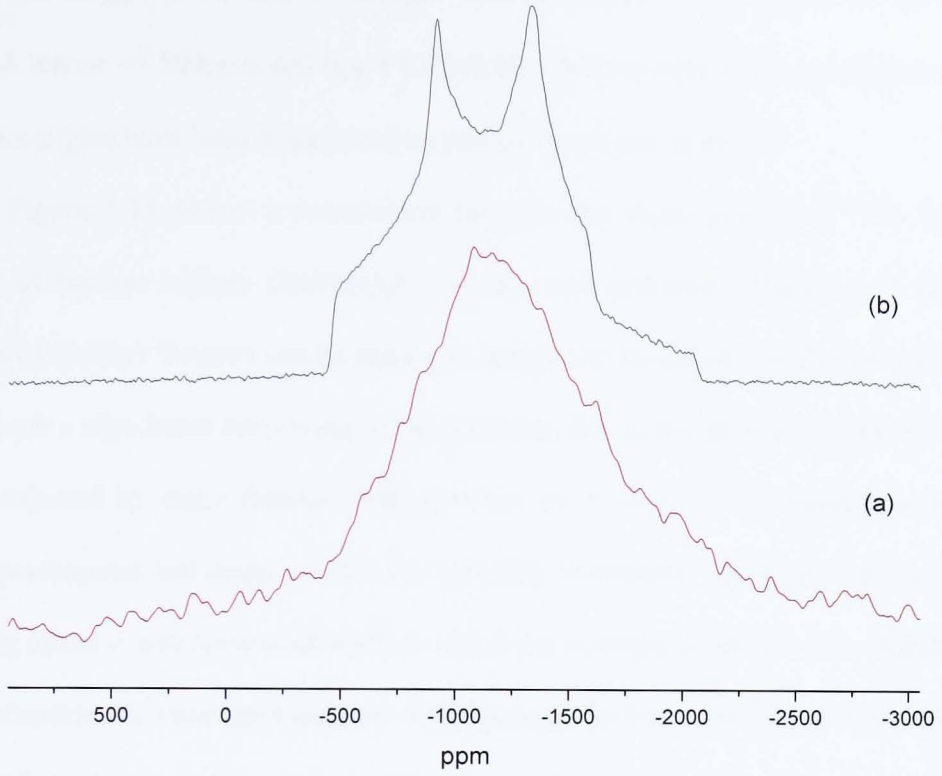

Figure 4.14 – ^{93}Nb NMR static spectra of (a) amorphous columbite and (b) crystalline columbite

The columbite spectrum is clearly a single site, consistent with the single niobium site in columbite. The NbO_6 units share an edge and form zig-zag chains along the c-axis, with octahedra in adjacent chains sharing corners to form double layers parallel to the bc plane[30]. The double layers are linked together along the [100] direction through MgO_6 units that also form zig-zag chains parallel to the c-axis. Despite the superficial appearance of being a straightforward lineshape, no set of quadrupolar parameters could come close to simulating this lineshape. Work subsequent to this thesis on this sample using lineshape analysis at four magnetic fields of 7.05, 9.4, 14.1 and 18.8 T allowed unambiguous determination of the NMR interaction parameters which indicated that chemical shift anisotropy is making a significant contribution to the static lineshape. The experimental parameters were

determined as χ_Q = 54.03±0.05MHz, η_Q = 0.23±0.05, δ_{iso} = –962±2ppm, the span of the CSA tensor = –509ppm and η_{CS} = 0.38±0.02. The two tensors are not aligned and the Euler angles have been determined as part of the on-going study.‡

Figure 4.15 shows a comparison between the static and MAS ^{93}Nb NMR spectra of barium niobate ($BaNb_2O_6$). In the static spectrum (Figure 4.15 (a)) a number of distinct features can be made out within the lineshape. In Figure 4.15 (b) we can see a significant narrowing of the spectrum due to the spinning, however it is still dominated by many features that probably are a result of overlapping second-order quadrupolar lineshapes in all the spinning sidebands. Even by varying the spinning speed it was somewhat unclear which the centreband feature was. $BaNb_2O_6$ is an orthorhombic structured material with space group Pmma and has pairs of edge-shared NbO_6 that then share corners with other such units in adjacent layers that form perpendicular to the c-axis[37,38]. It is probable that with this local environment that the quadrupole coupling is large and that the observed lineshapes, both MAS and static, are only partially excited and the features are singularities that are coming through. For a true lineshape analysis at a higher field, as well as forming the line by piecing the spectrum together from different frequency offsets would be necessary and it would be unwise to try and extract parameters from this data. However it illustrates that ^{93}Nb can show a wide range of interactions and care must be taken interpreting such spectra.

‡ This additional data was taken in collaboration with M.E. Smith as well as J.V. Hanna and K.J. Pike, ANSTO, Australia

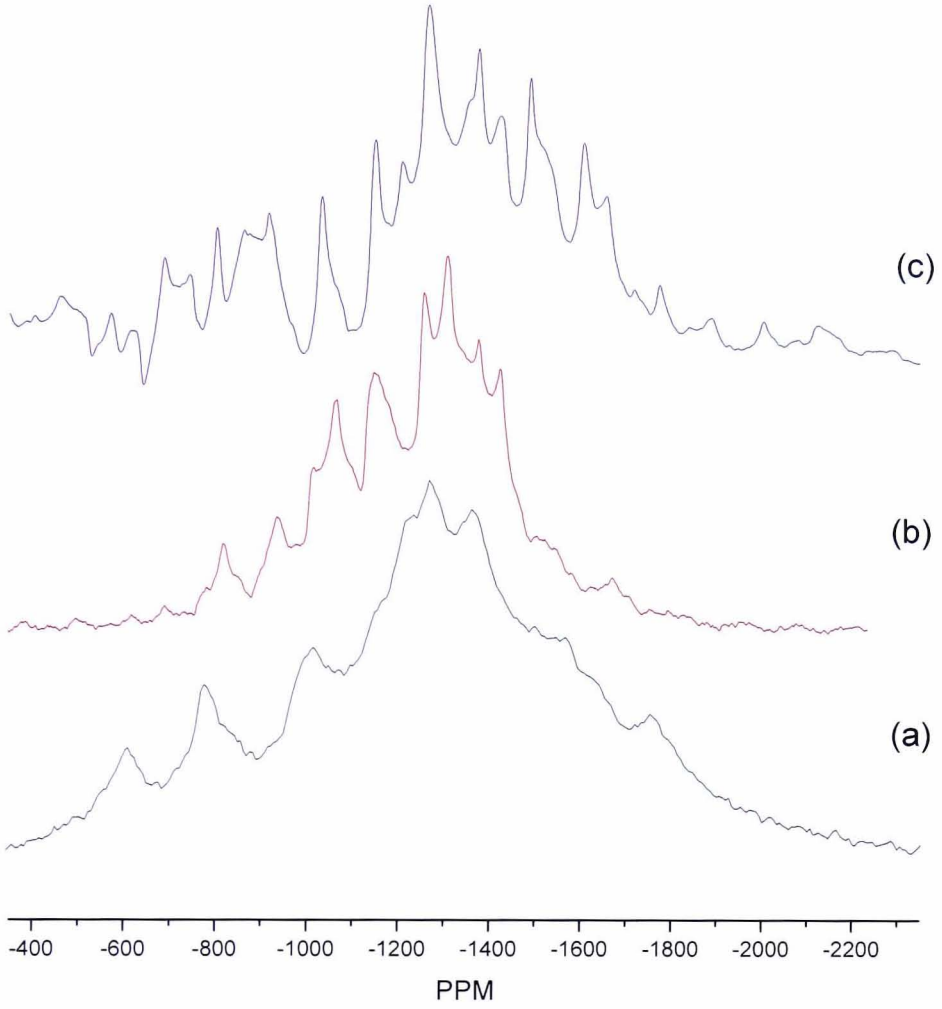

Figure 4.15 – ^{93}Nb NMR spectra of (a) barium niobate static, (b) barium niobate MAS and (c) zinc niobate MAS.

Similar observations about the ^{93}Nb experiencing large quadrupole interactions which then leads to a only partially excited lineshape making unwise to try and extract parameters can be made for zinc niobate. Figure 4.15 (c) shows the ^{93}Nb MAS NMR spectrum of zinc niobate ($ZnNb_2O_6$). This phase displays a (1:2) fully ordered columbite structure. It is orthorhombic (Pbcn) with the NbO_6 units sharing corners[39]. There is variation in the Nb-O bondlength of 1.83-2.27Å which is quite a strong variation and should give rise to a significant quadrupole interaction. From the spectrum it can be seen that zinc niobate produces a complex, very broad spectrum that begins to break up under the MAS rates available, but has a whole range of

spinning sidebands. The spectrum is consistent with a large quadrupole interaction although on the basis of this spectrum no value can be extracted.

Figure 4.16 (a) shows the spectrum for the perovskite barium zinc niobate, $BaZn_{0.33}Nb_{0.67}O_3$ (BZN). When the A-site cation is Ba^{2+}, 1:2 ordering of the two B site cations takes place along the [111] direction, whereas the ordering is 1:1 when the A-site is occupied by a Pb^{2+} cation. Generally Ba-based perovskites have a higher order-disorder transition temperature than Pb-based perovskites. The ^{93}Nb MAS NMR spectrum, of a phase similar to the PMN type of phase at the core of this thesis is much narrower at only ~11 kHz than many of the other model compound phases examined here. There is some structure in the spectrum with the main peak at –940ppm with the shoulder at –980ppm, which could be indicative of different niobium next nearest environments in the perovskite structure. The shift range observed here for an NbO_6 is entirely consistent with the shift range recently outlined for such units[34].

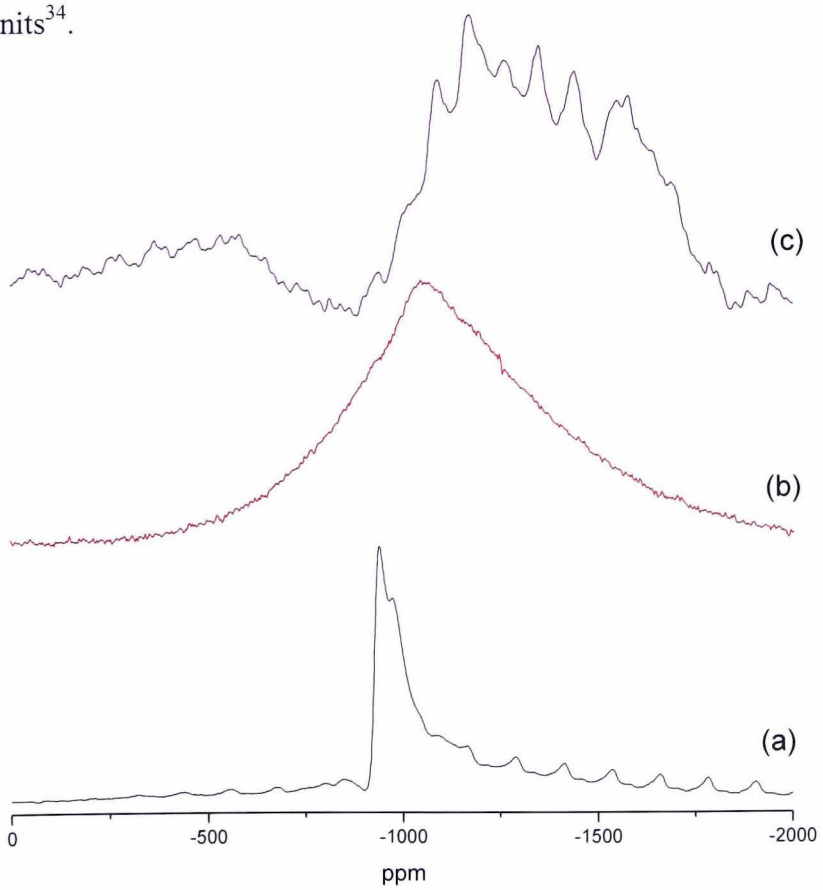

Figure 4.16 - ^{93}Nb MAS NMR of (a) $BaZn_{0.33}Nb_{0.67}O_3$, and sol-gel produced PSN (b) as-prepared and (c) heated to 1000°C.

The spectrum from unheated, as-prepared PSN ($PbSc_{0.5}Nb_{0.5}O_3$, Figure 4.16 (b)) shows a single broad line (~520ppm) at −1055ppm. Then when heated to 1000°C (Figure 4.16 (c)) the main peak is a very similar position at −1096ppm, but is slightly broader (~580ppm) and shows some structure. At room temperature PSN takes on a rhombohedral R3m structure with unit cell parameters a = 4.080Å and α = 89.89° which results in a relatively symmetric local environment for the NbO_6 units. The shift of PSN-rich compositions reported in PMN-PSN materials is at −970ppm[41]. In PSN the B cations could show varying degrees of order at the next, next nearest neighbour level perhaps causing the different shifts observed.

4.3.3 Discussion of ^{93}Nb NMR of Model Niobates

It can immediately be recognised that the large magnetic moment, 100% natural abundance and spin-9/2 means that a strong NMR signal is usually obtained for ^{93}Nb. However there is a very wide variation in the magnitude of the quadrupole interaction that niobium can experience. Hence even relatively fast MAS at 14.1 T could produce modest narrowing with very complex spectra with many sidebands as exemplified here by $BaNb_2O_6$ and $ZnNb_2O_6$. These spectra would need to be run at higher field with faster spinning, as well as potentially combining with static spectra perhaps even accumulated with different frequency offsets. Hence no detailed information about the quadrupole interaction has been possible. However for $MgNb_2O_6$ a lineshape that revealed both chemical shift anisotropy (CSA) and quadrupole interactions were present and it seems that in static ^{93}Nb NMR spectra CSA can play a significant role and should always be considered.

The shifts extracted here supplement the data recently presented by Lapina *et al.*[34] and add weight to the proposition that there is a distinct change of shift with

coordination. Figure 4.17 shows the shift scale proposed in ref. 34 and adds the shifts determined here where there is a high degree of certainty. On the basis of this data, the isotropic chemical shift for niobium should be able to identify unknown coordinations in materials. The ^{93}Nb NMR results of other complex systems also show similar shifts with in niobia-sodium phosphate glasses the peak shifts from −1100 to −1500 ppm as the NbO_6 changes from edge- to corner-sharing[42]. In the NbO_6 units in phase separated Nb_2O_5-SiO_2 sol-gel formed samples peaks were observed at −1300ppm[43]. Hence the values observed are at the lower end of the shift scale and are associated with more isolated NbO_6 units.

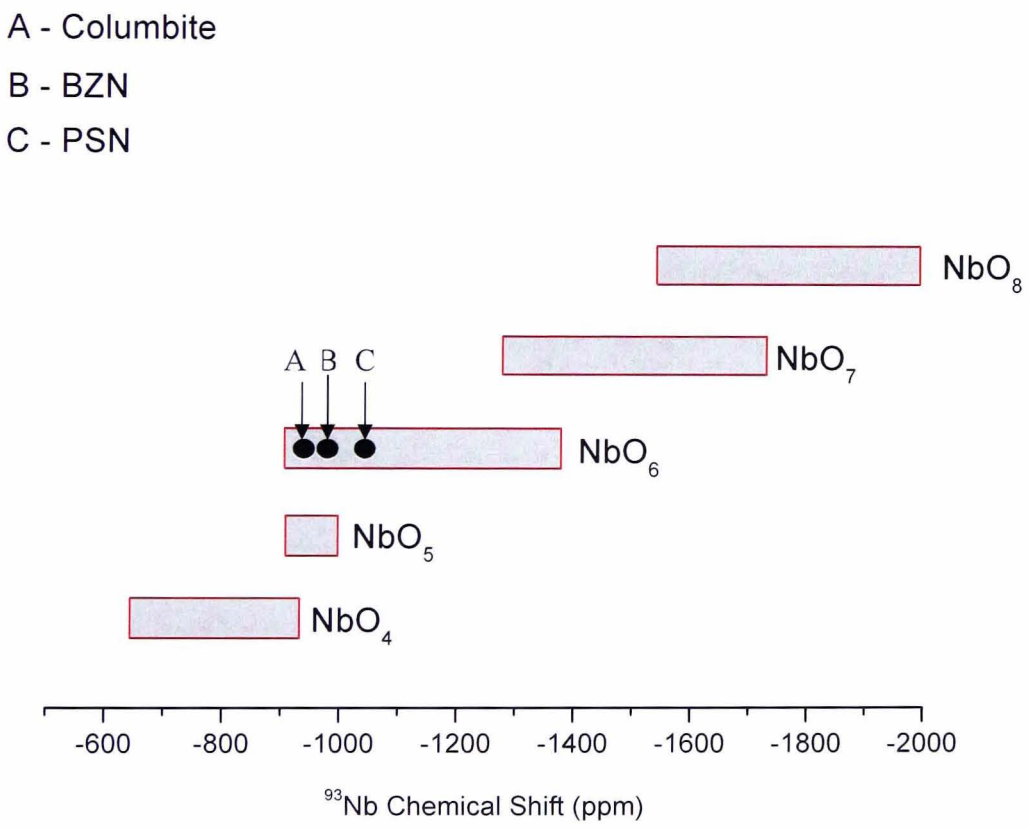

Figure 4.17 - ^{93}Nb chemical shift ranges of NbO_x units as proposed in reference [34] with the new data points added from this study.

In the BZN there is relatively small quadrupole interaction and consequently narrow spectral line for ^{93}Nb. In the spectrum there was a hint of multiple peaks which is similar in form to that observed from PMN-PSN solid solutions[41]. It could be that these are differing numbers of zinc and niobium next nearest neighbours indicating that ordering is not perfect, since if the ordering was perfect there would be one such configuration. PSN should also have a single environment, but the indication given from the ^{93}Nb spectrum is that there are multiple peaks from the 1000°C heat treated sample suggesting that ordering is still incomplete.

4.4 ^{45}Sc NMR Studies of Sol-Gel Prepared PSN

Scandium-45 is 100% naturally abundant, with a nuclear spin of 7/2 and only a moderate quadrupole moment. It also has a mid-range resonance frequency of 146.02 MHz at 14.1T so should be quite promising for solid-state NMR studies with a receptivity of 1780 compared to ^{13}C. Despite this there have been very few papers published concerning solid state ^{45}Sc NMR especially of inorganic solids. There has been a report from Sc_2O_3[44] and from zeolites[45]. From a range of local scandium coordination environments two recent papers have determined ^{45}Sc quadrupole interactions of 1.6 to 23.4 MHz[46,47]. It was also suggested that the isotropic chemical shift could distinguish different local coordinations[47].

Laguta recently published some ^{45}Sc NMR from a single crystal of PSN.[48,49] At 420K detailed analysis revealed three components above the phase transition with χ_Q values 8.8-10.6 MHz. The different resonances were attributed to ordered/disordered regions within the crystal. On cooling below the transition the

width of the resonances steadily grew, presumably due to increases in χ_Q, although ref. 47 did not extract a χ_Q value in this region.

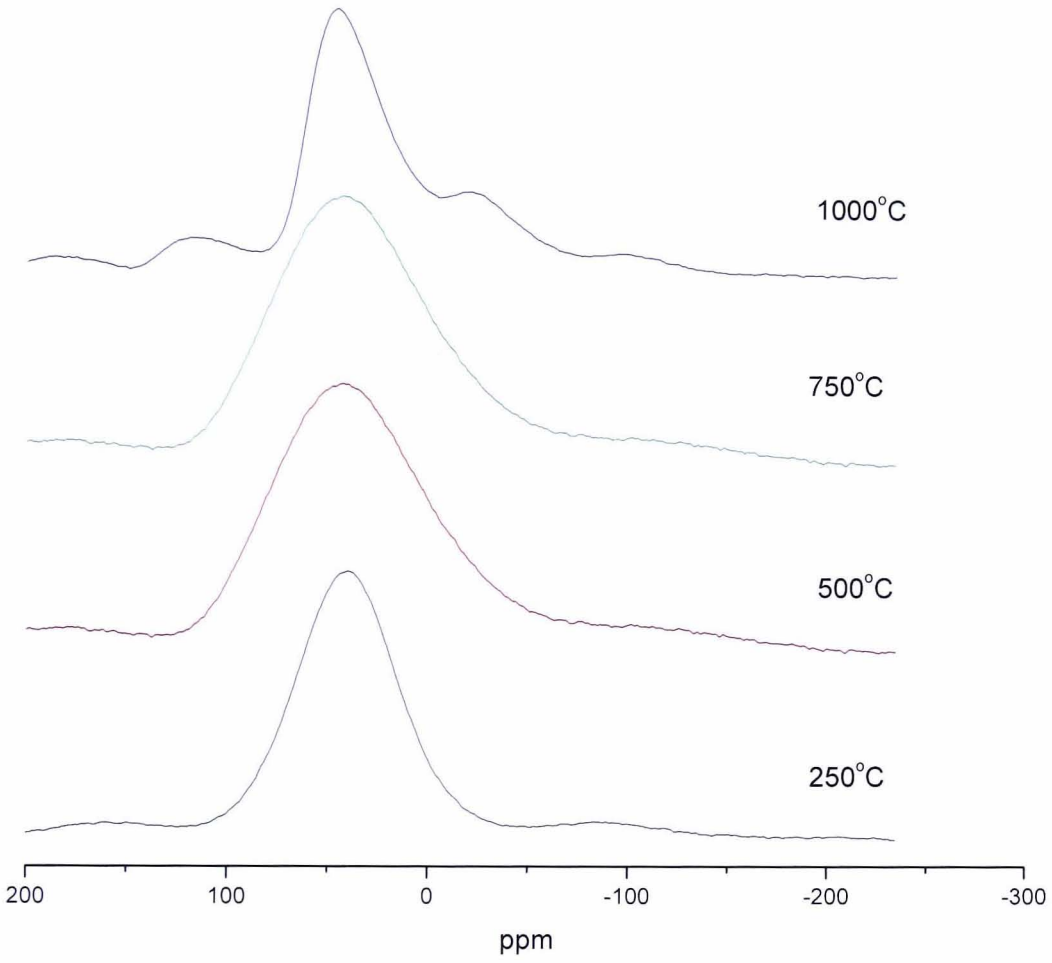

Figure 4.18 - ^{45}Sc MAS NMR spectra of sol-gel prepared PSN at (a) 250°C, (b) 500°C, (c) 750°C and (d) 1000°C

Sample	^{45}Sc NMR at 14.1T	
	Position (ppm)	Width (ppm)
250°C	41	56
500°C	44	81
750°C	46	86
1000°C	48	44

* Errors: Peak Position ± 2ppm, Widths ± 2 ppm

Table 4.8 – ^{45}Sc NMR data of sol-gel prepared PSN at 250°C, 500°C, 750°C and 1000°C giving the peak position and the linewidth.

Figure 4.18 shows the effect of heating on the ^{45}Sc MAS NMR spectra for sol-gel prepared PSN (whose ^{17}O MAS NMR spectra have been shown in figure 4.8). Good signal-to-noise is obtained. The peak does not show any really significant variation with a small increase in the peak position from 41 to 48ppm. The linewidth shows a more significant variation, starting off at 56ppm and then after intermediate heat treatments increases to ~85ppm probably indicating a more distorted/disordered intermediate state. After heating to 1000°C the line is narrower, which is a result of the crystallisation that has occurred in the sample. It can immediately be stated that the ^{45}Sc MAS NMR is strongly suggestive of a single scandium environment. This linewidth can be used to place an upper estimate on the quadrupole interaction which is $\chi_Q < 11.4$MHz. Hence the maximum isotropic chemical shift from the peak position and this upper estimate for χ_Q is 56ppm.

The shift at 56ppm puts it between ScO_8 and ScO_6, but closer to the ScO_6 position which agrees with the perovskite structure. The upper limit on the χ_Q value of 11.4 MHz is consistent with the linewidth observed by Laguta. However the spectrum obtained here is consistent with a single scandium site. The three signals observed by Laguta were assigned to regions with differing order and orientation in the single crystal. This might be averaged in a powder sample, but needs further investigation.

4.5 Conclusions and Further work

^{17}O MAS NMR has proved to be an effective probe of many oxide phases, a view that this chapter reinforces, but there may be some significant limitations in using it to observe the metal ordering in the ferroelectric relaxor phases. The new data from the three sol-gel formed pure oxides confirmed the view that subtle

differences in the formation mechanisms occur and that there is no single structural evolution mechanism for oxide sol-gel formation. Niobia starts off with the same two coordinations as the final crystalline oxide. As heat treatment progresses, these two environments change their relative intensity before readjusting to the equilibrium distribution. In contrast In_2O_3 starts off with a hydroxide/oxyhydroxide/mixed alkoxide environment until quite high temperature before the final oxide environment forms. Sc_2O_3 is a further contrast showing the single oxygen coordination that is present in the final oxide forming in the very initial stages and persisting throughout the heat treatment. This single peak is dominant throughout the formation, the first time this has been observed for a single site oxide; all others showing multiple oxygen coordinations in the amorphous state and evolving to a single oxygen site.

The more complex oxide phases that were ^{17}O-enriched and are more closely related to the PMN-PT system indicated that ^{17}O may have some limitations in providing clear insight into atomic ordering in such systems. Columbite showed 3 sharp oxygen signals and these could be assigned to the three different oxygen coordinations. The fact that three evenly spaced resonances were not observed suggests that in ferroelectric relaxor phases that can have atomic disorder and hence several sites it is likely that the resonances will be closely spaced. This appears to be the case for PSN where the local coordinations of Nb-O-Sc and Nb-O-Nb (with constant numbers of lead nearest neighbours) are not clearly separated.

^{93}Nb NMR has shown that whilst spectra can be readily collected there is a huge range of quadrupole interactions some of which can be very large. This means that while signal can be strong it can be highly distorted and not possible to extract accurate NMR interaction parameters. Some new parameters were collected and

shown that the recently proposed chemical shift scale for ^{93}Nb by Lapina looks robust with a good correlation of the isotropic chemical shift and coordination number that should allow identification of unknown local niobium environments. In materials where the quadrupole interaction is small enough that different environments can be resolved the shift of different next nearest neighbours can be picked up. The suggestion here is that there may be some atomic disorder in BZN. For improved ^{93}Nb data higher magnetic fields and very fast spinning would help the clarity of the spectra. Recently it has been proposed that for a spin-9/2 system the (±5/2,±3/2) satellite transition should be observed as the second-order quadrupolar broadening is only 1/18 that of the central transition providing much improved resolution[50]. For niobium such an approach would be highly useful applied to these materials to distinguish different sites.

A strong ^{45}Sc NMR signal was obtained from sol-gel prepared PSN that narrows as crystallisation occurs. The data indicates that there is a single scandium environment with an upper estimate for χ_Q of 11.4 MHz. This is consistent with the ^{45}Sc NMR of single crystal studies by Laguta *et al.*[48,49] where three different domains were detected. It is not clear yet how to completely reconcile the observation of a single environment here with the multiple domains observed by Laguta *et al.*

References

[1] A.E. Geissberger, P.J. Bray, *Bull. Am. Ceram. Soc.*, 60, 408 (1981)

[2] T.J. Bastow, S.N. Stuart, *Chem. Phys.*, 143, 459 (1990)

[3] V.W. Day, T.A. Eberspracher, W.G. Klemperer, C.W. Park, *J. Amer. Chem. Soc.*, 115, 8469 (1993)

[4] T.J. Bastow, A.F. Moodie, M.E. Smith, H.J. Whitfield, *J. Mater. Chem.*, 3, 697 (1993)

[5] G.A. Pzarnsky, A.V. McCormick, *J. Mater. Chem.*, 4, 1749 (1994)

[6] P. Florian, D. Massiot, G. Humbert, J.P. Coutures, *Comptes Rendues Acad. Sci. Paris, Série II*, 320, 99 (1995)

[7] T.J. Bastow, M.E. Smith, H.J. Whitfield, *J. Mater. Chem.*, 6, 1951 (1996)

[8] A.V. Chadwick, I.J.F. Poplett, D.T.S. Maitland, M.E. Smith, *Chem. Mater.*, 10, 864 (1998)

[9] D.M. Pickup, G. Mountjoy, M.A. Holland, G.W. Wallidge, R.J. Newport, M.E. Smith, *J. Mater. Chem.*, 10, 1887 (2000)

[10] T.J. Bastow, P.J. Dirken, M.E. Smith, H.J. Whitfield, *J. Phys. Chem.*, 100, 18539 (1996)

[11] M.A. Holland, D.M. Pickup, G. Mountjoy, E.S.C. Tsang, G.W. Wallidge, R.J. Newport, M.E. Smith, *J. Mater. Chem.*, 10, 2495 (2000)

[12] D.M. Pickup, G. Mountjoy, G.W. Wallidge, R.J. Newport, M.E. Smith, *Phys. Chem. Chem. Phys.*, 9, 2527 (1999)

[13] H.K.C. Timken, G.L. Turner, J.P. Gilson, L.B. Welsh, E. Oldfield, *J. Amer. Chem. Soc.*, 108, 7231 (1986)

[14] U.-T. Pingel, J.P. Amoureux, T. Anupõld, F. Bauer, H. Ernst, C. Fernandez, D. Freude, A. Samoson, *Chem. Phys. Lett.*, 294, 345 (1998)

[15] D. Freude, T. Loeser, D. Michel, U.T. Pingel, D. Prochnow, *Solid State Nucl. Mag. Reson.*, 20, 46 (2001)

[16] S. Wang, J.F. Stebbins, *J. Non-Cryst. Solids*, 231, 286 (1998)

[17] G.W. Wallidge R. Anderson, G. Mountjoy, D.M. Pickup, P. Gunawidjaja, R.J. Newport, M.E. Smith, *J. Mater. Sci.*, 39, 6743 (2004)

[18] E.R.H. van Eck, M.E. Smith, *J. Chem. Phys.*, 108, 14 (1998)

[19] D. Brown, *In The Chemistry of Niobium and Tantalum; Comprehensive Inorganic Chemistry Series*, Pergamon Press: Oxford, 1973; Vol. 3, p 553.

[20] B. Julian, C. Gervais, M.N. Ranger, J. Macquet, E. Cordoncillo, P. Escribano, F. Babonneau, C. Sanchez, *Chem. Mater.*, 16, 521 (2004)

[21] E. Oldfield, C. Coretsopoulous, S. Yang, L. Reven, H.C. Lee, J. Shore, O.C. Han, E. Ramli, *Physical Review B*, 40, 6832 (1989)

[22] A.V. Chadwick, G. Mountjoy, V.M. Nield, I.J.F. Poplett, M.E. Smith, J.H. Strange, M.G. Tucker, *Chem. Mater.*, 13, 1219 (2001)

[23] E. Scolan, C. Magnenet, D. Massiot, C. Sanchez, *J. Mater. Chem.*, 9, 2467 (1999)

[24] F. Ali, M.E. Smith, S. Steuernagel, H.J. Whitfield, *J. Mater. Chem.*, 6, 261 (1996)

[25] W.G. Klemperer, D.L. Richards, *Solid State NMR Spec. Inorganic Mater.*, 717, 256 (1999)

[26] G. Neue, C. Dybowski, M.L. Smith, M.A. Hepp, D.L. Perry, *Solid State Nucl. Mag. Reson.*, 6, 241 (1996)

[27] J. Brieger, R. Merkle, H. Bertagnolli, K. Muller, *Phys. Chem.*, 102, 1376 (1998)

[28] A. Baldwin, P.A. Thomas, R. Dupree, *J. Phys.: Condens. Matter*, 17, 7159 (2005).

[29] K.S. Knight, K.Z. Baba-Kishi, *Ferroelectrics*, 175, 341 (1995)

[30] S. Pagola, R.E. Carbonio, J.A. Alonso, M.T. Fernandez-Diaz, *J. Solid-State Chem.*, 134, 76 (1997)

[31] S. Prasad, P. Zhao, J. Huang, J.J. Fitzgerald, J.S. Shore, *Solid State Nucl. Mag. Reson.*, 19, 45 (2001)

[32] L.-S. Du, R.W. Schurko, N. Kim, C.P. Grey, *J. Phys. Chem. A*, 106, 7876 (2002)

[33] R.T. Hart, M.A. Anspach, B.J. Kraft, J.M. Zaleski, J.W. Zwanziger, P.J. DeSanto, B. Stein, J. Jacob, P. Thiyagarajan, *Chem. Mater.*, 14, 4422 (2002)

[34] O.B.Lapina, D.F. Khabibulin, K.V. Roamnenko, Z. Gan, M.G. Zuev, V.N. Krasil'nikov, V.E. Fedorov, *Solid State Nucl. Magn. Reson.*, 28, 204 (2005)

[35] L.P. Cruz, J. Rocha, J.D. Pedrosa de Jesus, J.M. Savariault, J. Galy, *Solid State Nucl. Mag. Reson.*, 15, 153 (1999)

[36] R. Hsu, E.N. Maslen, D. Du Boula, N. Ishizawa, *Acta Crystallogr. B*, 53, 420 (1997)

[37] M.H. Francombe, *Acta Cryst.*, 13, 131 (1960)

[38] F. Galasso, G. Layden, G. Ganug, *Mater. Res. Bull.*, 3, 397 (1968)

[39] M. Waburg and H. Müller-Buschbaum, *Z. Anorg. Chem.*, 508, 55 (1984)

[40] K.S. Knight and K.Z. Baba-Kishi, *Ferroelectrics*, 173, 341 (1995)

[41] G.L. Hoatson, D.H. Zhou, F. Fayon, D. Massiot, R.L. Vold, *Phys. Rev. B*, 66, 224103 (2002)

[42] A. Flambard, L.Montagne, L. Delevoye, G. Palavit, J.P. Amoureux, J.-J. Videau, *J. Non-Cryst. Solids*, 345-346, 75 (2004)

[43] K.O. Drake, D. Carta, L.J. Skipper, F.E. Sowrey, R.J. Newport, M.E. Smith, *Solid State Nucl. Magn. Reson.*, 27, 28 (2005)

[44] D. Riou, F. Fayon, D. Massiot, *Chem. Mater.*, 14, 2416 (2002).

[45] C.T. Brigden, D. Thompsett and C.D. Williams, *Dalton Trans.* (2004), 2829

[46] A.J. Rossini and R.W. Schurko, *J. Am. Chem. Soc.* 128, 10391 (2006)

[47] N. Kim, C.-H. Hsieh and J.F. Stebbins, *Chem. Mater.* 18, 3855 (2006)

[48] V.V. Laguta, M.D. Glinchuk, S.N. Nokhrin, I.P. Bykov, R. Blinc, A. Gregorovič, B. Zalar, *Phys. Rev. B*, 67, 104106 (2003)

[49] V.V. Laguta, M.D. Glinchuk, I.P. Bykov, R. Blinc, A. Gregorovič, B. Zalar, *Phys. Rev. B*, 69, 054103 (2004)

[50] J.P. Amoureux, J. Trébosc, *J. Magn. Reson.*, 180, 311 (2006)

Chapter Five

5.1 Introduction

The interesting and novel properties of the important ferroelectric relaxor materials PMN-PT were introduced in Chapter 1, indicating the necessity of a more detailed investigation into these complicated materials. Key is probably understanding the Morphotropic Phase Boundary (MPB) and the phase transition diagrams for both the entire compositional range and the MPB region, and if possible also the understand the local atomic structure. This chapter starts by describing in a little more detail the possible mechanisms behind the phase transitions in such relaxor ferroelectrics (section 5.2) before discussing previous NMR studies of PMN-PT and another similar relaxor ferroelectric material PMN-PSN (section 5.3). Then our own results are presented from the NMR studies of the NMR active nuclei in PMN-PT, i.e. ^{93}Nb, ^{207}Pb and ^{17}O. ^{93}Nb proves to be the most informative here and the intensity distribution is modelled in detail. From this some tentative suggestions as to the nature of the MPB, particularly its diffuse nature, are advanced.

5.2 MPB and Phase Transitions in PMN-PT materials

The first description of the MPB in PMN-xPT materials was given in a paper by Ouichi *et al.*[1], their plot of the Curie temperature against composition shows the presence of an almost vertical line at around x=0.4, which separates the pseudocubic phase from the tetragonal phase. This is the MPB, it is prevalent in a host of similar ferroelectric materials such as PZT and PZN-PT, it is characterised by a distinct

change of phase with composition that is almost entirely independent of temperature.

The MPB region in ferroelectric materials is of particular technological interest as it is around these compositions that these materials show a large increase in piezoelectric activity. This is often attributed to extrinsic contributions such as coexistence of different phases around the MPB[2], or the motion of ferroelectric domain walls.

In an important theoretical study, Vanderbilt and Cohen[3] used an extension of the Devonshire theory[4] to the eighth order so as to derive a description of the phases present in ferroelectric relaxors. Their theory predicts the presence of not one but three types of monoclinic phases in these materials and defines the nature of the boundaries between these phases. However the areas for both the theoretically predicted M_C and M_B phases are both relatively small in comparison to the M_A phase so will probably be extremely hard to detect experimentally in a complicated system like PMN-PT.

Some of the first experimental research into the MPB[5] indicated that the region must at least be a two-phase region as the rhombohedral (*R3m*) and the tetragonal (*P4mm*) phases are not group/subgroup related, thereby requiring a first-order phase transition to occur which is not the case. This therefore implies that the transition must occur via an intermediate phase. Noheda *et al.*[6] discovered that in PZT ($PbZr_{(1-x)}Ti_xO_3$) there exists an intermediate monoclinic phase Cm (M_A) at the MPB. If such a phase could be conclusively shown to exist in PMN-PT it would provide the most suitable explanation of the transformation of the rhombohedral phase to the tetragonal phase via the intermediate monoclinic phase. Thus a host of separate studies Ye *et al.*[7], Xu *et al.*[8], Singh and Pandey[9] and Noheda *et al.*[10] began a thorough examination of the phases around the MPB region culminating in the phase

diagram shown on Fig 1.9 (p14). It is important to note that the symmetry of the intermediate monoclinic phase in PMN-PT Pm (M_C) differs from that found in the PZT system (M_A). However the discovery of this M_C phase still does not provide an adequate explanation of the mechanism for the R – T phase transition as it is not sub-group related to either the rhombohedral or tetragonal phases.

Diffraction experiments by Guo *et al.*[11] on PZT ceramics have demonstrated the direct link between the monoclinic phase and the high electromechanical deformations due to the rotation of the polarisation between the [111] and [001] directions as also theoretically predicted by Fu and Cohen[12]. Thus in conventional ferroelectric phases of tetragonal $PbTiO_3$ and $BaTiO_3$ the polarisation vector points along the [001] and [111] directions respectively. However the monoclinic symmetry in PMN-PT near the MPB allows the polarisation vector a greater degree of freedom as it is only constrained to lie within a monoclinic plane defined by the pseudo-cubic [001] and [111] direction, that is the (110) plane. Hence as the polarisation direction can more easily adjust to the electric field it naturally results in a larger piezoelectric response. Thus it is the presence of this intermediate monoclinic phase, which allows the polarisation to rotate within the mirror plane under the application of an electric field, resulting in very high deformations or giant piezoactivity.

In a recent high-resolution X-ray diffraction study, Singh and Pandey[13] showed the presence of not one, but two monoclinic phases around the MPB in PMN-PT ceramics. One monoclinic phase of space group *Cm* (M_A) is believed to be stable in the composition range $0.27 \leq x \leq 0.3$ whilst the other monoclinic phase of space group *Pm* (M_C) exists in the range $0.31 \leq x \leq 0.34$ while it is the usual tetragonal (*P4mm*) and rhombohedral (*R3m*) phases above and below these regions respectively. This may help to explain why differences in symmetry were observed between the

intermediate monoclinic phase M_A discovered in PZT, and the monoclinic phase M_C observed by Noheda *et al.*[10] in PMN-PT materials.

One of the latest concepts regarding ferroelectric phases stems from the work of Ohwada *et al.*[14] Using neutron scattering data on a single crystal of PZN-8PT they suggest the presence of a low temperature phase in the PZN-xPT family that is not rhombohedral, but has an average cubic structure. They have termed this new phase "phase X". Thus though the phase structure of phase X is on average cubic, the true symmetry of this phase is still unknown. This phase was also experimentally confirmed by the work of Xu *et al.*[15] who further showed the existence of an outer layer, that has a structure that is different from that of the bulk, thus explaining why there may be discrepancies between earlier X-ray powder diffraction and recent neutron and high energy X-ray scattering results. The most recent work by Xu *et al.*[16] proposes that the lattice in PMN-xPT is indeed cubic on average yet has confined regions of ferroelectric polarisation where the phase is rhombohedral. Thus they claim that phase X is simply a special form of confined rhombohedral phase. In fact the electric field studies conducted by Ohwada *et al.*[14] also show that phase X always transforms into the M_A phase first with increasing field, following the polarisation rotation path of R – M_A – M_C – T, indicating a {111} rhombohedral type of polarisation in phase X. They have also proposed a modified phase diagram of the PMN-xPT system, which is reproduced in Figure 5.1

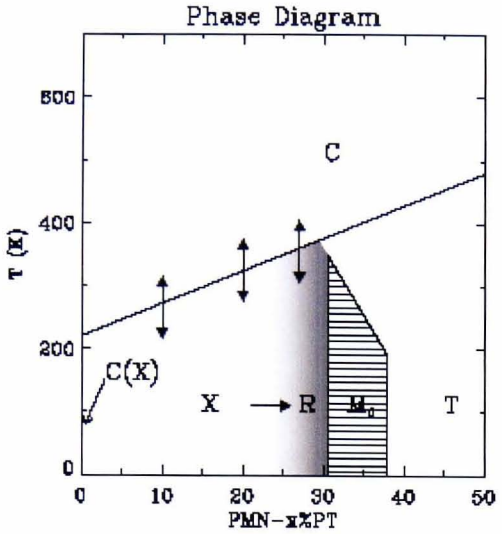

Figure 5.1- Schematic of revised phase diagram of PMN-xPT in zero field. The arrows indicate compositions that have been studied using high q-resolution neutron scattering techniques. Xu *et al.*[16]

5.3 Previous NMR studies of PMN-PT and related materials

It is important that a thorough understanding of prior NMR studies of PMN-PT and related materials is obtained, in order to provide a good foundation on which our own results on PMN-PT can be analysed. In this section some key NMR papers on PMN-PT and closely related materials such as $(1-x)Pb(Mg_{1/3}Nb_{2/3})O_3 - xPb(Sc_{1/3}Nb_{2/3})O_3$ (PMN-PSN) are discussed in order to provide insight into our own methodology and put our own work in context. The section has been divided into two main sections the first detailing the ^{207}Pb NMR studies while the latter discusses the ^{93}Nb NMR studies. It is interesting to note at this stage that no other published work has been found related to ^{17}O NMR on such phases.

5.3.1 ^{207}Pb NMR studies of PMN-PT and related materials

One of the first NMR papers published on PMN-PT materials was by Blinc *et al.*[17] which discusses the local structure of PMN based on the solid state NMR studies of a single crystal of pure PMN. The microscopic model they used to discuss relaxor polarisation consists of "soft" polar nanoregions (PNRs) or what they refer to as polar clusters with unit cells that can freely choose several different directions, while the direction of the total moment of the nanoregions remain the same. Using such an approach has allowed them to apply a standard spherical model to relaxor ferroelectrics and is in fact very similar to the actual spherical random bond random field model (SRBRF) proposed by Pirc *et al.*[18] to explain their NMR data. In this SRBRF model, the correlated motion of the various B^{I} and B^{II} ions gives rise to reorientable polar clusters. These polar clusters are also dynamic entities embedded in a polarisable matrix, they can vary both in size and orientation of the local polarisation. In the SRBRF model the order parameter field, is described as a continuous vector of variable length, which is also associated with the dipole moment of interacting reorientable polar clusters.

The ^{207}Pb NMR spectra were acquired using a spin–echo Fourier transform sequence measured in a wide bore magnet with the ν_L(Pb) being 79.4 MHz using a single crystal of pure PMN at 9.1T. The line shape is approximately Gaussian and its FWHM is 30kHz at 400K. They also point out that there is a significant increase in linewidth to 150kHz as the sample is cooled to 15K. They suggest that this large line width arises from a distribution of isotropic chemical shifts due to substitutional disorder. They also note that the local polarisation is very small and the local structure is approximately cubic. However since the spectral lineshape is not powder

like and has no singularities, there is a distribution of polar clusters characterised by a local polarisation that varies in both orientation and magnitude.

In conclusion they go on to suggest that as both the A site (^{207}Pb) and the B site (^{93}Nb) show frequency distributions, they can be accurately described by their SRBRF model reflecting the existence of polar clusters. This enables them to also categorise PMN itself as a "spherical glass" material rather than a dipolar glass material. They mention that the ^{207}Pb NMR spectra reflect the distribution of the anisotropic ^{207}Pb chemical shift tensors, while their ^{93}Nb NMR spectra show the distributions of the off centre shifts of the ^{93}Nb ions. Furthermore they go on to state that they believe that in PMN, the relaxor does not consist of static PNRs embedded in a non polar cubic matrix. They believe that there is a dynamic distribution of PNRs with variable orientation and magnitude of the local polarisation, which varies in time so that the NMR spectrum observed, is indeed simply the average spectrum over the NMR time scale. This may provide a suitable explanation as to why such PNRs may appear static on a neutron diffraction time scale of 10^{-12}s yet may appear as dynamic entities in the NMR time scale of 10^{-4}s where they appear, exist for a certain amount of time, disappear and reappear in a different form.

5.3.2 ^{93}Nb NMR studies of PMN-PT and related ferroelectric materials

The first report regarding ^{93}Nb NMR of PMN-PT materials appeared relatively recently in a paper by Cruz *et al.*[19] In this paper Cruz and co-workers performed 3Q MAS NMR on PMN. The spectra were recorded on a 9.4 T Bruker spectrometer with the sample spinning at a 32 kHz rate. From their spectra it was observed that PMN has two distinct peaks, a sharp resonance at 320ppm and a broad peak at 218ppm. They also assigned a large quadrupolar-coupling constant (C_Q) in excess of 20MHz to this broad peak. In order to explain these peaks they propose a tentative attribution suggesting that the niobium in regions exhibiting a 1:1 ordering of B-site cations led to the sharp peak at 320ppm, while the broad peak is a result of niobium present in a 'sea' like environment as illustrated in Figure 5.2 reproduced below.

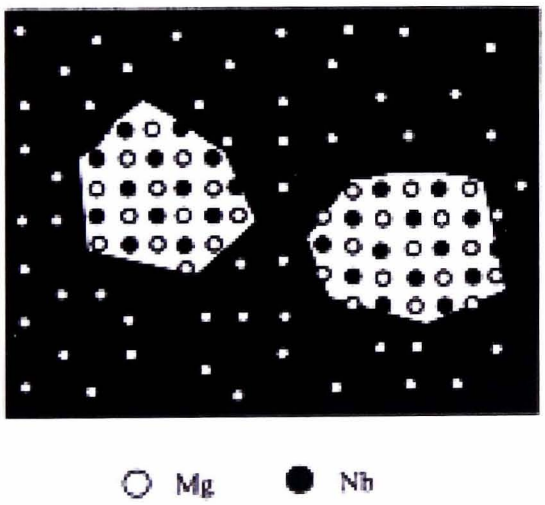

Figure 5.2 - PMN nanostructure showing regions with 1:1 ordering of the B-site cations[19]

One of the first papers that investigated a range of compositions of PMN-PT ceramic samples was that of Fitzgerald *et al.*[20], in which they undertook both static,

MAS and nutation ^{93}Nb NMR studies of a series of polycrystalline PMN-PT samples at 14.1T. From their interpretation of the MAS nutation studies in pure PMN they determined the presence of 3 niobium sites, a sharp resonance at around –902ppm and two overlapping broad resonances centred around –980ppm. They explain these three types of Nb(V) B-sites in PMN as due to differing Nb-O environments as a result of the different B-site Mg/Nb configurations. These 3 different Nb(V) sites are assigned to a range of B-site Mg/Nb configurations with local cubic, axial and rhombic symmetry and have been assigned quadrupolar coupling constants of 0.8, ~17 and >62 MHz respectively. Thus PMN has a range of three distinct types of distorted NbO_6 octahedra, with the atomic level Mg/Nb disorder causing the local Nb(V) B site regions to show differing microscopic dipolar behaviour. They believe that these distinct B-sites may account for the diffuse nature of the macroscopic phase transitions observed in PMN.

They also went on to study 7 further PMN-PT samples (PMN-5PT, PMN-10PT, PMN-15PT, PMN-20PT, PMN-25PT, PMN-34PT, and PMN-50PT) however what is interesting in the interpretation of these spectral results is that there is a gradual decrease in intensity of the sharp line at around -902ppm as the amount of Ti(IV) ions increase. This is explained by a reduction in symmetry of some of the near cubic Nb(V) sites. By PMN-34PT the sharp line has completely disappeared and the lineshape has changed to a broad symmetrical peak near -1000ppm. Thus increasing the Ti(IV) ion concentration in the B-sites of PMN, leads to a reduction in the Nb(V) ion B-site symmetry in the Mg-rich regions of PMN, and also leads to a general increase in site disorder owing to the fact that the B-site now has three species of cations present in it. This disorder results in increased chemical shift dispersion and range of quadrupolar coupling constants for the broad peak centred at around

-1000 ppm. Furthermore they also suggest that the Ti(IV) substitution for Nb(V) in both the Mg(II)-rich and Nb(V) rich regions of PMN is non-selective.

Though there are now several other NMR groups investigating a wide range of PMN-PT samples it is more relevant to discuss an interesting study by Hoatson *et al.*[21] on the related PMN-PSN series of materials. They have used high field MAS NMR techniques to characterise the electronic environment of the niobium(V) ions and the effects associated with the arrangement of the NbO_6 octahedra and the identities of the next-nearest-neighbour atoms. They have presented MAS NMR spectra for ^{93}Nb at both 14 and 19.6 T. In PMN they have identified 3 main components, 1 narrow peak and two broad components D_1 and D_2 and have assigned quadrupolar parameters to each of these peaks. For the sharp peak they have predicted a C_Q of approximately 12MHz while for both the broad peaks they have used Gaussian distributions of both δ_{iso}^{CS} and C_Q and shown these to be 10.9ppm and 28.6MHz for D_1 and 12.9ppm and 24.4 MHz for D_2 respectively. Thus all the observed C_Q values in PMN are between 12 and 30 MHz, thereby also significantly disagreeing with the results described in the earlier paper by Fitzgerald *et al.*[20] They have also assigned the narrow peak to a configuration of ^{93}Nb nuclei with only Mg^{2+} cations occupying the six nearest β neighbour sites (nβn); and have also assigned the two broad peaks to configurations with more than one Nb^{5+} cation in the nearest β sites. Another interesting observation they have made is that there seems to be a correlation between the integrated intensity of the distributions D_1 and D_2 and the dielectric response. Thus the combined intensity is being used as an indicator of whether the sample is a relaxor or normal ferroelectric. It seems that when this combined distribution intensity is above 20% the material behaves as a relaxor, while below this it is a normal ferroelectric. Finally they also go on to propose a modified

random site model of β-site order. Their Monte Carlo simulations show that a quantitative agreement of intensities is also achieved in their proposed model.

In one of the subsequent papers on ^{93}Nb NMR studies of PMN-PSN, Zhou *et al.*[22] have carried out a ^{93}Nb 3QMAS study on the same PMN-PSN samples described by Hoatson *et al.*[21] In this study 3QMAS ^{93}Nb spectra have been obtained at 19.6 T at high spinning speeds of 35.7kHz. Using such multi-quantum MAS techniques usually results in higher resolution than conventional MAS because the anisotropy in the indirect dimension is removed by eliminating the broadening contribution due to the fourth-rank term in the second-order quadrupolar hamiltonian. In PMN they have also identified 3 main components, 1 narrow peak and two broad components D_1 and D_2 and have assigned quadrupolar parameters to each of these peaks. For the sharp peak they have estimated a P_Q of approximately 9 MHz, while for the both the broad peaks they have used Gaussian distributions of both $\delta_{iso}{}^{CS}$ and C_Q and shown these to be 10.9ppm and 27.3MHz for D_1 and 12.9ppm and 9.4MHz for D_2 respectively thereby somewhat disagreeing their own previous study. However one of the interesting observations they have made is that for the pure-magnesium (6,0,0) (N_{Mg},N_{Sc},N_{Nb}) and pure niobium (0,0,6) configurations the observed P_Q is smaller, indicating a higher level of symmetry (Figure 5.3), while for configurations with both Mg^{2+} and Nb^{5+} ions the mismatch of cations greatly lowers the symmetry thereby increasing the value of P_Q.

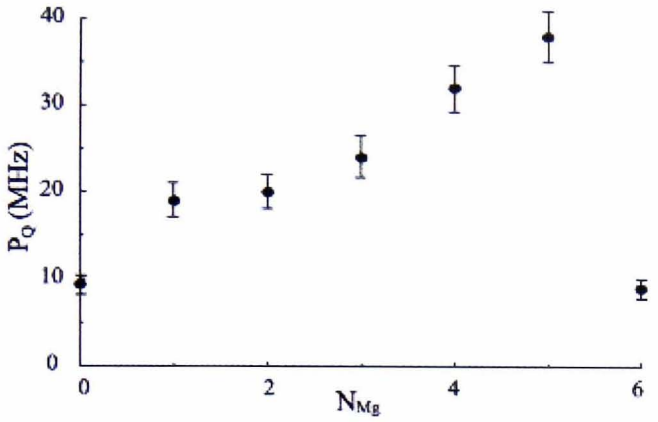

Figure 5.3 - ^{93}Nb quadrupole products of the seven nearest neighbour configurations in PMN-PSN containing only Mg^{2+} and Nb^{5+} cations.[22]

In fact it is curious to note that the five Mg, one Nb configuration (5,0,1) has the largest P_Q value. It is this large P_Q value (or large shift) that is responsible for the distinct gap observed between the sharp line and the broad distribution D_1 in the MAS spectra of PMN. Another interesting observation made in this paper is that there appears to be an empirical relationship between δ_{iso}^{CS} and N_{Mg} increasing N_{Mg} by one causes an increase of 13.7 ppm in δ_{iso}^{CS}, and a small variation in P_Q. A summary of these and other results are shown in Table 5.1.

Sample	Author	KEY PARAMETERS				Field(T)	Reference
		Shifts(ppm) / Width (Hz)	P_Q(MHz)	η	δ_{iso} (ppm)		
$LiNbO_3$	Ivanova(1995)	NA	.42 (ν_Q)	0	NA	5.0	NA
$LiNbO_3$	Prasad (2000)	-1004	22.1	NA	NA	14.1	$NbCl_5$ in acetonitrile
PMN	Cruz(1999)	320 (sharp) 218 (broad)	C_Q 8.5 (sharp) C_Q 21.5 (broad)	0.5 (sharp) 0.8 (broad)	NA NA	9.4	Solid Nb_2O_5
PMN	Prasad(1999)	NA NA NA	C_Q 1.2 (sharp) C_Q 17 (broad1) C_Q62 (broad2)	NA NA NA	NA NA NA	14.1	$NbCl_5$ in acetonitrile
$PbNb_2O_6$	Prasad(1999)	NA	C_Q 19	0.5	-1090	14.1	$NbCl_5$ in acetonitrile
PMN	Fitzgerald(1999)	-902 / 1950 (sharp) –989 / 12800 (broad)	C_q <1 (Sharp) Large C_Q for broad	NA NA	NA NA	14.1	$NbCl_5$ in acetonitrile
PZN	Fitzgerald(1999)	-898 / 5000 (sharp) –988 / 15200 (broad)	C_Q <1 (Sharp) Large C_Q for broad	NA NA	NA NA	14.1	$NbCl_5$ in acetonitrile
PMN	Fitzgerald(2000)	-902 / 1950 (sharp) –960 / 12800 (broad1) –989 / 12800 (broad2)	C_Q < 0.8 (Sharp) C_Q ~ 17 (broad1) C_Q> 62 (broad2)	NA NA NA	NA NA NA	14.1	$NbCl_5$ in acetonitrile
$PbNb_2O_6$	Prasad (2000)	-1113	16.8	NA	NA	9.4T	$NbCl_5$ in acetonitrile
$Pb_3Nb_4O_{13}$	Prasad (2000)	-995	13.7	NA	NA	9.4T	$NbCl_5$ in acetonitrile
$Pb_{1.83}Nb_{1.71}Mg_{0.29}O_{6.39}$	Prasad (2000)	-995	13.7	NA	NA	9.4T	$NbCl_5$ in acetonitrile
PMN Pyrochlore	Prasad (2000)	-1014	26.8	NA	NA	9.4T	$NbCl_5$ in acetonitrile
PMN	Hoatson (2002)	-895.5 (sharp) -952 (broad1) -921 (broad2)	C_Q 12 (Sharp) C_Q 28.6 (Broad1) C_Q 24.4 (Broad2)	0 0.4 0	NA 10.9 12.9	14.1 14.1 14.1	$NbCl_5$ in acetonitrile
PMN	Zhou (2004)	-892.6 (sharp) -944 (broad1) -976 (broad2)	C_Q 9 (Sharp) C_Q 27.3 (Broad1) C_Q 9.4 (Broad2)	0 0.4 0	NA NA NA	19.6 19.6 19.6	$NbCl_5$ in acetonitrile

* Errors: peak position ±1ppm, C_Q ±1.5ppm.

Table 5.1: The ^{93}Nb peak positions and linewidths for the niobium-containing samples in the literature at varying magnetic fields.

5.4 Characterisation studies for PMN-PT samples

As discussed previously in Chapter 3 of this thesis one of the major problems faced in the preparation of PMN-PT samples is the formation of an unwanted pyrochlore phase in addition to the pure perovskite phase that is desired. The next few paragraphs elucidate the methodology behind our sample preparation techniques already detailed in Chapter 3, before discussing the results obtained from the characterisation studies of these samples.

This current section specifically seeks to address the following key issues in the "two stage columbite method" generally used for the preparation of perovskite phase PMN-PT samples and answers some of the fundamental problems encountered while implementing this method of sample preparation.

- The primary calcining or sintering procedure – i.e. determining the optimal temperature.
- The addition of excess MgO at the precursor stage – establishing the exact amount of MgO to be used.
- Acid treatment of the prepared sample – understanding why and how this treatment affects the properties of the sample.

Initial trials of pure perovskite phase sample preparation began by using stoichiometric amounts of precursors in order to create a pure perovskite 0.9PMN-0.1PT sample. It was quickly established that stoichiometric amounts of precursors did not yield a pure perovskite phase sample, significant amounts of both excess PbO and pyrochlore phase were both present. However it was possible through careful selection of the sintering temperature to suppress the formation of PbO. The results of varying sintering temperatures on sample quality can be seen in the figure below.

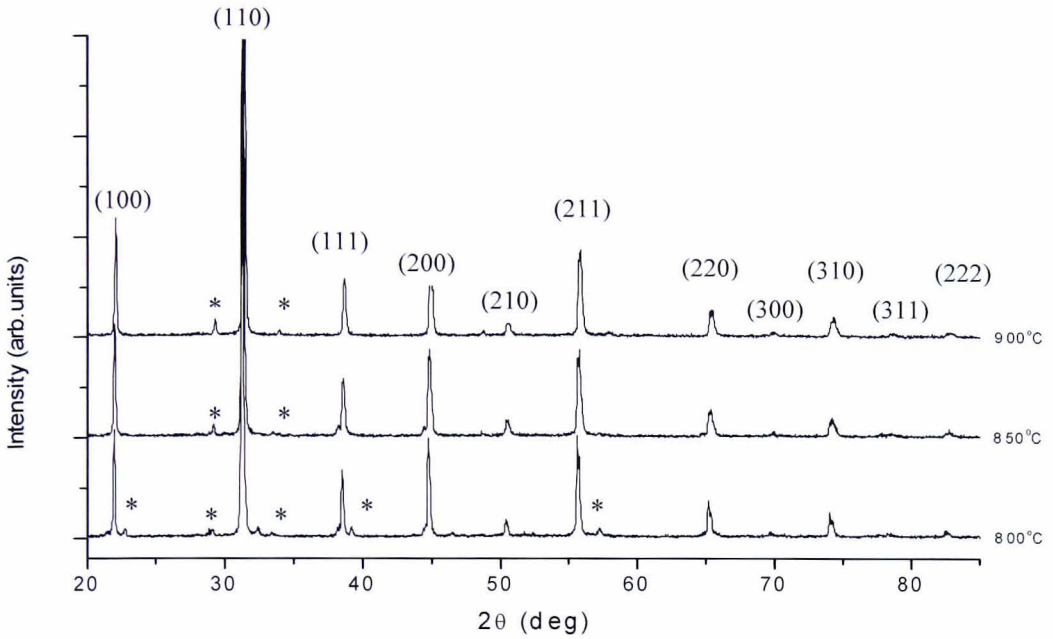

Figure 5.4 - 0.9PMN-0.1PT grown using different sintering temperatures, with the main reflections indexed and asterisks denoting minor impurity phases.

It can be clearly seen from Figure 5.4 that by using a sintering temperature of above 850°C almost completely suppresses the formation of PbO. This is very important for the dielectric property of the material as PbO present in the grain boundaries of the PMN-PT ceramic is known to reduce the overall dielectric constant compared to pure perovskite phase material.[23]

Furthermore in the same study by Wang and Schulze[23] they also made a valid case for using an excess of magnesium carbonate in the precursor stages to suppress the formation of the pyrochlore stage, however they do not specify the ideal amount for this purpose. Hence several 0.9PMN-0.1PT samples were prepared using varying mol% amounts of excess magnesium carbonate precursor. The results from these samples are shown in Figure 5.5.

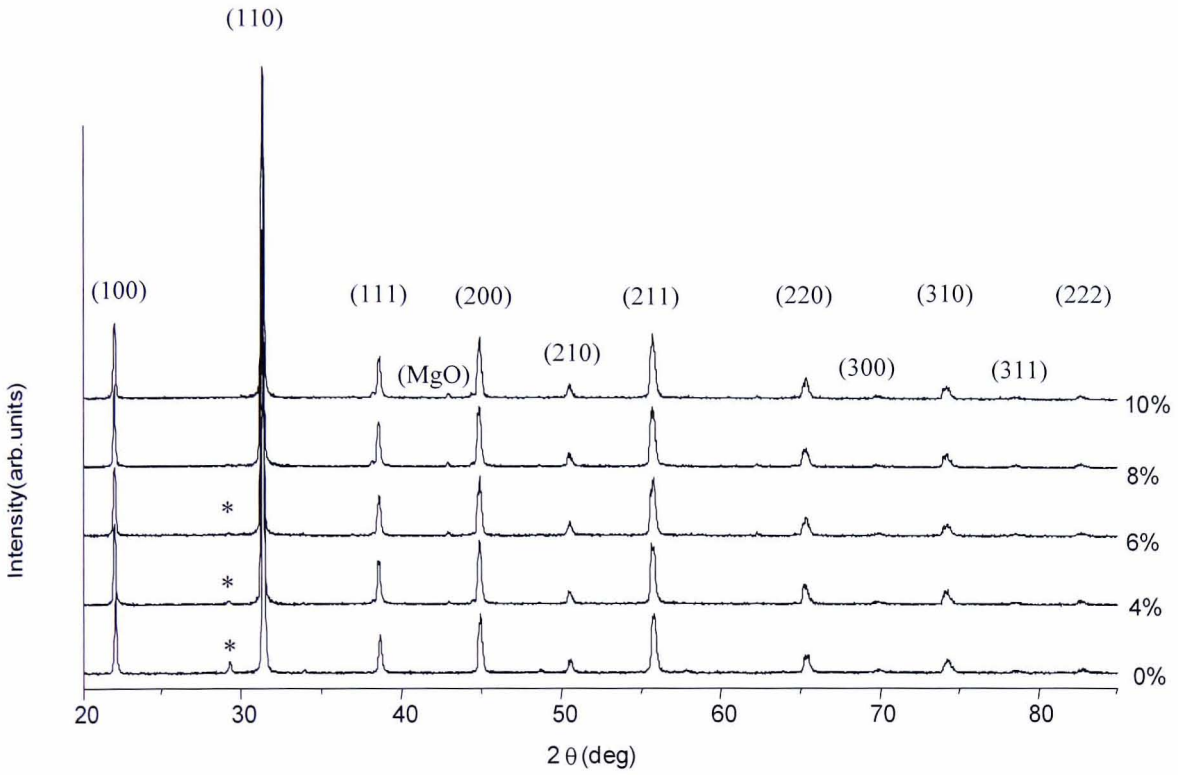

Figure 5.5 – 0.9PMN-0.1PT samples grown with excess magnesium carbonate in mol%. Asterisk indicates presence of Pyrochlore phase

Thus from the figure above it can be seen that by using a 8% mol excess of magnesium carbonate the formation of pyrochlore phase can be completely prevented as evidenced by the peak indicated with an asterisk in Figure 5.5. Unfortunately using excess Mg leads to a significant amount of excess MgO being present in the otherwise pure perovskite phase material. This may also have a considerable impact on the physical properties of the sample hence it is necessary to try and remove as much of the excess MgO without altering any of the other preparation criteria now established. The simplest means of doing this is by a simple acid treatment of the prepared sample, using a 1N concentration of acetic acid. The benefits of the acid treatment of the sample can be clearly seen in Figure 5.6.

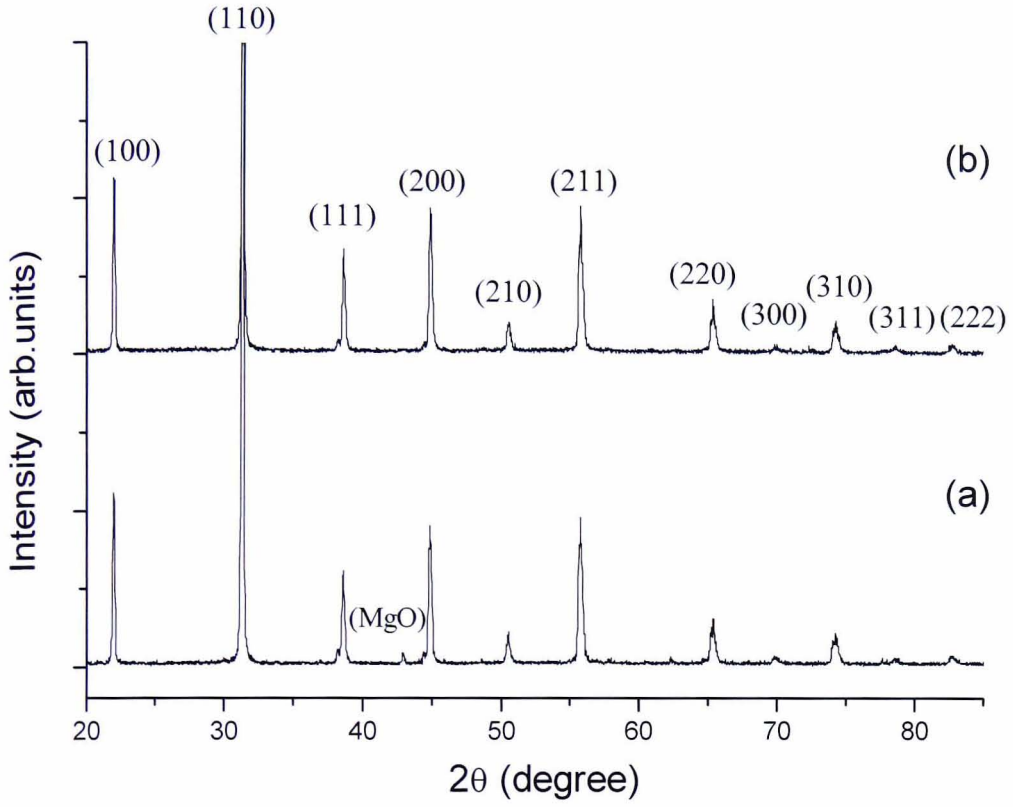

Figure 5.6 – 0.9PMN-0.1PT samples (a) before and (b) after acid treatment.

In Figure 5.6 above it can be clearly seen that in (a) peaks corresponding to MgO are visible at ~43° and ~62°, these peaks are greatly reduced in (b) after the acid treatment. Thus the resulting final powder showed only perovskite phase ceramics with only a small amount of excess MgO as a small impurity, corroborating the proposal of Wang and Schulze[23] that suggests that this small excess of MgO may now actually be embedded within the particles of PMN-PT, thereby being shielded from the acid.

All of the samples that were carefully prepared using the methodology described above and the preparation details as described in Section 3.8.1 of this thesis, were verified to be the correct composition and phase purity by means of X-Ray powder diffraction studies (XRD). The XRD profiles of the nine key PMN-PT

samples taken using CuKα radiation (1.5418Å) in Bruker AXS machine is shown below in Figure 5.7

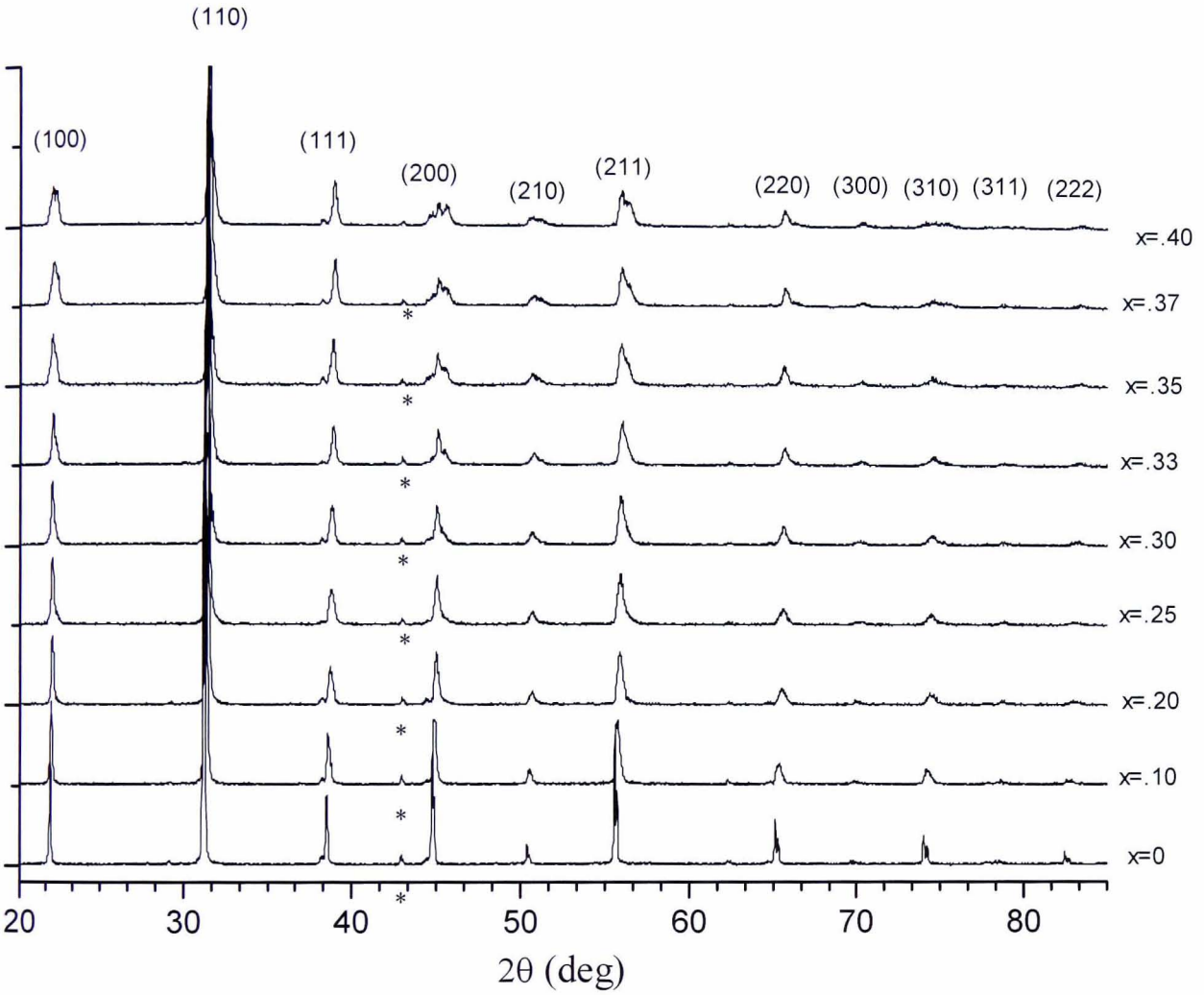

Figure 5.7 – XRD profiles of $PMN_{1-x}PT_x$ samples. Asterisk indicates the presence of MgO impurity.

From the XRD profiles shown above, we can see from the initial broadening and subsequent splitting of the peak at $2\theta = 45°$ as the PT content increases, indicating a continuous evolution of the phase from rhombohedral to tetragonal. The peaks also show that pure PMN contains a cubic phase and the solid solutions contain

primarily rhombohedral phase until the PT content is around 25%. When the PT concentration is 40% only a tetragonal phase can be observed. Thus there is a wide region between PT (25%-40%) where multiple phases can and do co-exist.

Compositional inhomogeneity is an undesirable effect in any sample, for this type of study, so that steps to minimise this have been made throughout the sample preparation procedure. It has been noted in our studies that there can be inconsistencies between two samples, even those being prepared simultaneously in a single batch using the same precursor materials and the same sintering and preparation procedures. Hence it is also important to know the actual versus nominal composition of these materials so that comparisons can be made with the literature in order to accurately determine the compositional quality of our own samples. The comparison of our cell-volume data compared with that of cell-volume data found in the literature[24] is shown in Figure 5.8 below.

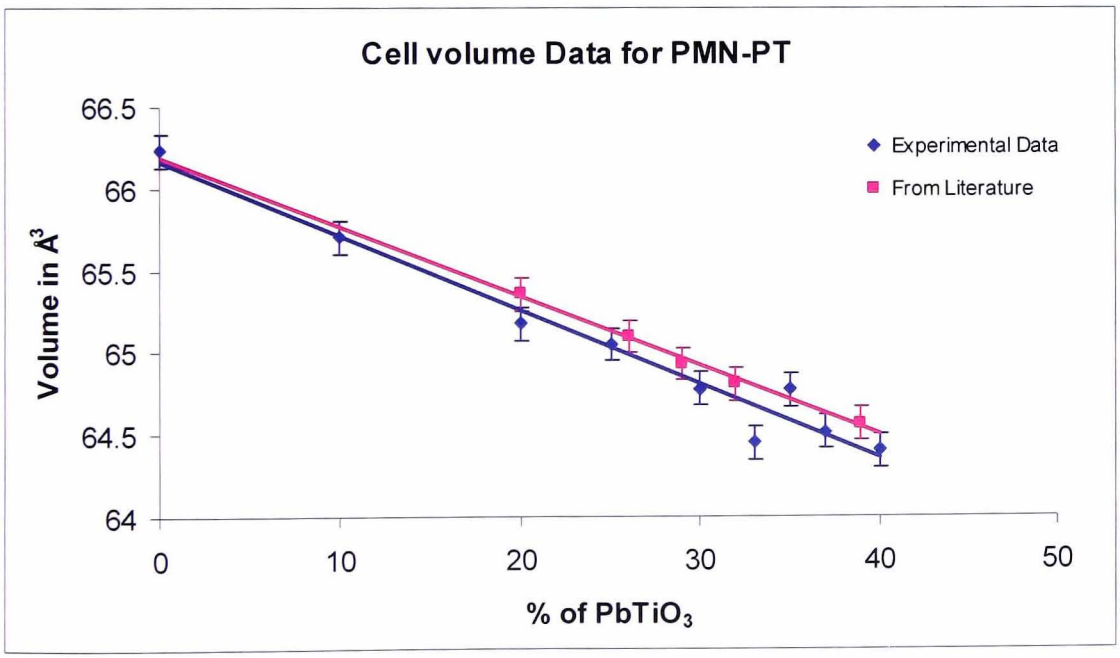

Figure 5.8 – Verification of the composition of our samples by a plot of the calculated cell value (blue) vs the quoted cell volume from the literature (pink).

Thus from Figure 5.8 it can be seen that with the possible exception of PMN-33PT all the samples lie within a ~1% PT concentration of their quoted PT concentrations.

In addition to the ceramics samples described above other lead based ferroelectric samples were created using the "sol-gel" method detailed in section 3.8.2. The XRD pattern for the sample ^{17}O enriched PMN is shown in Figure 5.9.

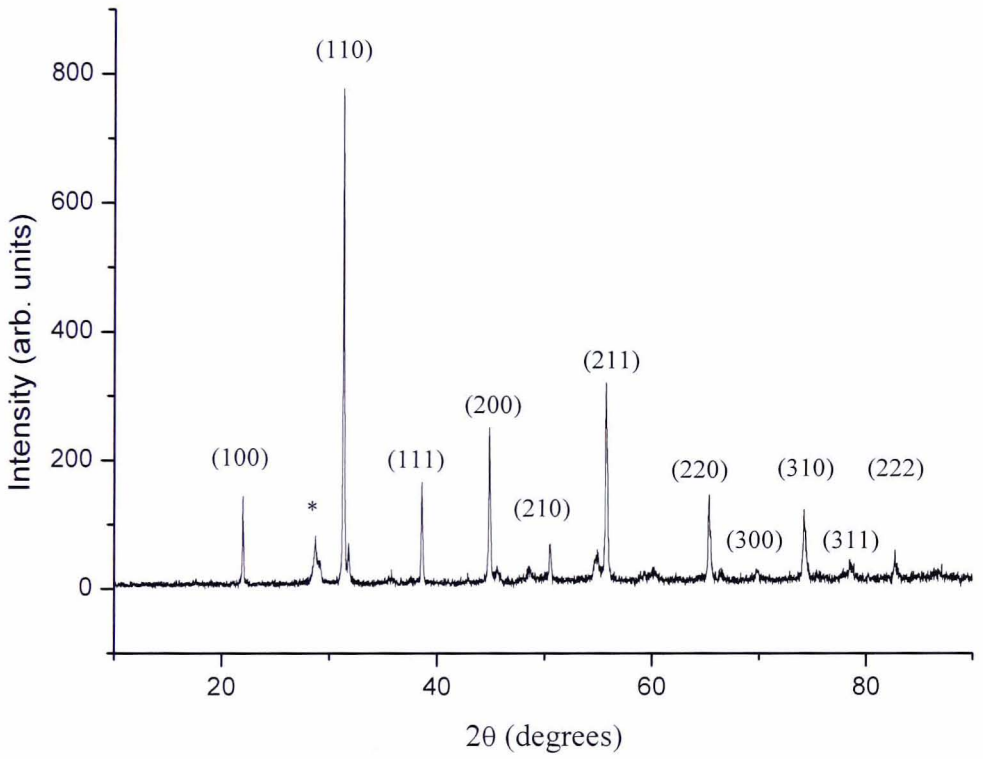

Figure 5.9 – XRD of ^{17}O-enriched PMN with minor pyrochlore phase indicated with an asterisk.

The sample is primarily perovskite phase but also shows a very minor reflection from a pyrochlore phase impurity.

5.5 ^{93}Nb NMR studies of PMN-PT samples

5.5.1 Background and Experimental data on PMN-PT

^{93}Nb is a spin $^{9}/_{2}$ quadrupolar nucleus with a relatively large nuclear quadrupolar moment (-0.22 x 10^{-28} Qm^{-2}) and 100% natural abundance[25]. In the solid state, any electric field gradients created by the surrounding electronic cloud of the nucleus interact with the nuclear electric quadrupole moment, potentially leading to a considerable broadening of the spectral lines making ^{93}Nb a moderately difficult nucleus to study by NMR. However from the discussions presented in sections 5.2 and 5.3 of this thesis it is quite clear that it is the study of this local Niobium(V) coordination environment that is the key to understanding more about interesting properties of this material. Therefore the interpretation of the results and observations presented in this section provides insight into

- evidence of at least three different types of Nb(V) environment
- short-range chemical Mg/Nb ordering

Figure 5.10 shows a comparison between three static Nb spectra for some typical samples. The CMX – Infinity 600 Spectrometer was used with the Varian 3.2mm MAS probe with the frequency for ^{93}Nb set to 146.661 MHz.

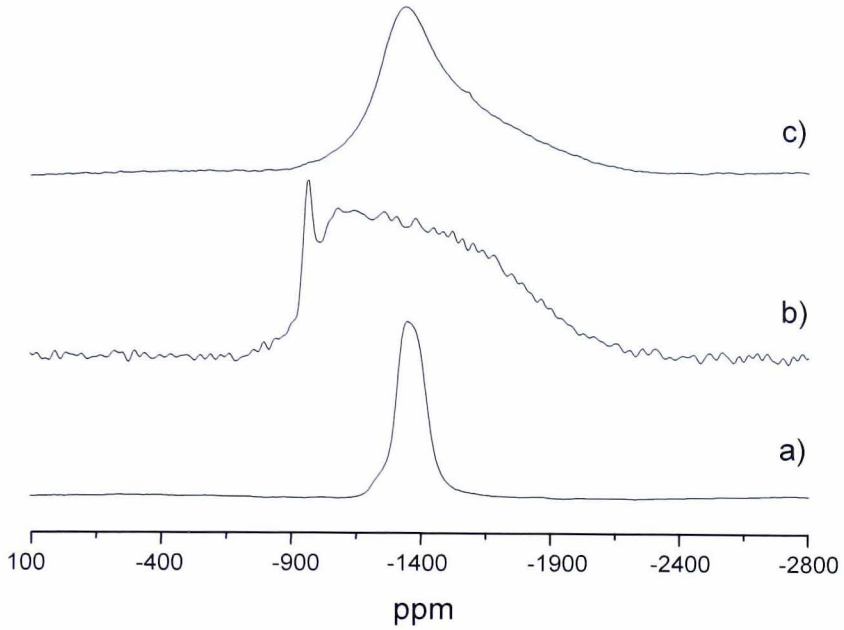

Figure 5.10 – Static ^{93}Nb spectra of a) Lithium niobate, b)PMN and c) PMN-35PT

From Figure 5.10 it is quite clear that the line-widths of the PMN and PMN-PT samples are significantly wider than that of lithium niobate, which has already been presented and discussed in Chapter 4 of this thesis. The PMN spectrum is ~750ppm wide whereas the PMN-35PT spectrum is considerably less at around ~350ppm linewidth whereas the lithium niobate spectra is only ~124ppm across. The greater width in PMN and PMN-35PT is almost certainly a result of second-order quadrupolar broadening. What makes it especially difficult to deconvolve the spectrum is that there is probably a distribution of parameters, so that the lines of PMN and PMN-35PT are not well defined second-order quadrupolar lineshapes. Figure 5.11 shows the static ^{93}Nb spectra for the 9 key PMN-PT samples

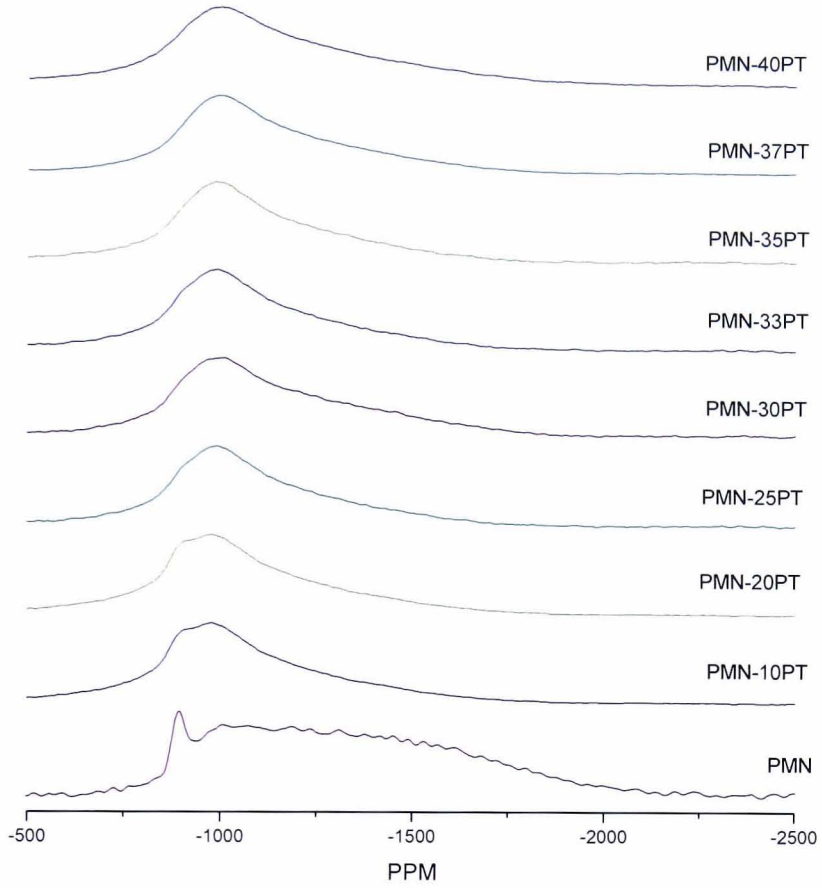

Figure 5.11 – Static ^{93}Nb spectra of PMN-PT samples

From the PMN spectra shown in Figure 5.11, it is clear that there are two distinct Nb(V) sites which is in agreement with Cruz *et al.*[19] However it is quite clear that this changes rapidly upon the introduction of even small amounts of PT in the solid solution. In order to understand these changes we performed a nutation experiment as described in detail in section 2.7 of this thesis.

The 'Oldfield Echo' pulse sequence was used as detailed in section 3.5.2 Using this pulse sequence results in some small distortion of signal by the acquisition delay, as the FID of the entire echo is utilised. Hence the advantage of this echo sequence compared to a single pulse sequence is that an echo is formed that does not have the distortions associated with the corruption of the start of the FID after a single pulse. This echo pulse sequence can also then be used to measure the value of T_2 relaxation times which gives some information about the local structure and possible

neighbours of the system around the ^{93}Nb nuclei. The spin–spin relaxation time T_2 (previously discussed in section 2.2) is obtained from the intensity of spectra for different values of the echo time τ. τ has been arrayed so that the T_2 relaxation times can be computed based on 10 different τ values. Two different sets of τ values were used, with long values of τ (50μs -1500μs) and another with short values of τ (10μs - 200μs).

Table 5.2 below shows the T_2 relaxation times obtained for various samples. The error was estimated in detail on the crystalline sample niobates like Li, Na, Ba. All further experiments were carried under initial experimental conditions, producing data with similar signal to noise, such that the error is estimated to be the same.

Sample	***T_2Relaxation Time (ms) ±0.05***
1. Lithium Niobate	0.315
2. Sodium Niobate	0.515
3. Barium Niobate	0.570
4. PMN	0.162
5. PMN-0.10PT	0.349
6. PMN-0.20PT	0.558
7. PMN-0.25PT	0.629
8. PMN-0.30PT	0.788
9. PMN-0.33PT	0.873
10. PMN-0.35PT	0.957
11. PMN-0.37PT	0.968
12. PMN-0.40PT	1.01
13. $MgNb_2O_6$ ^{17}O Enriched (Crystalline)	0.495
14. $MgNb_2O_6$ ^{17}O Enriched (Amorphous)	0.029
15. Nb_2O_5 – ^{17}O Enriched	0.039

Table 5.2 - The ^{93}Nb T_2 relaxation times obtained for various niobium containing samples.

The interesting increase of T_2 times with increasing PT concentrations in the PMN-PT samples can be more easily observed in Figure 5.12 shown below.

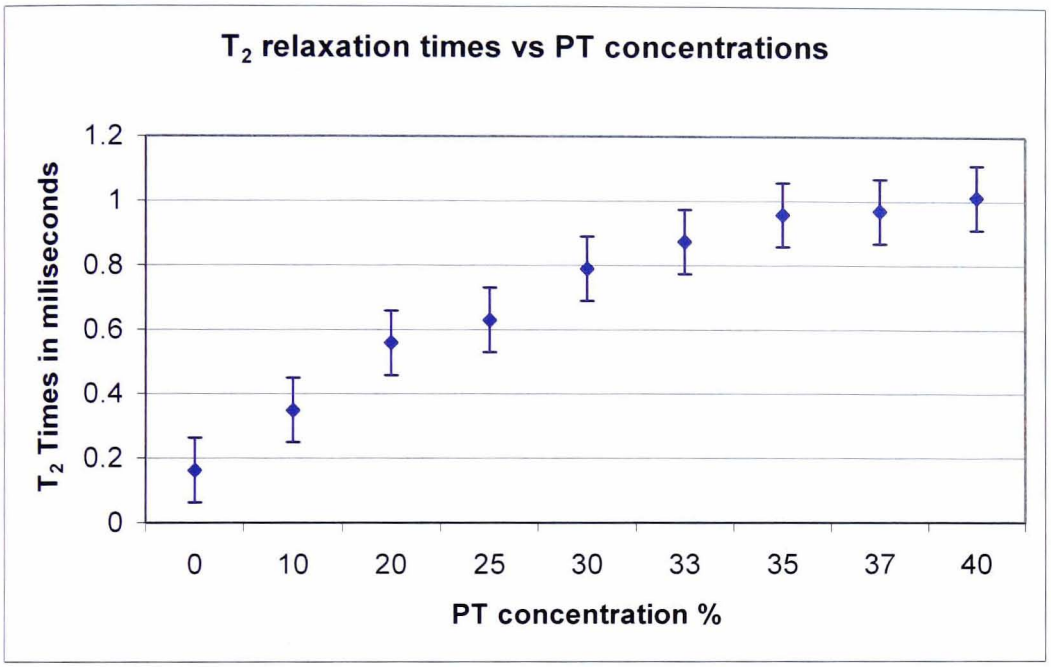

Figure 5.12 – Plot of T_2 relaxation times vs PT concentration for static PMN-xPT samples.

A gradual increase in the T_2 times with increasing concentration is quite apparent, another interesting observation is that the PMN-25PT sample appears to have a lower than expected T_2 time though this deviation is small. However it is quite clear that there are changes taking place in the materials as PT concentrations increase in the solid solutions, these changes are however very subtle and do not reveal themselves in the spectra shown in Figure 5.12. Also in attempt to quantify these spectra, a plot showing the line width of the spectra displayed in Figure 5.13 we can see that there is no particular discernible trend as in the case of the T_2 relaxation times.

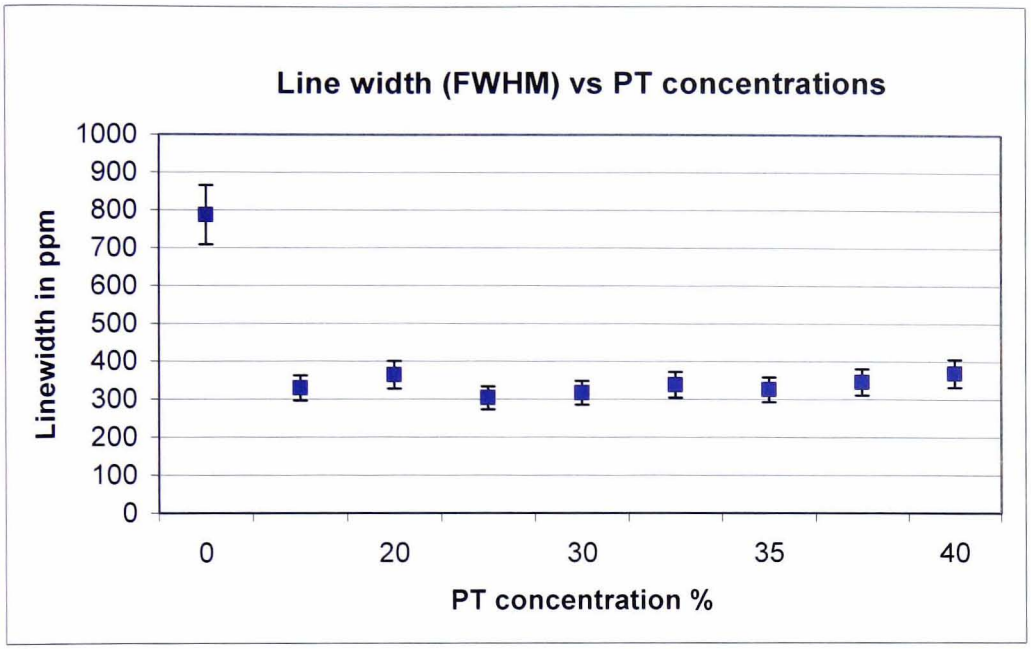

Figure 5.13 – Plot of FWHM line widths vs PT concentration for PMN-xPT samples

Thus from the results shown above it became quite clear that in order to obtain further information on these subtle changes taking place in the materials on addition of PT to the solid solution, as clearly observed through the T_2 relaxation plot, it was necessary to perform high speed MAS experiments as detailed in section 2.7.1 of this thesis. In order to compare the difference in resolution between the static and MAS spectra Figure 5.14 shows both the static and MAS spectra for the pure PMN sample.

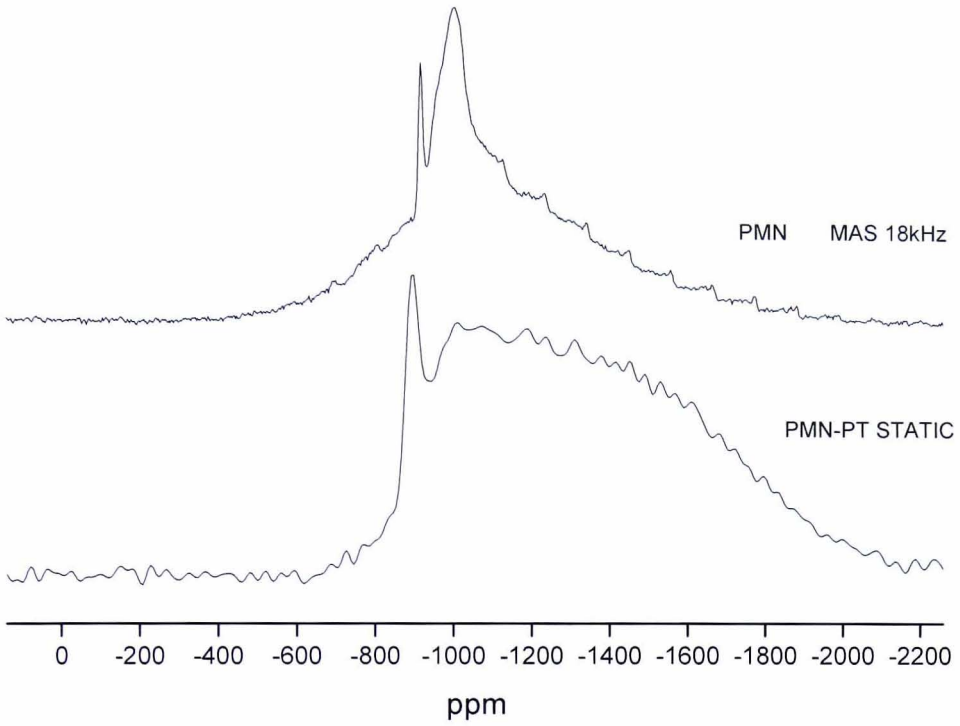

Figure 5.14 – A comparison between the static and 18kHz MAS spectra for PMN

The static spectrum shows a broad asymmetric line of width ~750ppm there is also the presence of a much sharper line at shift –895ppm. On spinning these are much sharper with a moderately broad line of 120ppm. The MAS lineshape for the sharp peak has now decreased to a width of around 10ppm. Thus a considerable decrease in line width and clearer resolution of all the peaks is observed. The PMN-xPT spectra obtained from our MAS experiments are shown in Figure 5.15 below

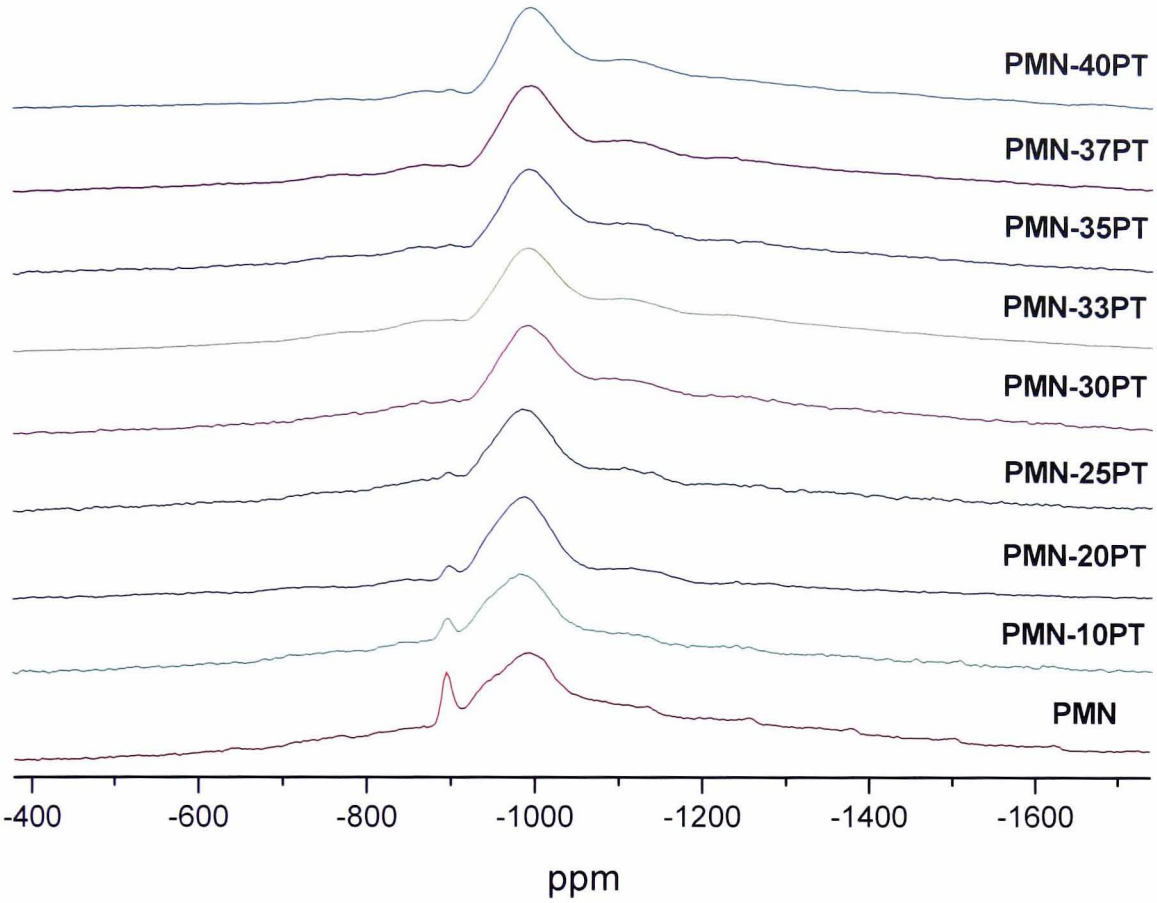

Figure 5.15 – 18kHz MAS Spectra of PMN-xPT solid solutions

From Figure 5.15 it is now quite clear that there are quite distinct changes taking place in the spectra. A preliminary deconvolution of these spectra using DMFIT allowed the realisation that there were three distinct, contributions to the ^{93}Nb MAS NMR lineshape which agreed with recent work published by Hoatson *et al.*[21]

An example of the DMFIT deconvolution for the PMN spectra showing the three distinct niobium environments is shown below in Figure 5.16

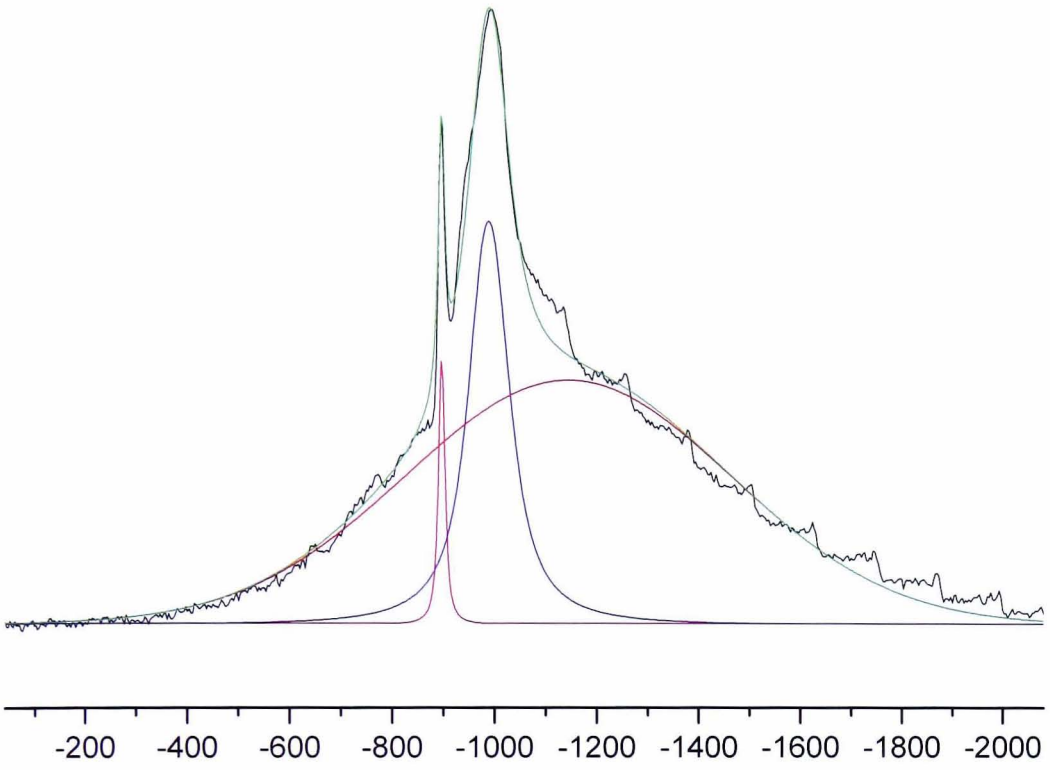

Figure 5.16 – Example of a deconvolution of PMN spectra using DMFIT

The key feature that is immediately visible from the spectra Figure 5.15 is the presence of a sharp line that is clearly visible in PMN but gradually decreases in intensity on addition of PT disappearing around the 25% PT concentration. Furthermore given the frequency positions of the numerous spinning sidebands clearly visible in figure 5.16 it is apparent that these sidebands are associated with this sharp peak. In order to better understand this spectrum SIMPSON simulations were conducted, for the PMN sample using the parameters obtained from the DMFIT deconvolution shown above in Figure 5.16 as a starting point.

The resulting SIMPSON simulation could not reproduce the PMN-spectrum in Figure 5.16 which indicated that the parameters extracted from DMFIT were probably inaccurate. This inaccuracy is probably due to a combination of factors such as not being in the infinite spinning speed regime that DMFIT assumes and more importantly, is also due to the parameters showing a broad distribution owing to

atomic disorder in these compounds. Hoatson *et al.*[21] published a paper on PMN-PSN using distributions of quadrupolar parameters. A SIMPSON simulation was performed using our experimental conditions and the quadrupolar parameters published in Hoatson *et al.*[21] for PMN. The parameters used are χ_Q of 12MHz for the sharp line and χ_Q of 28.6 and 24.4 MHz for the peaks D_1 and D_2 respectively. This simulation is shown below in Figure 5.17

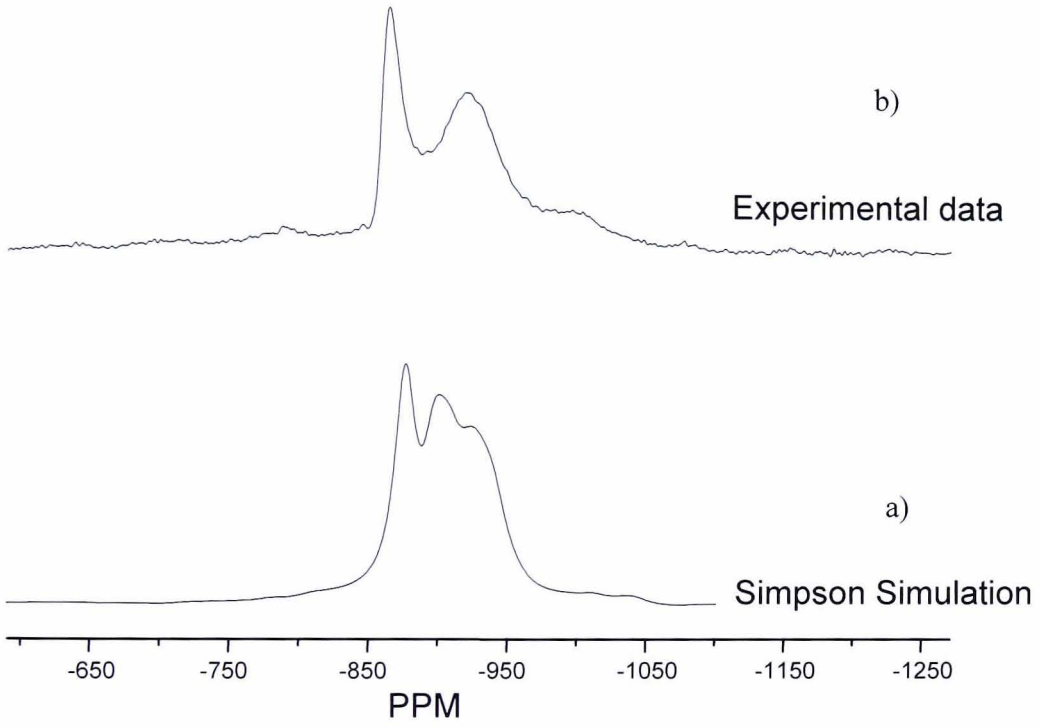

Figure 5.17 – a) SIMPSON simulation of PMN using Hoatson *et al.*[21] quadrupolar parameters and our experimental conditions and b) our experimental data.

The similarities between the spectra and the simulation are now more apparent. This allowed SIMPSON to be used as an optimisation tool in order to determine some of the characteristic properties of PMN-xPT samples.

The first analysis performed was to check the impact of spinning speed on the spectra. This can be seen in Figure 5.18

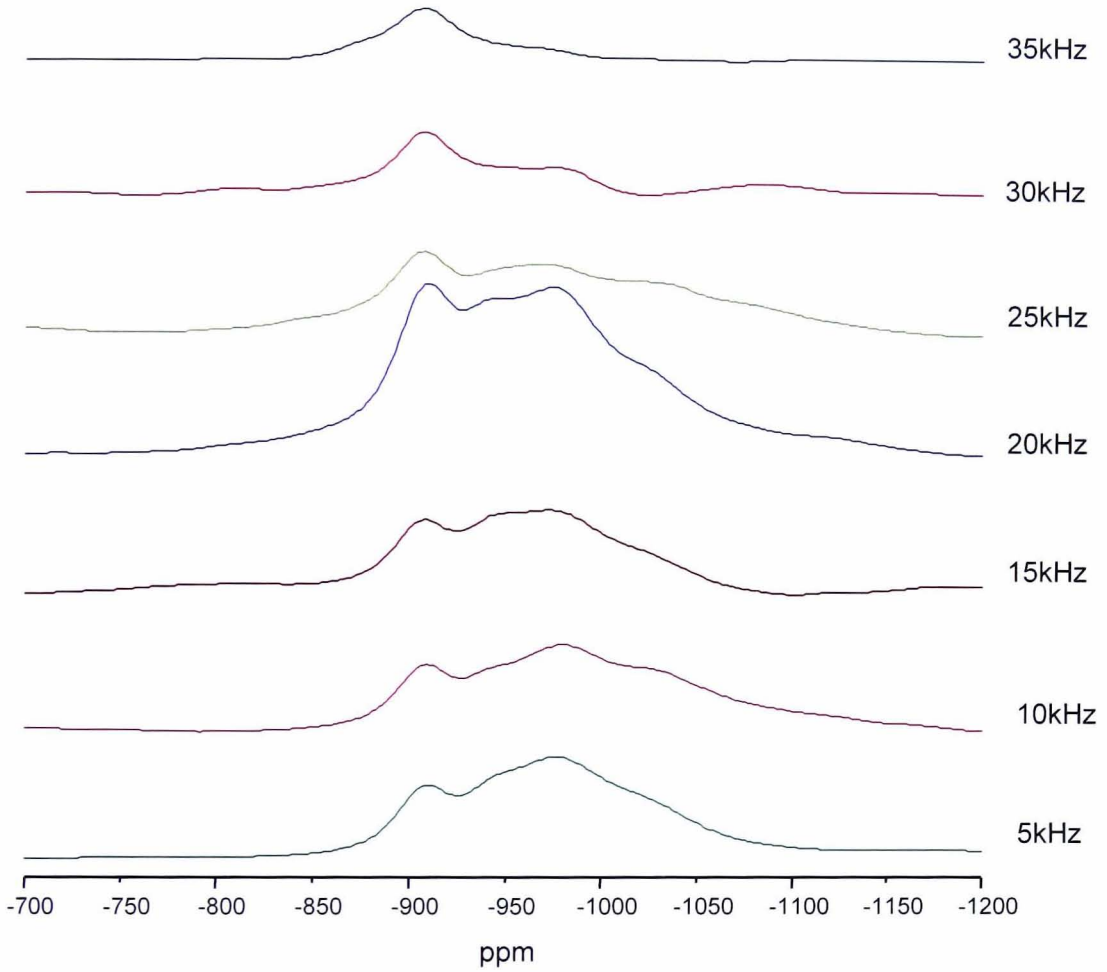

Figure 5.18 - SIMPSON simulation of ^{93}Nb MAS NMR data of PMN run at various spinning speeds

It can be clearly seen that spinning speed has an effect on the lineshape and that when there are potentially large quadrupolar interactions such as for ^{93}Nb then care should be exercised so this is taken into account. It can be seen in the simulation that the sufficient narrowing of the lineshape is achieved at 20kHz. The second series of Simpson simulations were run to check the effect of varying pulse lengths on PMN spectra. These can be seen in Figure 5.19.

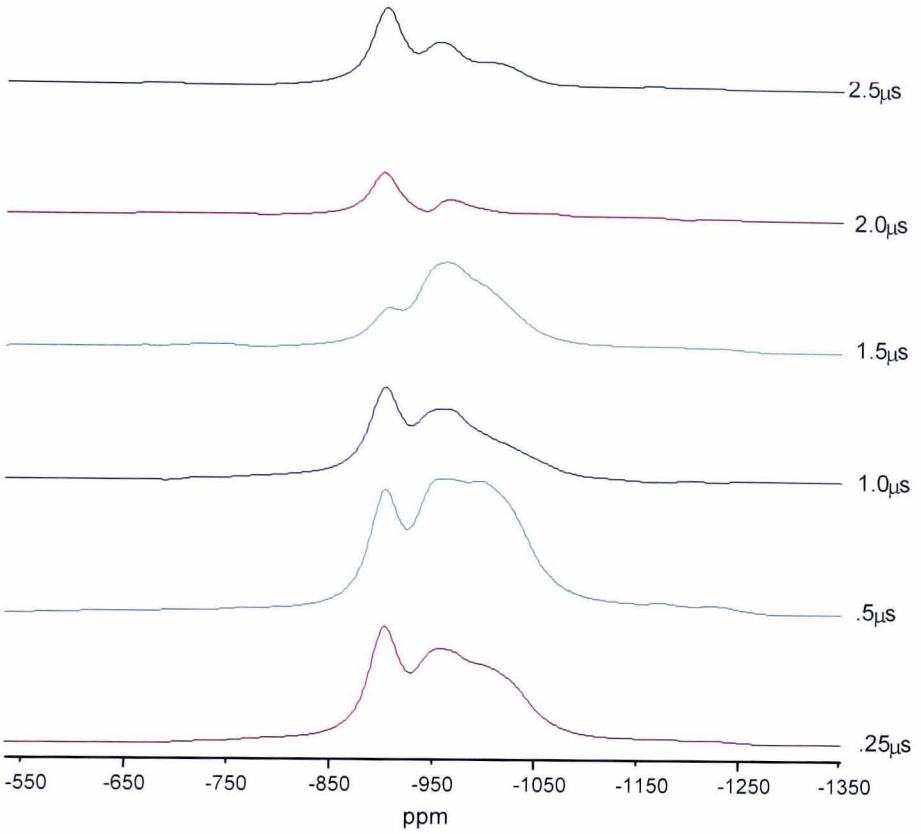

Figure 5.19 – Simulated nutation study using SIMPSON for PMN.

This figure clearly shows what we confirmed from our experimental nutation studies, that PMN has a very short relaxation time, and hence a very short pulse length of 0.25μs is sufficient to provide the best resolution spectra for these materials.

The lineshape clearly changes as the actual length of the 90° pulse varies. The most likely explanation for this is that although the nutation frequency is normally a constant for a given sample, for quadrupolar nuclei in samples showing a range of quadrupolar interactions there can be a variation in the actual nutation frequency for the different sites within the sample. Hence the pulse length changes although as this is being observed by a nominal 90° pulse length different components will be tipped differently which causes the change in the observed lineshape. Thus the safest strategy to adopt to obtain the most representative lineshape is to use a short pulse.

The 9 PMN-xPT solid solutions studied so far provided a suitable range of PT concentrations, especially in the most interesting region around the MPB, however it was decided in order to gain a more thorough insight into the entire composition range of PMN-xPT solid solutions, some additional PMN-xPT samples both at very low PT concentrations (<10%PT) and at very high PT concentrations (>50%) would also be added to our ^{93}Nb MAS NMR study. Thus 5 additional samples were obtained of PMN-xPT, with x = 0.04 (i.e. low concentration) and at relatively higher concentrations of x = 0.5, 0.55, and 0.7. The characterisation of these samples have been described in detail elsewhere[26] and hence will not be discussed here. The ^{93}Nb MAS NMR spectra of these samples are shown in Figure 5.20

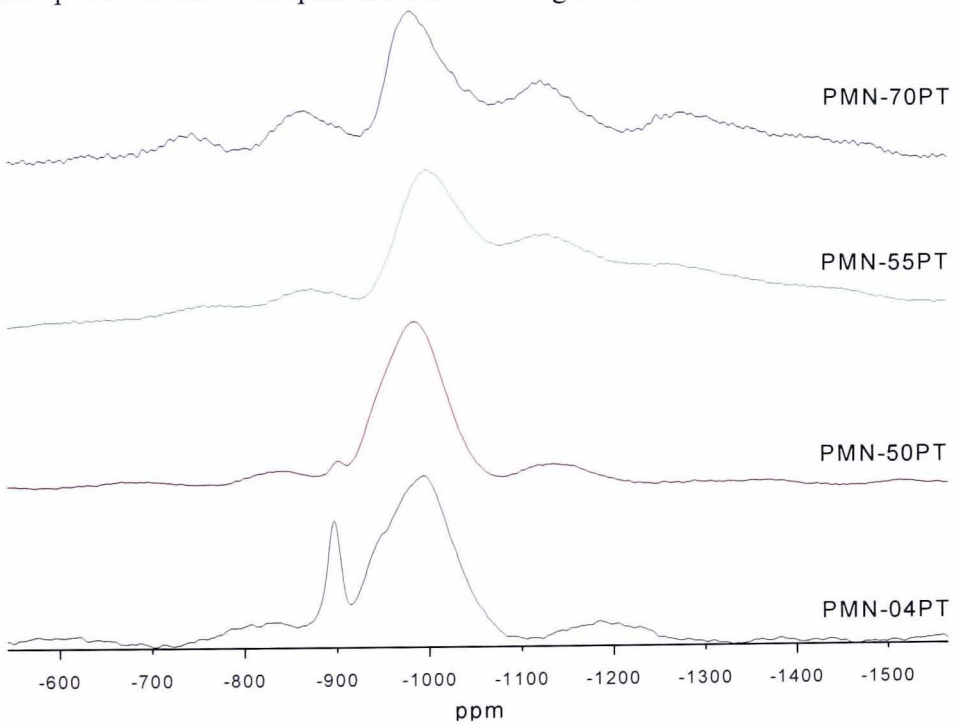

Figure 5.20 - 18kHz ^{93}Nb MAS Spectra for very high and very low Ti concentration PMN-PT Samples

However by now it was also quite clear that the lineshapes of the two broad peaks in the PMN-xPT samples were not generated from a single set of quadrupolar parameters they are due to a distribution of quadrupolar parameters. Hence the simple

Gaussian/Lorentzian lineshapes being used in the deconvolution of the spectra could not accurately determine these parameters.

The Quadfit program (Section 3.7.2) was specifically written to deal with the case when there is a distribution of parameters. It has the possibility of implementing either a Gaussian or Czjzek[27] distribution of parameters. The Czjzek distribution has been successfully used to describe distributions of quadrupolar parameters in amorphous fluorides[27] that are similar to what is encountered here.

The program allowed for a simultaneous variation of both η and C_Q, where η has been held constant at 0 for simplicity, due to the fact that its variation does not have much effect on the width of the line. Here single magnetic field data is being used, and there are too many degrees of freedom, i.e., there are several peaks with a mean value and distribution of C_Q for each peak, to allow completely unambiguous determination of the actual parameters. Hence the philosophy adopted here is to use as a starting point the three sets of parameters determined by Hoatson since for PMN these allowed a satisfactory SIMPSON simulation. In these simulations shown the peaks correspond to the sharp line (C_Q = 12 MHz), D_1 (C_Q = 24.4 MHz) and D_2 (C_Q = 28.6 MHz). The fits were judged satisfactory by eye, which within the accuracy and resolution of the data this was all that was warranted. The fit was not free since the mean C_Q was not allowed to vary (apart from for the very highest values of PT (i.e. > 40 mol%) since no close fit could be obtained by exactly using these initial C_Q values.

The Quadfit deconvolutions of all 13 PMN-xPT samples are shown below (Figure 5.21 to 5.33) and the results have been summarised in Table 5.3. Note the broad underlying intensity clearly seen in Figure 5.16 which is believed to be from the non-central transitions was removed by subtracting a Gaussian prior to the simulation described above of the narrower central transition features.

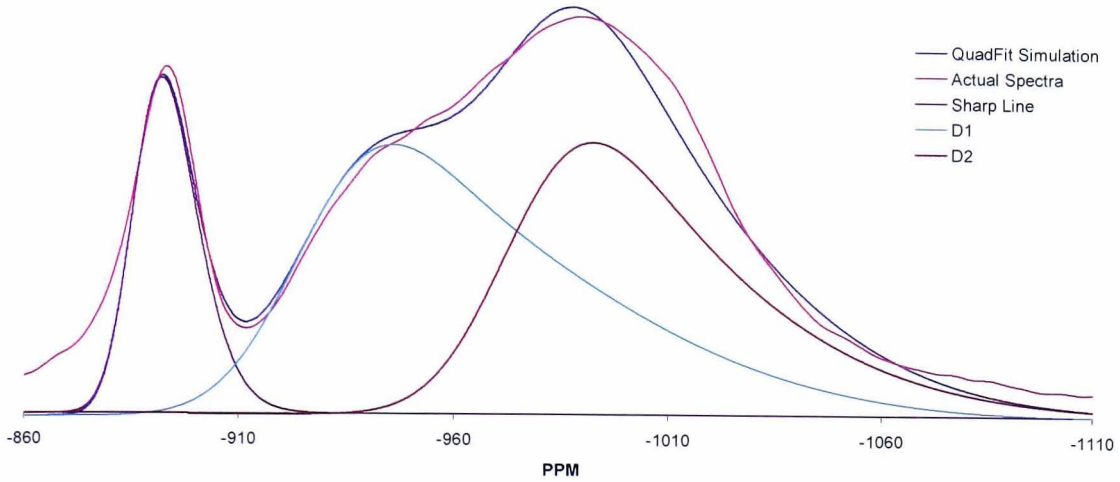

Figure 5.21 – Deconvolution of PMN spectra using Quadfit

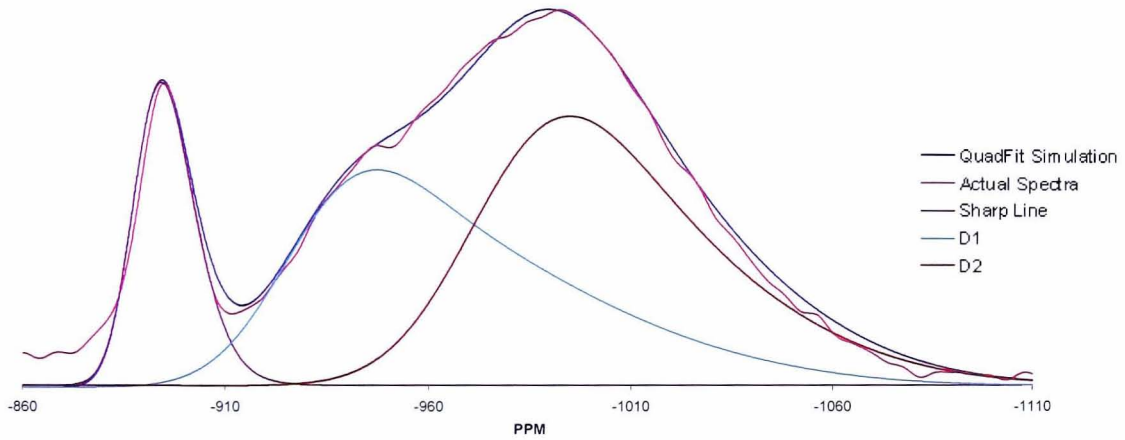

Figure 5.22 – Deconvolution of PMN-04PT spectra using Quadfit

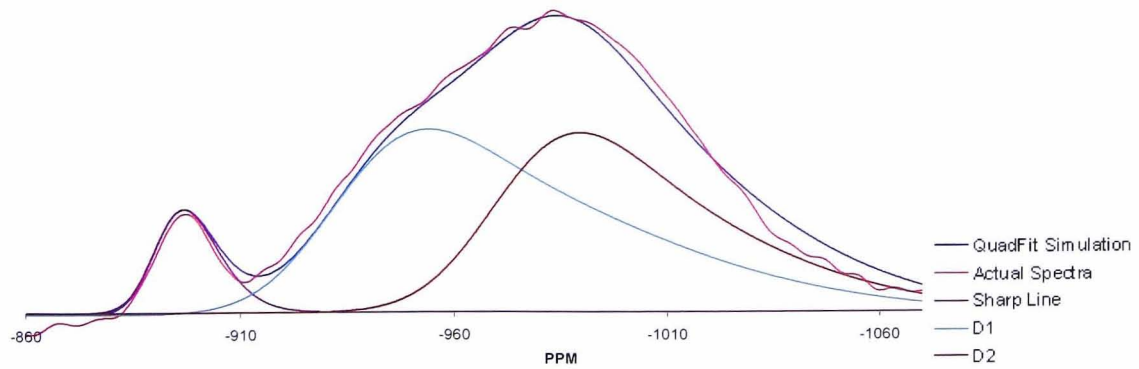

Figure 5.23 – Deconvolution of PMN-10PT spectra using Quadfit

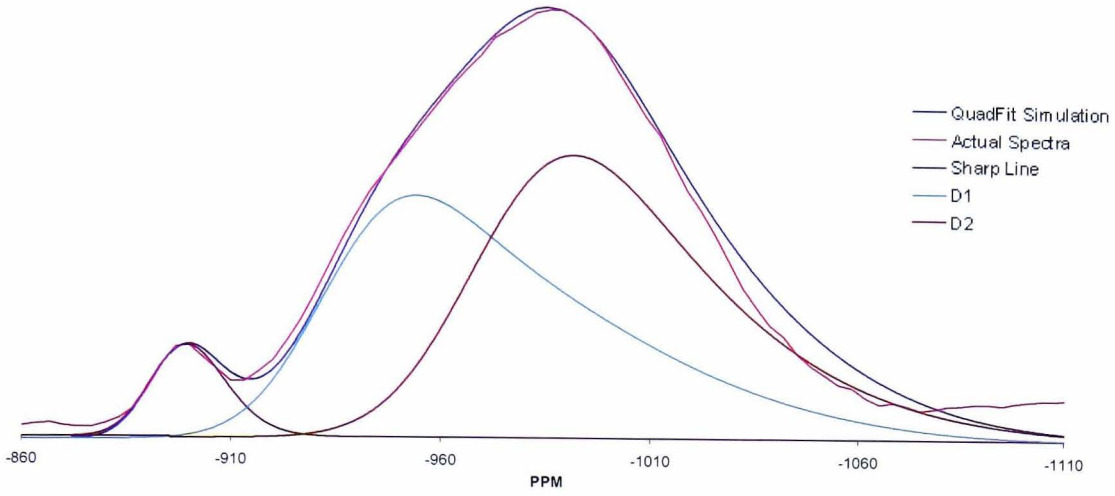

Figure 5.24 – Deconvolution of PMN-20PT spectra using Quadfit

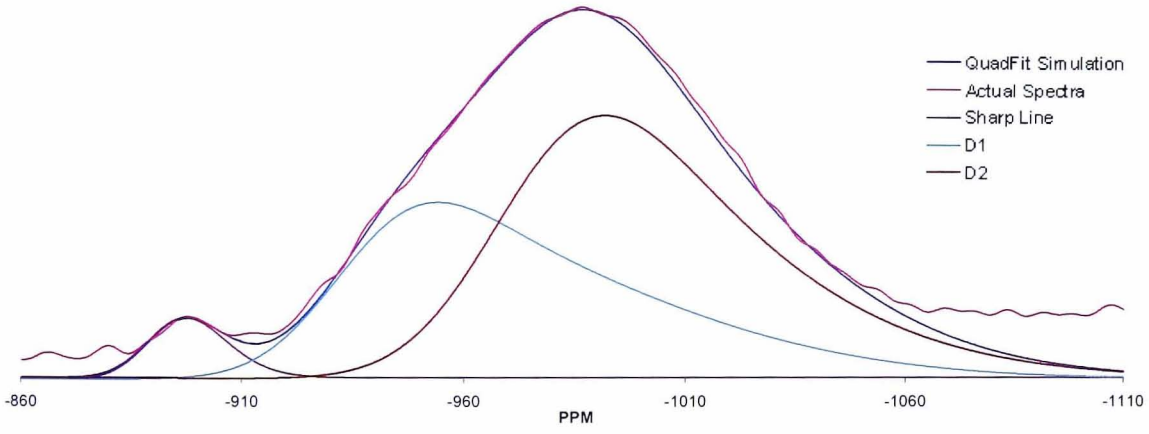

Figure 5.25 – Deconvolution of PMN-25PT spectra using Quadfit

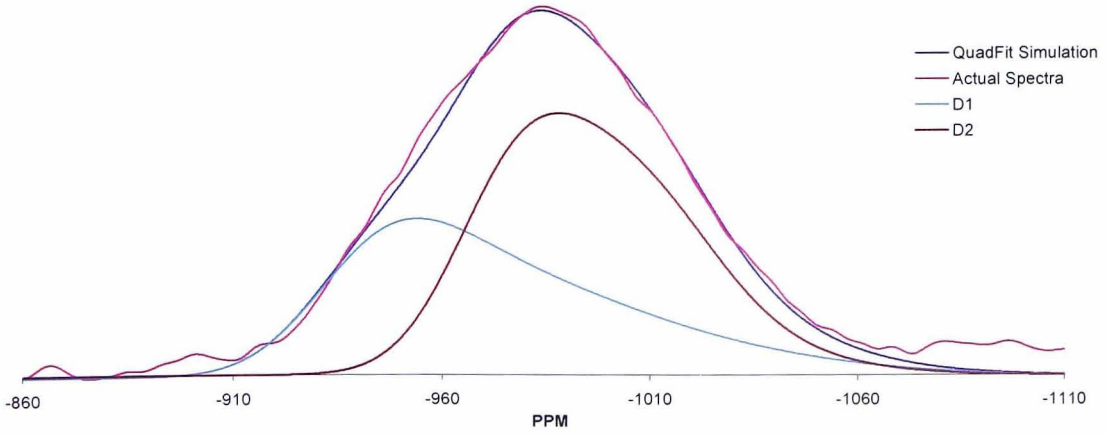

Figure 5.26 – Deconvolution of PMN-30PT spectra using Quadfit

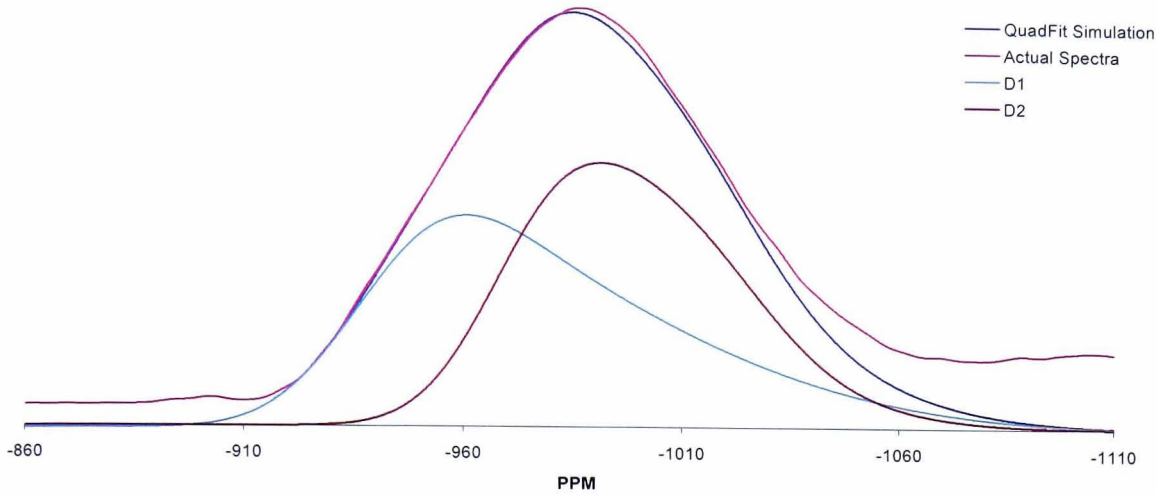

Figure 5.27 – Deconvolution of PMN-33PT spectra using Quadfit

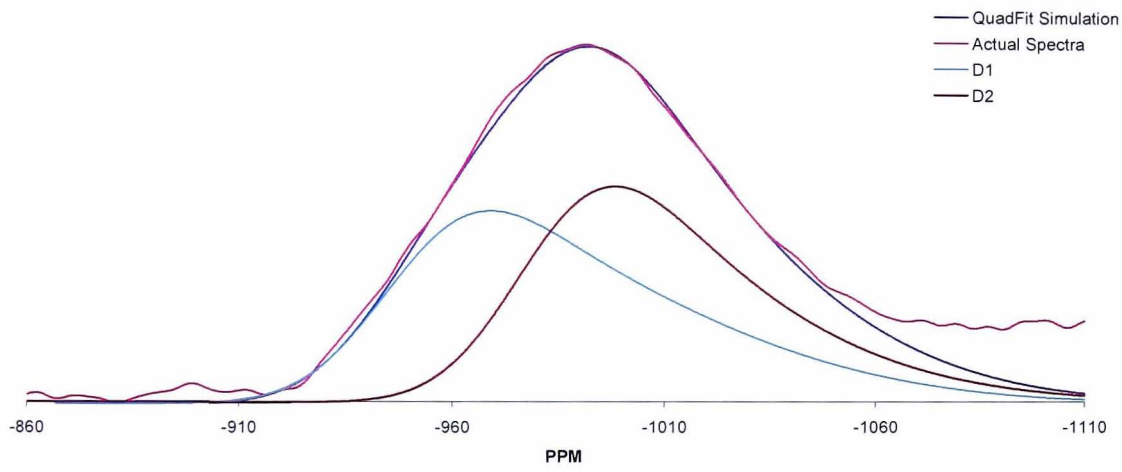

Figure 5.28 – Deconvolution of PMN-35PT spectra using Quadfit

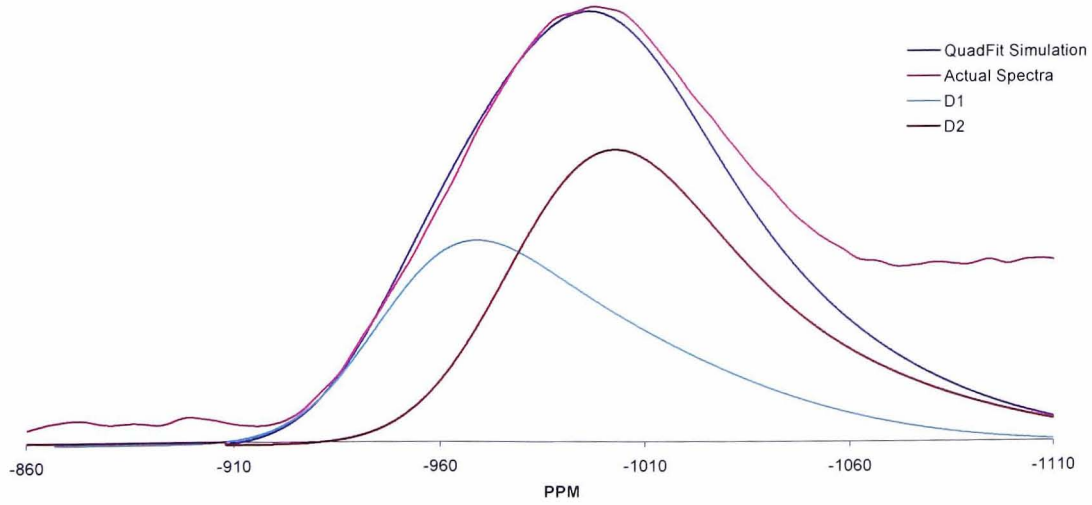

Figure 5.29 – Deconvolution of PMN-37PT spectra using Quadfit

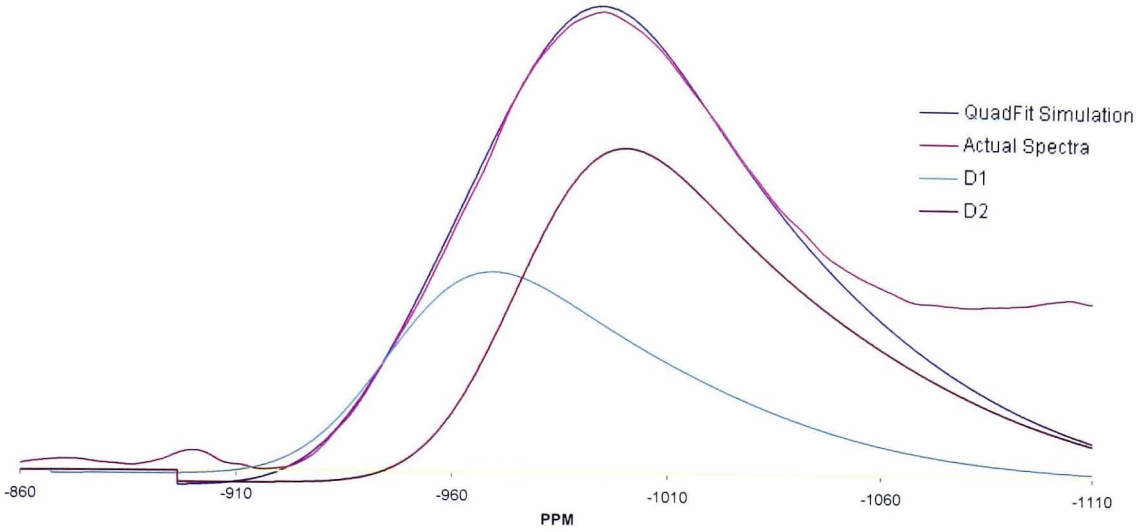

Figure 5.30 – Deconvolution of PMN-40PT spectra using Quadfit

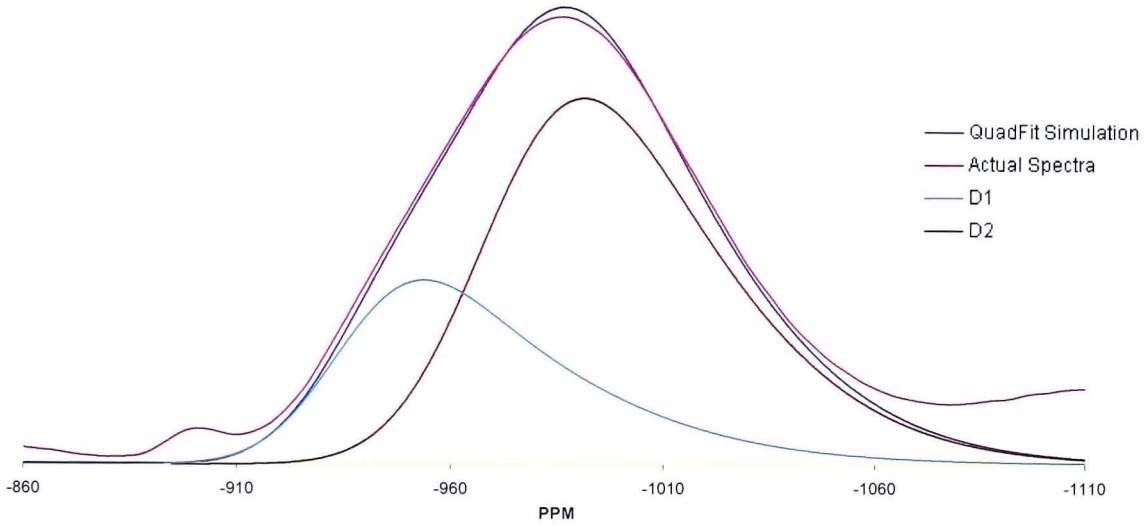

Figure 5.31 – Deconvolution of PMN-50PT spectra using Quadfit

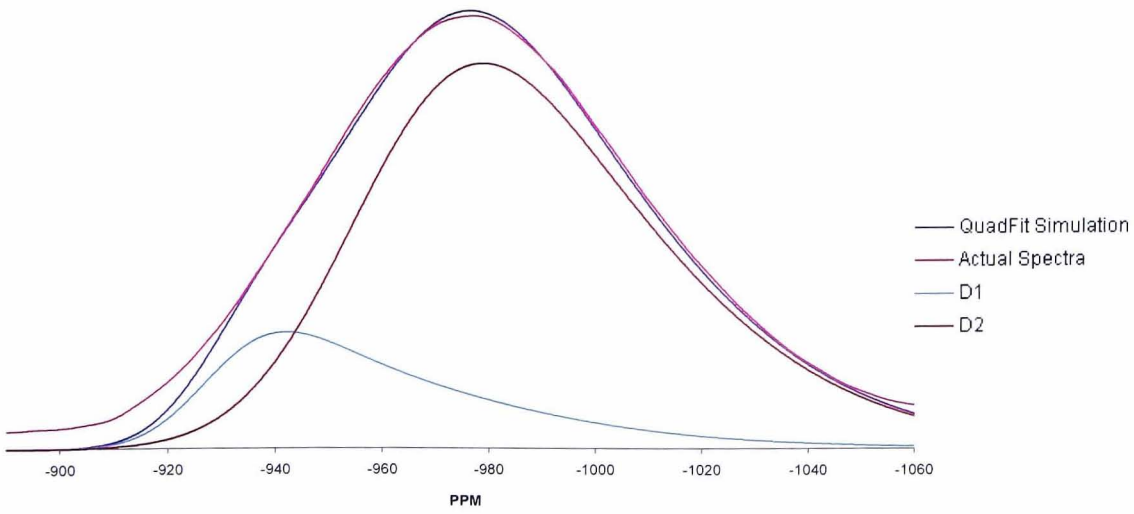

Figure 5.32 – Deconvolution of PMN-55PT spectra using Quadfit

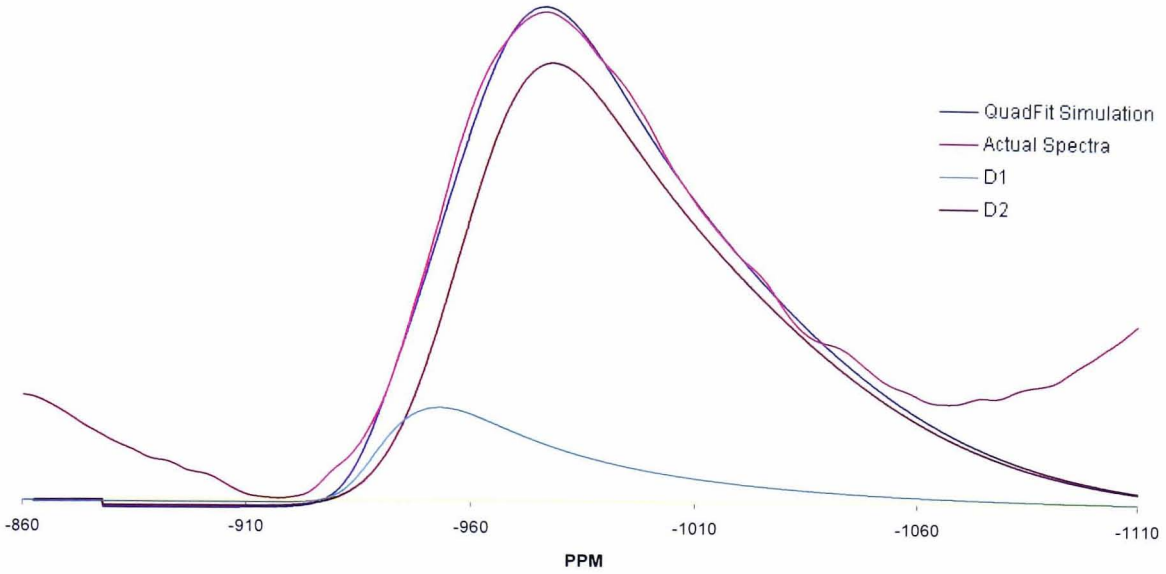

Figure 5.33 – Deconvolution of PMN-70PT spectra using Quadfit

Sample	^{93}Nb MAS NMR at 14.1T					
	peak	Shift ± 5 (ppm)	Broadening (Hz)	χ_Q Width ± 0.2 (MHz)	χ_Q Centre ± 0.2 (MHz)	Integral Int ±1%
PMN	Sharp	-895	300	2	12	14%
	D1	-924	800	6	28.6	46%
	D2	-977	800	6	24.4	40%
PMN-04PT	Sharp	-895	300	2	12	14%
	D1	-924	800	6	28.6	40%
	D2	-977	1000	6	24.4	47%
PMN-10PT	Sharp	-895	300	2	12	7%
	D1	-928	800	6	28.6	51%
	D2	-970	800	6	24.4	42%
PMN-20PT	Sharp	-895	400	2	12	5%
	D1	-926	800	6	28.6	45%
	D2	-968	1000	6	24.4	50%
PMN-25PT	Sharp	-895	400	2	12	4%
	D1	-928	800	6	28.6	40%
	D2	-970	1000	6	24.4	56%
PMN-30PT	D1	-928	800	6	28.6	42%
	D2	-964	800	2	24.4	58%
PMN-33PT	D1	-928	900	6	28.6	50%
	D2	-962	850	2	24.4	50%
PMN-35PT	D1	-928	900	6	28.6	50%
	D2	-964	900	6	24.4	50%
PMN-37PT	D1	-928	900	6	28.6	41%
	D2	-968	1100	10	24.4	59%
PMN-40PT	D1	-928	900	6	28.6	37%
	D2	-957	900	7	24.4	63%
PMN-50PT	D1	-928	800	6	24.4	32%
	D2	-963	1000	5	24	68%
PMN-55PT	D1	-928	500	6	24.4	20%
	D2	-959	1000	5	24	80%
PMN-70PT	D1	-928	500	6	24.4	13%
	D2	-948	700	6	24	87%

Table 5.3 - Deconvolution parameters of ^{93}Nb MAS spectra for PMN-xPT solid solutions.

Examining Table 5.3, several clear trends emerge, below 25 mol. % PT, the spectra require three peaks for accurate simulation. There is clearly a sharp line whose integrated intensity decreases from 14% in the initial PMN sample, disappearing beyond the 25 mol. % PT. The other two peaks, correspond to much broader features with much larger χ_Q values and have been assigned on the basis of Hoatson's data as D_1 = 24.4 MHz and D_2 = 28.6 MHz. Up to PMN-40PT these χ_Q values allowed simulations of the spectra. It is difficult to discern any clear trend in these integrated intensities until 40 mol. % PT from which point onwards the peak D_2 begins to dominate. It can also be noted, that there are some small variations in the shift at high PT content, however more accurate determination of the shift would be necessary before anything certain can be deduced. Now that some spectral variations have been determined these should be connected to the atomic ordering that is believed to be taking place in the compound.

5.5.2 Modelling ^{93}Nb NMR data from PMN-PT

As discussed previously Blinc *et al.*[17] showed that the distribution of Mg^{2+} and Nb^{5+} is not completely random but follows some form of ordering on the B-site of the material. High Resolution Electron Microscopy (HREM) studies[28] have shown that there are alternating nanodomains dispersed in a disordered matrix. These nanodomains are also considered to consist of alternating planes of β' and β'' sites. The β'' layers are believed to be occupied solely by Nb^{5+} ions, while there are several competing models which differ primarily in the composition of the β' layer. For example Pirc *et al.*[19] detail their spherical random bond random field (SRBRF) model where they talk about the motion of the various β' and β'' layers giving rise to polar

clusters in the material. Hoatson *et al.*[21] have introduced the idea of using quantitative NMR data to obtain a more accurate description of the distribution around the β' layer in the PMN-PSN series of materials. Here on the basis of the deconvolutions described on the 13 PMN-xPT samples a similar insight into the specific nearest β neighbour (nβn) will be attempted, for PMN-PT using the relative integrated peak intensities shown in Table 5.3. Furthermore the specific (nβn) environments, will be assigned to specific spectral features. The variation of the intensity of these features will be used to corroborate our assignments.

To describe the niobium coordination the nearest β neighbour configurations are designated by the number of Mg, Ti and Nb cations (N_{Mg}, N_{Ti} and N_{Nb}); each number can range from 0 to 6 with the requirement that their sum is 6. This is because in our definition of nearest β neighbour we are talking about the closest 6 β cations to our central Nb^{5+} ion. In reality these are actually the next-next nearest neighbour to the central Nb^{5+} ion as we are ignoring the neighbouring first shell of 6 oxygen ions and then the next shell of eight Pb^{2+} ions, as these do not change, and only consider this next-next neighbouring β cation shell. In Figure 5.34 each of the points represents a specific nβn configuration. Thus it is quite clear that a total of 28 possible nβn configurations exist for PMN-xPT materials.

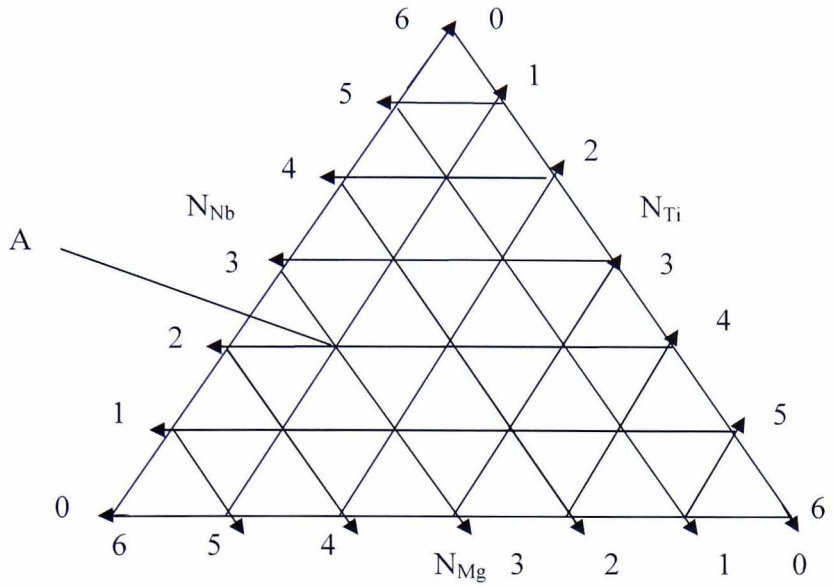

Figure 5.34 – The 28 nβn configuration of the Nb^{5+} cations and their assignments. The three vectors represent indicate the numbers of each cation and hence there triplet co-ordinate (N_{Mg},N_{Ti} and N_{Nb}). For example point A represents a central niobium that corresponds to 1 Ti, 2Nb and 3 Mg neighbours.

Thus for PMN-xPT solid solutions the stoichiometric formulae can be represented as $Pb(\beta'_{1/2}\beta''_{1/2})O_3$ with β' being a random mixture of Mg^{2+}, Nb^{5+} and Ti^{4+} cations while β'' is a pure Nb layer. Given the chemical composition of the sample

$$(1-x)Pb\left(Mg_{1/3}Nb_{2/3}\right)O_3 - xPbTiO_3 \tag{5.1}$$

the different cation concentrations can be expressed as

$$Mg = \frac{1-x}{3};\ Nb = \frac{2(1-x)}{3};\ \text{and Ti} = x$$

However these cations are now divided between the two layers (β' and β'') described above. Hence if we consider the probability of having a B-cation in the β'-type layer which is an Nb^{5+} with a nβn configuration (N_{Mg},N_{Ti} and N_{Nb}) then this can only have niobium in the next coordination layer (i.e. β''), so that

$$P_{\beta' Nb}(N_{Mg},N_{Ti}, x) = \tfrac{1}{2}C_{\beta' Nb}\delta(N_{Mg},N_{Ti}) \text{ where } \delta = 1 \text{ when } N_{Mg} = N_{Ti} = 0 \tag{5.2}$$

Furthermore as already shown in Figure 5.34, each Nb^{5+} cation in the β'' layer can have 28 possible configurations from the cations that come from the two adjacent β' layers as illustrated in Figure 5.35 below

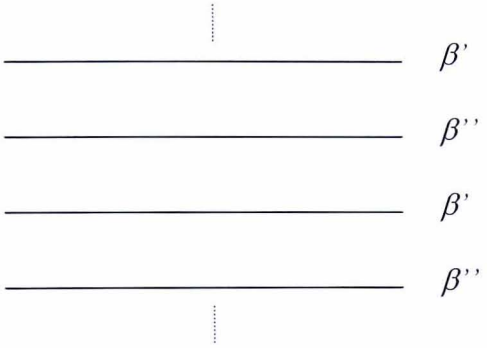

Figure 5.35 - Alternating β' *and* β'' layers illustrating the two β' layers next to each β'' layer.

$$P_{\beta'' Nb}(N_{Mg}, N_{Ti}, x) = \frac{1}{2}\frac{6!}{N_{Mg}!N_{Ti}!N_{Ti}!}(C_{\beta' Mg})^{N_{Mg}}(C_{\beta' Ti})^{N_{Ti}}(C_{\beta' Nb})^{N_{Nb}} \qquad (5.3)$$

Hence for Nb we have

$$\frac{1}{2}+\frac{1}{2}C_{\beta' Nb} = \frac{2(1-x)}{3}$$

$$\text{Hence } C_{\beta' Nb} = \frac{1-4x}{3} \qquad (5.4)$$

The $C_{\beta' x}$ concentration can be also be similarly derived for the Ti and Mg cations

$$\frac{1}{2}C_{\beta' Mg} = \frac{1-x}{3} \text{ so that}$$

$$C_{\beta' Mg} = \frac{2(1-x)}{3} \qquad (5.5)$$

And similarly for Ti

$\frac{1}{2}\, C_{\beta' Ti} = x$, so that

$$C_{\beta' Ti} = 2x \qquad (5.6)$$

Thus the summation of the probability over the N_{Ti} and N_{Mg} is simply the total Nb^{5+} concentration $C_{Nb} = 2(1-x)/3$. Hence in order to "view" the probability of the random site model having a Nb^{5+} cation with nβn configuration (N_{Mg},N_{Ti},N_{Nb}) it is necessary to normalise our Eqn 5.2 with respect to C_{Nb}. Thus equation (5.7) below represents our model used to compute the random site model probablilities for the series of 28 possible nβn configurations for niobium in the β' layer.

$$P_{RS}(N_{Mg}, N_{Ti}, x) = \frac{1}{2}\frac{3}{2(1-x)}\frac{6!}{N_{Mg}!N_{Ti}!N_{Nb}!}(C_{\beta' Mg})^{N_{Mg}}(C_{\beta' Ti})^{N_{Ti}}(C_{\beta' Nb})^{N_{Nb}} \qquad (5.7)$$

Figure 5.36 below shows the random site predictions compared with our experimental results displayed previously in Table 5.3 and shown in parenthesis in the following diagrams.

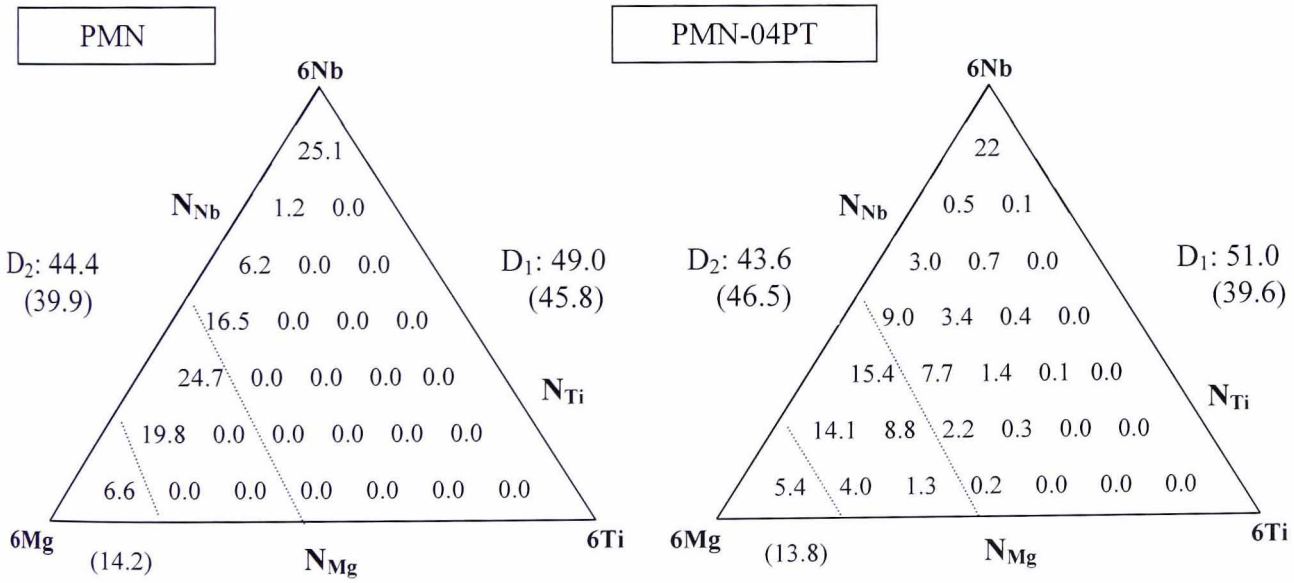

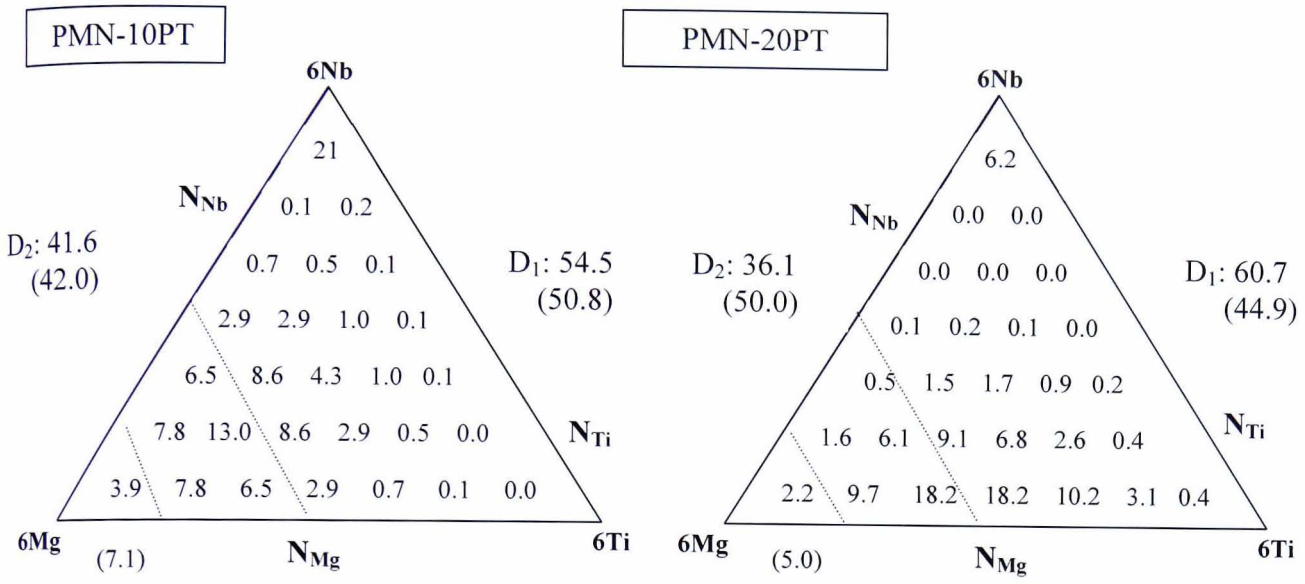

Figure 5.36 - Theoretical Random Site Predictions compared against experimental results (in parenthesis) at 14.1T for Ti concentrations <0.25

In the figures shown above we have divided each of the triangles into 3 distinct regions, the narrow peak corresponds to the configurations devoid of any niobium and in the cases illustrated above are only related to the $N_{Mg} = 6$ and $N_{Ti} = 0$ configuration, the two broad sites D_1 and D_2 have been assigned to 22 and 5 configurations both containing varying number of Nb^{5+}. Thus as can be clearly seen there is a very high level of agreement between the random site model and our experimental results, however what becomes clear is that this model will breakdown for x values greater than 0.25. This is simply due to the fact that as the concentration of Ti ions increases i.e. as the %PT approaches 25% relative to the concentration of Nb ions, a higher fraction of the Nb cations are required to maintain the pure Nb (β'') layer leaving only Mg and Ti cations on the β' layers. In order to illustrate this point consider the following numerical example. At x = 0.25 the concentrations of the cations in the β' layer can be calculated such that the β layer becomes a 50:50 mixture of Mg and Ti cations and no Nb, while the β'' layer still remains pure Nb.

Until x = 0.25 Ti concentration; the β'' layer will be purely niobium cations. Perhaps unsurprisingly it is also around this area of concentration that MPB and its various phase transitions are seen, as previously detailed in Section 5.2.

Thus in order to compute the predicted random site intensities of the ^{93}Nb spectra for PT concentrations > 0.25 we can now use the modified expression shown below. Note it is a simplified version of equation 5.7 as we are now sure that all of the Nb cations are in the β'' layer only. As the niobium is only in one layer the concentration which accounts for the probability of the distribution between the sites (normalisation factor) is no longer necessary as this probability now has to be 1.

$$P_{RS}(N_{Mg}, N_{Ti}, x) = \frac{6!}{N_{Mg}!N_{Ti}!}(C_{\beta' Mg})^{N_{Mg}}(C_{\beta' Ti})^{N_{Ti}} \qquad \text{(for x > 0.25)} \qquad (5.8)$$

The random site predictions versus the actual experimental results for the remaining PMN-xPT samples are shown below in Table 5.4

Number of Mg	PMN-PT Samples - Ti > 25%								
	PMN-25PT	PMN-30PT	PMN-33PT	PMN-35PT	PMN-37PT	PMN-40PT	PMN-50PT	PMN-55PT	PMN-70PT
0	1.6	2.3	2.9	3.3	3.8	4.7	8.8	11.8	26.2
1	9.4	12.1	13.9	15.2	16.5	18.7	26.3	30.3	39.3
2	23.4	26.4	28.1	29.0	29.9	31.1	32.9	32.4	24.6
3	31.3	30.8	30.2	29.6	28.9	27.7	22.0	18.5	8.2
4	23.4	20.2	18.3	17.0	15.7	13.8	8.2	6.0	1.5
5	9.4	7.1	5.9	5.2	4.6	3.7	1.7	1.0	0.2
6	1.6	1.0	0.8	0.7	0.6	0.4	0.1	0.1	0.0
D1	34.4	40.8	44.8	47.5	50.3	54.4	68.0	74.4	90.1
Exp D1	40%	42%	50%	50%	41%	37%	32%	20%	13%
D2	65.6	59.2	55.2	52.5	49.7	45.6	32.0	25.6	9.9
Exp D2	56%	58%	50%	50%	59%	63%	68%	80%	87%

Table 5.4 – Modified Random Site model for Ti concentrations greater than 0.25

These intensities are shown in a tabular form as opposed to the triangular diagrams of Figure 5.36, because at these compositions the only non-zero intensities fall along the bottom line of the triangle.

5.5.3 Discussion of ^{93}Nb NMR data from PMN-PT

It is quite clear from the models presented that there is a significant agreement between the modified random site predictions above and our own experimental results for low PT concentrations. We should however be aware of the limitations of this analysis and the conclusions that can be drawn from this. First there is a degree of arbitrariness where the demarcation between D_1 and D_2 has been established in the modelled intensities. Since we have no other basis on how to assign things the environments ascribed to these are kept constant. However the NMR data support the model that has been advanced here at low PT concentration as is observed in Figure 5.15 and 5.37(a) that the intensity of the sharp component which is assigned to the coordination of Nb by 6Mg, decreases steadily as Ti is added. For the sharp component it is also interesting to note that the observed intensity is always above the modelled intensity. Although at this stage the reason for this systematic discrepancy between the experimental and theoretical intensity of the sharp line is unsure, one can speculate that if the order in the β' were not completely random, but there is some preference for Mg clustering owing to cation size then this could result in a less preferable Nb environment with 6Mg. This would need to studied further. It is clear that the results of the NMR experiments for PMN are in accordance with a model of the local structure in which there are alternating layers β' (Nb and Mg randomly distributed in 1:1 ratio) and β'' layers (Nb only) normal to the (111) directions.

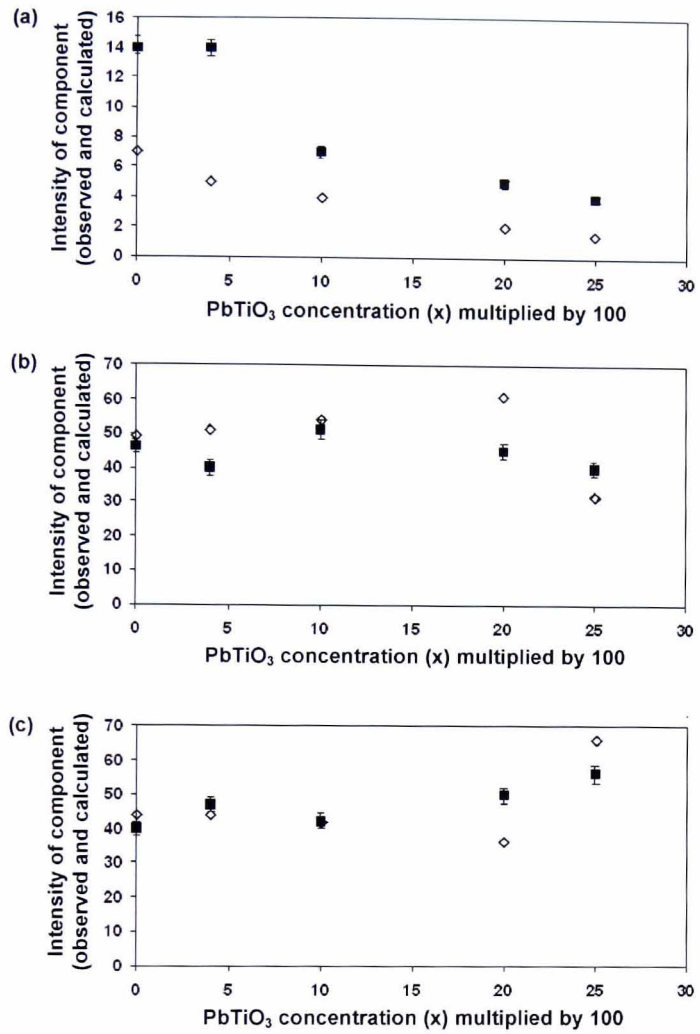

Figure 5.37 – Graphs of the observed and calculated percentage intensities for samples with $x \leq 0.25$ for (a) the sharp component; (b) D1; (c) D2. The solid squares represent observed intensities and the open diamonds calculated values from probabilities. Observed and calculated intensities each total 100% at each x.

This model gives rise to the rock salt arrangement of β' and β'' sites in the ordered regions and accounts for additional observed intensity in diffraction experiments at half integral positions ½ (h,k,l) when h, k and l are all odd, when Nb and Mg alternate, as observed, for example, in the experiments of [29]. On doping with $PbTiO_3$ for $x \leq 0.25$, our results are consistent with a model in which the β'' layers are preserved as Nb-only. Accordingly, Ti enters the β' layers, which are then modelled as a random distribution of Mg, Nb and Ti although again from the intensity of the sharp line this

may not be completely true and some clustering may be expected. Also in these complex spectra more experiments would be necessary to unambiguously define the true distinction between different sites. This includes faster spinning at higher magnetic fields and the use of 2D-MQ experiments. Without this increased sophistication it would inappropriate to currently push this modelling further. However it can be noted that the intensity of the peaks D_1 and D_2 begins to show significant discrepancy from the modelled distribution at higher PT content. This must be a result of the peaks becoming more similar and this can be seen as the clear presence of two broad peaks at low PT content (e.g. Fig. 5.21) is not apparent at e.g. 35PT (Fig. 5.28). From MQ data not shown here there is clearly an increasing distribution to the components at higher PT content.

5.6 ^{207}Pb NMR studies of PMN-PT samples

Piette and Weaver[30] reported the first NMR signals from ^{207}Pb in 1958. It is the stable isotope with the highest atomic number, that has a spin quantum number of I=1/2. Therefore the ^{207}Pb nucleus has no electric quadrupole moment, unlike the ^{93}Nb nucleus, but exhibits a large chemical shift anisiotropy owing to the large paramagnetic contribution to the shift from its numerous outer shell electrons. Thus the ^{207}Pb nucleus can act as a local probe, being particularly sensitive to any displacements of the ^{207}Pb cations from cubic positions. Unfortunately, long relaxation times, poor signal to noise ratios, large chemical shift ranges and typically broad line-shapes make it particularly challenging to obtain particularly results from ^{207}Pb NMR.

Fayon *et al.*[31] have measured the chemical shift parameters of the lead sites in a range of inorganic compounds. They discovered an empirical relationship between the isotropic chemical shifts and both the coordination number and mean Pb-O bond length. For covalent compounds, they showed that the isotropic chemical shift of lead has the strongest correlation with oxygen hybridisation and the electronegativity of the second nearest neighbour. Though owing to the disordered nature of PMN and PMN-xPT materials there are as of yet, no accurate references of the Pb-O bond lengths as determined through empirical NMR studies. However PMN is known to have a perovskite lattice structure with an average cubic unit cell symmetry[32]. The Pb(II) ions in PMN are surrounded by twelve oxygens with Pb-O bond lengths ranging from 2.47-3.25Å[33]. The disordered B-site occupancy leads to a wider distribution of Pb sites. These ferroelectric relaxors materials are known to exhibit a high degree of covalency of the Pb-O bonds.

The ^{207}Pb NMR spectra shown in Figure 5.38 were acquired at 4.7T (^{207}Pb: 40.88MHz) using a Chemagnetics-200 spectrometer. Most of the spectra were acquired using a "home-built" static 9mm probe, though a few spectra were obtained using a 4mm Bruker MAS probe spinning at approximately ~11 kHz. This was primarily to check the effect of MAS on the line width of the PMN-PT samples. The ^{207}Pb chemical shifts have been referenced with respect to solid lead nitrate, which has a known chemical shift of –3494ppm and is used commonly as a secondary standard with respect to aqueous 1.0 M $Pb(NO_3)_2$ at –2961ppm both of which are quoted with respect to the primary shift of ^{207}Pb with $Pb(CH_3)_4$ at 0 ppm. A spin echo pulse sequence as previously described in section 3.5.2 was used optimised with a pulse length of 2.5 μs and a recycle delay of 10 s. The relatively short relaxation time of PMN and PMN-PT samples has been reported[17] to be related to the motion of the Nb^{5+} cations and also to the proximity of a phase transition.

The large line width of these spectra shown in Figure 5.38 is probably best explained by the dominance of the CSA interaction which produces a wide distribution of shift values. This probably occurs as the structure undergoes phase transitions from the initial cubic phase upon addition of Titanium to PMN. It is however quite likely that the wide observable Gaussian like structure is composed of a whole range of Pb sites making the deconvolution of these spectra somewhat speculative on the basis of the data presented here.

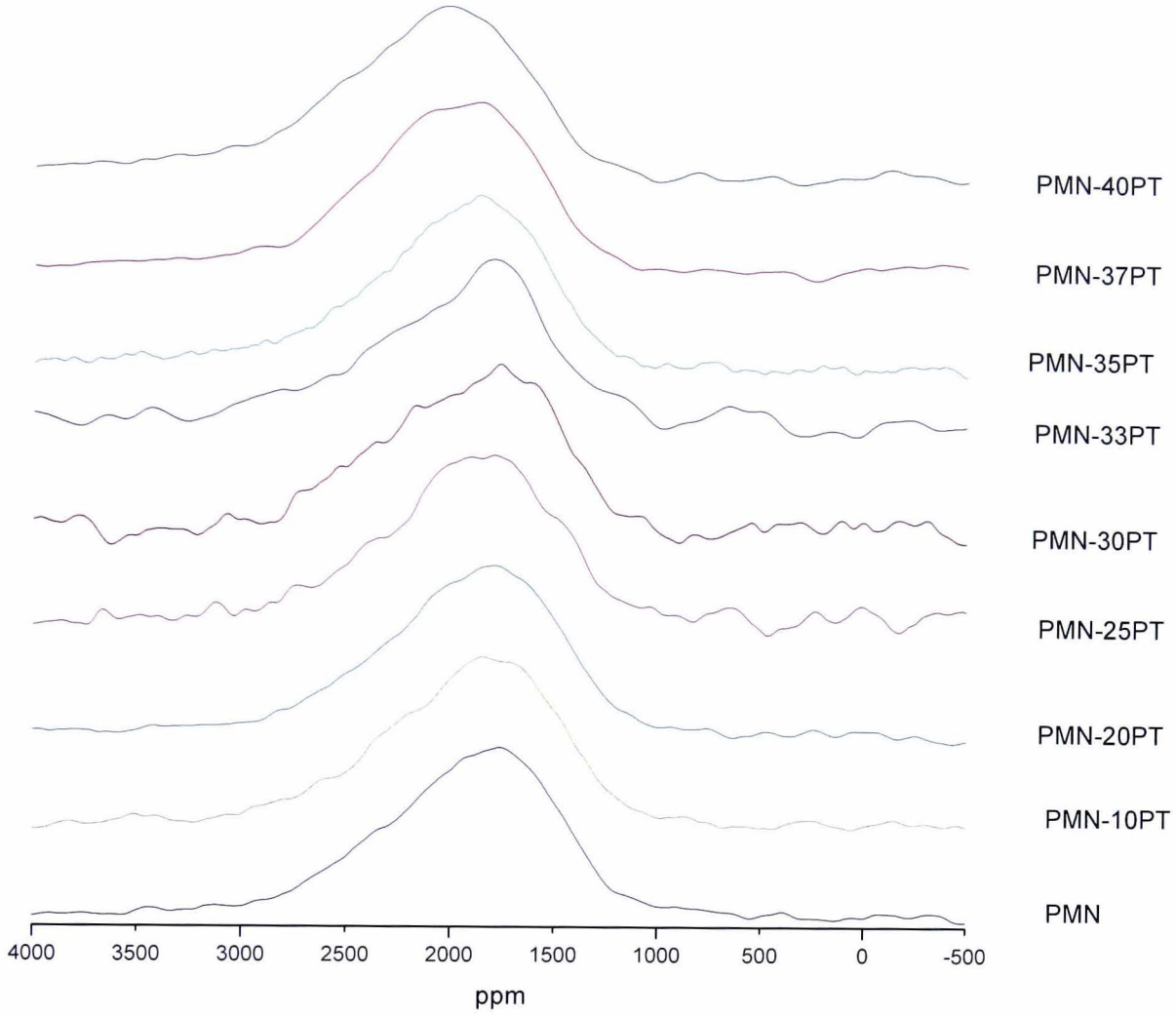

Figure 5.38 - Static ^{207}Pb NMR spectra for the 9 PMN-PT samples

Sample Name	Peak Position /ppm (±10ppm)	Peak Width /Hz (±50Hz)
PMN - Static	1980	35650
PMN - MAS 12kHz	2000	32400

Table 5.5- Shift and linewidths for ^{207}Pb NMR of PMN - Static vs MAS

The differences in shifts for the PMN-PT spectra that can be seen in Table 5.5 above is probably best explained by differing covalence of the Pb-O bonds. It is curious to note that it seems that both the shift and the linewidth are independent of the concentration of titanium in the samples. Furthermore from figure 5.39 shown below it is also apparent that even the MAS spectra fails to significantly narrow the spectral linewidth enough in these materials to provide a clearer picture of the individual lead sites in such complex ferroelectric relaxor materials.

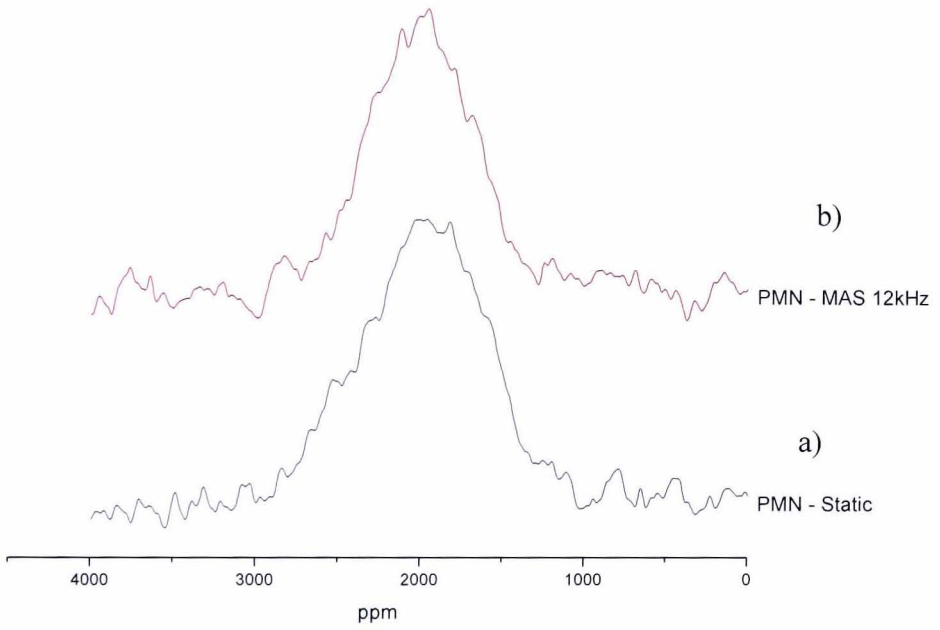

Figure 5.39 - ^{207}Pb NMR spectra showing a) Static Spectra b) MAS spectra at 12kHz

Very recently Zhou *et al.*[34] using a 2D-PASS spectra were able to separate the isotropic and anisotropic chemical shifts in PMN. They determined that $\mu(\delta_{iso})$ or the mean value of δ_{iso} was around –1343 ppm with $\sigma(\delta_{iso})$ the standard deviation around 206 ppm and that δ_{aniso} ranges from –575 to –360 ppm while the asymmetry parameter η ranged from 0.6 to 0.9, showing that the shielding tensor is not axially symmetric. The strong linear correlations between the isotropic and anisotropic

chemical shifts show that the Pb-O bonds vary from more ionic to more covalent environments. Thus they explain that the existence of these different Pb-O bonds is directly dependant on the distributions of the mixed B site cations.

Hence it would be an interesting study to see if indeed, in the PMN-xPT samples the lead distorts away from the larger Mg and Ti cations and towards the niobium cations. Hence from our own ^{93}Nb NMR study of PMN-xPT samples in section 5.5 of this chapter, we identify two broad disordered components as D_1 and D_2. These components involve niobium cations with at least one nearest β site Nb neighbour, hence it follows that these components should have a direct relationship on the large off-centre A-site distortions of the Pb^{2+} cation. This may also explain why D_1 and D_2 account for a more significant proportion of the material if it is a relaxor ferroelectric.

5.7 ^{17}O NMR studies of PMN-PT samples

The application of solid state NMR to probe these ferroelectric relaxor materials is targeted at investigating the link between the atomic scale structure/ordering and their properties. In many other systems ^{17}O solid state NMR has been shown to be a very good probe of ordering in inorganic materials, even when they are structurally disordered[35,36,37]. Here the MAS NMR spectra of two ^{17}O-enriched perovskite samples, pure PMN and PMN-35PT (close to the MPB), both in their initial as-formed amorphous state and in the final crystalline product, are presented (Fig. 5.40) to see what information ^{17}O NMR can provide.

Figure 5.40(a) shows the spectrum of the amorphous sol-gel formed PMN with a moderately well defined peak at ~470ppm, but there is also some broader structure stretching down to lower frequencies with perhaps some features present at 360 and 290ppm. On crystallisation (Fig. 5.40(b)) the PMN sample shows a ~50% reduction in linewidth and also a significant change in the dominant peak position to ~378 ppm, although this might be two quite closely spaced lines at 487 and 380 ppm. In Fig. 5.40(c), the ^{17}O MAS NMR spectrum from amorphous PMN-35PT, shows the broadest structure of all these samples such that in the initial amorphous state a width of ~405ppm is observed, although it is possible to make out two distinct overlapping broad peaks, a more intense one centred at 383ppm and a second at 172ppm. The key sample to form is a well crystallised PMN-35PT, but as can be seen from figure 5.40(d) it proved very difficult to obtain a spectrum with a satisfactory signal to noise ratio. The sample was manufactured several times to ensure that as little ^{17}O label as possible was lost as in some of the earlier batches some of the label may have been lost due to leaks resulting in no ^{17}O signal being detected. In Fig. 5.40(d) it is just about possible to make out a peak at ~373ppm, but any finer details cannot be

determined from this spectrum. The principal shift range associated with all these PMN-based materials appears to be relatively close to one another and lies from 300 to 500ppm.

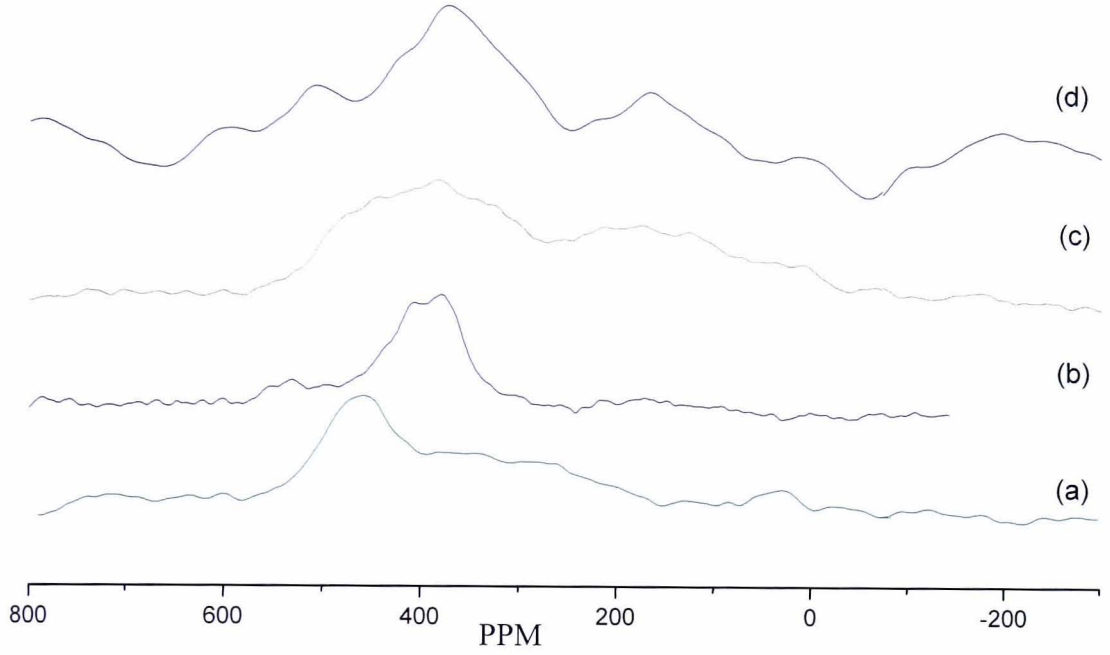

Figure 5.40 - ^{17}O MAS NMR spectra of enriched sol-gel samples (a) amorphous PMN, (b) crystalline PMN, (c) amorphous PMN-35PT, (d) crystalline PMN-35PT

Sample	^{17}O NMR at 8.45T	
	Position (ppm)	Width (ppm)
Amorphous PMN	468	195
	360	not determined
Crystalline PMN	410	not determined
	378	95
Amorphous PMN-35PT	383	405
	172	
Crystalline PMN-35PT	373	129

* Errors: Peak Position ± 2ppm, Widths ± 2 ppm

Table 5.6 - ^{17}O MAS NMR data amorphous and crystalline perovskite relaxor samples

The key question here is can the ^{17}O NMR provide any additional insight into the ordering of the metals in the PMN perovskite (ABO_3) structure, particularly the metals on the B sites which correspond to the β' and β'' layers. Such ordering is believed to important for the relaxor properties of these materials. The spectra of oxygen-enriched precursor oxides for PMN-PT are reported in Chapter 4 or have been previously given in detail[35]. Additionally the ^{17}O MAS NMR of the closely related columbite, both in the initial, amorphous precursor phase and in the final highly crystalline product, where there are local magnesium and niobium nearest neighbour environments have been discussed in section 4.2.3.3. Also ^{17}O MAS NMR has very recently been reported[38] from PT which showed two very sharp resonances at 647 and 443 ppm from axial and equatorial oxygens respectively. These peaks both correspond to Ti-O-Ti with additional coordination to lead, but as is widely seen in perovskites[39] it is usually the B cation that strongly defines the ^{17}O shift.

In the initial amorphous PMN precursor the ^{17}O MAS NMR peaks of the component pure oxides would be at 47ppm (MgO), 290ppm (PbO) and 565ppm (for ONb_2 in Nb_2O_5). So a peak at 468 ppm and extending over the range ~550-150 ppm is an indication of the variety of local coordinations. The fact that there is not a whole set of well defined individual peaks is probably an indication of the variation in each of the local environments due to variations in bond length in the amorphous state. Then on crystallisation there is the definite peak at 378 ppm and a very great reduction in the broad component. PMN is a cubic perovskite so that there should be one inequivalent structural oxygen. However there can be different metal neighbours to this oxygen site (see Fig. 5.41).

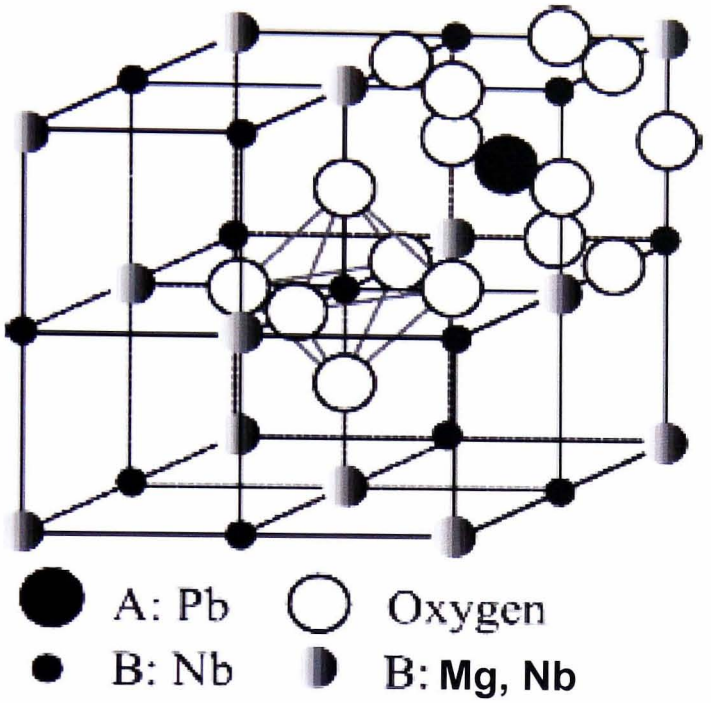

Figure 5.41 Schematic view of the PMN structure showing the atomic distribution.

The above structure shows in a more conventional crystal structure with the atomic positions and the (111) planes being the β' (mixed Nb, Mg) and β'' (pure Nb layers). These are the B cations and the oxygens clearly link these B cations between adjacent layers. There will also be bonds to Pb, but this bonding will effectively be constant for all oxygens. Hence the bonds will be Mg-O-Nb and Nb-O-Nb in the ratio 2:1. The peak at 378 ppm is towards the middle of the range for the pure component oxides so it is likely that the ^{17}O enrichment has been successfully achieved in the PMN. It is somewhat surprising that separate resonances from the two supposed fragments Mg-O-Nb and Nb-O-Nb are not seen. In silicates all the distinct resonances from different fragments are usually readily resolved. Here a possible reason for the lack of resolution is that the oxygens have bonds to the lead as well as the other metals thereby any change of an individual metal will have less effect on the shift.

The crystalline nature of this sample is indicated by the reduction in the width of the main peak and the removal of the broad underlying component.

For PMN-35PT similar peaks and effects of heat treatment are observed. The peaks in the amorphous state show a shift that extends over an even broader range than for the precursor PMN. This can be anticipated as there are more different cations in PMN-PT than PMN. The crystalline product again shows a decrease in the width but it is not as narrow as for the PMN. These differences between PMN and the PMN-PT mixture are both probably due to the fact that the B site can have a third occupant, titanium, and although still a nominal cubic perovskite there could be a larger range of distortions of local environments giving rise to a broader distribution of sites. This would need to be proved by further experiments. However again it is noteworthy that in this crystalline, but atomically disordered material distinct resonances cannot be observed from the different fragments as had been hoped to quantify the ordering with the PMN-PT structure.

5.8 Conclusions and Further work

In this chapter MAS and static NMR have been applied to different nuclei (^{17}O, ^{93}Nb, ^{207}Pb) in order to ascertain the applicability of solid state NMR to obtain a clearer picture of the composition dependence of the local structure in the PMN-PT series of materials and try and relate this to their intriguing ferroelectric relaxor behaviour. Even though NMR is one of the few techniques available that allows us to probe this novel yet complex perovskite ferroelectric material at this length scale, there have been relatively few NMR studies of this class of materials especially PMN-PT. This is most likely a result of the nuclei in this system being challenging for NMR studies, a conclusion this thesis reinforces.

Three key nuclei were studied – ^{17}O, ^{207}Pb and ^{93}Nb. For direct 1D static and MAS spectra of ^{207}Pb although good quality spectra could be obtained they were broad and generally featureless and did not provide any real insight since there was insufficient resolution to allow any further analysis. It may be that more sophisticated NMR techniques such as 2D-PASS NMR could be employed to separate out different components of the lineshape. The ^{17}O results were also somewhat inconclusive as again in the 1D MAS data clear resolution of different sites was not possible. This is probably a result of the level of enrichment in the initial sample and the ability to contain the enrichment under the high temperature heat treatment that is necessary to form the samples. If very high initial enrichment is used (70-90at%, very expensive!) and it can be retained then perhaps 2D sequences can be used (such as multiple quantum) to separate out the different components. However a conclusion here is that direct, 1D MAS does not produce highly resolved spectra of the different M-O-M' fragments that are expected to be present.

It needs to be recognised that such materials while crystalline nevertheless because of atomic disorder contain a whole range of environments that cannot be separated since they are effectively a continuum of environments. Other cases in inorganic materials where ^{17}O NMR has provided information about the atomic ordering (e.g. sol-gel silicates and melt quench glasses) nearest neighbour effects are relatively simple and bipolar (i.e. M-O-M' bonds), whereas here the ordering effects of the β' and β'' layers are much less straightforward. In the ABO_3 perovskite structure there are B-O-B' links but unlike the other examples where oxygen has been used to distinguish such units, here the oxygen also has links to Pb which remain constant and mean that there is less variation due to the B bonding. Also in the PMN-PT there will be several different B-O-B' bonds e.g. Nb-O-Mg, Nb-O-Pb, etc. which

may result in a number of overlapping peaks and a broad distribution of resonances (broadened further by the structural variations between sites in these materials), but more work is necessary to understand the main causes of the line broadening.

The most important observation here has been the ^{93}Nb NMR since in the three previous reports from PMN[19,20,21] there was no agreement as to the correct NMR interaction parameters for the niobium sites. Our data strongly agrees with that of Hoatson *et al.*[21] suggesting that those of the other workers must indeed be incorrect and this is a key observation as the only previous detailed study of ^{93}Nb NMR in PMN-PT will consequently have used completely incorrect parameters to simulate their ^{93}Nb NMR spectra from PMN-PT. Hence there are three distinguishable niobium populations (at least with low PT content), a much more symmetric environment associated with 6 magnesiums (C_Q = 12 MHz) and the two other associated with mixtures of magnesium, niobium and titanium (C_Q = 24.4 and 28.6 MHz). The next, next nearest neighbours for each of the two broader resonances can be consistently, if not unambiguously assigned by using the two layer model suggested by Hoatson *et al.*[21] for PMN-PSN. This model could be adopted directly in PMN-PT for <25% PT with two layers, a purely niobium-containing one and a randomly mixed (Mg, Nb, Ti) one. The intensity distribution indicates that the mixed layer is largely randomly mixed, but with a slight tendency for Mg to cluster. Here the assignment of particular species with lines D_1 and D_2 is still problematic, but at low PT contents the intensity variation can be approximately explained. For PMN-PT this model had to be modified from that for PMN-PSN as in that system it was always possible to maintain a pure niobium layer at *all* PSN concentrations. The new model developed for PT >25%, whereby excess Ti (rather than a random mixing) occurs in the initially pure niobium layer was able to provide an accurate description of the observed intensity changes,

with the structural assignment of all the peaks being consistent across the *whole* composition range. Perhaps one could speculate that the NMR reported here is giving an important clue as to the diffuse nature of the relaxor ferroelectric transition and the type of phase it might occur in. Ferroelectric transitions are related to local structural distortion. In PMN-PT the ^{93}Nb and ^{17}O NMR shows clearly that the atomic disorder produces a whole range of sites with a range of *local* structural distortions, that blur the macroscopic bulk transition in these samples.

There are two clear sets of further study that could be undertaken. One would be better constrain the ^{93}Nb NMR and hence the spectral intensities and the distribution of interaction parameters by a combination of higher field data and multiple quantum experiments. The other would be to put down a challenge to theoretical physicists by giving the local ordering and the range of distortions modelled by NMR and seeing what the calculated ferroelectric transition profile should be – an intriguing question that may remain intractable to calculation/computation for some time to come.

References

[1] H. Ouchi, K. Nagano, S. Hayakawa, *J. Am. Ceram. Soc.*, 48, 630-635 (1965)

[2] L. Bellaiche, D. Vanderbilt, *Physical Review Letters*, 83 [4], 1347-1350 (1999)

[3] D. Vanderbilt, M.H. Cohen, *Physical Review B*, 63, 094108 (2001)

[4] A.F. Devonshire, *Philos. Mag.*, 40, 1040 (1949)

[5] O. Noblanc, P. Gaucher, G. Calvarin, *J. Appl. Phys.*, 79 [8] 4291-4297 (1996)

[6] B. Noheda, J.A. Gonzalo, L.E. Cross, R. Guo, S.E. Park, D.E. Cox, G. Shirane, *Physical Review B*, 61, 8687 (2000)

[7] Z.G. Ye, B. Noheda, M.Dong, D.Cox, G. Shirane, *Physical Review B*, 64, 184114 (2001)

[8] G. Xu, H. Luo, H. Xu, Z. Yin, *Physical Review B*, 64, 020102 1-3 (2001)

[9] A.K. Singh, D. Pandey, *J. Phys. Condens. Matter*, 13 L931-L936 (2001)

[10] B. Noheda, D.E. Cox, G. Shirane, J. Gao, Z.G. Ye, *Physical Review B*, 66, 054104 1-10 (2002)

[11] Y. Guo, H. Luo, D. Ling, H. Xu, T. He, Z. Yin, *J. Phys. Condens. Matter,* 15, L77-82 (2003)

[12] H. Fu, R.E. Cohen, *Nature 403*, 281 (2000)

[13] A.K. Singh, D. Pandey, *Physical Review B*, 67, 064102 1-12 (2003)

[14] K. Ohwada, K. Hirota, P.W. Rehrig, Y. Fujii, G. Shirane, *Physical Review B*, 67, 094111 (2003)

[15] G. Xu, Z. Zhong, Y. Bing, Z.G. Ye, G. Shirane, *Physical Review B*, 67, 104102 (2003)

[16] G. Xu, D. Viehland, J.F. Li, P.M. Gehring, G. Shirane, *J. Phys. Condens. Matter,* 0307144 v2 (2004)

[17] R. Blinc, A. Gregorovic, B. Zalar, R. Pirc, V.V. Laguta, M.D. Glinchuk, *Physical Review B*, 63, 024104 (2000)

[18] R. Pirc, R. Blinc, *Physical Review B*, 60, 13 470 (1999)

[19] L.P. Cruz, J. Rocha, J.D. Pedrosa de Jesus, J.M. Savariault, J. Galy, *Solid State Nucl. Mag. Reson.,* 15, 153-158 (1999)

[20] J. J. Fitzgerald, S. Prasad, J. Huang, J.S. Shore, *J. Am. Ceram. Soc.,*122, 2556 (2000)

[21] G.L. Hoatson, D.H. Zhou, F. Fayon, D. Massiot, R.L. Vold, *Physical Review B,* 66, 224103 (2002)

[22] D.H. Zhou, G.L. Hoatson, R.L. Vold, *J. Mag. Reson.,* 167, 242-252 (2004)

[23] H.C. Wang, W.A. Schulze, *J. Am. Ceram. Soc.,*73, 825-832 (1990)

[24] Prof. P.A. Thomas, private communication, (2004)

[25] M.E. Smith, E.R.H van Eck, *Prog. Nucl. Mag. Reson. Spectrosc.,* 34, 159 (1999)

[26] D. Zekria, "Phases and Structures of Lead Magnesium Niobate Titanate", *D.Phil Thesis,* Somerville College, Oxford (2004)

[27] G. Czjzek, J. Fink, F. Gotz, H. Schmidt, *Prog. Nucl. Mag. Reson. Spectrosc., Physical Review B,* 23, 2513 (1981)

[28] J. Chen, H.M. Chan, M.P. Harmer, *J. Am. Ceram. Soc.,*72, 593 (1989)

[29] B. Chaabane, J. Kriesel, B. Dkhil, P. Bouvier, M. Mezouar, *Phys. Rev. Lett.,*90, 257601 (2003)

[30] L.H. Piette, H.E. Weaver, *J. Chem. Phys.,*28, 735-736 (1958)

[31] F. Fayon, I. Farnan, C. Bessada, J. Coutures, D. Massiot, J.P. Coutures, *J. Am. Chem. Soc.,* 119, 6837-6843 (1997)

[32] A. Verbaere, Y. Piffard, Z.G. Ye, E. Husson, *Mater. Res. Bull.,* 27, 1227-1234 (1992)

[33] N. de Nathan, E. Husson, G. Calvarin, J.R. Gavarri, A.N. Hewat, J.A. Morrel *J. Phys. Condens. Mater.,* 3, 8159-8171 (1991)

[34] D.H. Zhou, G.L. Hoatson, R.L. Vold, F. Fayon, *Physical Review B,* 69, 134104 (2004)

[35] K.J.D. Mackenzie, M.E. Smith, '*Multinuclear Solid-State NMR of Inorganic Materials'*, Pergamon, 2002

[36] P.N. Gunawidjaja, M.A. Holland, G. Mountjoy, D.M. Pickup, R.J. Newport, M.E. Smith, *Solid State NMR,* 23, 88 (2003)

[37] D.M. Pickup, F.E. Sowrey, R.J. Newport, P.N. Gunawidjaja, K.O. Drake, M.E. Smith, *J. Phys. Chem. B,* 108, 10872, (2004)

[38] A. Baldwin, P.A. Thomas, R. Dupree, *J. Phys: Condens. Matter*, 17, 7159, (2005)

[39] T.J. Bastow, P.J. Dirken, M.E. Smith, H.J. Whitfield, *J. Phys. Chem.*, 100, 18539, (1996)

Chapter Six

6.1 Introduction

The first reported paper describing the interesting ferroelectric properties of the A-site, complex perovskite compound NBT ($Na_{0.5}Bi_{0.5}TiO_3$), was by Smolenskii *et al.*[1] in 1960. Interestingly this was the same group who also first reported on the interesting ferroelectric properties of PMN-PT two years earlier. Though lead-based ferroelectrics such as PZT, PLT and PMN-PT are well known to exhibit some of the highest piezoelectric co-efficients[2], the toxicity of lead and the high vapour pressure of lead oxide make it more difficult to produce these easily and safely. Furthermore this also leads to these materials being unsuitable for more specific biological applications. Hence a small number of researchers became increasingly involved in the research of lead-free piezoelectric materials. NKBT ($Na_{1-x}K_xBi_{0.5}TiO_3$) is a promising candidate for use in biological applications and devices as single crystal forms are readily available and have enhanced ferroelectric and electromechanical properties. Furthermore the sintering temperature of 1150°C is compatible with existing multilayer[3] technologies. However even though controlling the stoichiometry of NKBT is much easier than that of lead-containing ferroelectric materials, the volatilisation of the bismuth during the heat treatment often brings about some unwanted effects on the physical properties of the material.

However compared to their lead-based counterparts there is a shortage of literature detailing these materials, and there have been no reported NMR studies of NKBT single crystals to date.

6.2 NBT, KBT and NKBT

NBT ($Na_{0.5}Bi_{0.5}TiO_3$) is a prototype perovskite relaxor ferroelectric[4]. As a characteristic of such relaxor ferroelectrics it shows a broad dielectric anomaly, the temperature of which is dependent upon frequency. On average NBT possesses a rhombohedral (R) structure of R3c symmetry in which the Bi is severely under-bonded[5]. A recent EXAFS experiment[6] has indicated that this may be because previous crystallographic studies have underestimated the Bi-O bond length, and that it is quite possible that there are between 3 and 4 short Bi-O bonds. Unfortunately crystallographic data is not sufficiently sensitive to the local structure for a more complete model to be solved.

KBT ($K_{0.5}Bi_{0.5}TiO_3$) is also an A-site substituted perovskite ferroelectric compound[1]. There have been very few studies related to KBT, however, Smolenskii *et al.*[1] using X-ray diffraction techniques confirmed the perovskite structure of this material. In several subsequent XRD studies as a function of temperature, several authors have commented on an *unidentified intermediate phase,* which is both stable and ferroelectric at temperatures above 540 K. However there is still no clear agreement about the nature of this phase and some authors even regard this phase as antiferroelectric.

Doping NBT with potassium leads to the formation of NKBT ($Na_{1-x}K_xBi_{0.5}TiO_3$) and introduces a morphotropic phase boundary (MPB) in the material (the concept of MPB and its importance in ferroelectrics has already been discussed in detail in section 5.2 of this thesis) at around 20% K doping. As with the PMN-PT series of ferroelectrics the phase transition at the MPB is from Rhombohedral to Tetragonal (T,P4mm)[7]. It is of general interest to follow this structural change from the R to the T phase at an atomic

structural level and compare this to the average crystallographic structure. As discussed in detail for PMN-PT in Section 5.2 of this thesis we know that the phase transitions in PMN-PT take place via intermediate monoclinic phases and that the B-cations follow a random-site distribution among alternating B-cation filled planes. However as there is no compositional disorder on the B-sites of this material, it will be particularly interesting to see the role of the A-site substituting cations in NKBT and compare the local structural mechanisms with that of the PMN-PT system.

As details of the sample preparation have already been described in Section 3.8.3 of this thesis they will not be repeated in this Chapter.

6.3 ^{23}Na NMR studies of NKBT samples

^{23}Na is a quadrupolar nucleus with a magnetic spin quantum number I = 3/2. As it has 100% natural abundance it has much better NMR spectral sensitivity than ^{17}O NMR. As with all quadrupolar nuclei (such as the ^{93}Nb discussed in greater detail in the previous chapter) the use of higher magnetic fields and higher MAS speeds helps to significantly narrow the second-order quadrupolar broadening. Generally in simple sodium compounds ^{23}Na MAS NMR spectra show quite symmetrical Na environments with quite narrow resonances, in these compounds the quadrupolar interaction parameters are often close to zero. However in more complex Na compounds, such as NKBT, well defined ^{23}Na second-order quadrupolar line shapes are clearly visible.

One of the key objectives in ^{23}Na NMR studies is to try and derive a relationship between a measured NMR parameter (such as chemical shift or the quadrupolar coupling constant χ_Q) and some structural parameters of the material. In fact good correlations

have been found between δ_{iso} and the mean Na-O bond length for groups of sodium-containing compounds such as crystalline silicates[8] and aluminosilicates[9], crystalline germanates[10], borates and carbonates[10] and sodium aluminium flourides[11].

An interesting study of alkali borate glasses by Ratai *et al.*[12] has shown that the ^{23}Na δ_{iso} value becomes more positive on the substitution of K for Na. These observations led to Stebbins[13] suggesting that based on the behaviour of such binary glasses the average size of the sites occupied by a given cation (Na in this case) *increases* with partial substitution by a smaller cation and *decreases* with partial substitution of a larger cation, leading to the conclusion that there must be several other competing factors that determine the actual behaviour of the material.

Another interesting ^{23}Na MAS NMR study by Philips *et al.*[14] on crystalline albite ($NaAlSi_3O_8$) showed that as the composition is doped with increasing amounts of K, the ^{23}Na NMR lineshapes become less resolved due to inhomogeneous line broadening. When the same experiment was repeated at a higher field, as the spectra are now less influenced by the second-order quadrupolar effects, the still substantial broadening is more likely to reflect a range of isotropic chemical shifts, arising from the inhomogeneous distribution of K and Na throughout the sample.

Hence for the ^{23}Na MAS NMR study of the 9 NKBT samples, it was decided to perform the experiment at two different fields 8.45 T and 14.1 T, so that the field dependence of the second-order quadrupolar effects would allow better determination of the interactions taking place within the material. Furthermore in order to investigate the effects of the MAS speed on the linewidths and lineshapes of the spectra all the 8.45 T sodium spectra were acquired at 3 different spinning speeds ~8kHz, ~12kHz, ~16kHz.

Sample	8 kHz		12 kHz		16 kHz	
	Position (ppm)	Width (Hz)	Position (ppm)	Width (Hz)	Position (ppm)	Width (Hz)
25NKBT	-26.2	336	-27	330	-25.7	329
35NKBT	-25.9	367	-26.8	340	-25.6	356
50NKBT	-25.4	472	-26.2	450	-24.9	440
65NKBT	-23.3	501	-24.1	470	-23	471
78NKBT	-24.8	530	-24.8	530	-24.8	515
83NKBT	-23.3	546	-23.7	540	-23.7	515
NBT	-23.2	564	-23	550	-23	574

* Errors: Peak Position ± 1ppm, Width ± 5 Hz

Table 6.1 – ^{23}Na MAS NMR spectral linewidths and shifts at spinning speeds of ~8kHz, ~12kHz, ~16kHz.

As can be seen from Table 6.1 there is no significant difference between the linewidths at three spinning speeds. Hence it can be seen that full narrowing is occurring at 12kHz, so that even though there may be a distribution of interaction parameters they are being narrowed at 12kHz. Hence the actual lineshapes of the spectra are an accurate representation of the sodium environment in the samples. Figure 6.1 below shows the ^{23}Na MAS NMR spectra of the 9 NKBT samples at two different fields

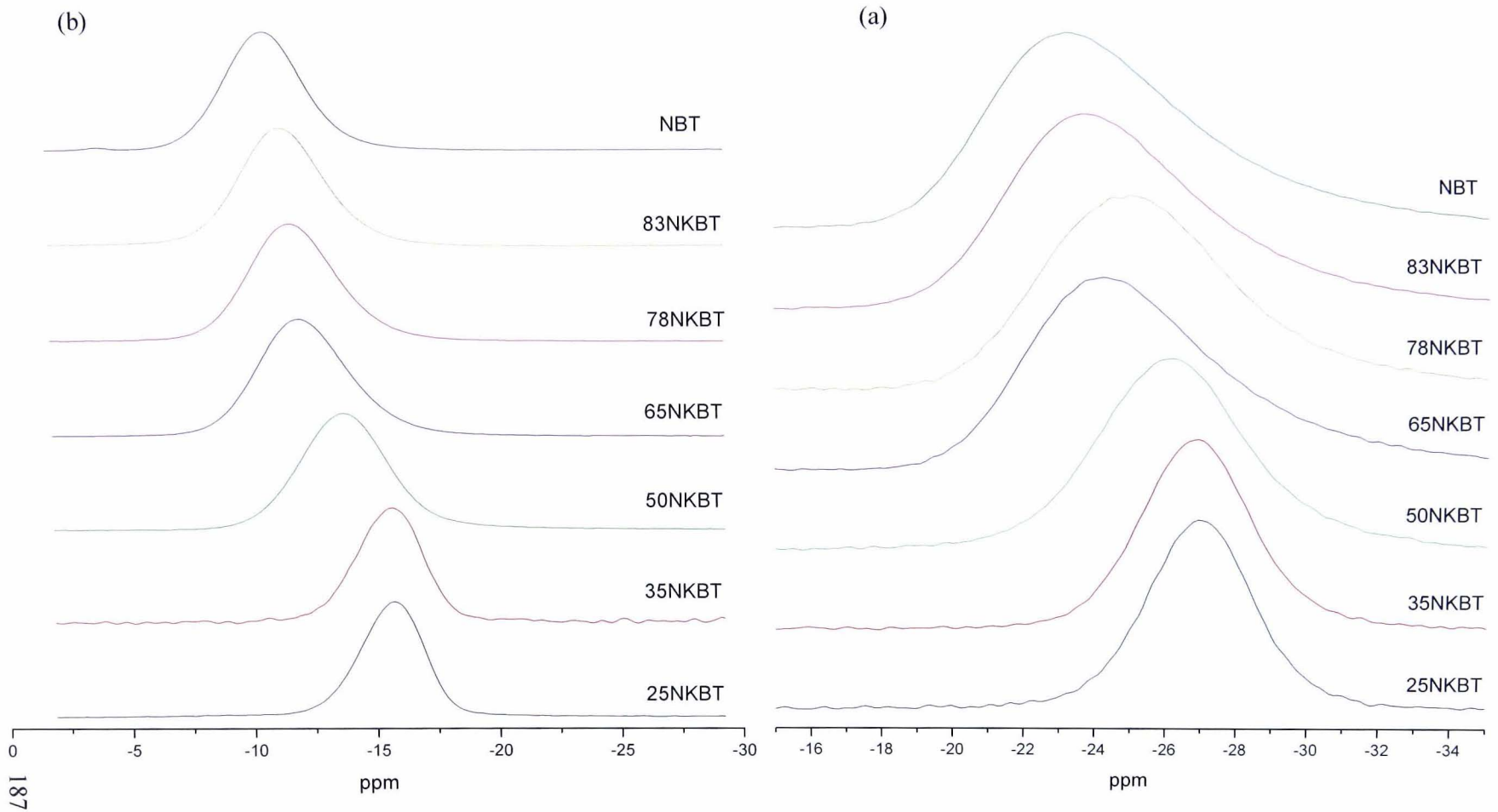

Figure 6.1 – ^{23}Na MAS NMR spectra for NKBT Samples at (a) ~12kHz at 8.45T and (b) ~18kHz at 14.1 T

From Figure 6.1 it is possible to discern that there is a gradual decrease in linewidth and also a negative shift as the K concentration increases. Based on the field dependence of the centre of gravity of a particular peak it is also possible to derive an estimate of the chemical shifts and the quadrupolar effect parameter P_Q. Furthermore P_Q can be used to compute χ_Q based on the relationship $P_Q = \chi_Q(1+\eta^2/3)^{1/2}$. The peak position can also be used to compute the isotropic chemical shift δ_{cs}

$$\delta_{peak} = \delta_{iso} - \frac{P_Q^2}{40\nu_0^2} \tag{6.1}$$

Thus based on the data from two different fields an estimate of both P_Q and δ_{iso} can be found, and these results are shown in Table 6.2 below.

Samples	B0=8.45T		B0=14.1T		P_Q(MHz)	δ_{iso} (ppm)
	Peak Position (ppm)	Linewidth (Hz)	Peak Position (ppm)	Linewidth (Hz)		
25NKBT	-27.0	330	-15.6	450	2.54	-9.2
35NKBT	-26.8	340	-15.6	480	2.52	-9.3
50NKBT	-26.2	450	-13.7	640	2.67	-6.6
65NKBT	-24.1	470	-12.0	660	2.62	-5.2
78NKBT	-24.8	530	-11.7	640	2.73	-4.3
83NKBT	-23.7	540	-11.3	610	2.65	-4.4
100NKBT	-23.0	550	-10.7	580	2.65	-3.7

* Errors: Peak Position ±1 ppm, Widths ±5 Hz, P_Q ± 0.1 MHz, δ_{iso} ±1 ppm

Table 6.2 – ^{23}Na peak positions and linewidths for the sodium-containing NKBT samples at magnetic fields of 8.45 and 14.1T with the isotropic chemical shift and the calculated quadrupolar effect parameter

The spectra with higher concentrations of K appear to be more symmetric. However upon addition of increasing amounts of Na the linewidths begin to increase and the lineshapes appear more asymmetrical. This is quite common phenomenon in quadrupolar nuclei as the asymmetry is usually a result of the superposition of different sites that show small variation in their δ_{iso} while showing a greater variation in the actual site distortion which is manifested through a greater variation in the quadrupolar parameter P_Q. (Refer Table 6.2)

Also it is worthy to note that the sample 78NKBT where the alleged MPB is believed to lie in this system[7] appears to have slightly different characteristics from both the sample with slightly greater or slightly lower K concentrations. This is probably caused by the increased disorder on the A-site as a result of possibly two phases co-existing as an inhomogeneous distribution at the local order level of the material. Hence there is certainly an interesting influence of competing local interactions on the resulting average crystallographic structure around the MPB.

6.4 ^{39}K MAS NMR study of NKBT samples

^{39}K has a natural abundance of 93.1% yet its small magnetic moment and quadrupolar properties (it is a spin I= 3/2 nucleus) mean that to date there have been relatively few NMR studies. ^{39}K MAS NMR often requires the addition of a low frequency converter known as a low-gamma box as most commercial probes do not ordinarily tune to the Larmor frequency of potassium. For our MAS NMR experiments the Larmor frequency of ^{39}K on the 14.1T magnet was 28MHz.

All the ^{39}K MAS NMR spectra shown in Figure 6.2 below have been acquired at 14.1T using the 'Oldfield echo' pulse sequence. The samples were spun at ~18kHz using a Chemagnetics 3.2mm probe and rotor. The samples were all referenced using the shift with respect to dilute aqueous KCl.

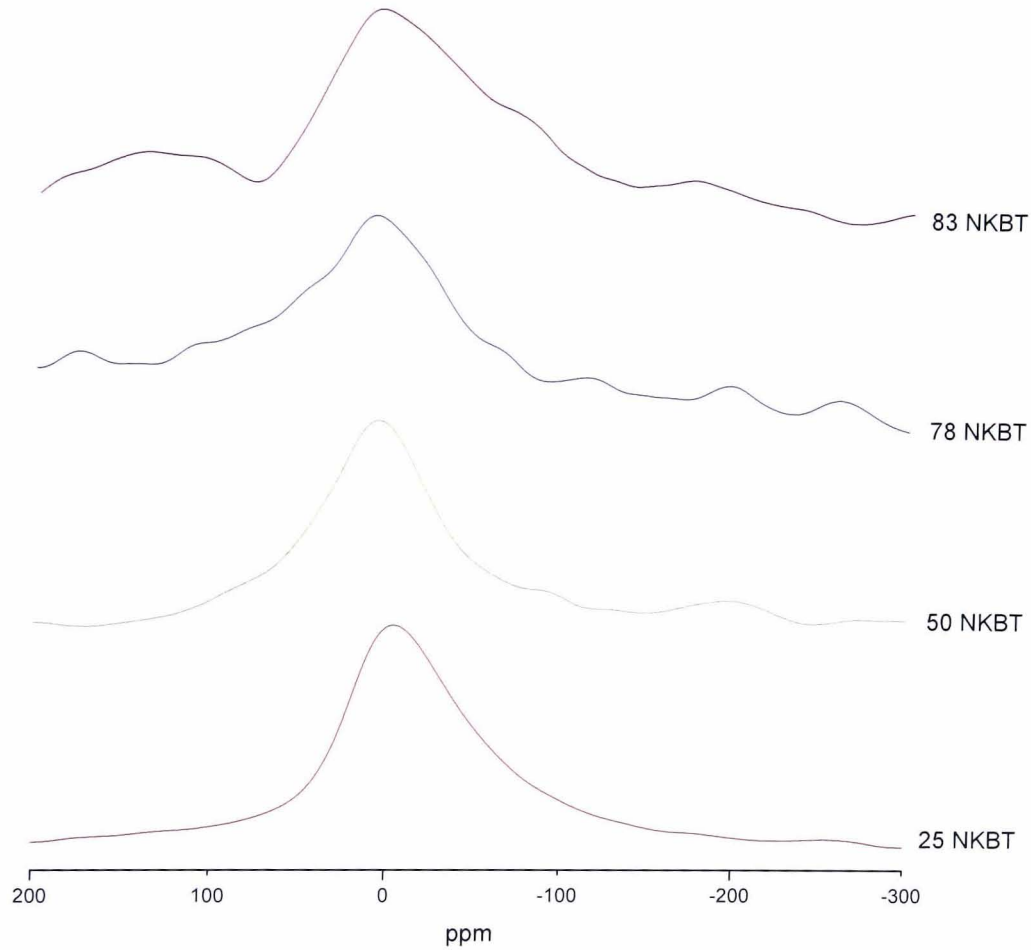

Figure 6.2 – 18kHz ^{39}K MAS NMR spectra for 4 selected NKBT Samples at 14.1 T

Unfortunately the large linewidths as can be seen in the spectra shown in Figure 6.2 above are dominated by chemical shift dispersion though there is also considerable influence of the second-order quadrupolar interaction. It is therefore quite likely that this wide Gaussian-like feature is therefore composed of a considerable range of overlapping K sites making the deconvolution of the spectra more speculative than informative.

From the spectra shown above it is however apparent that as the potassium concentration decreases the spectra becomes more asymmetrical although they do not exhibit any change in overall peak position. Linewidths cannot be accurately measured as there is significant artificial line-broadening owing to both a reduction in potassium concentrations and the combination of the chemical shift dispersion and second-order quadrupolar broadening. No obvious change in the spectral line shape is noticed on either side of the MPB.

However as this is probably the first ^{39}K MAS NMR study of the NKBT series of materials to our knowledge, when combined with the more informative ^{23}Na MAS NMR study in the previous section we can now begin to form a much clearer picture of the changes taking place on the A-site of this material.

6.4 Conclusions and Further work

The ^{23}Na and ^{39}K MAS NMR data have been reported from the A-site substituted phase NKBT. The ^{23}Na data is the more informative and hints that these may be some interesting changes close to the MPB. More detailed work with higher–precision on the compositions around the MPB would be more informative. It may also be possible to look at the ^{17}O environment in these materials by preparing enriched samples using a sol-

gel route. NMR studies at higher fields will also be a distinct advantage as this would reduce errors of the extrapolated isotropic shifts.

References

[1] G. A. Smolenskii, A.I. Agranovskaya, *Soviet Phys.-Solid State* (English translation), 1, 1429 (1959)

[2] S.E. Park, T.R. Shrout, *J.Appl. Phys.*, 82 [4], 1804 (1997)

[3] S.E. Park, S.J. Chung, I.T. Kim, K.S. Hong., *J. Am. Ceram. Soc.*, 77 2641 (1994)

[4] G. A. Smolenskii, A.I. Agranovskaya, *Soviet Phys.-Solid State* (English translation), 2, 2982 (1960)

[5] G.O. Jones, P.A. Thomas, *Acta Cryta B*, 58, 168 (2002)

[6] V.A. Shuvaeva, D.Zekria, A.M. Glaser, Q. Jiang, S.M. Weber, P. Bhattacharya, P.A. Thomas, *Physical Review B*, 71, 174114 (2005)

[7] G. O. Jones, J. Kriesel, V. Jennings, M.A. Geday, P.A. Thomas, A.M. Glazer, *Ferroelectrics*, 270, 191 (2002)

[8] X. Xue, J.F. Stebbins, *Phys. Chem. Minerals*, 20, 297 (1993).

[9] A.M. George, J.F. Stebbins, *Amer. Mineralogist*, 80, 878 (1995)

[10] A.M. George, S. Sen, J.F. Stebbins, *Solid State Nucl. Mag. Reson.*, 10, 9 (1997)

[11] J.F. Stebbins, I. Farnan, N. Dando, S.Y. Tzeng, *J. Amer. Ceram. Soc.*, 75, 3001 (1992)

[12] E. Ratai, M. Janssen, H.Eckert, *Solid State Ionics*, 105, 25 (1998)

[13] J.F. Stebbins, *Solid State Ionics*, 112, 137 (1998)

[14] B.L. Phillips, R.J. Kirkpatrick, G.L. Hovis, *Phys. Chem. Minerals*, 16, 262 (1988)